

HYDRODYNAMICS AND RISK ANALYSIS OF  
ICEBERG IMPACTS WITH OFFSHORE STRUCTURES

By

Kevin Andrew McTaggart

B. Sc. (Civil Engineering) Queen's University at Kingston

M. E. Sc. (Civil Engineering) University of Western Ontario

A THESIS SUBMITTED IN PARTIAL FULFILLMENT OF  
THE REQUIREMENTS FOR THE DEGREE OF  
DOCTOR OF PHILOSOPHY

in

THE FACULTY OF GRADUATE STUDIES  
CIVIL ENGINEERING

We accept this thesis as conforming  
to the required standard

THE UNIVERSITY OF BRITISH COLUMBIA

November 1989

© Kevin Andrew McTaggart, 1989

In presenting this thesis in partial fulfilment of the requirements for an advanced degree at the University of British Columbia, I agree that the Library shall make it freely available for reference and study. I further agree that permission for extensive copying of this thesis for scholarly purposes may be granted by the head of my department or by his or her representatives. It is understood that copying or publication of this thesis for financial gain shall not be allowed without my written permission.

Civil Engineering  
The University of British Columbia  
2075 Wesbrook Place  
Vancouver, Canada  
V6T 1W5

Date:

November 9, 1989

## Abstract

The evaluation of design iceberg impact loads for offshore structures and the influence of hydrodynamic effects on impact loads are examined. Important hydrodynamic effects include iceberg added mass, wave-induced oscillatory iceberg motions, and the influence of a large structure on the surrounding flow field and subsequent velocities of approaching icebergs. The significance of these phenomena has been investigated using a two-body numerical diffraction model and through a series of experiments modelling the drift of various sized icebergs driven by waves and currents approaching a large offshore structure. Relevant findings from the hydrodynamic studies have been incorporated into two probabilistic models which can be used to determine design iceberg collision events with a structure based on either iceberg kinetic energy upon impact or global sliding force acting on the structure. Load exceedence probabilities from the kinetic energy and sliding force models are evaluated using the second-order reliability method. Output from the probabilistic models can be used to determine design collision parameters and to assess whether more sophisticated modelling of various impact processes is required. The influence of the structure on velocities of approaching icebergs is shown to be significant when the structure horizontal dimension is greater than twice the iceberg dimension. As expected, wave-induced oscillatory motions dominate the collision velocity for smaller icebergs but have a negligible effect on velocity for larger icebergs.

# Table of Contents

<b>Abstract</b>	<b>ii</b>
<b>List of Tables</b>	<b>x</b>
<b>List of Figures</b>	<b>xii</b>
<b>Nomenclature</b>	<b>xvii</b>
<b>Acknowledgements</b>	<b>xxv</b>
<b>1 Introduction</b>	<b>1</b>
1.1 Significance of Icebergs in Offshore Operations . . . . .	1
1.1.1 Icebergs at Hibernia . . . . .	3
1.1.2 Iceberg Management Methods . . . . .	3
1.2 Iceberg Impact Forces . . . . .	4
1.2.1 Impact Force as a Function of Iceberg Kinetic Energy . . . . .	5
1.3 Hydrodynamic Considerations for Iceberg Collisions . . . . .	6
1.3.1 Oscillatory Iceberg Motions . . . . .	8
1.3.2 Modification of Iceberg Motions by a Fixed Structure . . . . .	9
1.3.3 Variation of Added Mass with Proximity to Structure . . . . .	9
1.4 Risk Analysis of Iceberg Collisions . . . . .	10
1.4.1 Selection of a Suitable Design Event . . . . .	10
1.4.2 Methods of Ranking Collision Severity . . . . .	12

1.4.3	Methods of Evaluating Exceedence Probabilities . . . . .	13
1.5	Scope of the Present Investigation . . . . .	14
1.5.1	Verification of Numerical Ice Mass Motion Model . . . . .	14
1.5.2	Numerical Study of Iceberg Collision Hydrodynamics . . . . .	15
1.5.3	Physical Modelling of Iceberg Drift Motions Near a Structure . . . . .	15
1.5.4	Kinetic Energy Reliability Model . . . . .	16
1.5.5	Impact Force Reliability Model . . . . .	16
<b>2</b>	<b>Numerical Iceberg Motion Model</b>	<b>17</b>
2.1	General Framework of Model . . . . .	17
2.2	Oscillatory Iceberg Motions . . . . .	18
2.2.1	Theoretical Basis of Diffraction Solution . . . . .	18
2.2.2	Definition of Co-ordinate Systems and Modes of Motion . . . . .	20
2.2.3	Re-formulation of Velocity Potential . . . . .	22
2.2.4	Solution of Diffraction and Radiation Potentials . . . . .	24
2.2.5	Solution of Equations of Motion . . . . .	28
2.3	Mean Drift Motions . . . . .	33
2.3.1	Evaluation of Zero Frequency Added Mass . . . . .	35
2.3.2	Water Drag Forces . . . . .	36
2.3.3	Current Field Near a Large Structure of Arbitrary Shape . . . . .	38
2.3.4	Current Field Near a Large Cylindrical Structure . . . . .	40
2.3.5	Wave Drift Forces . . . . .	41
2.4	Verification of Numerical Model . . . . .	45
2.4.1	Wave-Induced Motions . . . . .	45
2.4.2	Wave Drift Forces . . . . .	50
2.4.3	Zero Frequency Added Masses . . . . .	50

2.4.4	Boundary Element Computation of Current Near Structure . . . .	53
<b>3</b>	<b>Hydrodynamic Aspects of Iceberg Collisions</b>	<b>56</b>
3.1	Modelling of Iceberg Geometry . . . . .	56
3.2	Effective Iceberg Added Mass . . . . .	58
3.2.1	Transient Motions of a Floating Body . . . . .	58
3.2.2	Effective Added Mass for Iceberg Drift Motions . . . . .	60
3.2.3	Effective Added Mass for Iceberg Collisions . . . . .	61
3.2.4	Effective Added Mass Example Problem . . . . .	67
3.3	Iceberg Hydrodynamic Coefficients in Open Water . . . . .	75
3.3.1	Wave Drift Force Coefficients and Surge RAO's . . . . .	75
3.3.2	Zero Frequency Added Mass Coefficients . . . . .	83
3.3.3	Infinite Frequency Added Mass Coefficients . . . . .	84
3.3.4	Water Drag Coefficients . . . . .	87
3.4	Hydrodynamic Interactions between Icebergs and a Large Structure . . .	89
3.4.1	Configuration for Modelling Hydrodynamic Interactions . . . . .	90
3.4.2	Variation of Zero Frequency Added Mass . . . . .	91
3.4.3	Variation of Infinite Frequency Added Mass . . . . .	92
3.4.4	Influence of Structure on Current Driven Impact Velocities . . . .	92
3.4.5	Variation of Wave Drift Forces . . . . .	94
3.4.6	Variation of Oscillatory Surge Motions . . . . .	101
3.4.7	Implications of Hydrodynamic Interactions for Iceberg Collisions .	102
<b>4</b>	<b>Physical Modelling of Iceberg Drift Near a Large Structure</b>	<b>103</b>
4.1	Similitude Requirements . . . . .	104
4.2	Description of Experiments . . . . .	105
4.2.1	Towing Tank . . . . .	105

4.2.2	Structure Model . . . . .	107
4.2.3	Iceberg Models . . . . .	107
4.2.4	Model Iceberg Drag Coefficients . . . . .	109
4.2.5	Environmental Conditions for Drift Studies . . . . .	110
4.2.6	Experimental Procedure . . . . .	112
4.3	Digitizing of Iceberg Trajectories . . . . .	114
4.3.1	Video Camera Configuration . . . . .	115
4.3.2	Reduction of Video Co-ordinates . . . . .	115
4.4	Micro-Computer Digitizing System . . . . .	117
4.4.1	Description of Hardware . . . . .	119
4.4.2	Description of Software . . . . .	120
4.5	Error Analysis of Digitized Co-ordinates . . . . .	121
4.5.1	Mouse Operation Error . . . . .	122
4.5.2	Error Due to Variation of $z$ Co-ordinate . . . . .	124
4.5.3	Summary of Digitizing Errors . . . . .	126
4.6	Variability of Environmental Conditions . . . . .	126
4.7	Analysis of Observed Trajectories . . . . .	127
4.7.1	Reduction of Iceberg Co-ordinates Relative to Structure . . . . .	128
4.7.2	Plotting of Iceberg Trajectories . . . . .	128
4.7.3	Estimation of Impact Velocity and Eccentricity . . . . .	130
4.7.4	Error Estimates for Velocities and Eccentricities . . . . .	135
4.7.5	Presentation of Results . . . . .	136
4.8	Numerical Modelling of Wave Tank Experiments . . . . .	137
4.8.1	Simplified Numerical Drift Model . . . . .	152
4.8.2	Comparison of Numerical and Physical Models . . . . .	157
4.8.3	Comparison of Open Water Velocities for Wave Driven Motions . . . . .	160

4.8.4	Discrepancies between Physical and Numerical Models . . . . .	162
<b>5</b>	<b>Kinetic Energy Design Collision Event</b>	<b>164</b>
5.1	Design Criteria for Iceberg Collisions . . . . .	165
5.2	Description of Second-Order Reliability Method . . . . .	166
5.2.1	Introduction of Failure Function . . . . .	167
5.2.2	Solution in Standard Normal Space . . . . .	168
5.2.3	Failure Probability for Linearized Failure Surface . . . . .	168
5.2.4	Failure Probability for Curved Failure Surface . . . . .	170
5.2.5	SORM Solution for Dependent, Non-Normal Variables . . . . .	173
5.3	Formulation of Failure Function for Iceberg Kinetic Energy . . . . .	175
5.3.1	Idealization of Iceberg Geometry . . . . .	177
5.3.2	Iceberg Added Mass . . . . .	178
5.3.3	Iceberg Velocity . . . . .	178
5.3.4	Summary of Failure Function . . . . .	181
5.4	Application to Selection of a Design Iceberg Collision . . . . .	181
5.4.1	Exceedence Probabilities for a Single Collision . . . . .	182
5.4.2	Extension to Multiple Collisions . . . . .	183
5.5	Example Design Problem for Large Iceberg Population . . . . .	185
5.5.1	Design Criterion . . . . .	185
5.5.2	Statistical Distributions for Input Variables . . . . .	186
5.5.3	Correlated Input Variables . . . . .	188
5.5.4	Computation of Exceedence Probabilities . . . . .	188
5.5.5	Parameters for Design Collision Event . . . . .	189
5.5.6	Exceedence Probabilities without Wave-Induced Motions . . . . .	190
5.6	Example Design Problem for Small Iceberg Population . . . . .	191

<b>6</b>	<b>Impact Sliding Force Design Event</b>	<b>194</b>
6.1	Iceberg Loading of Offshore Structures . . . . .	195
6.1.1	Ice Forces for Head-on Impact . . . . .	195
6.1.2	Ice Forces for Eccentric Impact . . . . .	197
6.1.3	Selection of Effective Ice Pressure . . . . .	198
6.2	Failure Function for Iceberg Impact Force Reliability Model . . . . .	202
6.3	Impact Velocity Phase of Reliability Model . . . . .	204
6.3.1	Equations of Drift Motion . . . . .	205
6.3.2	Initial Conditions for Simulated Drift Trajectories . . . . .	205
6.3.3	Hydrodynamic Coefficients for Drift Motions . . . . .	207
6.3.4	Variation of Water Velocity . . . . .	207
6.3.5	Iceberg Impact Velocity . . . . .	208
6.4	Impact Force Model . . . . .	208
6.4.1	Development of Impact Forces . . . . .	209
6.4.2	Collision Geometry . . . . .	209
6.4.3	Pressure Calculation Method . . . . .	211
6.4.4	Iceberg Equations of Motion . . . . .	212
6.4.5	Time-Stepping Procedure . . . . .	213
6.5	Example Problem for Large Iceberg Population . . . . .	215
6.5.1	Design Criterion and Input Distributions . . . . .	215
6.5.2	Design Event for Constant Ice Pressure . . . . .	217
6.5.3	Design Event for Varying Ice Pressure with Area . . . . .	219
6.6	Example Problem for Small Iceberg Population . . . . .	220
6.6.1	Design Collision for Constant Ice Pressure . . . . .	221
6.6.2	Design Collision for Varying Ice Pressure . . . . .	222

<b>7</b>	<b>Conclusions</b>	<b>224</b>
7.1	Effective Added Mass . . . . .	224
7.2	Oscillatory Surge Motions . . . . .	225
7.3	Influence of Structure on Iceberg Hydrodynamics . . . . .	226
7.4	Kinetic Energy Reliability Model . . . . .	228
7.5	Impact Force Reliability Model . . . . .	228
7.6	Recommendations for Future Research . . . . .	229
	<b>Bibliography</b>	<b>231</b>

## List of Tables

2.1	Hydrodynamic Properties of Barge . . . . .	46
3.1	Input Parameters for Comparison of Ramp and Time Stepping Models . . . . .	71
4.1	Specifications for BC Research Towing Tank . . . . .	107
4.2	Dimensions of Model Icebergs . . . . .	109
4.3	Environmental Conditions for Model Tests . . . . .	111
4.4	Number of Tests for Each Model and Environmental Condition . . . . .	113
4.5	Occurrence of Impacts for Experiments . . . . .	130
4.6	Errors between Numerical and Physical Models for Collision Eccentricity . . . . .	159
4.7	Errors between Numerical and Physical Models for Velocity Ratio . . . . .	159
4.8	Comparison of Open Water Drift Velocities for First Wave Condition . . . . .	161
4.9	Comparison of Open Water Drift Velocities for Second Wave Condition . . . . .	161
5.1	Input Distributions for Example Design Problem . . . . .	186
5.2	Distribution Moments for All Icebergs and Impacting Icebergs . . . . .	187
5.3	Results for Large Iceberg Design Collision . . . . .	190
5.4	Results for Small Iceberg Design Collision . . . . .	193
6.1	Input Distributions for Large Iceberg Example Design Problem . . . . .	216
6.2	Results for Large Iceberg Collision, Constant Ice Pressure . . . . .	218
6.3	Results for Large Iceberg Collision, Pressure-Area Variation . . . . .	220
6.4	Results for Small Iceberg Collision, Constant Ice Pressure . . . . .	222

6.5 Results for Small Iceberg Collision, Pressure-Area Variation . . . . .	223
--	-----

## List of Figures

1.1	Major Iceberg Drift Paths . . . . .	2
1.2	Schematic of an Iceberg Collision with a Fixed Structure . . . . .	7
1.3	Boundary Element Grid for Three-Dimensional Solution, Elevation View	11
1.4	Boundary Element Grid for Two-Dimensional Solution, Plan View . . . .	11
2.1	Co-ordinate Systems for Iceberg Motion Model . . . . .	21
2.2	Control Surface for Far-field Wave Drift Force Computation . . . . .	43
2.3	Barge for Verifying Diffraction Computations . . . . .	46
2.4	Barge Surge Motions in Head Waves . . . . .	47
2.5	Barge Heave Motions in Head Waves . . . . .	47
2.6	Barge Pitch Motions in Head Waves . . . . .	48
2.7	Barge Sway Motions in Beam Waves . . . . .	48
2.8	Barge Heave Motions in Beam Waves . . . . .	49
2.9	Barge Roll Motions in Beam Waves . . . . .	49
2.10	Barge Wave Drift Forces in Head Waves . . . . .	51
2.11	Barge Wave Drift Forces in Beam Waves . . . . .	51
2.12	Zero Frequency Added Masses for Vertical Circular Cylinders . . . . .	52
2.13	Zero Frequency Added Masses Approaching Structure . . . . .	54
2.14	Current Velocity in Vicinity of Structure . . . . .	55
3.1	Frequency Dependent Added Mass and Damping for Example Iceberg . .	68
3.2	History Term for Example Iceberg . . . . .	69

3.3	Effective Added Mass for Example Iceberg, Ramp Forcing Function . . . . .	70
3.4	Collision Duration for Ramp and Time Stepping Models . . . . .	73
3.5	Effective Added Mass for Ramp and Time Stepping Models . . . . .	73
3.6	Impact Force for Ramp and Time Stepping Models . . . . .	74
3.7	Ice Penetration for Ramp and Time Stepping Models . . . . .	74
3.8	Computed Surge RAO's, Aspect Ratio = 0.1 . . . . .	78
3.9	Computed Surge RAO's, Aspect Ratio = 0.2 . . . . .	79
3.10	Computed Surge RAO's, Aspect Ratio = 0.4 . . . . .	79
3.11	Computed Surge RAO's, Aspect Ratio = 0.6 . . . . .	80
3.12	Computed Surge RAO's, Aspect Ratio = 0.8 . . . . .	80
3.13	RAO's from Numerical Model and High Frequency Approximation . . . . .	83
3.14	Computed Wave Drift Coefficients, Aspect Ratio = 0.1 . . . . .	84
3.15	Computed Wave Drift Coefficients, Aspect Ratio = 0.2 . . . . .	85
3.16	Computed Wave Drift Coefficients, Aspect Ratio = 0.4 . . . . .	85
3.17	Computed Wave Drift Coefficients, Aspect Ratio = 0.6 . . . . .	86
3.18	Computed Wave Drift Coefficients, Aspect Ratio = 0.8 . . . . .	86
3.19	Computed Zero Frequency Added Masses . . . . .	87
3.20	Computed Infinite Frequency Added Masses . . . . .	88
3.21	Variation of Drag Coefficient with Aspect Ratio . . . . .	89
3.22	Zero Frequency Added Mass near Structure . . . . .	92
3.23	Infinite Frequency Added Mass near Structure . . . . .	93
3.24	Relative Impact Velocities for Current Driven Head-on Collisions . . . . .	94
3.25	Variation of Wave Drift Coefficients with Proximity to Structure . . . . .	95
3.26	Influence of Wave Period on Wave Drift Forces near Structure . . . . .	96
3.27	Open Water Wave Drift Force Coefficient . . . . .	97
3.28	Wave Drift Force Variation Amplitude Coefficient . . . . .	97

3.29	Wave Drift Force Variation Decay Coefficient . . . . .	98
3.30	Wave Drift Force Variation Phase Coefficient . . . . .	98
3.31	Influence of Aspect Ratio on Wave Drift Forces near Structure . . . . .	99
3.32	Influence of Lateral Offset on Wave Drift Forces near Structure . . . . .	100
3.33	Variation of Oscillatory Surge Motions near Structure . . . . .	101
4.1	Elevation View of BC Research Towing Tank . . . . .	108
4.2	Elevation View of Structure and Iceberg Models . . . . .	108
4.3	Drag Coefficients for 400 mm Diameter Iceberg Model . . . . .	110
4.4	Overhead View of 400 mm Iceberg Approaching Structure . . . . .	114
4.5	Elevation View of Video Image Planes . . . . .	117
4.6	$x-y$ and $x'-y'$ Co-ordinate Systems and Relevant Dimensions . . . . .	118
4.7	Schematic of Video Digitizing System . . . . .	119
4.8	Elevation View of Reference Distance and Corresponding Image Distance . . . . .	124
4.9	Observed Iceberg Trajectory and Displacement vs. Time Graphs . . . . .	129
4.10	Observed Trajectory for Wave Condition 1, Model 1 . . . . .	131
4.11	Far-field and Near-field Eccentricities of Approach for an Iceberg . . . . .	133
4.12	Iceberg Eccentricity and Velocity, Currents, Model 1 . . . . .	138
4.13	Iceberg Eccentricity and Velocity, Currents, Model 2 . . . . .	139
4.14	Iceberg Eccentricity and Velocity, Currents, Model 3 . . . . .	140
4.15	Iceberg Eccentricity and Velocity, Currents, Model 4 . . . . .	141
4.16	Iceberg Eccentricity and Velocity, Wave Condition 1, Model 3 . . . . .	142
4.17	Iceberg Eccentricity and Velocity, Wave Condition 1, Model 4 . . . . .	143
4.18	Iceberg Eccentricity and Velocity, Wave Condition 2, Model 3 . . . . .	144
4.19	Iceberg Eccentricity and Velocity, Wave Condition 2, Model 4 . . . . .	145
4.20	Iceberg Eccentricity and Velocity, Wave-Current Condition 1, Model 1 . . . . .	146

4.21	Iceberg Eccentricity and Velocity, Wave-Current Condition 1, Model 2 . . .	147
4.22	Iceberg Eccentricity and Velocity, Wave-Current Condition 1, Model 3 . . .	148
4.23	Iceberg Eccentricity and Velocity, Wave-Current Condition 2, Model 1 . . .	149
4.24	Iceberg Eccentricity and Velocity, Wave-Current Condition 2, Model 2 . . .	150
4.25	Iceberg Eccentricity and Velocity, Wave-Current Condition 2, Model 3 . . .	151
4.26	Wave Drift Forces near Structure, No Current, 0.7 s Wave Period . . . . .	153
4.27	Wave Drift Forces near Structure, No Current, 1.0 s Wave Period . . . . .	153
4.28	Wave Drift Forces near Structure, Current, 0.7 s Wave Period . . . . .	154
4.29	Wave Drift Forces near Structure, Current, 1.0 s Wave Period . . . . .	154
4.30	Open Water Wave Drift Force Coefficients . . . . .	155
4.31	Amplitude Coefficient for Variation of Wave Drift Forces . . . . .	155
4.32	Decay Coefficient for Variation of Wave Drift Forces . . . . .	156
4.33	Phase Coefficient for Variation of Wave Drift Forces . . . . .	156
5.1	Standard Space for 2 Random Variables . . . . .	169
5.2	Influence of Curved Failure Surface . . . . .	171
5.3	Flow Chart for Second-Order Reliability Method . . . . .	176
5.4	Kinetic Energy Exceedence Probabilities for a Single Collision . . . . .	189
5.5	Comparison of SORM and Analytical Model Results . . . . .	191
5.6	Kinetic Energy Exceedence Probabilities for Small Iceberg Example . . .	192
6.1	Ice Indentation for Korzhavin's Experiments . . . . .	200
6.2	Pressure vs. Area Measurements for Ice Strength . . . . .	202
6.3	Initial Conditions for Iceberg Drift Trajectory toward Structure . . . . .	206
6.4	Eccentric Iceberg Collision Schematic, Plan View . . . . .	210
6.5	Large Iceberg Force Exceedence Probabilities, Constant Ice Pressure . . .	217
6.6	Large Iceberg Force Exceedence Probabilities, Pressure-Area Variation .	219

6.7. Small Iceberg Force Exceedence Probabilities, Constant Ice Pressure . . .	221
6.8 Small Iceberg Force Exceedence Probabilities, Pressure-Area Variation . .	223

## Nomenclature

- $a$  = acceleration ( $\text{m/s}^2$ ) or cylinder radius (m)
- $A(\omega)$  = Fourier transform of acceleration
- $[A]$  = matrix for solution of wave source strengths
- $[A_c]$  = matrix for solution of current source strengths
- $A_{C_w}$  = wave drift variation amplitude coefficient
- $A_F, B_F, C_F$  = coefficients for approximating iceberg trajectory in far-field
- $A_N, B_N, C_N$  = coefficients for approximating iceberg trajectory in near-field
- $A_n$  = normal contact area between ice and structure ( $\text{m}^2$ )
- $A_t$  = tangential contact area between ice and structure ( $\text{m}^2$ )
- $A_w$  = water cross-sectional area of iceberg ( $\text{m}^2$ )
- $A_{wp}$  = iceberg waterplane area ( $\text{m}^2$ )
- $[B]$  = matrix for solution of wave source potentials
- $[B_c]$  = matrix for solution of current source potentials
- $B_{C_w}$  = wave drift variation decay coefficient ( $\text{m}^{-1}$ )
- $[c]$  = hydrodynamic stiffness matrix
- $C_{C_w}$  = wave drift variation phase coefficient (m)
- $C_d$  = water drag coefficient
- $C_I$  = added inertia coefficient
- $C_m$  = added mass coefficient
- $C_w$  = wave drift force coefficient
- $C_{wo}$  = wave drift force coefficient in open water

- $d$  = water depth (m)
- $[D']$  = diagonal matrix of effective standard deviations
- $D_i$  = iceberg diameter (m)
- $D_s$  = structure diameter (m)
- $E(x^r)$  = expected value of  $x^r$
- $e_c$  = eccentricity of iceberg impact (m)
- $e'_c$  = dimensionless impact eccentricity
- $e_F$  = approach eccentricity in far-field (m)
- $e_N$  = approach eccentricity in near-field (m)
- $e_o$  = initial eccentricity of approach (m)
- $e'_o$  = dimensionless approach eccentricity
- $F$  = iceberg impact force (N)
- $\{F'\}$  = vector of unit exciting forces
- $F_a$  = air drag force (N)
- $F_C$  = Coriolis force (N)
- $F_c$  = maximum iceberg impact force (N)
- $F_{cr}$  = ice crushing force (N)
- $F_d$  = water drag force (N)
- $f_e$  = forcing function (s)
- $F_e(\omega)$  = Fourier transform of  $f_e$
- $\{F_e\}$  = excitation force vector
- $F_f$  = friction force (N)
- $\{f_k\}$  = source strength vector for potential  $\phi_k$  (dimensionless or m)
- $F_L$  = impact force load (N)
- $F_R$  = structure impact force resistance (N)

- $F_t$  = tangential force acting on iceberg (N)  
 $F_w$  = wave drift force (N)  
 $f_X(X)$  = PDF for variable  $X$   
 $F_X(X)$  = CDF for variable  $X$   
 $f_{\vec{X}}(\vec{X})$  = joint probability density function of  $\vec{X}$   
 $F_x, F_y$  =  $x - y$  force components acting on iceberg (N)  
 $G$  = Green's function ( $m^{-1}$ ) or failure function  
 $G^*$  = modified Green's function ( $m^{-1}$ )  
 $G(x', y', z')$  = co-ordinate system with origin at iceberg centre of gravity  
 $G(\vec{X})$  = failure function  
 $\{G'(\vec{Y}^*)\}$  = vector of first-order partial derivatives of  $G$   
 $[G''(\vec{Y}^*)]$  = matrix of second-order partial derivatives of  $G$   
 $h$  = iceberg draft (m)  
 $H$  = wave height (m)  
 $\{H\}$  = memory effect vector  
 $[H]$  = transformation matrix  
 $h_t$  = total vertical dimension of iceberg (m)  
 $H_{rms}$  = root-mean-square wave height (m)  
 $H_s$  = significant wave height (m)  
 $I$  = indentation factor  
 $[I]$  = identity matrix  
 $I_{ij}$  = iceberg moment or product of inertia ( $kg \cdot m^2$ )  
 $I_w$  = iceberg rotational inertia ( $kg \cdot m^2$ )  
 $J_0$  = Bessel function of first kind, order 0  
 $k$  = wavenumber ( $m^{-1}$ ) or contact factor

- $K_0$  = modified Bessel function of second kind, order 0  
 $k_F$  = ice force constant ( $\text{N}/\text{m}^{1/2}$ )  
 $k_s$  = video image scale factor (/pixel)  
 $KE$  = kinetic energy of impacting iceberg (Joules)  
 $L$  = distance from camera to  $x' - y'$  plane (m)  
 $L$  = history term (kg/s, kg·m/s, or, kg·m<sup>2</sup>/s )  
 $L_t$  = distance from camera to  $x - y - z$  origin (m)  
 $M$  = iceberg mass (kg)  
 $m$  = indenter shape factor  
 $[m]$  = iceberg mass matrix  
 $\{M'\}$  = vector of effective means  
 $M_v$  = virtual iceberg mass (kg)  
 $\mathbf{n}$  = unit normal vector  
 $n_c$  = number of collisions  
 $N_i$  = number of facets on iceberg surface  
 $n_k$  = unit normal velocity for mode  $k$   
 $n_L$  = number of iceberg collisions during structure lifetime  
 $N_{rv}$  = number of input random variables  
 $N_s$  = number of facets on structure surface  
 $n_x, n_y, n_z$  = directional cosines of normal vector pointing outward from body  
 $O(x, y, z)$  = co-ordinate system with origin at centre of structure at the waterline  
 $p_{cr}$  = ice crushing pressure ( $\text{N}/\text{m}^2$ )  
 $p_r$  = reference ice pressure ( $\text{N}/\text{m}^2$ )  
 $R_{ij}$  = element of original correlation matrix  
 $R_{0ij}$  = element of modified correlation matrix

- $R_F$  = structure force resistance (N)  
 $R_{KE}$  = structure kinetic energy resistance (Joules)  
 $r_{ti}$  = moment arm for frictional torque acting on iceberg (m)  
 $s_n$  = iceberg normal displacement relative to structure (m)  
 $s_{nc}$  = maximum normal displacement relative to structure (m)  
 $s_t$  = iceberg tangential displacement relative to structure (m)  
 $s_{tc}$  = maximum tangential displacement relative to structure (m)  
 $T$  = wave period (s)  
 $[T]$  = transformation matrix  
 $t_c$  = collision duration (s)  
 $T_c$  = wave period in presence of a current (s)  
 $T_L$  = operating life for structure (years)  
 $T_p$  = peak wave period  
 $T_r$  = rotational torsion acting on iceberg (N·m)  
 $u, v$  = iceberg velocity components (m/s)  
 $u_t$  = tangential velocity of iceberg face relative to structure face (m/s)  
 $u_w, v_w$  = water velocity components (m/s)  
 $V_c$  = iceberg impact velocity (m/s)  
 $V_d$  = iceberg drift velocity (m/s)  
 $V_f$  = iceberg translational velocity after collision (m/s)  
 $V_{Fx}, V_{Fy}$  = far-field velocity components (m/s)  
 $V_n$  = velocity component in direction of vector component n (m/s)  
 $V_n$  = iceberg velocity normal to structure (m/s)  
 $V_{Nx}, V_{Ny}$  = near-field velocity components (m/s)  
 $V_r$  = iceberg velocity relative to current (m/s)

- $V_s$  = iceberg significant oscillatory surge velocity (m/s)  
 $V_w$  = water velocity (m/s)  
 $V_{wo}$  = incident current velocity (m/s)  
 $\{Y\}$  = transformed vector of independent, standard normal variables  
 $\{Y^*\}$  = design point in standard normal  
 $Y_0$  = Bessel function of second kind, order 0  
 $\vec{x}$  = location of point in fluid domain  
 $\{X\}$  = vector of random variables  
 $\{X^*\}$  = design point  
 $x'', y''$  = video image co-ordinates (pixels)  
 $x_F, y_F$  = iceberg co-ordinates in far-field (m)  
 $x_g, y_g, z_g$  = location of iceberg centre of gravity relative to structure (m)  
 $x_N, y_N$  = iceberg co-ordinates in near-field (m)  
 $\{Z\}$  = random vector in transformed space  
 $z'_b$  =  $z'$  co-ordinate of iceberg centre of buoyancy (m)  
 $\alpha$  = incident wave direction ( $^\circ$ )  
 $\{\alpha\}$  = vector of sensitivity coefficients  
 $\beta$  = reliability index or incident current direction ( $^\circ$ )  
 $[\Gamma_0]$  = transformation matrix accounting for correlation of variables  
 $\Delta$  = iceberg penetration distance during collision (m)  
 $\Delta_c$  = maximum penetration distance (m)  
 $\delta_{ij}$  = correlation correction factor  
 $\delta_k$  = phase angle for mode  $k$  ( $^\circ$ )  
 $\Delta S$  = facet area ( $m^2$ )  
 $\Delta v$  = change in iceberg velocity in response to forcing function ( $s^2/kg$ )

- $\Delta y_s$  = distance between reference points for evaluating  $k_s$  (m)
- $\Delta y_s''$  = image distance between reference points (pixels)
- $\epsilon''$  = error in mouse digitizing position (pixels)
- $\epsilon_s''$  = image error in scale reference distance (pixels)
- $\epsilon_x$  = error in reduced  $x$  co-ordinate (m)
- $\epsilon_y$  = error in reduced  $y$  co-ordinate (m)
- $\epsilon_z$  = error in  $z$  co-ordinate (m)
- $\zeta_k$  = amplitude of oscillatory motion for mode  $k$  (m or rad)
- $\zeta'_k$  = response amplitude operator for mode  $k$  (m/m or /m)
- $\eta$  = vertical displacement of water surface (m)
- $\theta$  = angle of camera orientation from vertical ( $^\circ$ )
- $\theta_c$  = contact point angle between iceberg and structure (rad)
- $\theta_r$  = iceberg rotational displacement (rad)
- $\lambda$  = wavelength (m)
- $[\lambda]$  = radiation damping matrix
- $\lambda_c$  = mean rate of iceberg collisions (/year)
- $\lambda_L$  = length scale
- $\lambda_t$  = time scale
- $[\lambda_v]$  = viscous damping matrix
- $[\mu]$  = added mass matrix
- $\mu_f$  = ice friction coefficient
- $\mu_x^r$  =  $r$ 'th moment of random variable  $x$
- $\nu$  = kinematic viscosity of water ( $\text{m}^2/\text{s}$ )
- $\vec{\xi}$  = location of source on iceberg or structure surface
- $[\rho]$  = correlation coefficient matrix

- $\rho$  = water density (kg/m<sup>3</sup>)  
 $\rho_i$  = ice density (kg/m<sup>3</sup>)  
 $\sigma$  = standard deviation  
 $\sigma_c$  = uni-axial compressive strength of ice (N/m<sup>2</sup>)  
 $\sigma_x$  = standard error of reduced  $x$  co-ordinate (m)  
 $\sigma_y$  = standard error of reduced  $y$  co-ordinate (m)  
 $\psi_d$  = drift velocity modification factor  
 $\psi_s$  = oscillatory velocity modification factor  
 $\Phi$  = wave field velocity potential (m<sup>2</sup>/s)  
 $\phi$  = complex velocity potential (m<sup>2</sup>)  
 $\Phi_c$  = water current velocity potential (m<sup>2</sup>/s)  
 $\Phi_{cd}$  = diffracted current potential (m<sup>2</sup>/s)  
 $\Phi_{ci}$  = incident current potential (m<sup>2</sup>/s)  
 $\phi_k$  = potential due to unit motions in mode  $k$  (m/m or /m)  
 $\phi(x)$  = probability density function for standard normal distribution  
 $\Phi(x)$  = cumulative distribution function for standard normal distribution  
 $\phi_0$  = incident wave potential (m)  
 $\phi_7$  = diffracted wave potential (m)  
 $\omega$  = angular wave frequency (rad/s)  
 $\omega_f$  = iceberg rotational velocity after collision (rad/s)  
 $\omega_c$  = angular wave frequency in current (rad/s)  
 $\omega_p$  = peak angular wave frequency (rad/s)  
 $\omega_r$  = rotational velocity of iceberg (rad/s)

## Acknowledgements

I would like to express my appreciation to several people for their help during the course of my research. I am most grateful to the members of my advisory committee for their constructive comments. The co-operation and assistance of the staff of the BC Research Ocean Engineering Centre during the experimental program is greatly appreciated. I am also thankful to my various graduate student colleagues, particularly to those who helped with the experimental work at BC Research. The assistance of Professor Greg Lawrence with development of the micro-computer digitizing system is gratefully acknowledged. Most importantly, I would like to thank my research advisor Professor Michael Isaacson for his enthusiastic supervision and careful guidance throughout the duration of my work.

Financial support for this study was provided by the Natural Sciences and Engineering Research Council of Canada.

# Chapter 1

## Introduction

The quest for new petroleum reserves has led to exploration and production in offshore regions. As the search for new reserves continues, increasingly hostile environments are being encountered. Structural designers are being faced with the combined challenges of high loads and limited previous experience in such regions. Among the various environmental loads encountered, ice loads originating from landfast or drifting ice are among the most severe in many polar and sub-polar regions. The prediction of ice loads is very difficult due to the complexities of ice mass dynamics, collision mechanics, and material properties. The inherent uncertainties regarding ice loading necessitates the use of probabilistic methods for the development of rational structural design criteria.

### 1.1 Significance of Icebergs in Offshore Operations

Icebergs present one of the most severe threats to offshore installations in sub-polar regions, particularly off the coast of Newfoundland. The majority of icebergs are calved from glaciers on the coast of Greenland and are left to drift freely under the influence of winds, currents, and waves. Major iceberg drift patterns around Greenland and the eastern coast of Canada are illustrated in Figure 1.1.

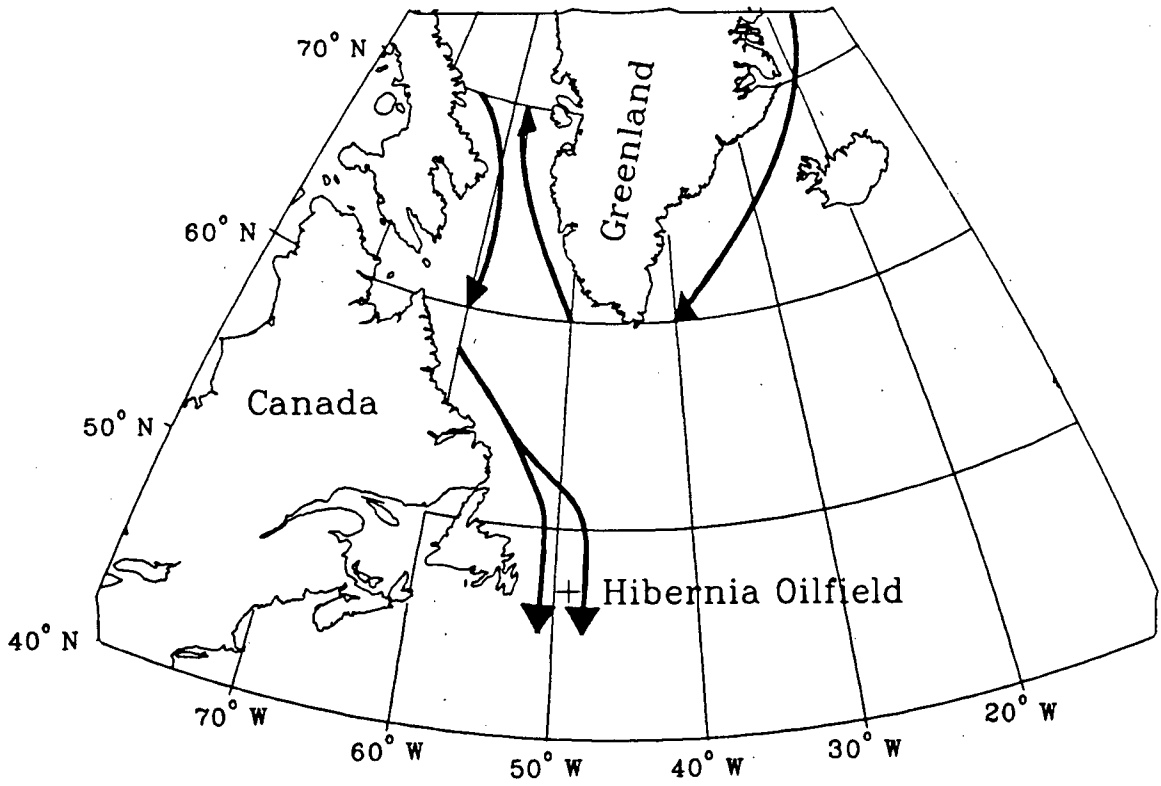


Figure 1.1: Major Iceberg Drift Paths (from Mobil [80])

### 1.1.1 Icebergs at Hibernia

Among the areas most susceptible to icebergs is the Hibernia oilfield, whose location illustrated in Figure 1.1 is among major drift tracks. Annual records of the number of icebergs reaching  $48^{\circ}$  N have been compiled by the International Ice Patrol (IIP) and indicate that an average of 379 icebergs reached  $48^{\circ}$  N annually between 1900 and 1979 [62]. The average iceberg mass in the Grand Banks region is estimated to be approximately 0.6 million tonnes [80].

### 1.1.2 Iceberg Management Methods

When operating in iceberg infested waters, an appropriate iceberg management system is essential. The following three options are available for reducing the risk of iceberg collision damage:

1. Iceberg towing,
2. Iceberg avoidance,
3. Iceberg destruction,
4. Utilization of a structure capable of withstanding iceberg impacts.

These four options will now be discussed in greater detail.

Iceberg towing can be accomplished using one or more tugs [10]. One of the most difficult aspects of iceberg towing is the selection of an appropriate direction for applying a towing force. An incorrectly applied towing force can increase the risk of an iceberg collision. Adverse weather phenomena such as fog and heavy seas greatly reduce the feasibility of towing operations. Because of its limitations, iceberg towing should not be the sole component of an iceberg management system.

Iceberg avoidance action in the form of site evacuation is often taken when an iceberg is approaching a semi-submersible drilling unit. A lead time of several hours is usually required for a semi-submersible to terminate drilling operations and to evacuate a site. Due to the unpredictability of iceberg motions, evacuation measures are often taken even when the probability of collision is relatively small.

Iceberg destruction can be accomplished using explosives placed on an iceberg. Due to the inherent instability of many icebergs, the placement of explosives on an iceberg can pose great danger to a landing crew. Like iceberg towing, iceberg destruction operations can be interrupted by adverse weather conditions. Another drawback of iceberg destruction is the possibility of a large iceberg being broken into a small number of large segments, thus resulting in no effective reduction of the risk of iceberg impact.

The remaining alternative is to build a structure capable of withstanding all iceberg impacts during its lifetime. The capability of withstanding iceberg collisions would probably not be economically justifiable for a semi-submersible unit; however, such capability would be very desirable for a fixed production structure. The construction of an iceberg resistant gravity based production structure for operation off the coast of Newfoundland has been proposed by Mobil Oil Company [80].

## 1.2 Iceberg Impact Forces

When evaluating iceberg collisions, the structural designer is primarily interested in the maximum impact force experienced by the structure. A representative iceberg collision is illustrated in Figure 1.2. Several methods are available for calculating iceberg impact loads [18], and are discussed in greater detail in Chapter 6. Each method is based upon the following equation:

$$F = p_{cr}(\Delta) A_n(\Delta) \quad (1.1)$$

where:

$A_n$  = normal contact area ( $\text{m}^2$ )

$F$  = impact force (N)

$p_{cr}$  = ice crushing pressure ( $\text{N}/\text{m}^2$ )

$\Delta$  = penetration distance (m)

The crushing pressure  $p_{cr}$  is a function of many variables, including ice compressive strength and the geometry of the collision. Determination of the normal contact area  $A_n$  is relatively simple given the geometry of the structure and ice mass.

### 1.2.1 Impact Force as a Function of Iceberg Kinetic Energy

Various methods are available for calculating the maximum impact load experienced during a collision, as discussed by Croasdale [19]. For icebergs impacting a large structure, the limit momentum approach can be used to equate the kinetic energy of the impacting iceberg with the energy dissipated during the collision and to predict the maximum impact load. For a direct iceberg impact, the following relationship will exist:

$$\frac{1}{2}(1 + C_m) M V_c^2 + \int_0^{\Delta_c} F_e(\Delta) d\Delta = \int_0^{\Delta_c} F(\Delta) d\Delta \quad (1.2)$$

where:

$C_m$  = iceberg added mass coefficient

$F_e$  = external environmental force acting on iceberg (N)

$F$  = impact force (N)

$M$  = iceberg mass (kg)

$V_c$  = impact velocity (m/s)

$\Delta_c$  = maximum penetration distance (m)

The external force  $F_e$  acting on the ice mass will include components from ocean currents, wind, waves, and Coriolis force. Hydrodynamic added mass is excluded from  $F_e$ , and is incorporated in the term  $C_m$ . Because of the small magnitude of external forces relative to impact forces, the external force term is usually neglected in equation 1.2. If the iceberg were to roll from a metastable equilibrium to a stable equilibrium during a collision, then additional kinetic energy would be available to contribute to impact forces acting on the structure. For eccentric iceberg collisions, the amount of kinetic energy dissipated during impact can be significantly reduced.

### 1.3 Hydrodynamic Considerations for Iceberg Collisions

Of the variables given in Equation 1.2, iceberg added mass and impact velocity will be primarily influenced by hydrodynamic effects. Although hydrodynamic effects have been largely neglected in previous studies, they can play a significant role in iceberg impacts [17,46,47,60]. The following three effects can influence the severity of iceberg collisions:

1. Wave-induced oscillatory iceberg motions,
2. Modification of iceberg motions by the presence of a large structure,
3. Variation of iceberg added mass with proximity to structure.

These phenomenon will now be discussed in greater detail.

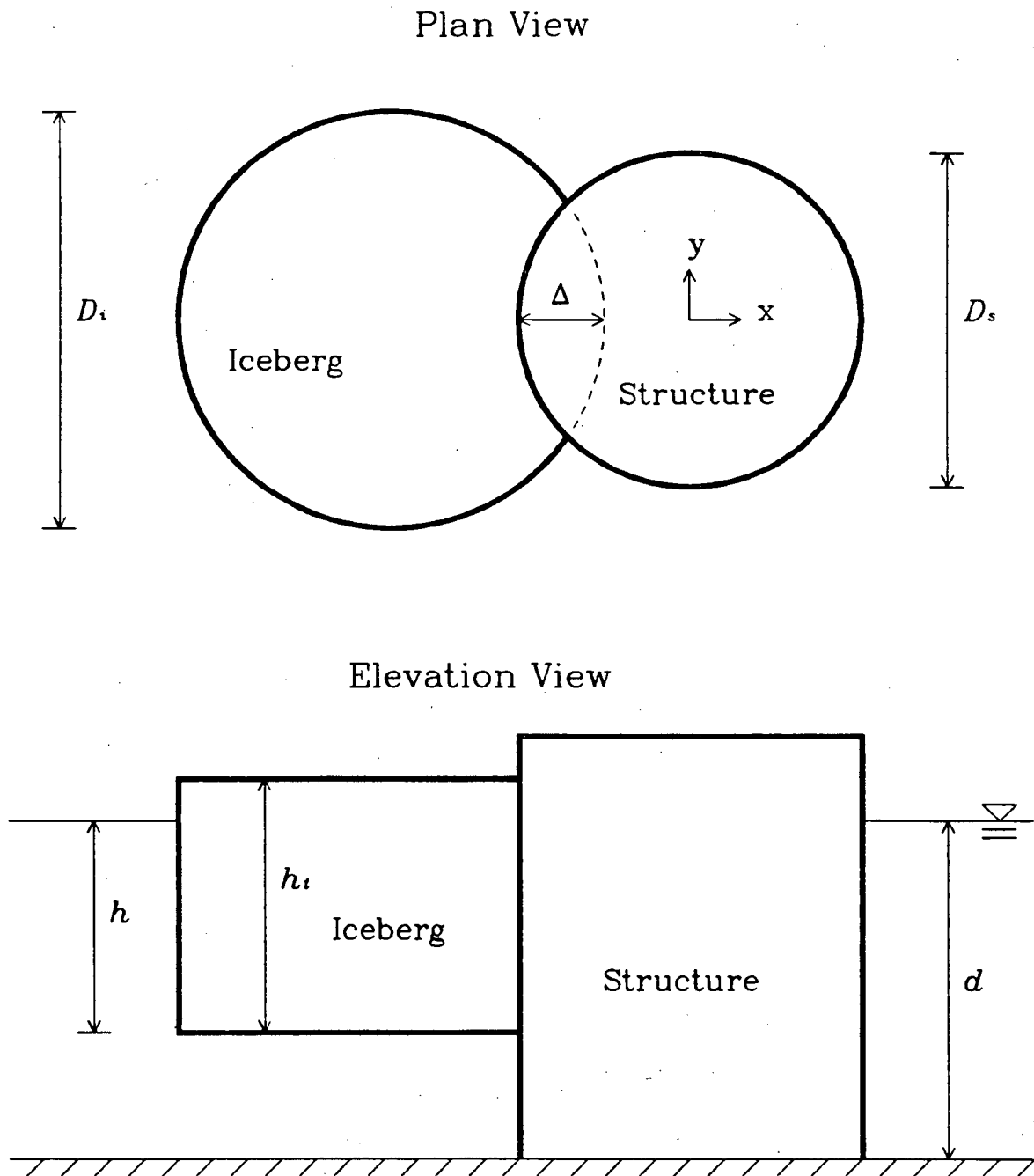


Figure 1.2: Schematic of an Iceberg Collision with a Fixed Structure

### 1.3.1 Oscillatory Iceberg Motions

Velocity input values for iceberg collision models are usually obtained from hourly observations of iceberg positions (e.g. [6]), thus giving mean drift velocities. Ideally, instantaneous iceberg velocities should be used in iceberg collision models. Although full-scale instantaneous velocity observations are very difficult to obtain, oscillatory motions can be computed relatively easily using numerical diffraction models. The problem of estimating maximum iceberg velocity is greatly simplified if mean and oscillatory velocities are assumed to be collinear. This assumption is quite reasonable considering the degree of interaction between winds, waves, and currents. The horizontal iceberg velocity will fluctuate during a given wave cycle, and will have a maximum value as follows:

$$V = V_d + V_s \quad (1.3)$$

where:

$V$  = maximum velocity during wave cycle (m/s)

$V_d$  = drift velocity (m/s)

$V_s$  = amplitude of oscillatory surge velocity (m/s)

For an iceberg in regular waves, the surge velocity amplitude is easily expressed as:

$$V_s = \frac{1}{2} H \zeta'_1 \omega \quad (1.4)$$

where:

$H$  = wave height (m)

$\zeta'_1$  = surge response amplitude operator

$\omega$  = angular wave frequency ( $s^{-1}$ )

The significance of wave-induced iceberg motions has been illustrated by Lever and Sen [60] and Salvalaggio and Rojansky [99]. Lever and Sen report that the kinetic energy

of a 10,000-100,000 tonne iceberg can be increased by a factor of 3-6 when the wave-induced oscillatory velocity is added to the mean drift velocity.

### **1.3.2 Modification of Iceberg Motions by the Presence of a Fixed Structure**

Due to the large dimensions of a gravity based structure, the incident flow field will be modified significantly by its presence. It is likely that the zero normal flow boundary condition at the structure will reduce the velocity of impacting icebergs. Several investigations have examined iceberg motions in the vicinity of a large structure. Hay and Company [35], Isaacson [43], and Isaacson and Dello Stritto [48] used a numerical potential flow model to predict wave and current induced iceberg motions. References [35] and [48] indicate that negative wave drift forces near a large structure can prevent smaller icebergs from impacting. NORDCO [90] examined wave-induced iceberg motions in the presence of a gravity based structure. Both numerical and physical models were used to examine motions for icebergs of similar size to the structure. It was found that iceberg motions were not significantly affected by the presence of the structure. A series of experiments was conducted by Salvalaggio and Rojansky [99] to examine wave-induced motions in the vicinity of a structure. They reported that no impact occurred if the iceberg length was less than approximately half the structure length, regardless of the incident wavelength.

### **1.3.3 Variation of Added Mass with Proximity to Structure**

Iceberg added mass is among the various factors contributing to the severity of collisions with an offshore structure. Application of equation 1.2 requires knowledge of iceberg added mass at the instant of impact. Investigations by Isaacson and Cheung

[46,47], have examined the variation of iceberg added mass with proximity to a fixed structure. Their results indicate that iceberg added mass can increase significantly as the iceberg approaches the structure.

Iceberg added mass is usually obtained using a form of the boundary element method. Isaacson [43] used a three-dimensional diffraction computation to obtain iceberg added mass in the vicinity of a structure. A typical three-dimensional boundary element discretization is illustrated in Figure 1.3. This method was restricted by numerical difficulties as the separation distance between the iceberg and structure became less than a typical facet dimension.

An alternative two-dimensional boundary element method solution has been developed by Isaacson and Cheung [46,47]. A two-dimensional discretization such as that shown in Figure 1.4 allows for the use of much smaller facet dimensions. Extension of two-dimensional results to three dimensions is done using correction factors from Yeung [119].

## 1.4 Risk Analysis of Iceberg Collisions

Due to the complex nature of the offshore environment, probabilistic methods should be utilized for the development of structural design criteria. Output from a risk analysis should ideally give the probability of structural failure over a given period of time (e.g. 1 year or the life of the structure).

### 1.4.1 Selection of a Suitable Design Event

When designing a structure to withstand iceberg collisions, it is necessary to select a suitable design event that the structure should be able to withstand [24]. The design event should have an associated impact severity level with a low probability of exceedence

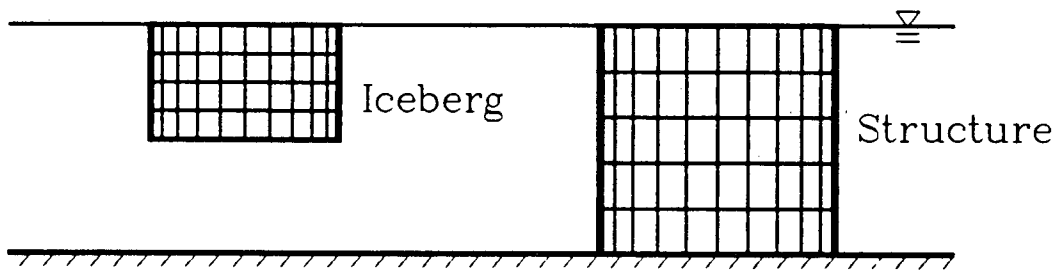


Figure 1.3: Boundary Element Grid for Three-Dimensional Solution, Elevation View

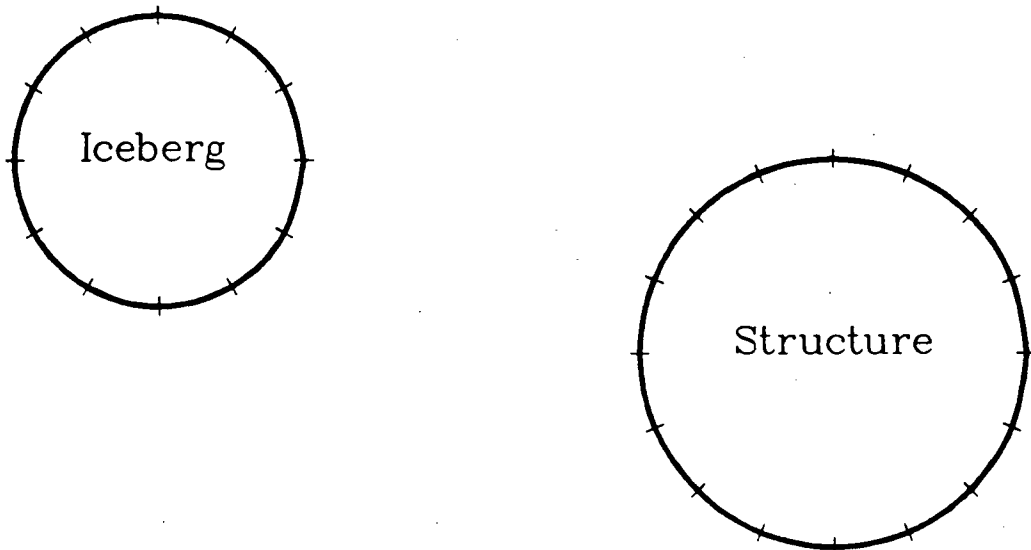


Figure 1.4: Boundary Element Grid for Two-Dimensional Solution, Plan View

and should be described by the most likely combination of parameter values for the given severity level. Typical collision parameters will include the following:

1. Iceberg dimensions,
2. Impact velocity,
3. Eccentricity of impact.

### 1.4.2 Methods of Ranking Collision Severity

The parameters of a design event will not only depend on the specified exceedence probability, but also on the method of ranking collision severity. For iceberg collisions with a large structure, the following criteria can be used for ranking collision severity:

1. Kinetic energy of impacting iceberg,
2. Kinetic energy dissipated during collision,
3. Maximum load experienced during collision.

Iceberg kinetic energy is the simplest criterion for ranking impact severity. Although due consideration must be given to hydrodynamic effects, impact load computations are not required when determining iceberg kinetic energy. Ranking of collision severity according to dissipated kinetic energy is a more sophisticated method which can account for the influence of eccentric impacts. Both hydrodynamics and collision mechanics must be evaluated when determining kinetic energy dissipated during a collision. Ranking of collision severity according to maximum impact load requires the greatest degree of computational effort. Ideally a sophisticated model which incorporates both hydrodynamics

and collision mechanics should be utilized. The primary advantage of load ranking according to impact force is that impact force is usually the quantity of principal interest to the structural designer.

### 1.4.3 Methods of Evaluating Exceedence Probabilities

When evaluating the probability of exceedence for a given collision severity level, one of the following three approaches can be used:

1. Analytical methods,
2. Monte Carlo simulation,
3. First or second order reliability methods (FORM or SORM)

Application of analytical methods is mainly limited to relatively simple systems involving few random variables. Probability density functions are described by uni-variate distributions for uncorrelated variables or by multi-variate distributions for correlated variables.

With the advent of computers, Monte Carlo methods have proven useful for the analysis of complex systems. Monte Carlo simulation utilizes random number generators to produce variables having specified statistical distributions, and is discussed extensively in references by Ang and Tang [2] and Naylor et al. [84]. A major disadvantage of Monte Carlo simulation is the large amount of computational effort required, particularly when evaluating small probabilities of exceedence.

The first and second order reliability methods (FORM and SORM) are based on work originally proposed by Hasofer and Lind [34]. Detailed descriptions of reliability methods are given in reference books by Ang and Tang [2], Madsen et al. [67], and Thoft-Christensen and Baker [110]. Of key importance in the application of reliability methods

is the concept of a failure function which is defined such that a value less than 0 indicates structural failure. Thus, the failure function can appear as follows:

$$G(\vec{X}) = R - L \quad (1.5)$$

where:

$G$  = failure function

$L$  = structural load

$R$  = structural resistance

$\vec{X}$  = vector of random variables

Using Equation 1.5, the probability of failure for a given structure can be calculated using an efficient computer algorithm presented by Rackwitz and Fiessler [97]. If the exceedence probability for a given load level is required, the structure resistance  $R$  can be treated as a deterministic quantity representing the given load level.

## 1.5 Scope of the Present Investigation

The present investigation examines the various hydrodynamic aspects of iceberg collisions with a large structure and their incorporation into probabilistic models for the evaluation of design iceberg collision events. The various phases of investigation are as follows.

### 1.5.1 Verification of Numerical Ice Mass Motion Model

A numerical model developed by Isaacson [43] has been used for modelling ice mass motions in the vicinity of a fixed structure. The model utilizes potential flow theory to compute oscillatory and mean drift motions. The objective of the initial phase of

investigation was to verify the reliability of the computational model through comparison with published results from other sources.

### **1.5.2 Numerical Study of Iceberg Collision Hydrodynamics**

The ice mass motion model has been used to examine hydrodynamic effects for various collision scenarios. Areas of interest include the following:

1. Prediction of iceberg oscillatory velocities in open water,
2. Variation of mean and oscillatory iceberg velocities with proximity to structure,
3. Effective added masses for drift motions and collisions,
4. Variation of iceberg added mass with proximity to structure.

A gravity based structure with a diameter of 100 m situated in a water depth of 100 m has been used as a representative large structure for computations.

### **1.5.3 Physical Modelling of Iceberg Drift Motions**

#### **Near a Large Structure**

A review of published experimental work revealed that little physical modelling data were available for validating the numerical iceberg drift model. Consequently, an experimental investigation has been conducted to examine iceberg drift motions near a large structure. Drift motions driven by both currents and waves have been modelled in a series of towing tank tests. The influence of the structure on iceberg velocities and approach eccentricities has been examined and compared with results of the numerical drift model.

### **1.5.4 Kinetic Energy Reliability Model**

A probabilistic model for determining an iceberg collision design event based on iceberg kinetic energy has been developed. The use of kinetic energy as a ranking criterion allows for the evaluation of a design event without computing impact forces. The model has been formulated such that statistical distributions for input variables can be obtained from available environmental data. A key aspect of the model is its inclusion of wave-induced oscillatory motions, which are evaluated using response amplitude operators obtained from diffraction computations. Output from the model can be used to assess the importance of iceberg geometry and wave-induced motions on iceberg kinetic energy.

### **1.5.5 Impact Force Reliability Model**

A second reliability model, based on iceberg impact force, has been formulated. It is likely that such an impact force reliability model would be used in the actual design of an offshore structure. The influence of the structure on drift motions of approaching icebergs is considered along with the variation of iceberg approach eccentricities. The relative importance of hydrodynamic effects compared to other phenomena, such as the variability of ice strength, can be examined using the impact force reliability model.

## Chapter 2

# Numerical Iceberg Motion Model

A major objective of the present investigation was to examine the importance of hydrodynamic effects for iceberg collisions. The numerical model ICEMOT developed by Isaacson [43,48] has been used to model iceberg motions in the vicinity of a large structure, and to predict relevant collision parameters. This chapter describes the main features and computational methods of ICEMOT.

### 2.1 General Framework of Model

Like previous numerical drift models [6,40], the present model utilizes a time-stepping procedure to compute iceberg drift motions driven by waves and currents. Due to the variation of currents and waves with proximity to the structure, wave drift forces and water drag forces can be re-evaluated at specified time intervals. Computations of oscillatory motion amplitudes can be also made at specified time intervals. Small amplitude motions are assumed when computing oscillatory motions; thus, the variation in iceberg proximity to the structure during a single wave period is neglected.

## 2.2 Oscillatory Iceberg Motions

The problem of predicting oscillatory iceberg motions is highly dependent on the size of the iceberg relative to the incident wavelength. A series of experiments by Lever et al. [59] indicated that an iceberg follows the motion of a fluid particle when the iceberg diameter to wavelength ratio  $D_i/\lambda$  is less than  $1/13$ . Under such conditions, oscillatory motions can be determined merely from a knowledge of the incident wave field. For larger icebergs (i.e.  $D_i/\lambda > 1/13$ ), the wave field is modified by the presence of the iceberg to such a degree that the diffracted wave field must be computed for accurate prediction of oscillatory motions. The diffraction problem is further complicated when a large structure is present in the wave field. The structure can have a significant effect on iceberg motions if its size is large relative to the iceberg. It is necessary to consider the presence of both the iceberg and the structure when solving for the diffracted wave field, which will also vary with the location of the iceberg relative to the structure.

Due to the inherently large size of icebergs, diffraction effects can be very significant. It is likely that a petroleum production structure built in iceberg-infested waters would also be large enough to cause significant diffraction. Consequently, the numerical model utilizes a two-body diffraction solution to determine oscillatory motion amplitudes of an iceberg near a large structure.

### 2.2.1 Theoretical Basis of Diffraction Solution

If a body is large enough that significant wave diffraction occurs, flow separation effects will be relatively unimportant [103], thus allowing the application of potential flow theory for predicting oscillatory motions. The diffraction problem is further simplified by utilizing linear wave theory, which can be considered valid when the incident wave height is small relative to incident wavelength and water depth.

The velocity potential solution for the wave field must satisfy the continuity equation throughout the fluid domain:

$$\nabla^2 \Phi = 0 \quad (2.1)$$

where:

$$\Phi = \text{wave field velocity potential (m}^2/\text{s)}$$

The potential flow linear diffraction solution must also satisfy the following boundary conditions:

$$\frac{\partial \Phi}{\partial z} = \frac{\partial \eta}{\partial t} \text{ at } z = 0 \quad (2.2)$$

$$\frac{\partial \Phi}{\partial t} + \eta g = 0 \text{ at } z = 0 \quad (2.3)$$

$$\frac{\partial \Phi}{\partial z} = 0 \text{ at } z = -d \quad (2.4)$$

$$\frac{\partial \Phi}{\partial n} = V_n \text{ on } S_i \quad (2.5)$$

$$\frac{\partial \Phi}{\partial n} = 0 \text{ on } S_s \quad (2.6)$$

where:

$d$  = water depth (m)

$g$  = gravitational acceleration (m/s<sup>2</sup>)

$n$  = unit normal vector pointing outward from body (m)

$S_i$  = iceberg surface

$S_s$  = structure surface

$V_n$  = velocity component in direction of  $n$  (m/s)

$z$  = elevation relative to still water level (m)

$\eta$  = vertical displacement of water surface (m)

In addition to the above boundary conditions, the diffraction solution must satisfy a radiation condition which requires that the diffracted wave from a body must radiate outward from the body.

### 2.2.2 Definition of Co-ordinate Systems and Modes of Motion

Before proceeding further with the formulation of the velocity potential solution, the co-ordinate systems (shown in Figure 2.1) and iceberg modes of motion will be defined. The  $G(x', y', z')$  co-ordinate system has its origin at the centre of gravity of the iceberg; thus, the origin of this system changes with time due to iceberg drift. The  $O(x, y, z)$  system has its origin fixed at the waterline at the centre of the structure. Relationships between the two co-ordinate systems are as follows:

$$x = x_g + x' \quad (2.7)$$

$$y = y_g + y' \quad (2.8)$$

$$z = z_g + z' \quad (2.9)$$

where:

$x, y, z$  = co-ordinates of point in  $O(x, y, z)$  system (m)

$x', y', z'$  = co-ordinates of point in  $G(x', y', z')$  system (m)

$x_g, y_g, z_g$  = co-ordinates of iceberg centre of gravity in  $O(x, y, z)$  system (m)

The respective axes of the two co-ordinate systems may be taken as parallel, as shown in Figure 2.1, since yaw motions are not considered.

The six modes of oscillatory iceberg motion are taken about the origin of the  $G(x', y', z')$  system and are as follows:

1. Surge - translational motions along  $x'$  axis,

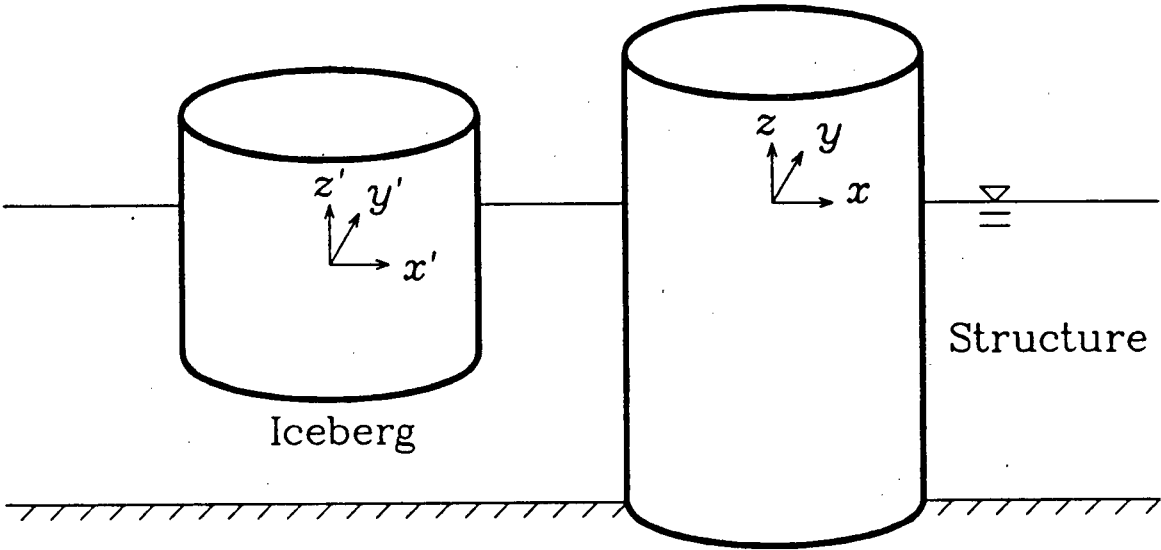


Figure 2.1: Co-ordinate Systems for Iceberg Motion Model

2. Sway - translational motions along  $y'$  axis,
3. Heave - translational motions along  $z'$  axis,
4. Roll - rotational motions about  $x'$  axis,
5. Pitch - rotational motions about  $y'$  axis,
6. Yaw - rotational motions about  $z'$  axis.

### 2.2.3 Re-formulation of Velocity Potential

The solution of the diffracted potential is greatly simplified if a complex velocity potential defined as follows is adopted:

$$\Phi(x, y, z, t) = \text{Re} \{ \phi(x, y, z) \exp(-i\omega t) \} \quad (2.10)$$

where:

$\Phi$  = real, time-varying velocity potential ( $\text{m}^2/\text{s}$ )

$\phi$  = complex velocity potential ( $\text{m}^2/\text{s}$ )

The complex potential consists of an incident potential  $\phi_0$ , a diffracted potential  $\phi_7$ , and potentials  $\phi_1 - \phi_6$  due to motions in each of the six component modes. Using unit forms of the above potentials, the complex potential of equation 2.10 can now be expressed as follows:

$$\phi = -\frac{i H \omega}{2} \left( \phi_0 + \phi_7 + \sum_{k=1}^6 \phi_k \zeta'_k \right) \quad (2.11)$$

where:

$H$  = incident wave height (m)

$\phi_0$  = incident wave potential (m)

$\phi_7$  = diffracted wave potential (m)

$\phi_k$  = radiation potential for motions in mode  $k$  (m or  $m^2$ )

$\zeta'_k$  = complex response amplitude operator for mode  $k$  (dimensionless or  $m^{-1}$ )

$\omega$  = angular frequency of incident waves ( $s^{-1}$ )

The zero flow boundary condition on the iceberg and structure surfaces establishes the following condition for the unknown diffraction potential:

$$\frac{\partial \phi_7}{\partial n} = -\frac{\partial \phi_0}{\partial n} \text{ on } S_i \text{ and } S_s \quad (2.12)$$

The following equation is used for describing the incident wave potential:

$$\phi_0 = \frac{g}{\omega^2} \frac{\cosh[k(z+d)]}{\cosh[kd]} \exp[ik(x \cos \alpha + y \sin \alpha)] \quad (2.13)$$

where:

$k$  = wavenumber ( $m^{-1}$ )

$\alpha$  = incident wave direction ( $^\circ$ )

The radiation potentials  $\phi_1 - \phi_6$  must satisfy the zero flow condition at the structure:

$$\frac{\partial \phi_k}{\partial n} = 0 \text{ on } S_s \text{ for } k = 1 - 6 \quad (2.14)$$

In addition, the normal velocity condition on the iceberg surface must be satisfied for each mode of oscillation as follows:

$$\frac{\partial \phi_k}{\partial n} = -i n_k \text{ on } S_i \text{ for } k = 1 - 6 \quad (2.15)$$

where:

$n_k$  = unit normal velocity for mode  $k$

The unit normal velocities are related to the iceberg geometry as follows:

$$n_1 = n_x \quad (2.16)$$

$$n_2 = n_y \quad (2.17)$$

$$n_3 = n_z \quad (2.18)$$

$$n_4 = y' n_z - z' n_y \quad (2.19)$$

$$n_5 = z' n_x - x' n_z \quad (2.20)$$

$$n_6 = x' n_y - y' n_x \quad (2.21)$$

where:

$n_x, n_y, n_z$  = directional cosines of normal vector pointing outward from the iceberg

The diffraction and radiation potentials must also satisfy the radiation condition mentioned previously. For the diffracted and radiated waves to propagate outward from the body, the following radiation equations must be satisfied at large distances from the body:

$$\sqrt{r} \left( \frac{\partial \phi_j}{\partial r} - i k \phi_j \right) = 0 \text{ as } r \rightarrow \infty \text{ for } j = 1 - 7 \quad (2.22)$$

where:

$r$  = distance from body in horizontal plane (m)

## 2.2.4 Solution of Diffraction and Radiation Potentials

The unknown potentials  $\phi_1 - \phi_7$  are solved using a source distribution method as described by Faltinsen and Michelsen [28], Garrison [31], and Hogben and Standing [36]. Using a series of sources located on the iceberg and structure surfaces, the potential  $\phi_k$

at a point in the fluid domain can be represented by:

$$\phi_k(\vec{x}) = \frac{1}{4\pi} \int_{S_i+S_s} f_k(\vec{\xi}) G(\vec{x};\vec{\xi}) dS \text{ for } k = 1 - 7 \quad (2.23)$$

where:

$f_k$  = source strength for potential  $\phi_k$  (dimensionless or m)

$G$  = Green's function ( $m^{-1}$ )

$\vec{x}$  = location of point in fluid domain

$\vec{\xi}$  = location of source on iceberg or structure surface

### Form of Green's Function

The Green's function is of a form that satisfies the conditions of equations 2.1 - 2.4 and 2.22 regardless of the values of the source strengths  $f_k(\vec{\xi})$ . The source strengths are then solved using the surface boundary conditions of equations 2.12, 2.14, and 2.15. Alternative integral and series forms of the Green's function [28,31,36] are as follows:

$$\begin{aligned} G(x, y, z; \xi, \eta, \zeta) = & \\ & \frac{2\pi(\nu^2 - k^2)}{k^2 d - \nu^2 d + \nu} \cosh[k(z + d)] \cosh[k(\zeta + d)] [Y_0(kr_1) - iJ_0(kr_1)] \\ & + 4 \sum_{j=1}^{\infty} \frac{\mu_j + \nu^2}{\mu_j d + \nu^2 d - \nu} \cos[\mu_j(z + d)] \cos[\mu_j(\zeta + d)] K_0(\mu_j r_1) \end{aligned} \quad (2.24)$$

$$\begin{aligned} G(x, y, z; \xi, \eta, \zeta) = & \\ & \frac{1}{R} + \frac{1}{R'} \\ & + 2 \text{P.V.} \int_0^{\infty} \frac{(\mu + \nu) \exp[-\mu d] \cosh[\mu(\zeta + d)] \cosh[\mu(z + d)] J_0(\mu r_1)}{\mu \sinh(\mu d) - \nu \cosh[\mu d]} d\mu \\ & + i \frac{2\pi(k^2 - \nu^2) \cosh[k(\zeta + d)] \cosh[k(z + d)]}{k^2 d - \nu^2 d + \nu} J_0(kr_1) \end{aligned} \quad (2.25)$$

where:

$J_0$  = Bessel function of first kind, order 0

$K_0$  = modified Bessel function of second kind, order 0

$Y_0$  = Bessel function of second kind, order 0

Terms  $\mu_j$  in equation 2.24 represent the successive real roots of the following equation:

$$\mu_j \tan(\mu_j d) + \nu = 0 \quad (2.26)$$

Additional terms of equations 2.24 and 2.25 are defined as follows:

$$\nu = \frac{\omega^2}{g} \quad (2.27)$$

$$R = \sqrt{(x - \xi)^2 + (y - \eta)^2 + (z - \zeta)^2} \quad (2.28)$$

$$R' = \sqrt{(x - \xi)^2 + (y - \eta)^2 + (z + 2d + \zeta)^2} \quad (2.29)$$

$$r_1 = \sqrt{(x - \xi)^2 + (y - \eta)^2} \quad (2.30)$$

The symbol P.V. in equation 2.25 denotes that the principal value of the integral is taken. Numerical evaluation of the Green's function between points  $\vec{x}$  and  $\vec{\xi}$  is done using the series formula for  $kr_1 > 0.1$ , while the integral form is used for  $kr_1 < 0.1$ .

### Discretized Solution of Source Strengths and Potentials

To enable the solution of the source strengths  $f_k(\vec{\xi})$ , the iceberg and structure surfaces are divided into discrete facets as shown in Figure 1.3 with point sources located at the centre of each facet. The normal derivative of the potential  $\phi_k$  at each facet can be expressed as a function of the source strengths as follows:

$$\frac{\partial \phi_{k_i}}{\partial \vec{n}} = -\frac{1}{2} f_{k_i} + \frac{1}{4\pi} \int_{S_i+S_s} f_{k_j} \frac{\partial G_{ij}}{\partial \vec{n}} dS \quad k = 1 - 7 \quad (2.31)$$

where:

$f_{kj}$  = source strength at facet  $j$  for potential  $k$

$G_{ij}$  = Green's function between centres of facets  $i$  and  $j$

$\phi_{ki}$  = potential at centre of facet  $i$

Using equation 2.31 and the required surface boundary conditions of equations 2.12, 2.14, and 2.15, seven matrix equations are formed for solution of the source strengths  $\phi_{kj}$ :

$$[A] \{f_k\} = \left\{ \frac{\partial \phi_k}{\partial n} \right\}, k = 1 - 7 \quad (2.32)$$

The matrix  $[A]$  is independent of the potential  $\phi_k$  being evaluated, with elements as follows:

$$A_{ij} = \frac{\Delta S_j}{4\pi} \frac{\partial G_{ij}}{\partial \vec{n}} \text{ for } i \neq j \quad (2.33)$$

$$A_{ij} = -\frac{1}{2} \text{ for } i = j \quad (2.34)$$

where:

$\Delta S_j$  = area of facet  $j$  ( $\text{m}^2$ )

Once the source strength vectors have been solved, the potentials  $\phi_k$  can be evaluated at the facet centres using a discretized form of equation 2.23:

$$\{\phi_k\} = [B] \{f_k\} \quad (2.35)$$

Elements of matrix  $[B]$  are:

$$B_{ij} = \frac{\Delta S_j}{4\pi} G_{ij} \text{ for } i \neq j \quad (2.36)$$

$$B_{ij} = \frac{1}{4\pi} \int_{\Delta S_i} \frac{1}{R} dS + \frac{\Delta S_i}{4\pi} G^*(\vec{x}_i; \vec{\xi}_j) \text{ for } i = j \quad (2.37)$$

where:

$G^*(\vec{x}_i; \vec{\xi}_j)$  = modified Green's function ( $\text{m}^{-1}$ )

Equation 2.37 is formulated so as to eliminate the singular  $1/R$  term of equation 2.25. The integral in equation 2.37 is evaluated for quadrilateral facets using expressions from Hogben and Standing [36], while the modified Green's function  $G^*$  is obtained from equation 2.25 as follows:

$$G^*(\vec{x}_i; \vec{\xi}_i) = G(\vec{x}_i; \vec{\xi}_j) - \frac{1}{R} \quad (2.38)$$

### 2.2.5 Solution of Equations of Motion

Once the diffracted wave field and its associated unit potentials  $\phi_1 - \phi_7$  have been solved, the oscillatory iceberg motions can be evaluated as follows:

$$\left( -\omega^2 ([m] + [\mu]) - i\omega ([\lambda] + [\lambda_v]) + [c] \right) \{\zeta'\} = \{F'\} \quad (2.39)$$

where:

- $[c]$  = hydrodynamic stiffness matrix
- $\{F'\}$  = vector of unit exciting forces
- $[m]$  = iceberg mass matrix
- $[\lambda]$  = radiation damping matrix
- $[\lambda_v]$  = viscous damping matrix
- $\{\zeta'\}$  = vector of response amplitude operators

Computation of the above terms will now be described in detail.

## Mass Matrix

The iceberg mass matrix  $[m]$  appears as follows:

$$[m] = \begin{bmatrix} M & 0 & 0 & 0 & 0 & 0 \\ 0 & M & 0 & 0 & 0 & 0 \\ 0 & 0 & M & 0 & 0 & 0 \\ 0 & 0 & 0 & I_{11} & -I_{12} & -I_{13} \\ 0 & 0 & 0 & -I_{12} & I_{22} & I_{23} \\ 0 & 0 & 0 & -I_{13} & -I_{23} & I_{33} \end{bmatrix} \quad (2.40)$$

where:

$I_{ij}$  = iceberg moment or product of inertia ( $\text{kg}\cdot\text{m}^2$ )

Equations for the moments and products of inertia are:

$$I_{11} = \int_V \rho_i x'^2 dV \quad (2.41)$$

$$I_{12} = \int_V \rho_i x' y' dV \quad (2.42)$$

$$I_{13} = \int_V \rho_i x' z' dV \quad (2.43)$$

$$I_{22} = \int_V \rho_i y'^2 dV \quad (2.44)$$

$$I_{23} = \int_V \rho_i y' z' dV \quad (2.45)$$

$$I_{33} = \int_V \rho_i z'^2 dV \quad (2.46)$$

where:

$\rho_i$  = iceberg density ( $\text{kg}/\text{m}^3$ )

### Added Mass Matrix

The added mass matrix  $[\mu]$  is evaluated using the radiation potentials for each mode of motion. Terms of the added mass matrix are based on the following integral equation:

$$\mu_{jk} = -\rho \operatorname{Re} \left\{ \int_{S_i} \phi_k n_j dS \right\} \quad (2.47)$$

where:

$n_j$  = unit normal velocity for mode  $j$  (from equations 2.16 - 2.21)

$\phi_k$  = unit radiation potential for mode  $k$  (m)

$\rho$  = water density (kg/m<sup>3</sup>)

The discretized form of equation 2.47 is:

$$\mu_{jk} = -\rho \operatorname{Re} \left\{ \sum_{i=1}^{N_i} \phi_{k_i} n_{j_i} \Delta S_i \right\} \quad (2.48)$$

where:

$N_i$  = number of facets on iceberg surface

$n_{j_i}$  = unit normal velocity for mode  $j$  at facet  $i$

$\phi_{k_i}$  = unit radiation potential for mode  $k$  at facet  $i$

### Radiation Damping Matrix

The radiation damping matrix  $[\lambda]$  is solved in a manner very similar to that used for evaluating the added mass matrix. Integral and discretized forms for the radiation damping matrix are:

$$\lambda_{jk} = -\rho \omega \operatorname{Im} \left\{ \int_{S_i} \phi_k n_j dS \right\} \quad (2.49)$$

$$\lambda_{jk} = -\rho \omega \operatorname{Im} \left\{ \sum_{i=1}^{N_i} \phi_{k_i} n_{j_i} \Delta S_i \right\} \quad (2.50)$$

### Viscous Damping Matrix

In addition to the radiation matrix, an empirical viscous damping matrix  $[\lambda^v]$  is introduced. Viscous damping can be significant for heave, pitch, and roll motions [43,103]; thus, the viscous damping matrix is assumed to be of the form:

$$[\lambda^v] = \begin{bmatrix} 0 & 0 & 0 & 0 & 0 & 0 \\ 0 & 0 & 0 & 0 & 0 & 0 \\ 0 & 0 & \lambda_{33}^v & 0 & 0 & 0 \\ 0 & 0 & 0 & \lambda_{44}^v & 0 & 0 \\ 0 & 0 & 0 & 0 & \lambda_{55}^v & 0 \\ 0 & 0 & 0 & 0 & 0 & 0 \end{bmatrix} \quad (2.51)$$

For the present problem, viscous damping coefficients are determined from empirical viscous damping ratios  $\lambda^{v'}$ . The following relationship is used for calculating viscous damping coefficients from damping ratios:

$$\lambda_{jj}^v = 2 \lambda_{jj}^{v'} \sqrt{c_{jj} (m_{jj} + \mu_{jj})} \quad (2.52)$$

where:

$c_{jj}$  = hydrostatic stiffness matrix term

$m_{jj}$  = mass matrix term

$\mu_{jj}$  = added mass matrix term

### Hydrostatic Stiffness Matrix

Like the mass matrix, the hydrostatic stiffness matrix is dependent only upon the iceberg geometry and appears as follows:

$$[c] = \begin{bmatrix} 0 & 0 & 0 & 0 & 0 & 0 \\ 0 & 0 & 0 & 0 & 0 & 0 \\ 0 & 0 & c_{33} & c_{34} & c_{35} & 0 \\ 0 & 0 & c_{34} & c_{44} & 0 & 0 \\ 0 & 0 & c_{35} & 0 & c_{55} & 0 \\ 0 & 0 & 0 & 0 & 0 & 0 \end{bmatrix} \quad (2.53)$$

Equations for the matrix are:

$$c_{33} = \rho g A_{wp} \quad (2.54)$$

$$c_{34} = -\rho g \int_{A_{wp}} y' dA \quad (2.55)$$

$$c_{35} = -\rho g \int_{A_{wp}} x' dA \quad (2.56)$$

$$c_{44} = -\rho g \int_{A_{wp}} y'^2 dA + m g z'_b \quad (2.57)$$

$$c_{55} = -\rho g \int_{A_{wp}} x'^2 dA + m g z'_b \quad (2.58)$$

where:

$A_{wp}$  = iceberg waterplane area ( $m^2$ )

$z'_b$  =  $z'$  co-ordinate of iceberg centre of buoyancy (m)

### Exciting Forces

The exciting forces acting on the iceberg are caused by the incident and diffracted waves. Integral and discretized forms of the exciting forces for unit amplitude incident

waves are:

$$F'_k = -\rho \omega^2 \int_{S_i} (\phi_0 + \phi_7) n_k dS \quad (2.59)$$

$$F'_k = -\rho \omega^2 \sum_{i=1}^{N_i} (\phi_{0_i} + \phi_{7_i}) n_{k_i} \Delta S_i \quad (2.60)$$

where:

$F'_k$  = force or moment for mode  $k$  in unit amplitude waves (N/m or N)

### Final Computation of Response Amplitude Operators

Once the hydrodynamic coefficients and exciting forces are known, the complex response amplitude operators (RAO's) are computed by solving equation 2.39. Motion amplitudes and phase angles are subsequently computed, with phase angles defined as follows:

$$\delta_k = \tan^{-1} \frac{\text{Im}(\zeta'_k)}{|\zeta'_k|} \quad (2.61)$$

where:

$\delta_k$  = phase angle for mode  $k$  ( $^\circ$ )

The physical meaning of the phase angle is dependent on the form of incident wave potential used. For the incident potential of equation 2.13, the phase angle represents a lag relative to an incident wave crest crossing the origin of the  $O(x, y, z)$  co-ordinate system.

## 2.3 Mean Drift Motions

The drift motions of an iceberg are caused by forces due to ocean currents, waves, winds and the Coriolis effect. When modelling iceberg motions in the vicinity of an

offshore structure, Coriolis and wind drag forces are typically small relative to water drag and wave drift forces [44]. The numerical model utilizes the following equations for evaluating iceberg drift motions:

$$a_x = \frac{1}{(M + \mu_{11})} (F_{d_x} + F_{w_x}) \quad (2.62)$$

$$a_y = \frac{1}{(M + \mu_{22})} (F_{d_y} + F_{w_y}) \quad (2.63)$$

where:

$a_x, a_y$  = iceberg acceleration components (m/s<sup>2</sup>)

$F_{d_x}, F_{d_y}$  = water drag force components (N)

$F_{w_x}, F_{w_y}$  = wave drift force components (N)

$\mu_{11}, \mu_{22}$  = zero frequency added mass components (kg)

The iceberg trajectory is then predicted using an Adams-Bashford time stepping method:

$$u(t + \Delta t) = u(t) + \frac{\Delta t}{2} [3 a_x(t) - a_x(t - \Delta t)] \quad (2.64)$$

$$v(t + \Delta t) = v(t) + \frac{\Delta t}{2} [3 a_y(t) - a_y(t - \Delta t)] \quad (2.65)$$

$$x_g(t + \Delta t) = x_g(t) + \frac{\Delta t}{2} [3 u(t) - u(t - \Delta t)] \quad (2.66)$$

$$y_g(t + \Delta t) = y_g(t) + \frac{\Delta t}{2} [3 v(t) - v(t - \Delta t)] \quad (2.67)$$

where:

$u, v$  = iceberg velocity components (m/s)

$x_g, y_g$  = iceberg location components (m)

For a typical simulation, the time stepping procedure begins when an iceberg enters the vicinity of a structure and continues until a collision occurs or the iceberg drifts freely past the structure

### 2.3.1 Evaluation of Zero Frequency Added Mass

Computation of an iceberg drift trajectory requires that the zero frequency added mass components  $\mu_{11}$  and  $\mu_{22}$  be known. The zero frequency added mass varies with the proximity of the iceberg relative to the structure; thus,  $\mu_{11}$  and  $\mu_{22}$  must be re-evaluated as the iceberg location changes. The procedure for computing zero frequency added mass is essentially the same as that used for evaluating wave frequency added mass. The principal difference in the numerical procedure is that the following zero frequency form of the Green's function given by Garrison [31] can be used for evaluating zero frequency radiation potentials:

$$G(x, y, z; \xi, \eta, \zeta) = \frac{1}{R} + \frac{1}{R_1} + \sum_{n=1}^{\infty} \left( \frac{1}{R_{2n}} + \frac{1}{R_{3n}} + \frac{1}{R_{4n}} + \frac{1}{R_{5n}} \right) \quad (2.68)$$

Terms in the above equation are evaluated as follows:

$$R = [r^2 + (z - \zeta)^2]^{1/2} \quad (2.69)$$

$$R_1 = [r^2 + (z + \zeta)^2]^{1/2} \quad (2.70)$$

$$R_{2n} = [r^2 + (z - 2n d - \zeta)^2]^{1/2} \quad (2.71)$$

$$R_{3n} = [r^2 + (z + 2n d + \zeta)^2]^{1/2} \quad (2.72)$$

$$R_{4n} = [r^2 + (z + 2n d - \zeta)^2]^{1/2} \quad (2.73)$$

$$R_{5n} = [r^2 + (z - 2n d + \zeta)^2]^{1/2} \quad (2.74)$$

$$r = [(x - \xi)^2 + (y - \eta)^2]^{1/2} \quad (2.75)$$

Successive terms of equation 2.68 are computed until convergence is obtained. In practice, the evaluation of zero frequency added mass requires significant computational effort; thus, added mass components are usually re-evaluated only once every few time steps.

### 2.3.2 Water Drag Forces

Evaluation of the water drag forces acting on the iceberg would ideally consist of integration of the normal pressures and shear (viscous) stresses acting on the iceberg surface; however, due to the complex nature of the flow around the iceberg, drag force components are instead evaluated using an empirical drag force coefficient as follows:

$$F_{d_x} = \frac{1}{2} \rho (u_w - u) |\vec{V}_w - \vec{V}| C_d A_w \quad (2.76)$$

$$F_{d_y} = \frac{1}{2} \rho (v_w - v) |\vec{V}_w - \vec{V}| C_d A_w \quad (2.77)$$

where:

$A_w$  = iceberg underwater cross-sectional area (m<sup>2</sup>)

$C_d$  = iceberg water drag coefficient

$\vec{V}$  = iceberg velocity vector (m/s)

$\vec{V}_w$  = water velocity vector (m/s)

$u_w, v_w$  = water velocity components (m/s)

The empirical water drag coefficient  $C_d$  is highly dependent on iceberg geometry. For typical full-scale situations, Reynolds numbers are sufficiently high that drag coefficients can be considered independent of Reynolds number.

The evaluation of water drag forces requires that the water velocity incident to the iceberg be known. If the structure is small relative to the iceberg, the free-stream current velocity is used for calculating water drag forces. Alternatively, if the structure is large relative to the approaching iceberg, then the modification of the flow field by the structure must be considered when evaluating water velocity. The water velocity  $\vec{V}_w$  used in equations 2.76 and 2.77 is based on the water velocity surrounding the structure and is evaluated at the location of the iceberg centre of gravity. The modification of the flow field by the iceberg is implicitly considered in the iceberg drag coefficient for the above

two cases.

Among the forces not considered in equations when evaluating the iceberg drift motions in ICEMOT are the convective forces arising from the spatial variation of the water velocities in the vicinity of the structure. If the flow in the vicinity of the structure is considered to be ideal, non-uniform, steady, and having no vertical component, then the total hydrodynamic force acting on the iceberg can be determined from Isaacson [45] to be as follows:

$$F_x = (M + \mu_{11})(u_w - u) \frac{\partial u_w}{\partial x} + (M + \mu_{22})(v_w - v) \frac{\partial v_w}{\partial x} - \mu_{11} \frac{du}{dt} \quad (2.78)$$

$$F_y = (M + \mu_{22})(v_w - v) \frac{\partial v_w}{\partial y} + (M + \mu_{11})(u_w - u) \frac{\partial u_w}{\partial y} - \mu_{22} \frac{dv}{dt} \quad (2.79)$$

To examine the implications of convective forces on the trajectory of an iceberg approaching a large structure, an iceberg moving with an incident current in the  $x$  direction and with a small eccentricity  $y$  relative to the structure (see Figure 2.1) can be considered. Considering first the  $x$  component of force, as the iceberg approaches the structure  $\partial u_w / \partial x$  is less than zero and  $(u_w - u)$  is greater than zero (neglecting wave drift force effects) so that the convective force component given as the first term on the right-hand side of equation 2.78 will be negative and cause the iceberg to decelerate in the  $x$  direction. Considering now the  $y$  component of force, for small non-zero values of  $y$ , both  $\partial v_w / \partial y$  and  $(v_w - v)$  are greater than zero so that the convective force component given as the first term of the right-hand side of equation 2.79 will be positive and will cause the iceberg to veer away from the structure. Significant coupling is likely to occur between the forces and motions in the  $x$  and  $y$  directions. The implications of the above convective forces on iceberg motions could be examined in greater detail by their incorporation into the numerical time-stepping model.

### 2.3.3 Computation of Modified Current Field in the Vicinity of a Large Structure of Arbitrary Shape

The current field in the vicinity of a large arbitrarily shaped structure is determined using a source distribution method similar to that used for computing the diffracted wave field. It is postulated that flow separation effects are significant only on the downstream side of the structure. Consequently, potential flow theory is used for modelling the flow field upstream of the structure during the approach of an iceberg.

The current field must satisfy Laplace's equation throughout the fluid domain:

$$\nabla^2\Phi_c = 0 \quad (2.80)$$

where:

$$\Phi_c = \text{water current velocity potential (m}^2/\text{s)}$$

The zero flow boundary conditions must be met at the seabed, the free surface, and at the structure surface:

$$\frac{\partial\Phi_c}{\partial z} = 0 \text{ at } z = -d \quad (2.81)$$

$$\frac{\partial\Phi_c}{\partial z} = 0 \text{ at } z = 0 \quad (2.82)$$

$$\frac{\partial\Phi_c}{\partial\vec{n}} = 0 \text{ on } S_s \quad (2.83)$$

The current potential is divided into incident and diffracted components as follows:

$$\Phi_c = \Phi_{c_i} + \Phi_{c_d} \quad (2.84)$$

where:

$$\Phi_{c_d} = \text{diffracted current potential (m}^2/\text{s)}$$

$$\Phi_{c_i} = \text{incident current potential (m}^2/\text{s)}$$

A uniform incident current is assumed and has the following form:

$$\Phi_{c_i} = V_{w_o} (x \cos \beta + y \sin \beta) \quad (2.85)$$

where:

$V_{w_o}$  = incident current velocity (m/s)

$\beta$  = incident current direction ( $^{\circ}$ )

The diffracted current is represented by a series of point sources on the structure surface such that the integral form of the diffracted potential is:

$$\Phi_{c_d}(\vec{x}) = \frac{1}{4\pi} \int_{S_s} f_c(\vec{\xi}) G(\vec{x}; \vec{\xi}) dS \quad (2.86)$$

where:

$f_c$  = source strength (m/s)

The Green's function of equation 2.68 is used to represent the diffracted current potential because it satisfies all governing equations except for the boundary condition at the structure surface (equation 2.83). The diffracted current source strengths are determined by solving the following set of simultaneous equations:

$$[A_c] \{f_c\} = \left\{ -\frac{\partial \Phi_{c_i}}{\partial \vec{n}} \right\} \quad (2.87)$$

where:

$[A_c]$  = matrix for solution of diffracted current source strengths

$\{f_c\}$  = vector of source strengths on structure surface (m/s)

$\{\partial \Phi_{c_i} / \partial \vec{n}\}$  = vector of incident current velocities normal to structure surface (m/s)

Elements of matrix  $[A_c]$  are as follows:

$$A_{c_{ij}} = \frac{\Delta S_j}{4\pi} \frac{\partial G}{\partial \vec{n}}(\vec{x}_i, \vec{\xi}_j) \quad \text{for } i \neq j \quad (2.88)$$

$$A_{c_{ij}} = -\frac{1}{2} \quad \text{for } i = j \quad (2.89)$$

It should be stressed that the diffracted current source strengths only need to be evaluated once and can subsequently be used to evaluate the current velocity at discrete points along the iceberg trajectory. Required equations for computing current velocity components are:

$$u_w(\vec{x}_g) = V_{wo} \cos \beta + \sum_{j=1}^{N_s} \frac{\Delta S_j}{4 \pi} \frac{\partial G}{\partial x}(\vec{x}_g, \vec{\xi}_j) f_{c_j} \quad (2.90)$$

$$v_w(\vec{x}_g) = V_{wo} \sin \beta + \sum_{j=1}^{N_s} \frac{\Delta S_j}{4 \pi} \frac{\partial G}{\partial y}(\vec{x}_g, \vec{\xi}_j) f_{c_j} \quad (2.91)$$

where:

$N_s$  = number of facets on structure surface

$\vec{x}_g$  = location of iceberg centre of gravity (m)

Equations 2.90 and 2.91 are re-evaluated as the iceberg location  $\vec{x}_g$  changes.

### 2.3.4 Computation of Modified Current Field in the Vicinity of a Large Cylindrical Structure

Evaluation of the current field is greatly simplified if the structure is a vertical circular cylinder extending from the seabed to the free surface. The following analytical solution for two-dimensional flow around a circular cylinder [109] is used:

$$\Phi_c(r, \theta) = V_{wo} \left( r + \frac{a^2}{r} \right) \cos(\theta - \beta) \quad (2.92)$$

$$r = \sqrt{x_g^2 + y_g^2} \quad (2.93)$$

$$\theta = \tan^{-1} \left( \frac{y_g}{x_g} \right) \quad (2.94)$$

where:

$a$  = structure radius (m)

$r$  = horizontal distance from centre of structure to centre of iceberg (m)

$\theta$  = angular co-ordinate between iceberg and structure ( $^{\circ}$ )

The above solution is well suited to practical application since offshore structures which are large enough to significantly modify current fields typically have shapes approximating vertical circular cylinders (e.g. [80]). An alternative procedure for computing the current field around a vertical structure of arbitrary plan shape has been presented by Isaacson and Cheung [46].

### 2.3.5 Wave Drift Forces

The wave drift force on an object is the mean wave force averaged over one wave period. The importance of wave drift forces on iceberg motions has been discussed by Hsiung and Aboul-Azm [40] and Isaacson [44].

The computation of wave drift forces has been discussed in detail by several authors (e.g. Faltinsen and Michelsen [28], Pinkster [96], Standing et al. [108]). If the assumption of linear wave theory is used, then the mean wave drift forces will be due primarily to the following sources:

1. Mean pressure increase due to relative water elevation on iceberg waterline,
2. Mean pressure decrease due to water velocity squared on iceberg surface.

Using the first-order real velocity potential, the mean drift forces and moments can be expressed as follows:

$$F_{wk} = \frac{\rho}{2g} \int_{wl_i} \overline{\left(\frac{\partial\Phi}{\partial t}\right)^2} n_k dwl + \frac{1}{2} \rho \int_{S_i} \overline{(\nabla\Phi)^2} n_k dS \quad k = 1 - 6 \quad (2.95)$$

where:

$F_{w_k}$  = wave drift force or moment for mode  $k$  (N or N·m)

$wl_i$  = iceberg waterline

Thus, the wave drift forces can be computed using the diffraction and radiation potentials which are determined for the computation of oscillatory motions.

Evaluation of equation 2.95 can be done using either a near-field or far-field method. The near-field method involves the direct solution of equation 2.95 at the body surface as discussed by Pinkster [96]. Alternatively, the far-field method utilizes a vertical cylindrical control surface with infinite radius  $r$  centred at the body, as shown in Figure 2.2. Wave drift forces result in the mean change in momentum of the wave field in the control volume. Development of the far-field method has been largely based on initial work by Newman [88]. The far-field method is limited to the evaluation of forces and moments in the horizontal plane (i.e. surge, sway, and yaw); however, only horizontal forces are required for the prediction of iceberg drift motions. The far-field method is used in the present model because of its greater computational efficiency and ease of programming.

### Application of the Far-field Method

The procedure for computation of wave drift forces using the far-field method is given by Faltinsen and Michelsen [28]. For the evaluation of drift forces acting on an iceberg in the vicinity of a structure, the procedure must be modified for the presence of the second body, as discussed by Loken [65].

The horizontal drift force components are evaluated using the following equations from [28]:

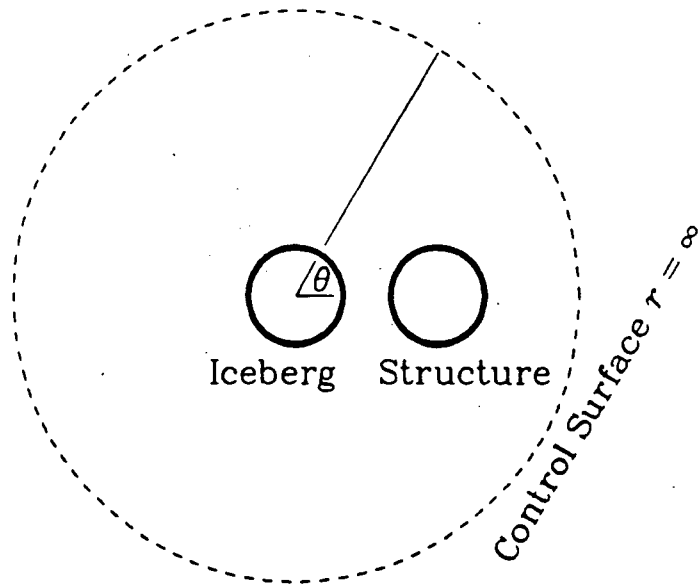


Figure 2.2: Control Surface for Far-field Wave Drift Force Computation

$$\begin{aligned}
F_{w_x} = & \\
& -\frac{\rho \omega H}{4 \sinh(kd)} \sqrt{\left(\frac{2\pi}{k}\right)} \left[ \frac{1}{4} \sinh(2kd) + \frac{kd}{2} \right] 2F(\alpha) \cos \left[ \gamma(\alpha) + \frac{\pi}{4} \right] \cos \alpha \\
& -\frac{\rho k}{2} \left[ \frac{1}{4} \sinh(2kd) + \frac{kd}{2} \right] \int_0^{2\pi} F^2(\theta) \cos \theta \, d\theta \quad (2.96)
\end{aligned}$$

$$\begin{aligned}
F_{w_y} = & \\
& -\frac{\rho \omega H}{4 \sinh(kd)} \sqrt{\left(\frac{2\pi}{k}\right)} \left[ \frac{1}{4} \sinh(2kd) + \frac{kd}{2} \right] 2F(\alpha) \cos \left[ \gamma(\alpha) + \frac{\pi}{4} \right] \sin \alpha \\
& -\frac{\rho k}{2} \left[ \frac{1}{4} \sinh(2kd) + \frac{kd}{2} \right] \int_0^{2\pi} F^2(\theta) \sin \theta \, d\theta \quad (2.97)
\end{aligned}$$

$$\begin{aligned}
F(\theta) \exp[i\gamma(\theta)] = & \\
& \frac{2\pi(\nu^2 - k^2)}{k^2 d - \nu^2 d + \nu} \sqrt{\frac{2}{\pi k}} \exp \left[ -i \frac{3\pi}{4} \right] \\
& \times \int_{S_i} Q(\xi, \eta, \zeta) \cosh[k(\zeta + d)] \exp[-ik\xi \cos \theta - ik\eta \sin \theta] \, dS \quad (2.98)
\end{aligned}$$

$$Q(\vec{\xi}) = \frac{H\omega}{8\pi} \left[ f_0(\vec{\xi}) + \sum_{k=1}^6 (-i f_k(\vec{\xi}) \zeta'_k) \right] \quad (2.99)$$

$$\gamma(\theta) = \tan^{-1} \left[ \frac{\text{Im}\{F(\theta) \exp[i\gamma(\theta)]\}}{\text{Re}\{F(\theta) \exp[i\gamma(\theta)]\}} \right] \quad (2.100)$$

$$F(\theta) = \frac{\text{Re}\{F(\theta) \exp[i\gamma(\theta)]\}}{\cos[\gamma(\theta)]} \quad (2.101)$$

where:

$F$  = force contribution term ( $\text{m}^{2.5}/\text{s}$ )

$Q$  = diffracted and radiation source strength term ( $\text{m}/\text{s}$ )

$\alpha$  = incident wave direction (rad)

$\gamma$  = phase term (rad)

$\nu = \omega^2/g$  ( $\text{m}^{-1}$ )

$\theta$  = angular co-ordinate for location on control volume (rad)

The computational method utilizing the above equations proceeds in the following sequence:

1.  $Q(\vec{\xi})$  is evaluated at each facet on the iceberg surface using equation 2.99,
2. Using equations 2.98, 2.100, and 2.101,  $F(\theta)$  and  $\gamma(\theta)$  are evaluated at 90 discrete values of  $\theta$  between 0 and  $2\pi$ ,
3.  $F_{wx}$  and  $F_{wy}$  are computed using numerical integration to evaluate equations 2.96 and 2.97.

## 2.4 Verification of Numerical Model

Due to the complexity of the iceberg motion model, a series of numerical tests was conducted to verify the validity of the model. Output from the model was compared with analytical, numerical, and physical modelling results found in the literature. Areas of the model which were subjected to verification included the following:

1. Wave-induced oscillatory motions,
2. Wave drift forces,
3. Zero frequency added masses,
4. Boundary element evaluation of current field in vicinity of structure.

### 2.4.1 Wave-Induced Motions

For verification of oscillatory motion computations, it was decided to examine the response of a barge which had been the subject of previous investigations [92,95,108]. Relevant parameters of the barge are given in Table 2.1 and Figure 2.3.

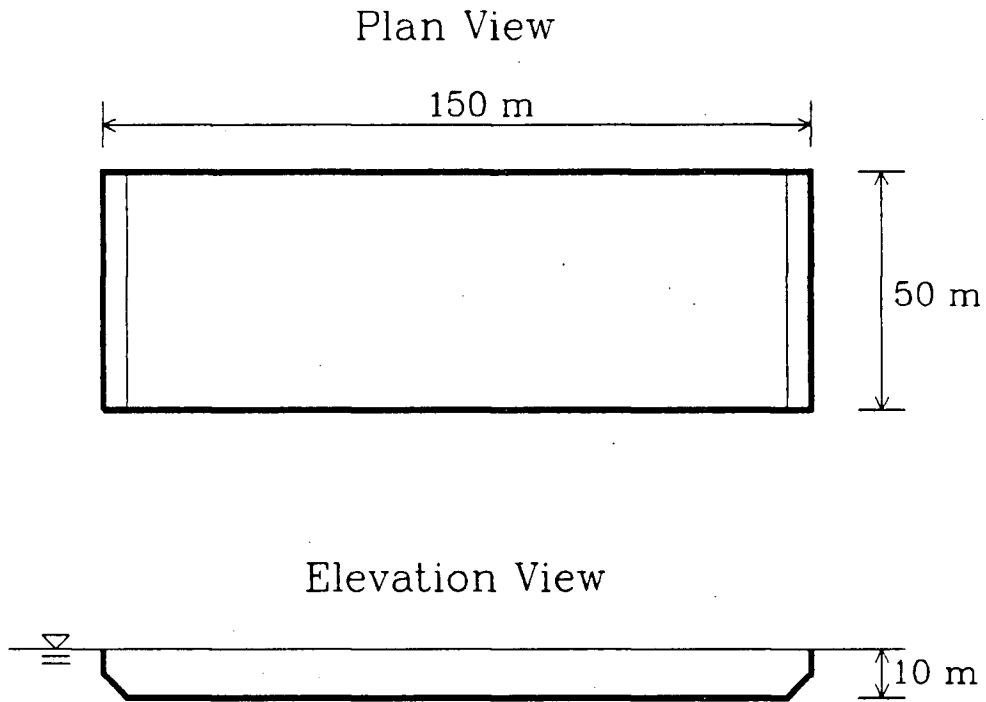


Figure 2.3: Barge for Verifying Diffraction Computations

Table 2.1: Hydrodynamic Properties of Barge (from [92])

Length	150 m
Breadth	50 m
Draft	10 m
Displaced volume	73750 m <sup>3</sup>
$z_g$	0 m
Transverse gyradius	20 m
Longitudinal gyradius	39 m
Vertical gyradius	39 m
Natural heave period	10.4 s
Natural pitch period	12.1 s
Natural roll period	9.4 s

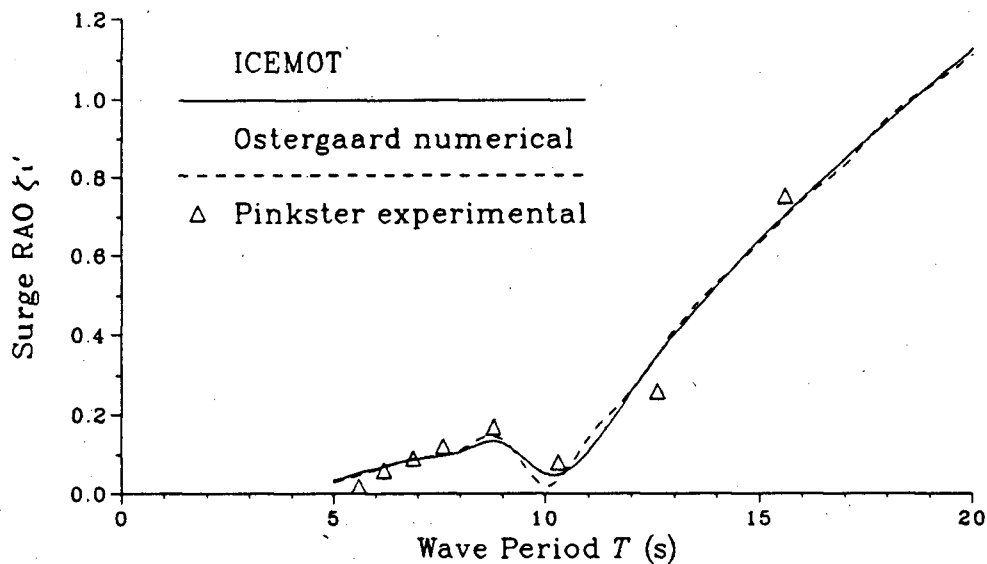


Figure 2.4: Barge Surge Motions in Head Waves

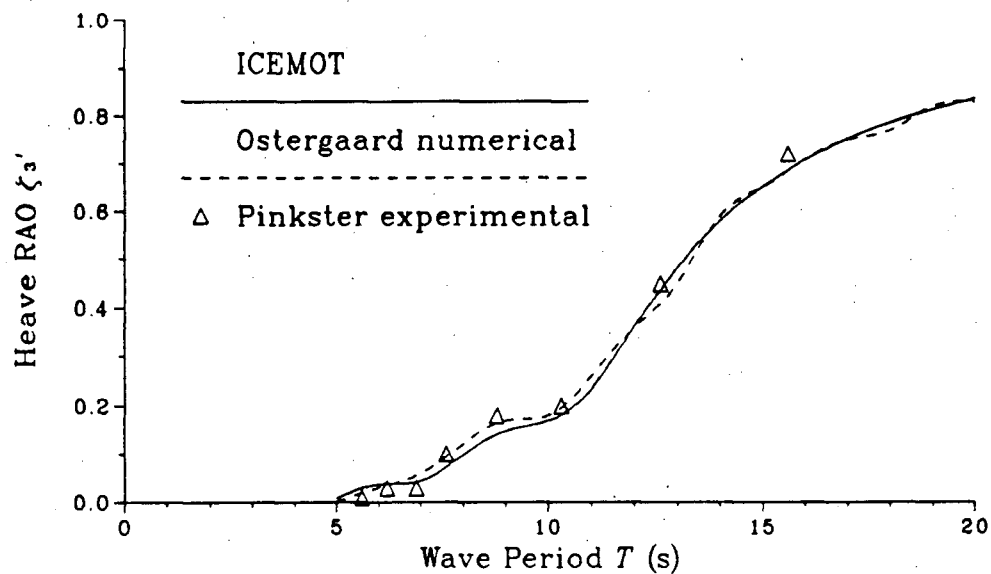


Figure 2.5: Barge Heave Motions in Head Waves

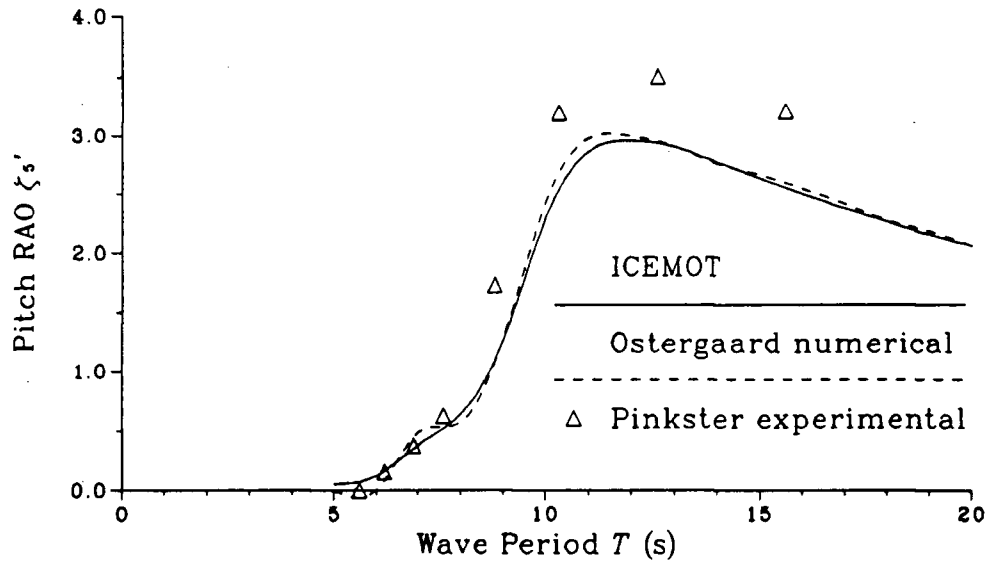


Figure 2.6: Barge Pitch Motions in Head Waves

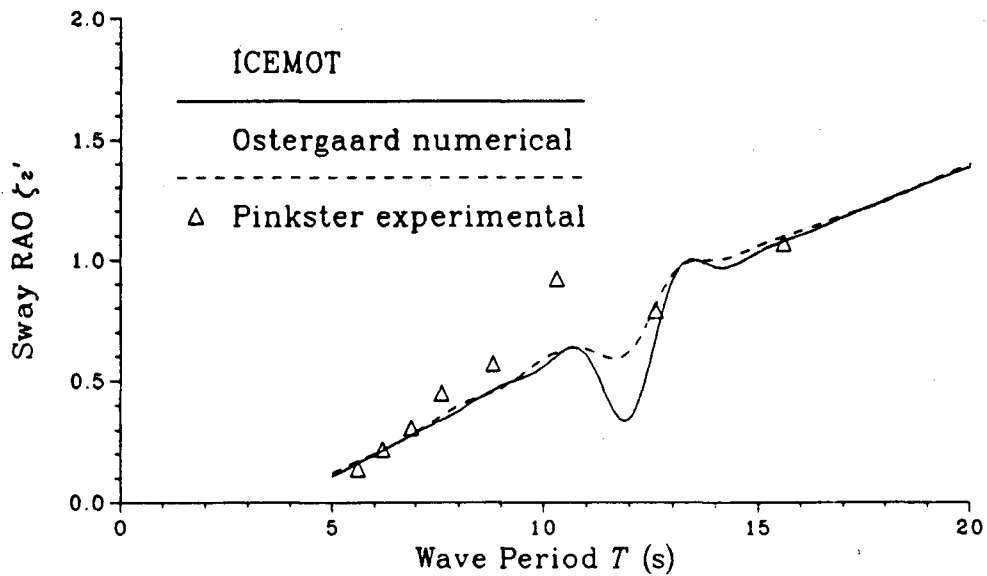


Figure 2.7: Barge Sway Motions in Beam Waves

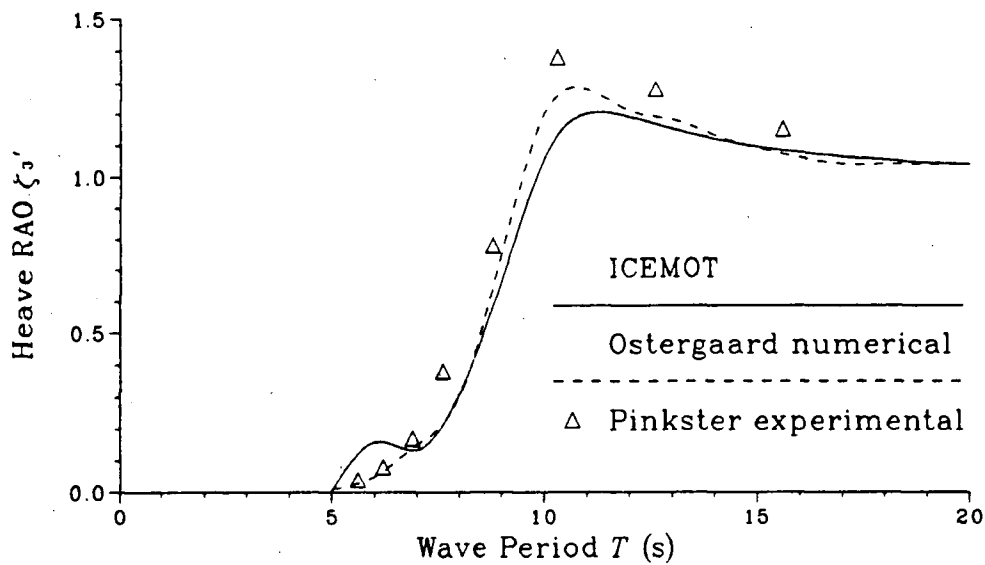


Figure 2.8: Barge Heave Motions in Beam Waves

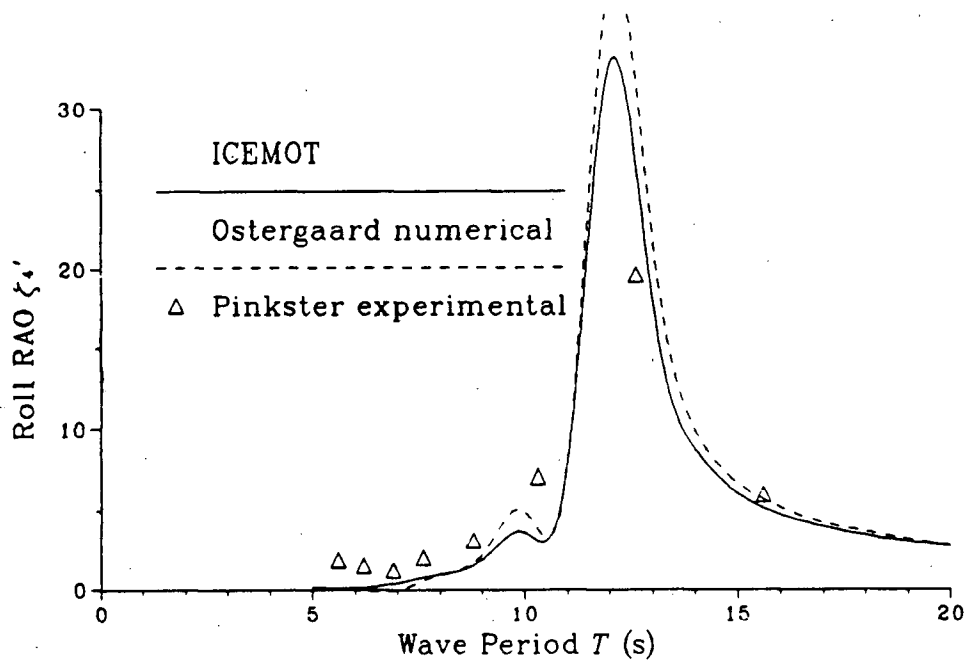


Figure 2.9: Barge Roll Motions in Beam Waves

Response computations were made for head waves and beam waves with periods ranging from 5 s to 20 s. The geometry of the barge was modelled using 142 facets. Viscous damping coefficients were set equal to zero for all cases. Figures 2.4 - 2.9 show comparisons with numerical results from Ostergaard and Schellin [92] and experiments by Pinkster [95]. The agreement among results supports the validity of the program ICEMOT. Differences between numerical and physical response values are most pronounced near the natural heave and roll periods of the barge. These discrepancies are due mainly to the absence of viscous damping in the numerical models.

### 2.4.2 Wave Drift Forces

Wave drift forces acting on the barge described above were also computed for verification. Results were originally compared with those published by Pinkster [95]; however, poor agreement was obtained. An explanation of the poor agreement between results was given by Standing et al. [108] who suggested that Pinkster's application of the near-field method caused significant errors arising from the evaluation of the waterline integral term of equation 2.95. Results from ICEMOT were subsequently compared with far-field computations by Standing et al. [108]. Figures 2.10 and 2.11 indicate relatively good agreement between results when one considers that wave drift forces are a second-order effect.

### 2.4.3 Zero Frequency Added Masses

Zero frequency added mass computations were verified using values published by Yeung [119]. Using an analytical solution for velocity potential, Yeung computed added mass and damping coefficients for vertical circular cylinders. Added masses were evaluated for cylinders having diameter  $D$  equal to water depth  $d$ , with the draft to water

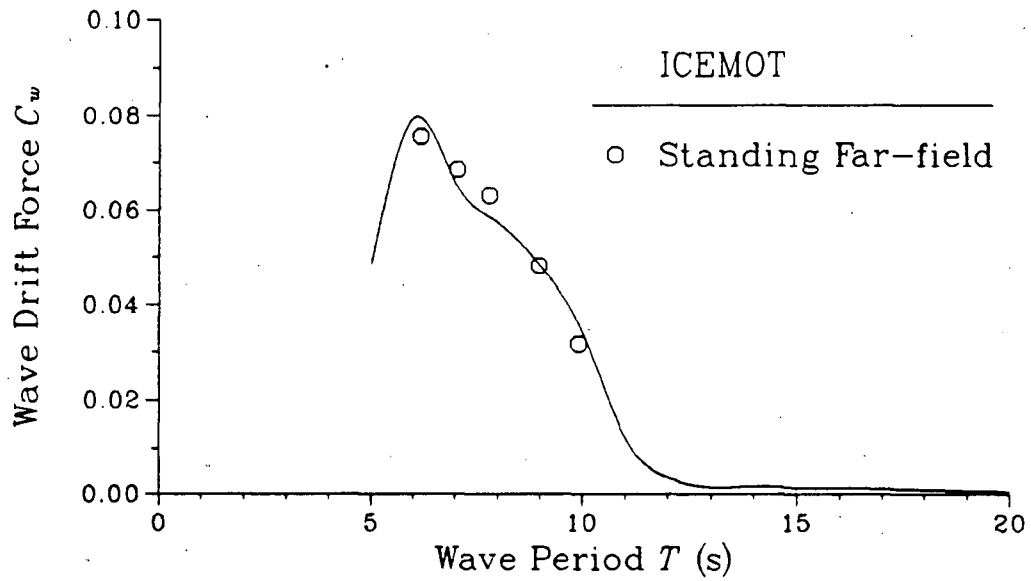


Figure 2.10: Barge Wave Drift Forces in Head Waves

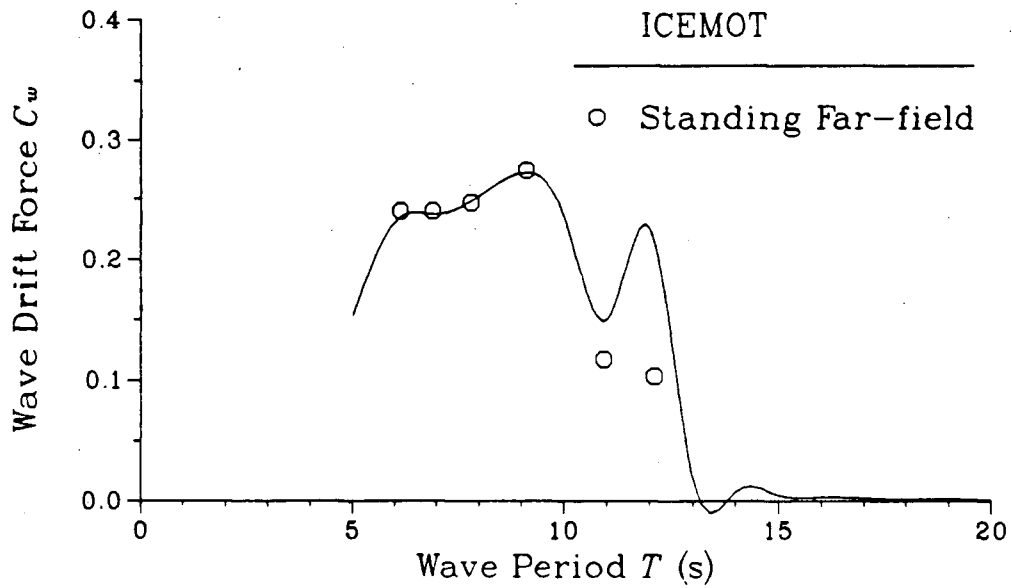


Figure 2.11: Barge Wave Drift Forces in Beam Waves

depth ratio  $h/d$  varying between 0 and 1. The surface of each cylinder was modelled using between 100 and 200 facets, depending on its geometry. The results presented in Figure 2.12 indicate excellent agreement between the analytical and numerical solutions. It appears that the number of facets used for each cylinder was sufficient to obtain accurate results using the boundary element method.

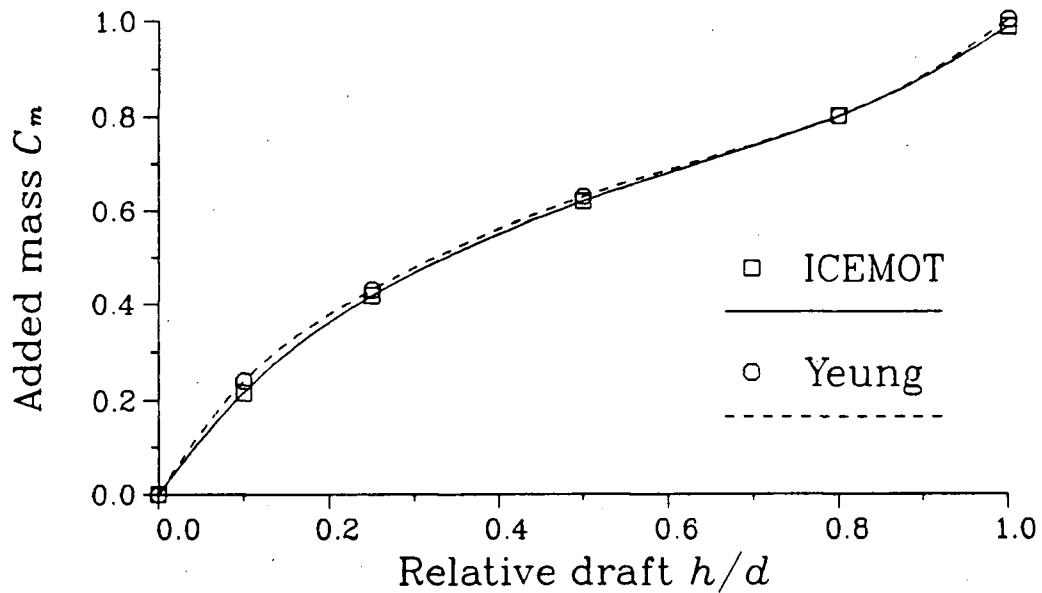


Figure 2.12: Zero Frequency Added Mass Coefficients for Vertical Circular Cylinders,  $D = d$

For the interaction case of an iceberg approaching a structure, the presence of the structure must be considered when evaluating iceberg added mass. Isaacson and Chngung [46] have indicated that facet sizes must be less than the distance between the iceberg and the structure for accurate added mass predictions using the boundary element method.

To assess the validity of ICEMOT for the interaction case, iceberg added masses for a two-dimensional example were computed and compared with results by Yamamoto [118]. The iceberg and structure were modelled as surface-piercing vertical circular cylinders

extending from the seabed, thus creating a two-dimensional flow field. Iceberg and structural diameters were taken as 100 m, with a corresponding water depth of 10 m for the numerical computations. Added mass computations were made for several facet grids, with each grid having less than the 200 facet limit imposed by the program ICEMOT. Optimal results were obtained using a structure mesh of  $32 \times 2$  facets (circumferential  $\times$  vertical) and an iceberg mesh of  $32 \times 4$  facets. It should be noted that inaccuracies in the boundary element method typically arise from flow sources at the centre of facets being too close together. The optimal grid described above would partly alleviate this problem due to staggering of iceberg and structure facet centres in the vertical direction.

Computed added masses using the optimal grid are presented in Figure 2.13. For separation distances greater than half a facet dimension, computed added masses are within 4% of those given by Yamamoto [118]. The boundary element values rapidly diverge from actual values for smaller separation distances. Greater accuracy in computed added masses for small separation distances could be achieved by using smaller facets on the portions of the iceberg and structure surfaces near the points of closest approach. Alternatively finer meshes for the entire iceberg and structure surfaces could be used to obtain accurate values for a smaller separation distance  $s$ ; however, the number of required facets for a three-dimensional boundary element solution would increase as  $1/s^2$  with the corresponding computer memory and number of computations increasing as  $1/s^4$ .

#### 2.4.4 Boundary Element Computation of Current Near Structure

The validity of the boundary element method for computing the current near a structure was tested using a vertical circular cylinder extending to the seabed. The analytical

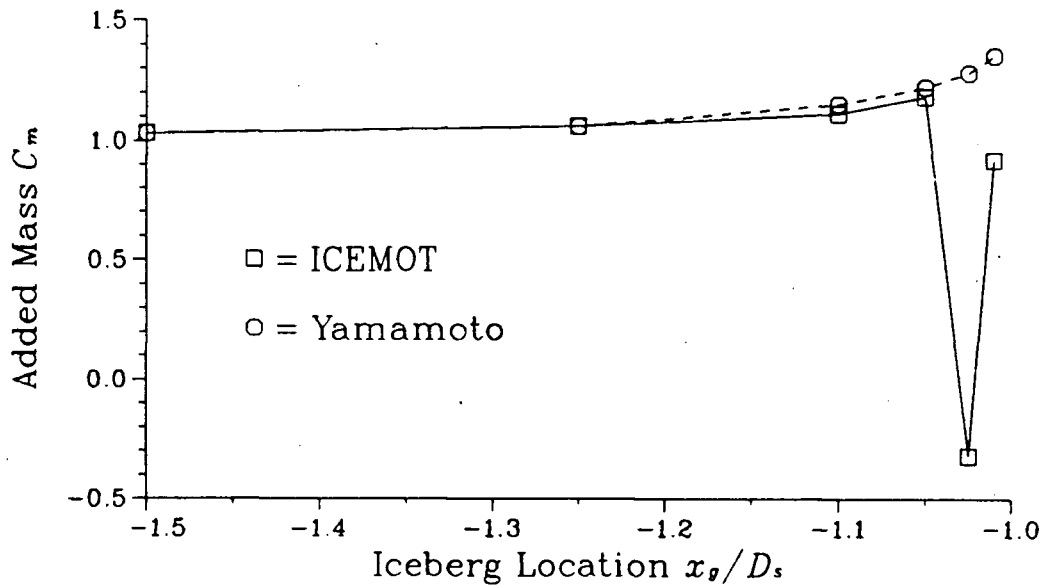


Figure 2.13: Zero Frequency Added Masses Approaching Structure

solution for flow around a cylinder (equation 2.92) provided a convenient means for verification. The diameter of the cylinder was set equal to the water depth. The cylinder surface was modelled using 144 facets; thus, a typical facet dimension was approximately 1/7th of the cylinder diameter.

The comparison of numerical and analytical current velocities presented in Figure 2.14 indicates that the boundary element method gives excellent results even within one facet diameter of the cylinder. Application of the boundary element for computing current fields is recommended when large structures of arbitrary shape are encountered.

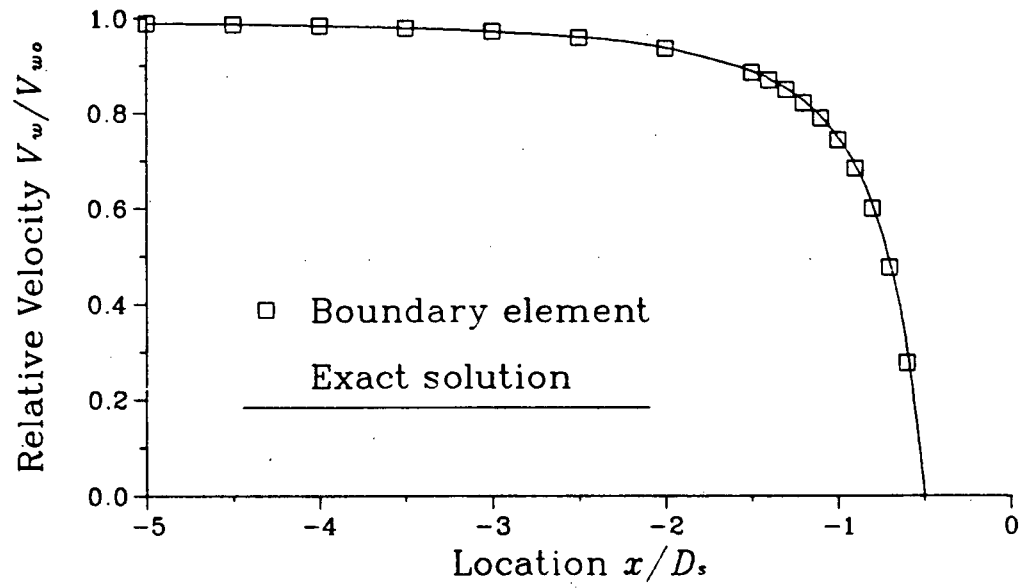


Figure 2.14: Current Velocity in Vicinity of Structure

## Chapter 3

### Hydrodynamic Aspects of Iceberg Collisions

As stated previously, a major objective of the present investigation is to examine the significance of hydrodynamic effects on iceberg collisions with a large offshore structure. Using the program ICEMOT, various aspects of collision hydrodynamics have been examined, with particular attention given to supplementing existing knowledge regarding iceberg hydrodynamics.

#### 3.1 Modelling of Iceberg Geometry

The present study uses vertical circular cylinders for modelling iceberg geometry. Cylinders have been used to model icebergs by several previous investigators, including Arunachalam et al. [5], Hay and Company [35], Isaacson and Cheung [46], Kobayashi and Frankenstien [52], McTaggart and Davenport [76], and Salvalaggio and Rojansky [99]. Consequently, much data is available in the literature regarding the hydrodynamics of cylinders.

Although the modelling of icebergs as random shapes would be more realistic, the modelling of random shapes would introduce several problems. The selection of representative shapes would be difficult and highly subjective. In addition, the complex geometry of a random iceberg would require a large number of facets to accurately describe its geometry. Further problems would be introduced by hydrodynamic stability requirements,

most notably the vertical alignment of centres of gravity and buoyancy. Among regular shapes, the circular cylinder is convenient for hydrodynamic modelling because rotational motions in the horizontal plane do not require evaluation.

When selecting a geometry for modelling icebergs, consideration should also be given to the mechanics of collisions. Results from Bass et al. [7] indicate that impact forces will be more severe if the impacting face of the iceberg is vertical; thus, a vertical circular cylinder will likely give a conservative impact force for a given impact scenario.

It is assumed that 1/7th of the volume of the modelled icebergs is above water, with hydrodynamic stiffness and inertial properties evaluated accordingly. A useful upper limit to iceberg aspect ratio  $h/D_i$  is determined by hydrostatic stability requirements. For a vertical circular with 1/7th of its volume above water, hydrostatic instability occurs when its aspect ratio exceeds approximately 0.86. The present investigation considers icebergs with aspect ratios to a maximum value of 0.8.

Although the influence of non-cylindrical shapes on iceberg hydrodynamics has not been considered in the present investigation, reference can be made to studies by Bass and Sen [8] and Lever et al. [58,61]. Bass and Sen used a numerical diffraction model to evaluate added mass and damping coefficients for various random iceberg shapes. Their results indicate that the greatest limitation imposed by a cylindrical iceberg geometry is that the variation of hydrodynamic coefficients with length/width ratio cannot be modelled. The influence of shape on wave-induced oscillatory motions was examined experimentally by Lever et al. for iceberg models having cubical, spherical, cylindrical, and trapezoidal geometries. For icebergs having non-vertical sides, the heave response was shown to be significantly different from icebergs having vertical sides due to the non-linearity of restoring forces in heave. Due to the absence of resonance effects for surge motions, the influence of iceberg shape on surge motions was much less than for heave motions.

## 3.2 Effective Iceberg Added Mass

Iceberg added mass is among the parameters that must be known when evaluating iceberg drift motions or for estimating the maximum energy that can be dissipated during a collision with an offshore structure. Due to the variation of added mass with frequency, the selection of a suitable value must be considered carefully. The numerical model of Isaacson [43] uses zero frequency added mass for the evaluation of iceberg drift motions, which are considered to be of low frequency relative to wave-induced oscillatory motions. Examination of various iceberg collision models [7,14,18,25,50] indicates that added mass is considered when evaluating iceberg kinetic energy and impact forces. Although not explicitly stated, it appears that zero frequency added mass is used in each of the above collision models.

Detailed studies of ship added masses during collision have been presented by Motora et al. [82] and Petersen and Pedersen [94]. Effective added masses are developed based on the kinetic energy and momentum absorbed during rapid deceleration of ships in collisions. For collisions of short duration, the effective added mass approaches the infinite frequency value. Conversely, the effective added mass approaches the zero frequency value for collisions of long duration.

### 3.2.1 Transient Motions of a Floating Body

Before considering effective added mass in greater detail, the basic principles of transient floating body motions will be presented. More detailed discussions of floating body transient motions are given by Mei [77] and Wehausen [115].

Recall that the oscillatory motion of a floating body are given by equation 2.39.

Alternatively, transient motions of a floating body can be expressed as:

$$[M + \mu(\infty)] \{\ddot{x}(t)\} + \{H(t)\} + [c] \{x(t)\} = \{F_e(t)\} \quad (3.1)$$

where:

$\{F_e\}$  = excitation force vector

$\{H\}$  = memory effect vector

The memory effect vector  $\{H\}$  is dependent on the floating body motions prior to time  $t$ . Components of  $\{H\}$  can be evaluated as follows:

$$H_i = \sum_{j=1}^6 \int_{-\infty}^t L_{ij}(t - \tau) \ddot{x}_j(\tau) d\tau \quad i = 1 - 6 \quad (3.2)$$

where:

$L_{ij}$  = history term (kg/s, kg·m/s, or kg·m<sup>2</sup>/s )

The excitation forces of  $\{F_e\}$  can be due to a variety of sources such as incident and diffracted waves, water drag forces, and forces experienced during a collision with another body.

Solution of the convolution integral of equation 3.2 requires that the history term  $L$  be known for a given body. From Wehausen [115],  $L$  can be evaluated by taking the cosine transform of the frequency dependent added mass or the sine transform of the frequency dependent damping as follows:

$$L_{ij}(t) = \frac{2}{\pi} \int_0^{\infty} [\mu_{ij}(\omega) - \mu_{ij}(\infty)] \cos \omega t dt \quad (3.3)$$

$$= \frac{2}{\pi} \int_0^{\infty} \frac{\lambda_{ij}(\omega)}{\omega} \sin \omega t dt \quad (3.4)$$

Thus, if the frequency dependent added mass or damping of a floating body is known, the history term  $L$  can be easily evaluated. The transient motions of a floating body can then be rigorously evaluated using equation 3.1.

### 3.2.2 Effective Added Mass for Iceberg Drift Motions

Although equation 3.1 provides a correct method for evaluating transient iceberg motions, its form is inconvenient for predicting iceberg drift motions. Recalling that the drift motions of an iceberg are not subjected to hydrostatic stiffness effects, equation 3.1 can be re-written for iceberg drift motions in one direction as follows:

$$[M + \mu(\infty)] \ddot{x}(t) + \int_{-\infty}^t L(t - \tau) \ddot{x}(\tau) d\tau = F_e(t) \quad (3.5)$$

Evaluation of the convolution integral of equation 3.5 is simplified by considering the following properties of  $L$ :

$$L(t) = 0 \quad \text{for } t \leq 0 \quad (3.6)$$

$$L(t) \approx 0 \quad \text{for } t > t_L \quad (3.7)$$

where:

$t_L$  = decay time for  $L$

Equation 3.7 suggests that  $L(t)$  can be considered equal to zero after a decay time  $t_L$  for a given body. The convolution integral of equation 3.5 can then be re-written as follows:

$$\int_{-\infty}^t L(t - \tau) \ddot{x}(\tau) d\tau = \int_{-\infty}^t L(\tau) \ddot{x}(t - \tau) d\tau \quad (3.8)$$

$$\approx \int_0^{t_L} L(\tau) \ddot{x}(t - \tau) d\tau \quad (3.9)$$

The right hand side of equation 3.9 can be easily evaluated numerically.

To simplify the evaluation of iceberg drift motions, it is convenient to develop an effective added mass coefficient  $C_m$  such that equation 3.5 can be approximated as follows:

$$M (1 + C_m) \ddot{x}(t) = F_e(t) \quad (3.10)$$

A solution for effective added mass can be readily obtained if it is assumed that the excitation force  $F_e$  and associated acceleration  $\ddot{x}$  vary slowly relative to the history decay

time  $t_L$ . This assumption is likely to be quite reasonable for a freely drifting iceberg, thus allowing equation 3.5 to be re-written as:

$$\left[ M + \mu(\infty) + \int_0^{t_L} L(\tau) d\tau \right] \ddot{x} = F_e \quad (3.11)$$

Solution of the above integral is made using the following relation from Wehausen [115]:

$$\int_0^{\infty} L(t) \cos \omega t dt = \mu(\omega) - \mu(\infty) \quad (3.12)$$

Taking  $\omega = 0$  in equation 3.12, equation 3.11 can then be re-written as:

$$[M + \mu(0)] \ddot{x} = F_e \quad (3.13)$$

Thus, it is appropriate to use zero frequency added mass for the evaluation of iceberg drift motions due to slowly varying excitation forces.

### 3.2.3 Effective Added Mass for Iceberg Collisions

When evaluating iceberg collisions with a structure, an estimate of added mass is required to assess the resulting collision forces. Effective added masses for head-on collisions can be based on either of the following momentum and energy relationships for an iceberg crushing against a rigid structure:

$$(1 + C_m) M V_c = \int_0^{t_c} F(t) dt \quad (3.14)$$

$$\frac{1}{2} (1 + C_m) M V_c^2 = \int_0^{\Delta_c} F(\Delta) d\Delta \quad (3.15)$$

where:

$F$  = collision force between iceberg and structure (N)

$t_c$  = collision duration (s)

$V_c$  = initial iceberg velocity (m/s)

$\Delta$  = distance travelled by iceberg during collision (m)

$\Delta_c$  = maximum  $\Delta$  for collision (m)

Evaluation of effective added mass based on each of the above equations requires that the force integral on the right hand side be solved. A time-stepping procedure must typically be used, with transient iceberg motions during the collision ideally based on equation 3.5. The evaluation of effective added mass can be somewhat simplified if the variation of impact force with time is assumed to be of a known form.

### Maximum Impact Force

The maximum impact force to occur during a head-on iceberg collision can be estimated using the kinetic energy balance of equation 3.15. The normal contact area for a cylindrical iceberg impacting a cylindrical structure can be approximated as follows (see Chapter 6):

$$A_n(\Delta) = 2 h_t \left( \frac{D_i \Delta}{1 + D_i/D_s} \right)^{1/2} \quad (3.16)$$

It is assumed in the above equation that the penetration distance  $\Delta$  is small relative to the iceberg and structure diameters  $D_i$  and  $D_s$  respectively. Substituting equations 1.1 and 3.16 into the kinetic balance of equation 3.15, the maximum iceberg displacement and impact force are as follows:

$$\Delta_c = \left[ \frac{3 (1 + C_m) M V_c^2}{8 p_{cr} h_t \left( \frac{D_i}{1 + D_i/D_s} \right)^{1/2}} \right]^{2/3} \quad (3.17)$$

$$F_c = \left[ \frac{3 p_{cr}^2 h_t^2 (1 + C_m) D_i M V_c^2}{1 + D_i/D_s} \right]^{1/3} \quad (3.18)$$

Equation 3.18 is particularly useful for examining the relative importance of each collision parameter on impact severity.

The assumption of a vertical circular cylinder for iceberg geometry will typically overestimate the contact area  $A_n$  for a given penetration distance  $\Delta$ . For an iceberg of irregular geometry impacting an offshore structure, the reduction in contact area for a given penetration distance will lead to a smaller maximum impact force  $F_c$  and a larger maximum penetration distance  $\Delta_c$ .

### Collision Duration and Added Mass for Ramp Impact Force

The duration of an iceberg collision can be estimated using the momentum balance of equation 3.14. No analytical solution for collision duration is readily available from the momentum balance; however, collision duration can be easily estimated if the variation of impact force with time is assumed to be of a known form.

When considering how impact force  $p_{cr} A_n$  varies with time, it should be noted from equation 3.16 that the impact force during a collision may be expressed in the form:

$$F = k_F \Delta^{1/2} \quad (3.19)$$

where:

$$k_F = \text{force constant (N/m}^{1/2}\text{)}$$

Thus, the iceberg velocity  $d\Delta/dt$  during the collision can be related to the force as follows:

$$\frac{d\Delta}{dt} = \frac{2 F (dF/dt)}{k_F^2} \quad (3.20)$$

Given that the collision force  $F$  is equal to zero at the beginning of a collision and that the initial impact velocity  $d\Delta/dt$  is non-zero,  $dF/dt$  must approach infinity at the beginning of a collision. Although a step forcing function will satisfy the above requirements, results from numerical impact models by Bass et al. [7] and Duthinh and Marsden [25] indicate

that it is more reasonable to adopt a ramp impact force function as follows:

$$F(t) = \begin{cases} 0 & t < 0 \text{ and } t > t_c \\ \frac{t}{t_c} F_c & 0 \leq t \leq t_c \end{cases} \quad (3.21)$$

Note that the above forcing function does not satisfy the requirement that  $dF/dt$  approach infinity at the beginning of a collision. Adopting the ramp force assumption, the momentum balance of equation 1.2 can then be expressed as:

$$(1 + C_m) M V_c = \frac{1}{2} t_c^2 F_c \quad (3.22)$$

Substituting equation 3.18 into equation 3.22, the collision duration for a ramp impact force is:

$$t_c = 2 \left[ (1 + C_m) \frac{\pi \rho_i}{4 p_{cr}} \right]^{2/3} \left[ \frac{(1 + D_i/D_s) V_c}{3} \right]^{1/3} D_i \quad (3.23)$$

As stated previously, the assumption of a vertical circular cylinder iceberg geometry will likely lead to overestimates of the maximum impact force  $F_c$ ; thus, the actual collision duration will likely be greater than the estimate given by equation 3.23.

A technique for predicting effective collision added masses has been developed by Motora et al. [82], who assume that the variation of collision force with time is of a known form. If the hydrodynamic inertial and damping forces acting on the iceberg are taken as being linear, then a Fourier transform technique can be applied. The assumption of linear damping forces is valid provided that the damping forces arise from radiation damping rather than viscous damping. Although viscous damping can have a significant effect on heave, pitch, and roll motions, its influence is usually small for surge motions.

For application of the Fourier transform technique, the response of an iceberg to the following ramp forcing function can be considered:

$$f_e(t) = \begin{cases} 0 & \text{for } t < 0 \\ t & \text{for } t \geq 0 \end{cases} \quad (3.24)$$

where:

$f_e =$  forcing function (s)

The external forcing function  $f_e$  could be representative of the force applied to an iceberg by a structure during a collision. To obtain the Fourier transform of the iceberg acceleration, the Fourier transform of the external forcing function  $f_e$  can be multiplied by the acceleration admittance function of the iceberg oscillatory motions (equation 2.39) as follows:

$$A(\omega) = \frac{i \omega}{i \omega M_v(\omega) + \lambda(\omega)} F_e(\omega) \quad (3.25)$$

where:

$A(\omega) =$  Fourier transform of iceberg acceleration

$F_e(\omega) =$  Fourier transform of external force  $f_e(t)$

$M_v(\omega) =$  virtual iceberg mass at frequency  $\omega$  (kg)

Taking the inverse Fourier transform of equation 3.25 and then integrating with respect to time, Motora et al. [82] have shown that the change in velocity due to the ramp forcing function of equation 3.24 is:

$$\begin{aligned} \Delta v(t) = & \frac{\frac{1}{2}t^2}{M_v(0)} - \frac{2}{\pi} \int_0^\infty \frac{\lambda(\omega)}{M_v^2(\omega) \omega^2 + \lambda^2(\omega)} \frac{\cos \omega t}{\omega^2} d\omega \\ & + \frac{2}{\pi} \int_0^\infty \frac{\lambda(\omega)}{M_v^2(\omega) \omega^2 + \lambda^2(\omega)} \frac{1}{\omega^2} d\omega \end{aligned} \quad (3.26)$$

where:

$\Delta v =$  change in iceberg velocity in response to forcing function ( $s^2/kg$ )

Taking a momentum balance over the duration  $t_c$  of the ramp force, the effective added mass can be obtained by:

$$M (1 + C_m) = \frac{\int_0^{t_c} f_e(t) dt}{\Delta v(t_c)} \quad (3.27)$$

$$= \frac{1/2 t_c^2}{\Delta v(t_c)} \quad (3.28)$$

Substituting equation 3.26 into 3.27, the effective added mass based on a momentum balance for a ramp force can be determined by:

$$M (1 + C_m) = \left[ \frac{1}{M_v(0)} - \frac{4}{\pi t_c^2} \int_0^\infty \frac{\lambda(\omega)}{M_v^2(\omega) \omega^2 + \lambda^2(\omega)} \frac{\cos \omega t}{\omega^2} d\omega + \frac{4}{\pi t_c^2} \int_0^\infty \frac{\lambda(\omega)}{M_v^2(\omega) \omega^2 + \lambda^2(\omega)} \frac{1}{\omega^2} d\omega \right]^{-1} \quad (3.29)$$

Thus, the effective added mass for a given iceberg is merely a function of collision duration  $t_c$  which can be estimated using equation 3.23. The assumption of a ramp impact force greatly simplifies the required computation for predicting effective added mass.

To evaluate the influence of the shape of the assumed forcing function on added mass estimates, one can consider collision forces arising from step and ramp forcing functions, between which the actual forcing function will likely lie. The collision duration predicted for a step forcing function will be one half of the value predicted for a ramp forcing function; thus, the actual collision duration will be no less than half the value predicted by equation 3.23 provided that all parameters of equation 3.23 are known. With regard to the influence of forcing function on effective added mass, Matora et al. have shown that the momentum-based effective added mass for a step force can be up to 30% greater than the effective added mass for a ramp force of equivalent duration; however, differences between equivalent added masses for step and ramp forcing functions are typically much smaller for most collision durations. In summary, the influence of the assumed forcing function shape will likely have only a small effect on predicted equivalent added masses. It is likely that differences between an assumed ramp forcing function and the actual forcing function for an iceberg collision will result in only minor differences between

effective added mass estimates.

### Collision Duration and Effective Added Mass by Time-Stepping

Assumptions regarding the variation of impact force with time can be avoided if a numerical time-stepping procedure is used to determine collision duration and effective added mass. The motions of an iceberg during a collision can be rigorously evaluated using the equation of transient motion for a floating body (equation 3.1). For a head-on impact with a structure, the equation of motion for an iceberg can be written as:

$$\ddot{\Delta}(t) = \frac{F(t) - \int_{-\infty}^t L(t - \tau) \ddot{\Delta}(\tau) d\tau}{M [1 + C_m(\infty)]} \quad (3.30)$$

Equation 3.30 can be evaluated numerically to determine iceberg displacement and associated impact force at any time during a collision. Numerical integration of impact force  $F$  with respect to time  $t$  and distance  $\Delta$  can be used to obtain estimates for effective added mass based on momentum (equation 3.14) and kinetic energy (equation 3.15) respectively.

#### 3.2.4 Effective Added Mass Example Problem

Effective added masses and relevant parameters have been evaluated for an example cylindrical iceberg having a diameter  $D_i$  of 100 m, a draft  $h$  of 50 m, and situated in a water depth  $d$  of 100 m. Frequency dependent added mass and damping for surge motions were computed using the program ICEMOT, and were also obtained from Yeung [119]. Due to facet size limitations, added mass and damping were available for a maximum frequency  $\omega$  of 1.25 rad/s. For higher frequencies it was assumed that added mass and damping coefficients reached their infinite frequency values of 0.321 and 0 respectively at  $\omega = 3.0$  rad/s, with intermediate values in the range  $1.25 \text{ rad/s} < \omega < 3.0 \text{ rad/s}$

estimated using linear interpolation. Note that the upper frequency limit of 3.0 rad/s was selected such that the following relationship from Wehausen [115] would be satisfied:

$$\int_0^{\infty} (\mu(\omega) - \mu(\infty)) d\omega = 0 \quad (3.31)$$

Frequency dependent added mass and damping for the example iceberg are presented in Figure 3.1.

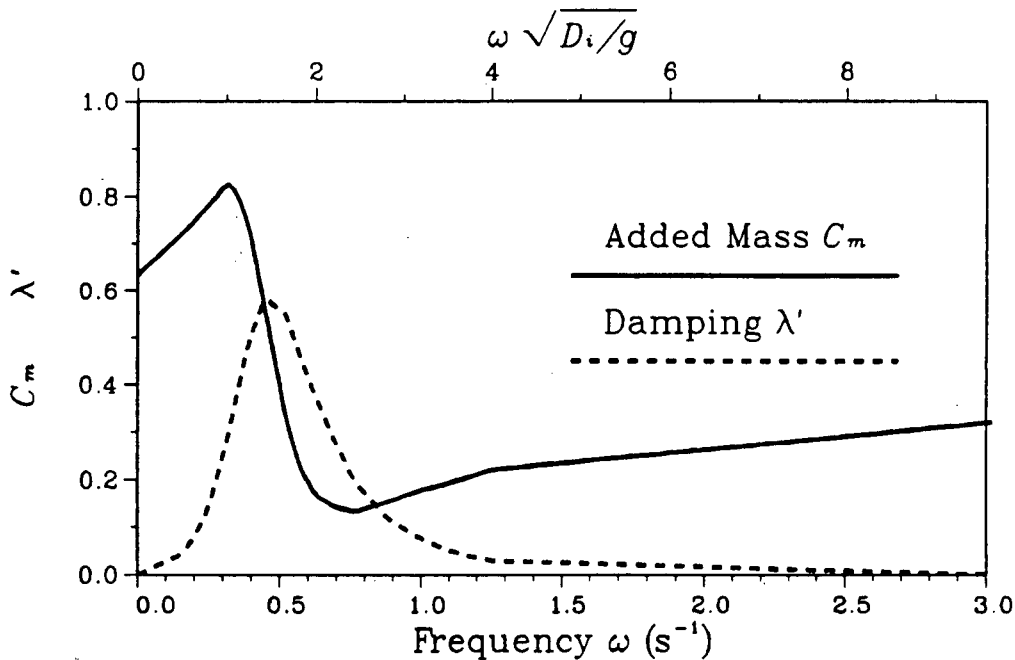


Figure 3.1: Frequency Dependent Added Mass and Damping for 100 m  $\times$  50 m Iceberg

The history term obtained from the sine transform of the frequency dependent damping (equation 3.4) is presented in Figure 3.2, and is shown to have a decay time  $t_L$  of approximately 20 s for the example iceberg. Estimates of  $t_L$  for other icebergs can be developed using dimensional analysis. If the assumptions of inviscid flow and a vertical circular cylinder are maintained,  $t_L$  is a function of the following variables:

$$t_L = f(D_i, h, d, g, \rho, \rho_i) \quad (3.32)$$

In terms of dimensionless variables, equation 3.32 can be re-written as:

$$t_L \sqrt{\frac{g}{D_i}} = f(h/D_i, h/d, \rho_i/\rho) \quad (3.33)$$

The computed values for the example problem suggest that  $t_L \sqrt{g/D_i}$  will be of the order of 10 for an iceberg having an aspect ratio  $h/D_i$  of 0.5 and a relative draft  $h/d$  of 0.5.

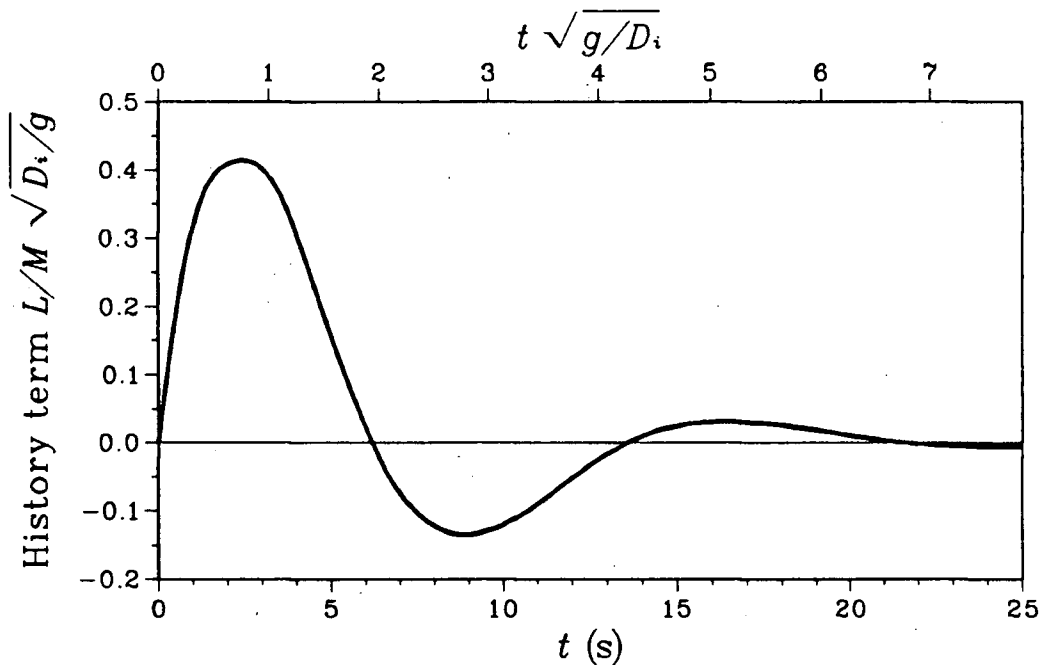


Figure 3.2: History Term for 100 m  $\times$  50 m Iceberg

### Effective Added Masses for Ramp Forcing Function

Effective added masses for a ramp forcing function obtained from equation 3.29 are shown in Figure 3.3. For collisions of short duration the added mass is approximately equal to the infinite frequency value, while the zero frequency added mass is approached for collisions of long duration. These results are in agreement with those presented by Motora et al. [82] and Petersen and Pedersen [94].

In considering the general applicability of computed added masses, it is useful to note that the added mass of a vertical circular cylinder subjected to a ramp forcing function can be expressed as follows:

$$C_m = f(D_i, h, d, g, t_c, \rho, \rho_i) \quad (3.34)$$

In terms of dimensionless variables:

$$C_m = f\left(h/D_i, h/d, t_c \sqrt{g/D_i}, \rho_i/\rho\right) \quad (3.35)$$

The results of Figure 3.3 indicate that infinite frequency added mass can be used in iceberg collision design when  $t_c \sqrt{g/D_i} < 0.5$ , while zero frequency added mass should be used when  $t_c \sqrt{g/D_i} > 3$ . For design purposes the zero frequency added mass provides a convenient and somewhat conservative value for effective added mass.

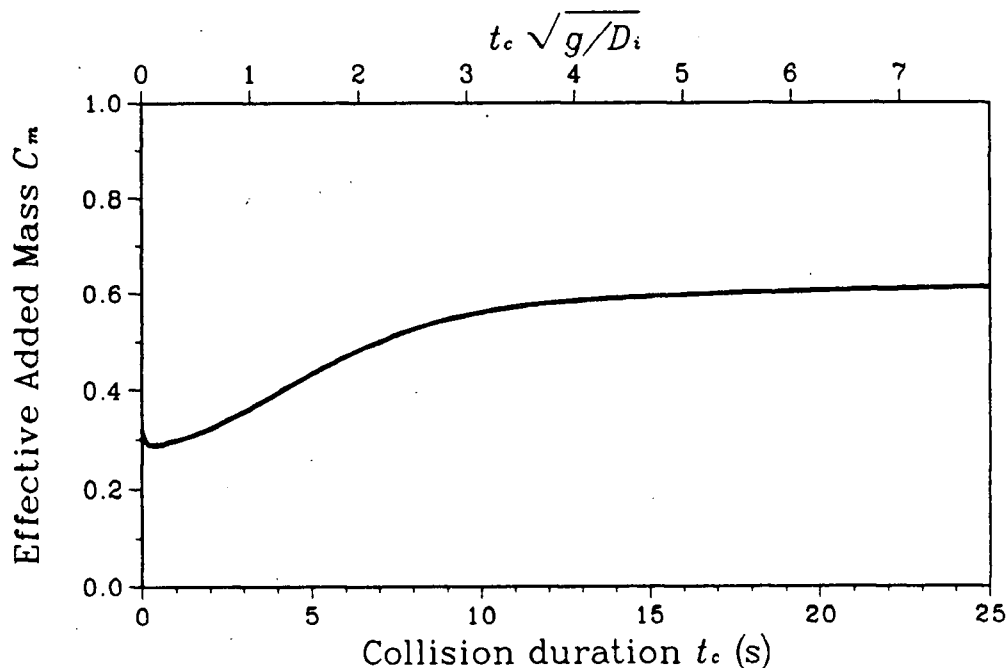


Figure 3.3: Effective Added Mass for 100 m  $\times$  50 m Iceberg, Ramp Forcing Function

Table 3.1: Input Parameters for Comparison of Ramp and Time Stepping Models

Water depth, $d$	100 m
Structure diameter, $D_s$	100 m
Iceberg diameter, $D_i$	100 m
Iceberg draft, $h$	50 m
Iceberg height, $h_t$	57 m
Impact velocity, $V_c$	1.0 m/s
Ice pressure, $p_{cr}$	0.02 - 5.0 MPa

### Comparison of Ramp and Numerical Impact Force Models

To assess the validity of assuming a ramp impact force function, collision parameters have been evaluated using both the ramp impact force assumption and a numerical time stepping procedure based on equation 3.30. Input parameters for the example problem are given in Table 3.1. Note that computations were made for input ice pressures varying between 0.02 MPa and 5 MPa.

Estimates of effective added masses and collision durations for the ramp force function were made using successive iterations of equation 3.23 and effective added masses presented in Figure 3.3. Due to the relatively minor influence of effective added mass on collision duration, convergence was always achieved in two iterations. After determining effective added mass for a given collision, the maximum ice indentation  $\Delta_c$  and maximum impact force  $F_c$  were evaluated using equations 3.17 and 3.18 respectively.

Iceberg collisions were also evaluated using a numerical time-stepping procedure based on equation 3.30, with a time interval of 0.01 times the collision duration estimated from equation 3.23. The convolution integral of equation 3.30 was evaluated numerically at each time step. Iceberg velocities and displacements during collisions were obtained by

numerical integration of equation 3.30. At the end of each collision, the effective added mass was determined by the momentum balance of equation 3.14.

Results from the ramp force and numerical time-stepping models are shown in Figures 3.4 - 3.7. Collision durations presented in Figure 3.4 indicate that the ramp force model over-estimates collision duration by approximately 50%. This result corresponds with numerical impact force models by Bass et al. [7] and Duthinh and Marsden [25], which suggest that the ramp force model will under-estimate forces in the early stages of a collision, thus leading to over-estimates of collision duration.

Effective added masses presented in Figure 3.5 are in good agreement. According to Motora et al. [82], ramp force added masses for collisions of short duration should approach the infinite frequency added mass. The results presented for the ramp function approach a value of 0.29 rather than the infinite frequency value of 0.32. Errors in the estimated frequency dependent added mass and damping coefficients (Figure 3.1) are the likely source of this discrepancy.

Penetration distances and impact forces for the two models are virtually identical. The excellent agreement between the two models is primarily due to the relatively minor influence of effective added mass on penetration distance  $\Delta_c$  (equation 3.17) and impact force  $F_c$  (equation 3.18).

The above results indicate that the assumption of a ramp input force function can be used to estimate effective added mass. An estimate of collision duration can be made using equation 3.23. The appropriate added mass for collision design (i.e. infinite frequency or zero frequency) can then be selected based on the dimensionless parameter  $t_c\sqrt{g/D_i}$  and effective added masses given in Figure 3.3.

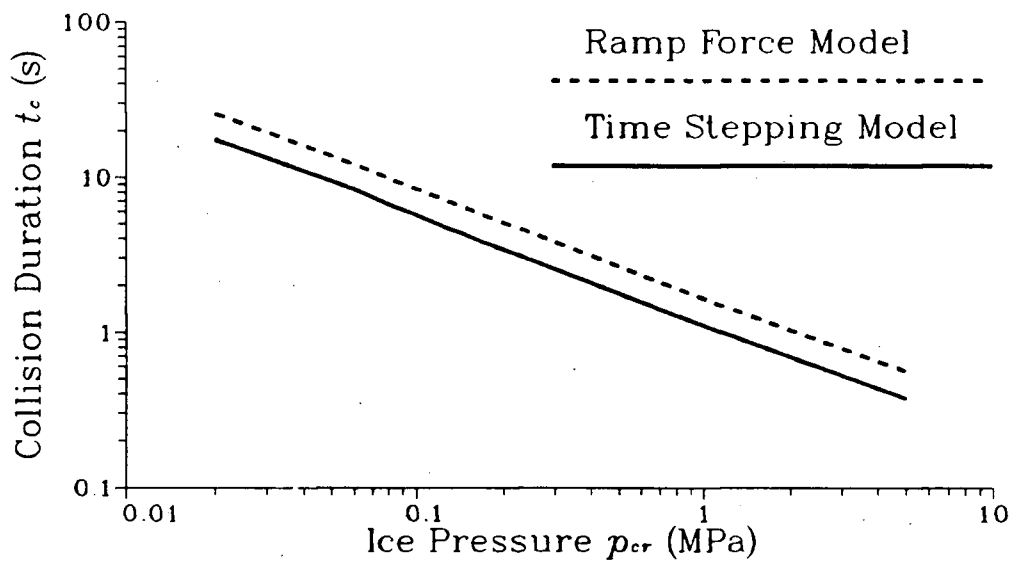


Figure 3.4: Collision Duration for Ramp and Time Stepping Models

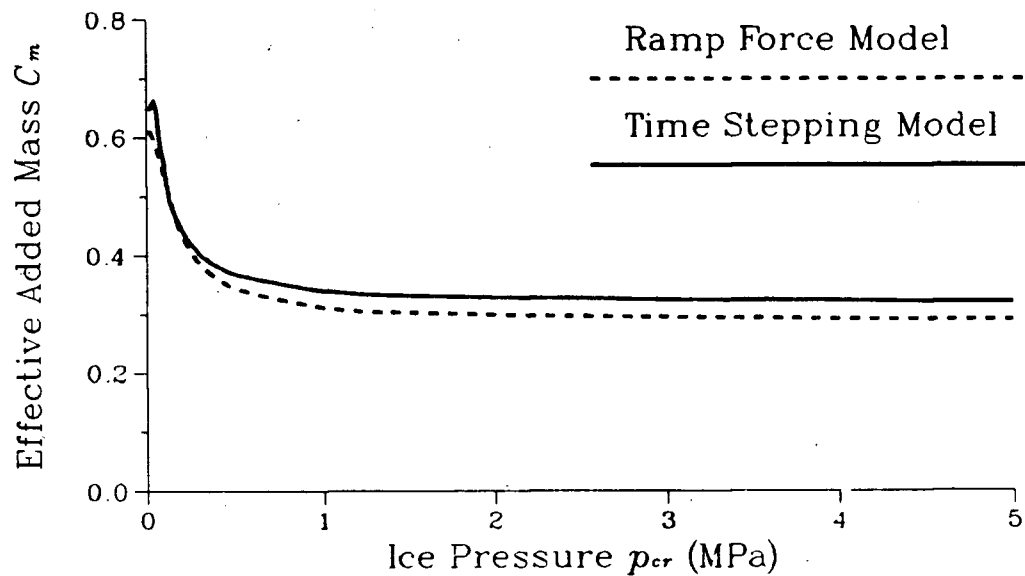


Figure 3.5: Effective Added Mass for Ramp and Time Stepping Models

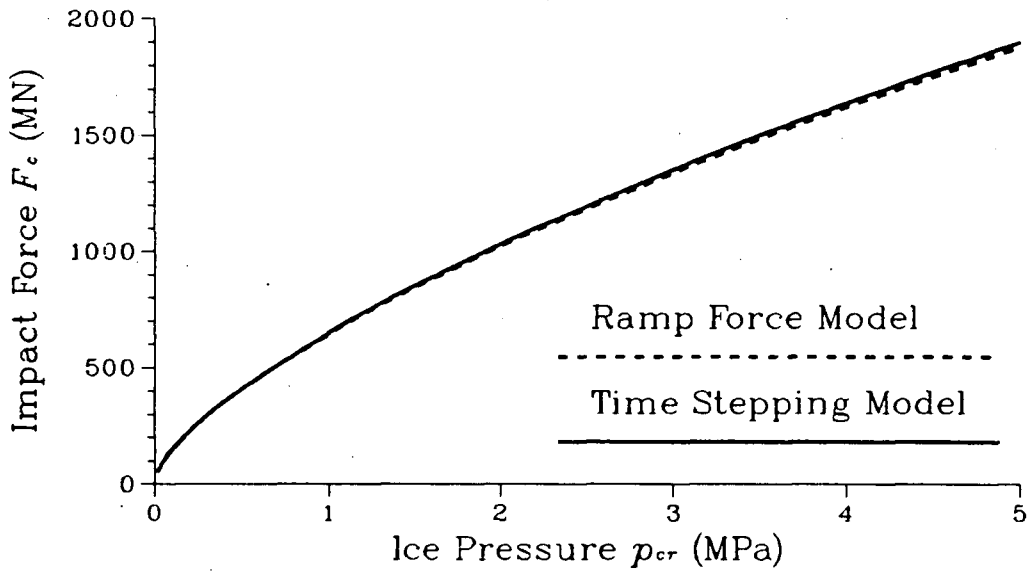


Figure 3.6: Impact Force for Ramp and Time Stepping Models

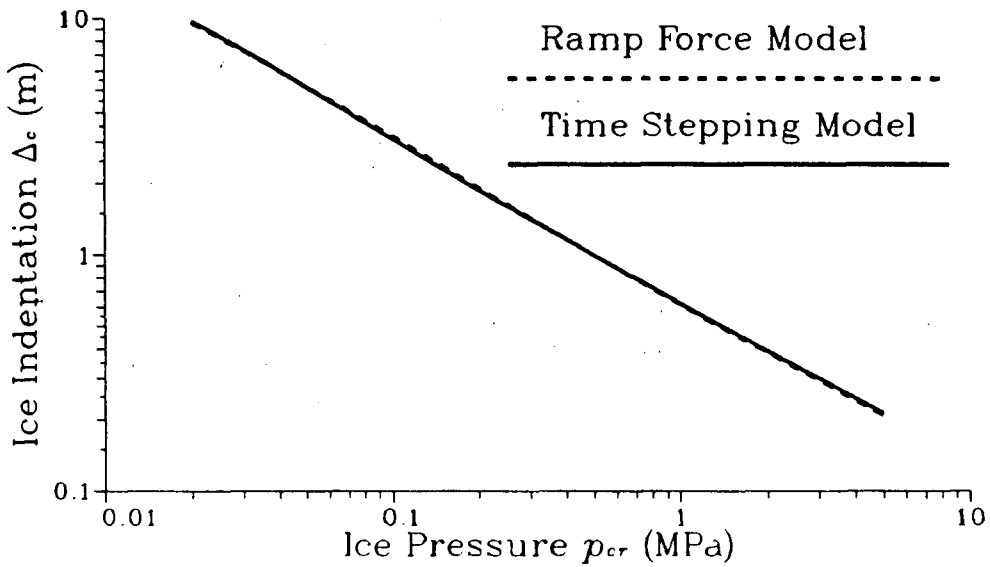


Figure 3.7: Ice Penetration for Ramp and Time Stepping Models

### 3.3 Iceberg Hydrodynamic Coefficients in Open Water

Information regarding iceberg hydrodynamics in open water (i.e. away from other bodies) was compiled using program ICEMOT and data in the literature. Open water hydrodynamic coefficients could be used to estimate impact velocities with small structures, and to make preliminary estimates of impact velocities with large structures. Parameters of primary interest included the following:

1. Surge response amplitude operators,
2. Wave drift force coefficients,
3. Zero frequency added mass coefficients,
4. Infinite frequency added mass coefficients,
5. Water drag coefficients.

The above parameters were compiled for a wide range of input conditions.

#### 3.3.1 Diffraction Computations of Wave Drift Force Coefficients and Surge RAO's

Wave drift force coefficients and surge RAO's are necessary for predicting iceberg drift and oscillatory velocities. The surge RAO  $\zeta'_1$  is the amplitude of oscillatory surge motions in unit amplitude waves, while the wave drift force acting on an iceberg can be expressed in terms of a wave drift coefficient as follows:

$$F_w = \frac{1}{2} C_w \rho g D_i H^2 \quad (3.36)$$

where:

$C_w$  = wave drift force coefficient

Although previous investigators have computed wave drift force coefficients and surge RAO's for specific cases (e.g. Arunachalam et al. [5], Hsiung and Aboul-Azm [40], Isaacson [43], Lever and Sen [59], NORDCO [90]), a comprehensive set of coefficients was lacking.

The compilation of hydrodynamic coefficients is made manageable if the assumptions of cylindrical iceberg geometry, linear wave theory, and inviscid flow are adopted. Linear wave theory can be considered valid for wave heights small relative to water depth and incident wavelength, while the assumption of inviscid flow will be valid if the iceberg diameter is large relative to the distance traversed by water particles during a wave period. Wave drift coefficients and surge RAO's can subsequently be considered as functions of 3 dimensionless parameters:

$$C_w = f\left(h/D_i, h/d, \frac{\omega^2 D_i}{2g}\right) \quad (3.37)$$

$$\zeta'_1 = f\left(h/D_i, h/d, \frac{\omega^2 D_i}{2g}\right) \quad (3.38)$$

### Parameter Ranges Adopted for Computations

The three independent parameters of equations 3.37 and 3.38 were selected such that each parameter would have a limited range of validity or interest. Due to hydrodynamic stability requirements, a maximum iceberg aspect ratio  $h/D_i$  of 0.8 was adopted. The dimensionless draft  $h/d$  (draft/depth) has a maximum possible value of 1. Boundary element computations introduce a further requirement that the gap between the seabed and iceberg bottom should be at least one facet diameter; thus,  $h/d$  was limited to a maximum value of approximately 0.9. The range of interest for the frequency parameter

$\omega^2 D_i/2g$  was based on limiting values for  $C_w$  and  $\zeta'_1$ . For  $\omega^2 D_i/2g < 0.5$ , the incident wavelength becomes large relative to iceberg diameter. Experimental results by Lever et al. [59] indicate that the iceberg moves as a water particle in this low frequency range, with the corresponding surge RAO from linear wave theory as follows:

$$\zeta'_1 = \frac{1}{\tanh(kd)} \quad (3.39)$$

Numerical results from the program ICEMOT and other sources (e.g. Hsiung and Aboul-Azm [40], Kobayashi and Frankenstien [52]) indicate that wave drift force coefficients approach 0 in this lower frequency limit.

As the frequency parameter  $\omega^2 D_i/2g$  becomes greater than 3 the incident wavelength becomes small relative to the iceberg diameter, requiring a large number of boundary element facets to maintain facet diameters less than  $\lambda/8$ . Oscillatory motions become relatively small and wave drift forces approach the following high frequency limit given by Maruo [74] for waves propagating in the  $x$  direction:

$$F_w = \frac{1}{8} \rho g H^2 \int_{-b}^b \sin^2 \beta_{wl} dy \quad (3.40)$$

where:

$-b, b$  = points on waterline where  $\beta_{wl} = 0^\circ$  and  $180^\circ$  respectively

$\beta_{wl}$  = angle between waterline plane tangent and wave direction ( $^\circ$ )

For a vertical circular cylinder, the high frequency limit for  $C_w$  is 1/6. The frequency parameter range adopted for the diffraction computations was  $0.5 < \omega^2 D_i/2g < 3.14$ , with the upper frequency limit being imposed by restrictions on facet size and the lower frequency limit governed by the small degree of wave diffraction for smaller icebergs.

### Discussion of Computed Surge Response Amplitude Operators

Computed surge RAO's are presented in Figures 3.8 - 3.12. Due to the absence of resonance effects for surge motions, the presented RAO's exhibit a relatively smooth variation with the frequency parameter  $\omega^2 D_i / 2g$ . It appears that the numerical surge RAO's model actual conditions reasonably well, with high frequency and low frequency values agreeing with expected trends.

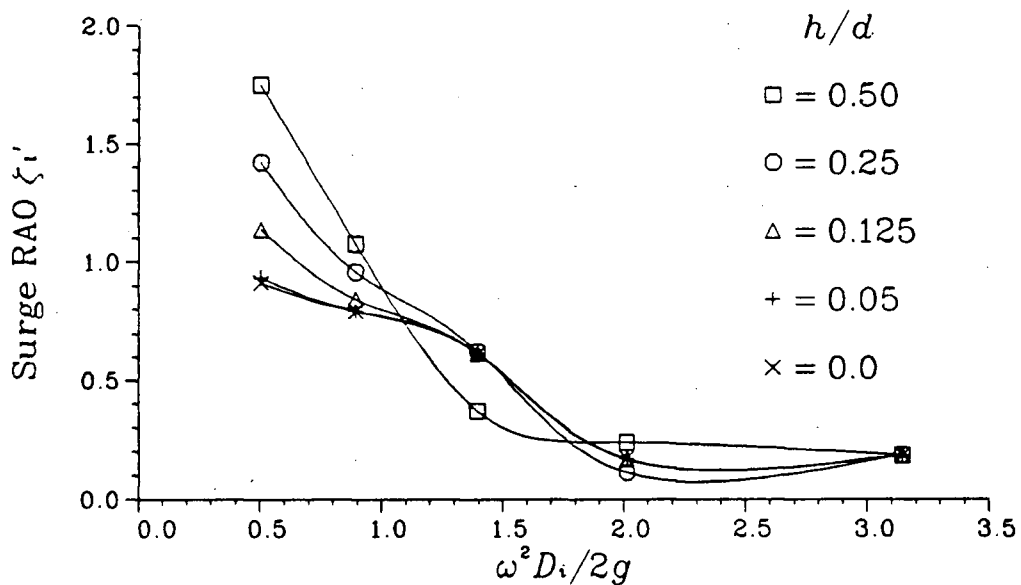


Figure 3.8: Computed Surge RAO's, Aspect Ratio  $h/D_i = 0.1$

### High Frequency Surge Response Amplitude Operators

A major limitation of the boundary element method for evaluation of iceberg surge response is the requirement that facet sizes be less than approximately one eighth the incident wavelength. For icebergs which are large relative to incident wavelength, a prohibitively large number of facets is required to model the iceberg surface. An alternative

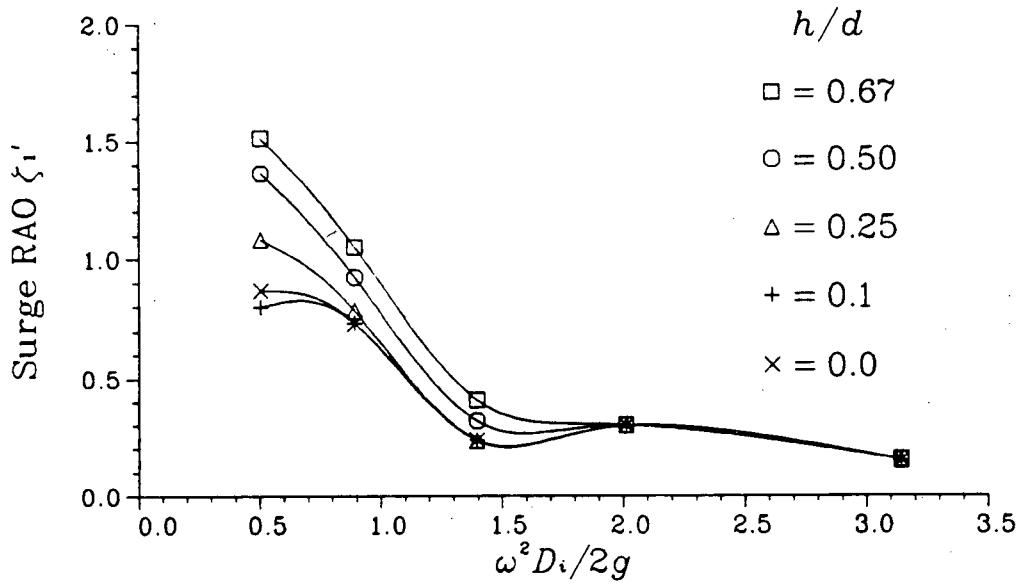


Figure 3.9: Computed Surge RAO's, Aspect Ratio  $h/D_i = 0.2$

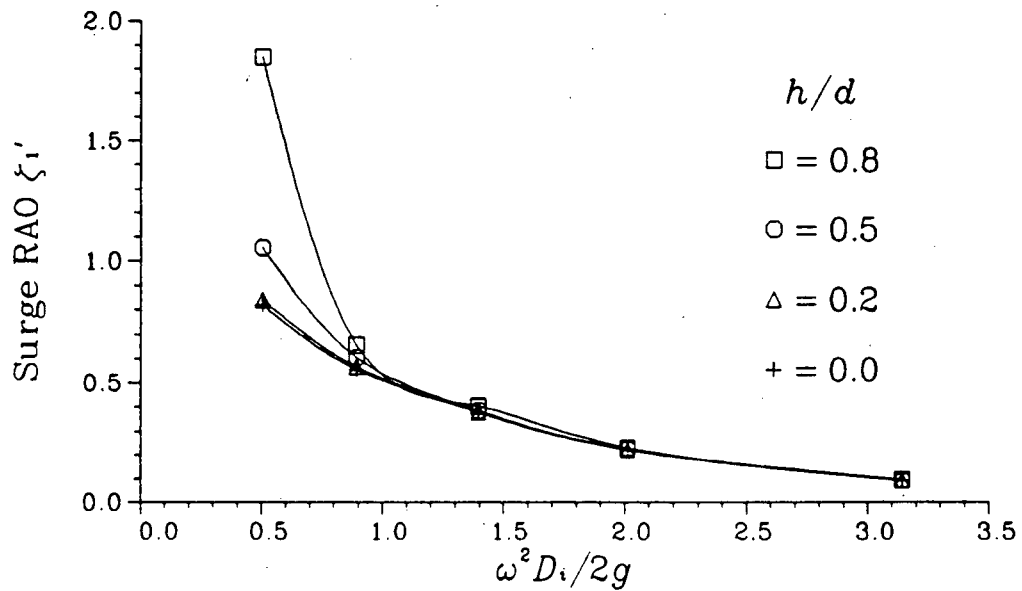


Figure 3.10: Computed Surge RAO's, Aspect Ratio =  $h/D_i = 0.4$

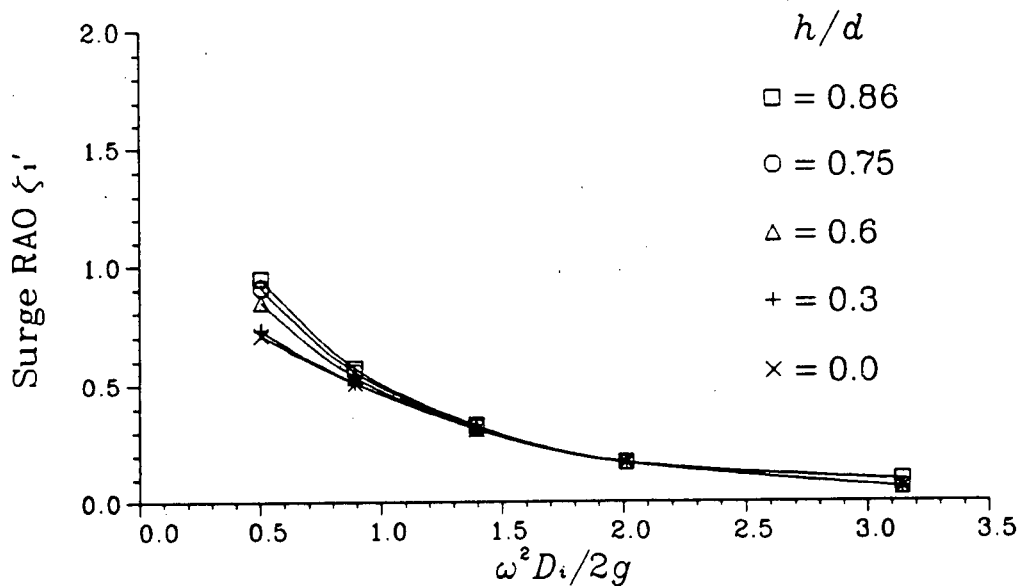


Figure 3.11: Computed Surge RAO's, Aspect Ratio  $h/D_i = 0.6$

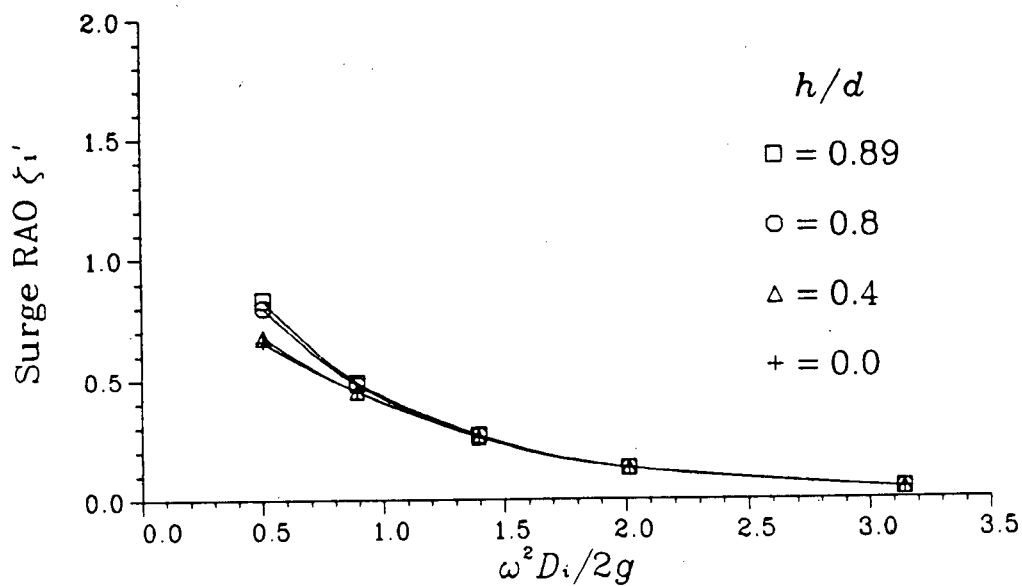


Figure 3.12: Computed Surge RAO's, Aspect Ratio  $h/D_i = 0.8$

solution has been developed for estimating iceberg surge response at high frequencies (i.e.  $\omega^2 D_i/2g > 3$ ). It is conservatively assumed that iceberg added mass and damping approach their infinite frequency values of  $C_m(\infty)$  and zero respectively for  $\omega^2 D_i/2g > 3$ . The surge response of an iceberg can subsequently be written as follows:

$$\omega^2 M [1 + C_m(\infty)] \zeta_1 = F_e \quad (3.41)$$

Using the solution of MacCamy and Fuchs (see [103]), the amplitude of the wave excitation force acting on a surface piercing circular cylinder extending to the seabed is as follows:

$$F_e = \frac{2 \rho g H}{k a} [J_1'^2(k a) + Y_1'^2(k a)]^{-1/2} \quad (3.42)$$

where:

$a$  = cylinder radius (m)

$J_1'$  = derivative of Bessel function of the first kind of order 1

$Y_1'$  = derivative of Bessel function of the second kind of order 1

For large values of  $ka$ , the wave field and associated excitation force acting on the cylinder will be dependent only on the cylinder geometry near the waterline; thus, equation 3.42 can be used to predict the excitation force on a body with a circular waterline at high frequencies. Evaluation of equation 3.42 is simplified if the following high frequency approximation is used:

$$J_1'^2(k a) + Y_1'^2(k a) = \left( \frac{\pi k a}{2} \right)^{1/2} \quad (3.43)$$

Substituting equation 3.43 into 3.42, the excitation force  $F_e$  is as follows:

$$F_e = 2 \sqrt{\frac{\pi}{2}} \frac{\rho H g^{5/2} a^{1/2}}{\omega^2} \quad (3.44)$$

The iceberg surge RAO for high frequencies can now be evaluated as:

$$\zeta'_1 = \sqrt{\frac{2}{\pi}} \frac{1}{(k a)^{2.5} (h/D_i) [1 + C_m(\infty)]} \quad (3.45)$$

If the deep water dispersion relation valid for  $k d > \pi$  is adopted, equation 3.45 can be re-written as:

$$\zeta'_1 = \sqrt{\frac{2}{\pi}} (\omega^2 D_i / 2g)^{-2.5} \frac{1}{(h/D_i) [1 + C_m(\infty)]} \quad (3.46)$$

To verify the high frequency surge approximation, results from equation 3.46 and the numerical diffraction model were compared for various iceberg aspect ratios  $h/D_i$  and are presented in Figure 3.13. A frequency parameter value  $\omega^2 D_i / 2g = 3.14$  was adopted because both the numerical model and high frequency approximation were postulated to be valid at this frequency. Diffraction computation results for deep water (i.e.  $d = \infty$ ) were used for comparison; however, the computed RAO's of Figures 3.8 - 3.12 indicate no variation of  $\zeta'_1$  with depth for  $\omega^2 D_i / 2g = 3.14$ . Figure 3.13 indicates excellent agreement between RAO's given by the numerical model and high frequency approximation for  $h/D_i \geq 0.3$ . The finite draft of the iceberg appears to significantly influence the excitation force for  $h/D_i < 0.3$  and  $\omega^2 D_i / 2g \leq 3.14$ , thus leading to conservative estimates of oscillatory surge motions. It is suggested that equation 3.45 be used in conjunction with Figures 5.31 - 3.12 for estimating iceberg surge response when  $\omega^2 D_i / 2g < 4$ .

### Discussion of Wave Drift Force Coefficients

Compared with computed surge RAO's, the wave drift force coefficients presented in Figures 3.14 - 3.15 exhibit a more erratic variation with the frequency parameter  $\omega^2 D_i / 2g$ . It should be noted that large wave drift forces occur at the natural heave frequency of each iceberg due to the influence of heave motions on wave drift forces, as discussed by Faltinsen and Michelsen [28]. In reality, viscous damping will attenuate heave motions

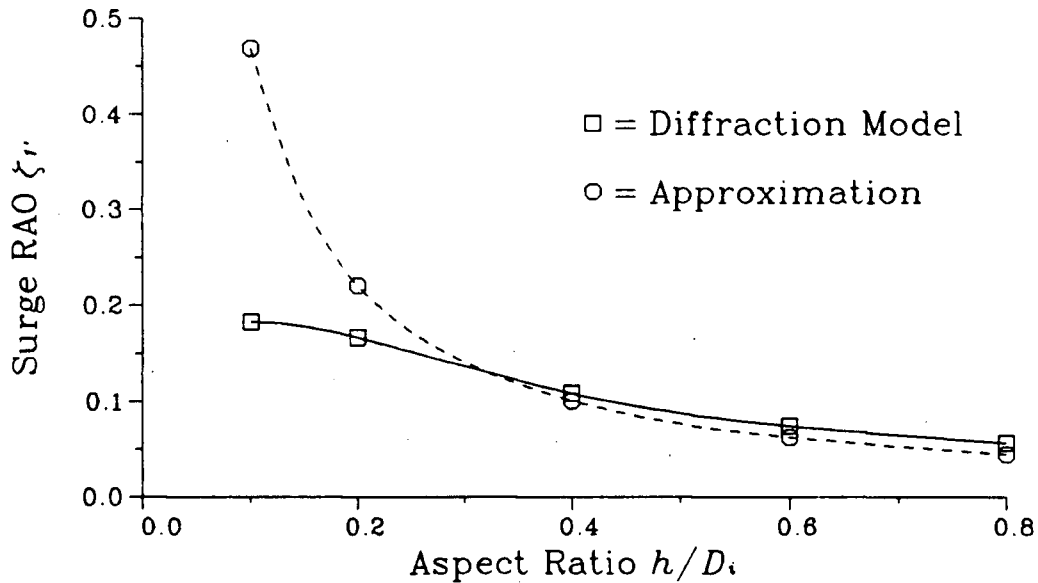


Figure 3.13: Comparison of RAO's for Numerical Model and High Frequency Approximation

and associated wave drift forces. Aside from heave resonance effects, the high and low frequency behaviour of the drift force computations appears as expected. The computed high frequency values are particularly good when compared with the asymptotic limit of 0.167 for a vertical circular cylinder.

### 3.3.2 Zero Frequency Added Mass Coefficients

As indicated previously, the zero frequency added mass of an iceberg can be used for predicting the drift motions of an iceberg and for estimating kinetic energy dissipated during collisions of long duration. For a vertical circular cylinder, its zero frequency added mass coefficient is a function of two dimensionless parameters:

$$C_m = f(h/D_i, h/d) \quad (3.47)$$

Computed zero frequency added masses are presented in Figure 3.19. The smooth

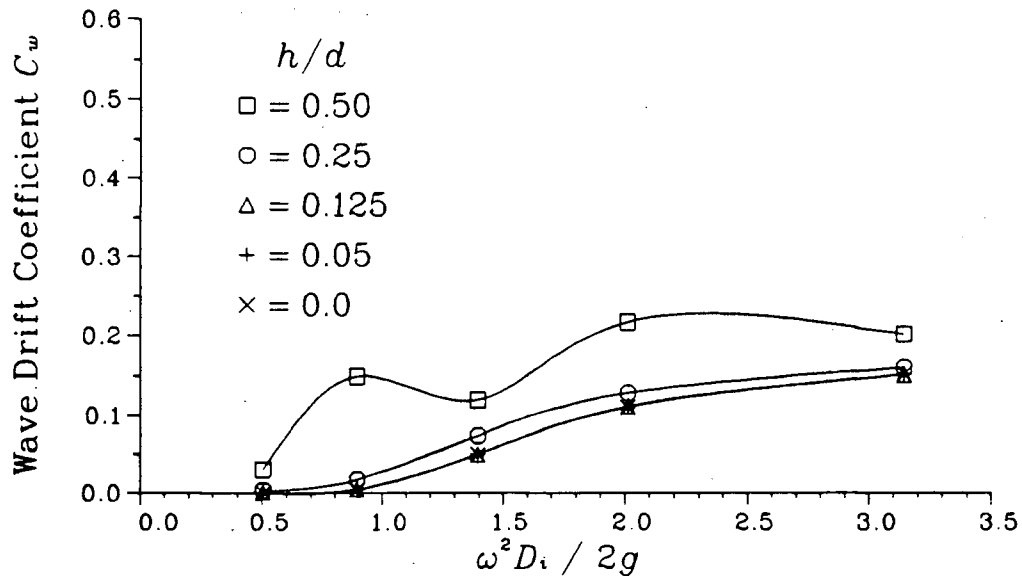


Figure 3.14: Computed Wave Drift Coefficients, Aspect Ratio  $h/D_i = 0.1$

nature of the curves in Figure 3.19 indicate that the computed added masses can be used as a convenient, reliable source of  $C_m$  values for design purposes.

### 3.3.3 Infinite Frequency Added Mass Coefficients

For iceberg collisions of short duration, the infinite frequency added mass can be used to estimate dissipated kinetic energy. Infinite frequency added masses can also be used to estimate iceberg surge response at high frequencies using equation 3.46.

The boundary element solution presented in Chapter 2 can be used to determine the added mass of a floating body for oscillations of infinite frequency. The following Green's function has been developed by Garrison and Berklite [32] for the infinite frequency potential:

$$G(x, y, z; \xi, \eta, \zeta) =$$

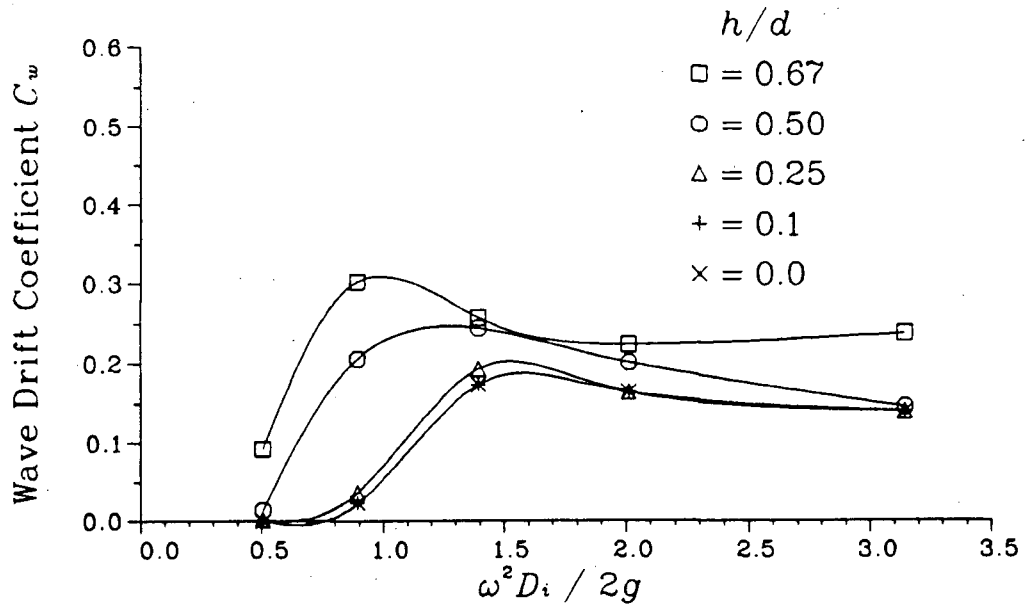


Figure 3.15: Computed Wave Drift Coefficients, Aspect Ratio  $h/D_i = 0.2$

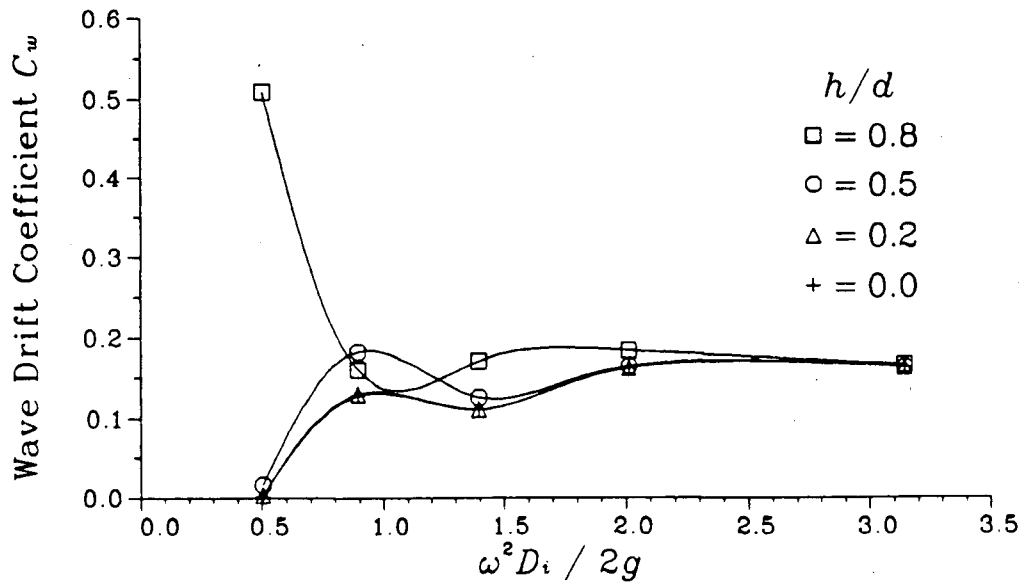


Figure 3.16: Computed Wave Drift Coefficients, Aspect Ratio  $h/D_i = 0.4$

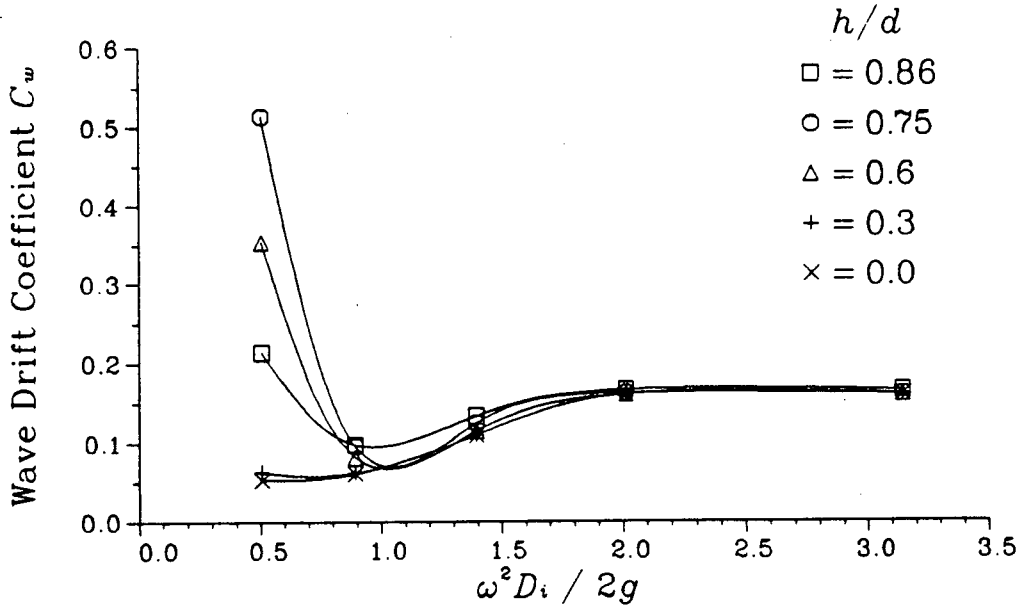


Figure 3.17: Computed Wave Drift Coefficients, Aspect Ratio  $h/D_i = 0.6$

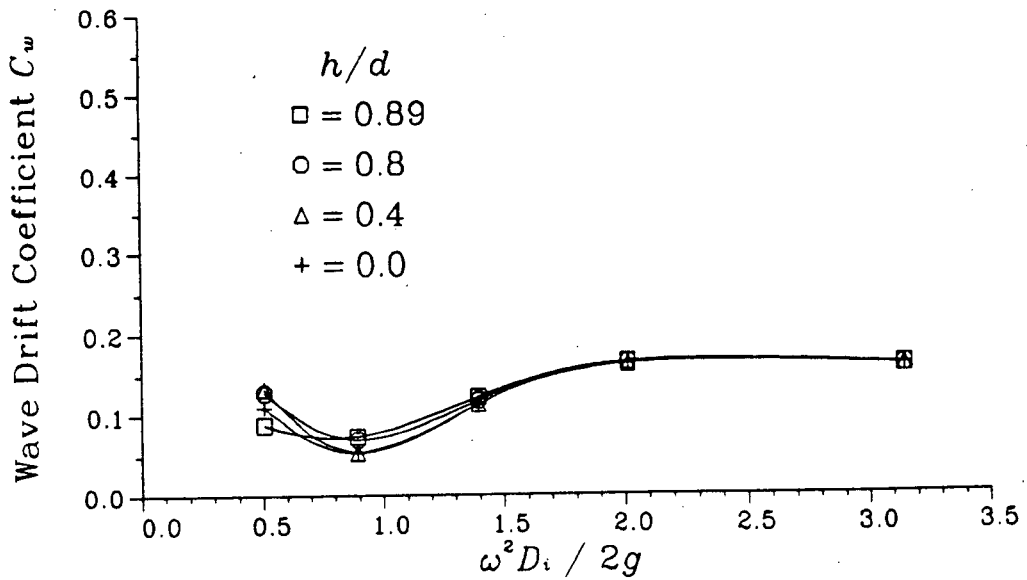


Figure 3.18: Computed Wave Drift Coefficients, Aspect Ratio  $h/D_i = 0.8$

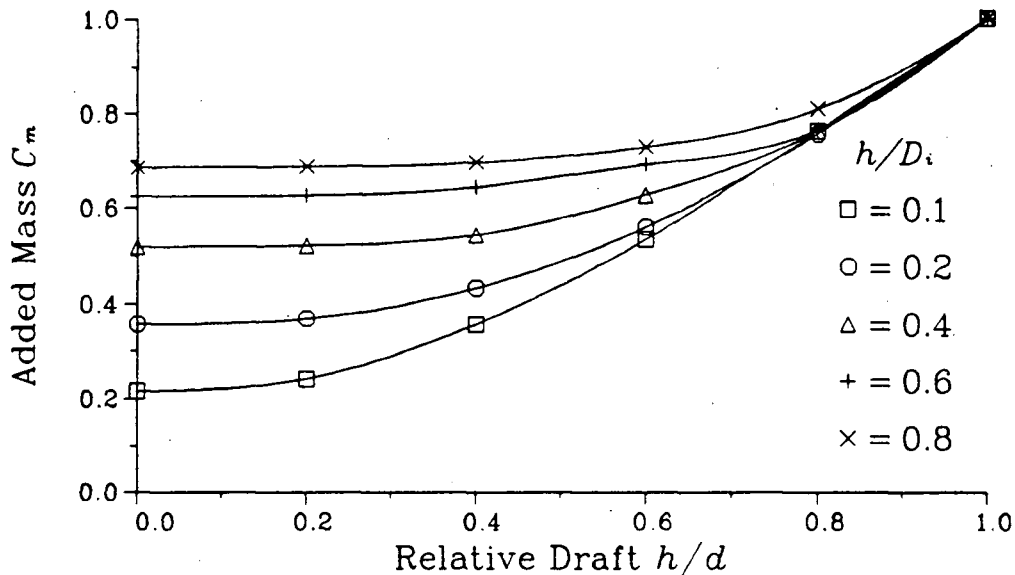


Figure 3.19: Computed Zero Frequency Added Masses

$$\frac{1}{R} - \frac{1}{R_1} + \sum_{n=1}^{\infty} \left[ (-1)^n \left( \frac{1}{R_{2n}} + \frac{1}{R_{4n}} \right) + (-1)^{n+1} \left( \frac{1}{R_{3n}} + \frac{1}{R_{5n}} \right) \right] \quad (3.48)$$

with terms in the above equation being the same as those given for equation 2.68. The infinite frequency Green's function of equation 3.48 was added to the program ICEMOT to enable the computation of infinite frequency added masses. Computed infinite frequency added masses for vertical circular cylinders are shown in Figure 3.20. Unlike the zero frequency values, infinite frequency added masses are virtually independent of relative draft  $h/d$ . The maximum value of the infinite frequency added mass coefficient is approximately 0.5, compared to a maximum of 1.0 for zero frequency.

### 3.3.4 Water Drag Coefficients

As mentioned previously, an empirical water drag coefficient is required for computing iceberg drift motions in the program ICEMOT. Icebergs typically have sufficiently

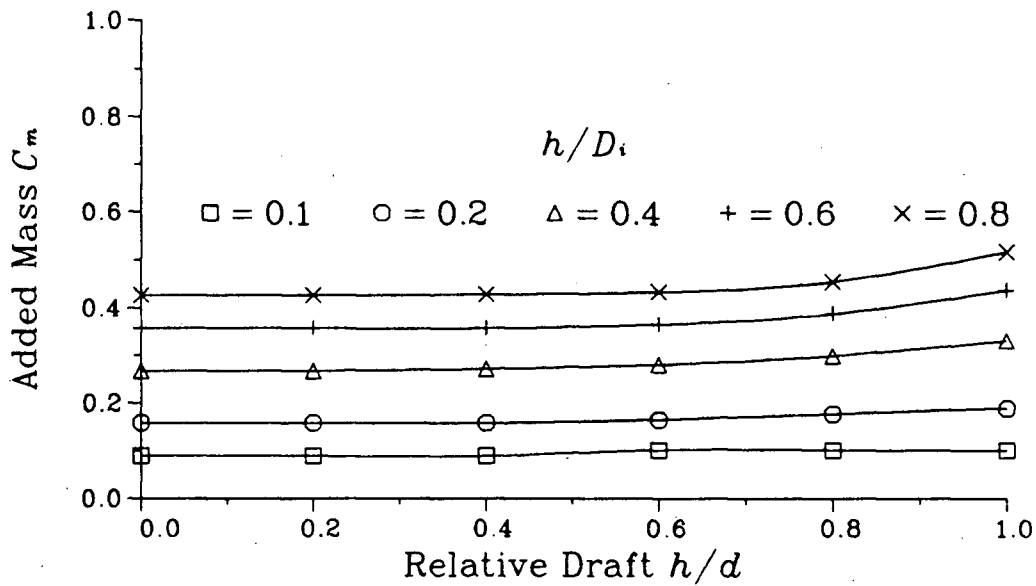


Figure 3.20: Computed Infinite Frequency Added Masses

low Froude numbers that wave-making resistance is negligible [117]. Reynolds numbers for drifting icebergs are typically super-critical; therefore, drag coefficients can also be considered independent of  $Re$ . The drag coefficient of a cylindrical iceberg thus can be considered as a function of two dimensionless parameters:

$$C_d = f(h/D_i, h/d) \quad (3.49)$$

For  $h/d \rightarrow 1$ , the flow around the iceberg will be essentially two-dimensional and the associated drag coefficient will be approximately 1.2 [9]. If the water is deep ( $h/d \rightarrow \infty$ ),  $C_d$  will depend on the iceberg aspect ratio  $h/D_i$  as illustrated in Figure 3.21. For aspect ratios representative of icebergs (i.e.  $h/D_i \leq 0.85$ ),  $C_d$  is approximately constant at 0.70 provided that the relative iceberg draft  $h/d$  does not approach unity. Consequently, a  $C_d$  value of 0.70 has been used for icebergs in the present investigation.

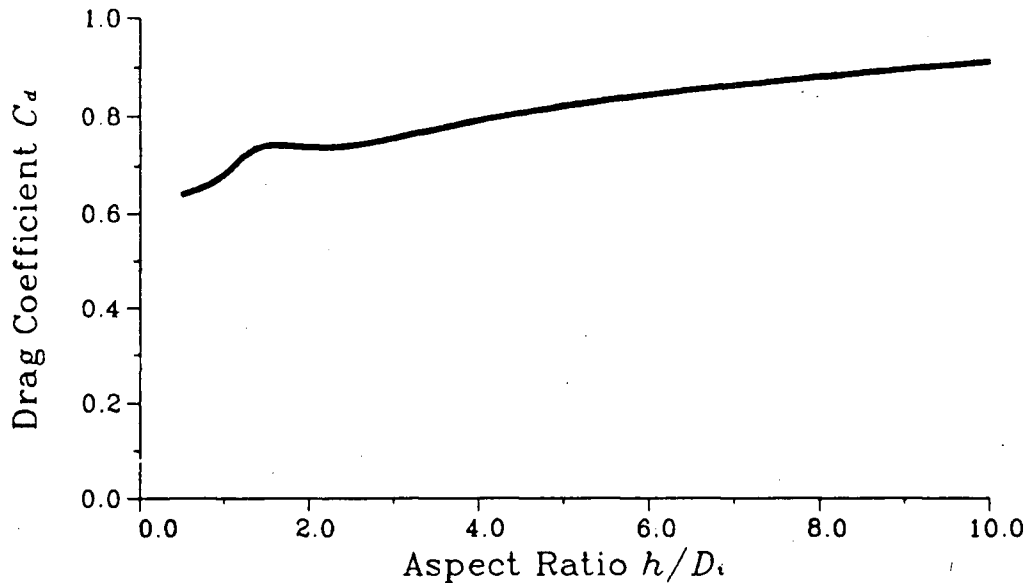


Figure 3.21: Variation of Drag Coefficient with Aspect Ratio  $h/D_i$  (from Blevins [9])

### 3.4 Hydrodynamic Interactions between Icebergs and a Large Offshore Structure

For iceberg impacts against a large structure, the presence of the structure can significantly modify the hydrodynamics of the iceberg. Added mass and velocity will both be affected as an iceberg approaches a large structure. Physical modelling studies by Lever et al. [59] and Salvalaggio and Rojansky [99] have shown that hydrodynamic effects can prevent an iceberg from impacting a large structure. Numerical studies by Isaacson [43] and Isaacson and Dello Stritto [48] have confirmed this phenomenon.

A comprehensive numerical investigation was conducted to examine iceberg hydrodynamics in the vicinity of a large structure. Main areas of concern include the following:

1. Variation of added mass with proximity to structure,

2. Influence of structure on current field and associated iceberg motions,
3. Variation of iceberg wave drift forces with proximity to structure,
4. Variation of oscillatory surge motions with proximity to structure.

### 3.4.1 Configuration for Modelling Hydrodynamic Interactions

When evaluating the hydrodynamics of an iceberg in the vicinity of a large structure, the number of relevant variables is significantly greater than for the open water case. As an example, the oscillatory response of a cylindrical iceberg in the vicinity of a surface-piercing cylindrical structure extending from the seabed is considered. The assumptions of linear wave theory and inviscid flow adopted for equation 3.38 are maintained. Additional parameters are required for describing the relative size of the structure and location of the iceberg relative to the structure such that the number of dimensionless variables is increased from three for the open water case to six for an iceberg near a structure:

$$\zeta'_1 = f_1 \left( h/D_i, h/d, \frac{\omega^2 D_i}{2g}, D_i/D_s, x_g/D_s, y_g/D_s \right) \quad (3.50)$$

where:

$D_s$  = structure diameter (m)

$x_g, y_g$  = location of iceberg relative to structure (m)

The large number of variables for the interaction problem makes it difficult to present general results such as those given for open water motions. Instead, a particular structure configuration was selected for modelling hydrodynamic interactions. The modelled structure was a surface-piercing circular cylinder extending from the seabed, with a diameter  $D_s$  of 100 m situated in a water depth  $d$  of 100 m. Similar configurations have been studied by Isaacson [43], NORDCO [90], and Salvalaggio and Rojansky [99], thus

providing a basis for comparing results. Although various values for iceberg diameter  $D_i$  were used for modelling hydrodynamic interactions with the structure, an aspect ratio  $h/D_i$  of 0.5 was maintained for all icebergs.

### 3.4.2 Variation of Zero Frequency Added Mass

Computations were made to examine the variation of iceberg zero frequency added mass for head-on approaches toward the example structure. The structure surface was modelled using 64 facets; thus, a typical facet dimension was approximately 20 m. Icebergs having diameters of 10 m, 20 m, 50 m and 100 m were modelled, with 81 facets for each iceberg. Due to limitations of the boundary element method, reliable computations could be made for a minimum separation distance of one half of a facet dimension, or approximately 10 m. Computed added masses presented in Figure 3.22 indicate that zero frequency added mass increases as an iceberg approaches a structure. This phenomenon corresponds with the results of Yamamoto [118] for two-dimensional flow around two circular cylinders.

When considering the influence added mass variation on iceberg collision severity, consideration should be given to the kinetic energy of the fluid-solid system. For an iceberg drifting toward a structure in an otherwise still fluid, the total kinetic energy of the iceberg and fluid system will be as given by Sarpkaya and Isaacson [103]:

$$KE = \frac{1}{2} (1 + C_m) M V^2 \quad (3.51)$$

For a conservative system where energy is constant, any increase in iceberg added mass must be accompanied by a corresponding decrease in iceberg velocity; thus, the kinetic energy of an iceberg upon impact will be equal to its energy far away from the structure. It should be noted that iceberg kinetic energy could change with proximity to the structure if external forces from currents and waves were acting on the iceberg.

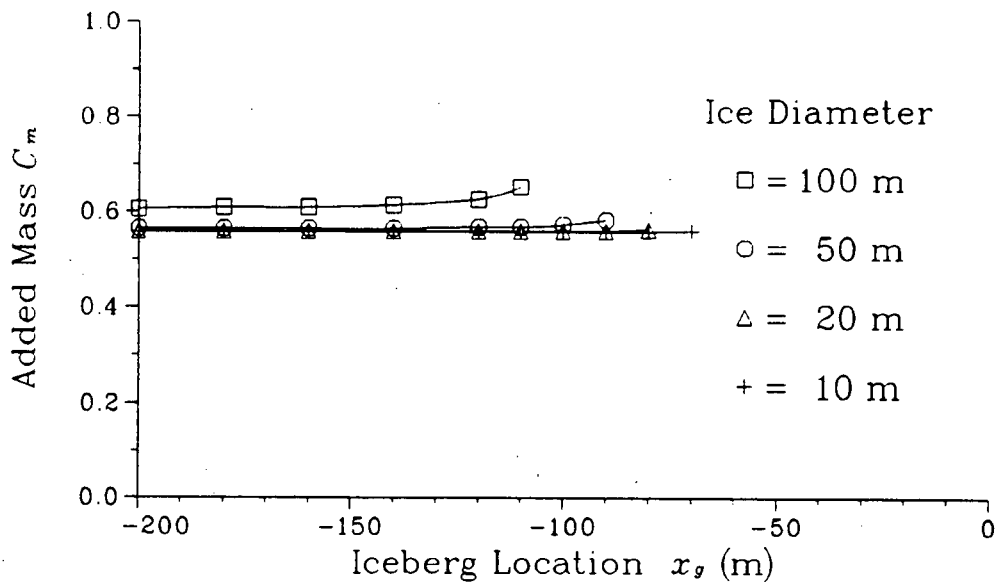


Figure 3.22: Variation of Zero Frequency Added Mass with Proximity to Structure

### 3.4.3 Variation of Infinite Frequency Added Mass

Infinite frequency added masses in the vicinity of the structure were also evaluated. The results presented in Figure 3.23 show that infinite frequency added mass is not significantly affected by the presence of the structure; however, it is possible that the influence of the structure could be more pronounced for smaller separation distances.

### 3.4.4 Influence of Structure on Current Driven Impact Velocities

The presence of a structure in a current field will affect water velocities and associated water drag forces near the structure. A series of numerical tests was conducted for current driven collisions with the example structure. The flow field around the structure was computed using the analytical solution of equation 2.92. Head-on iceberg approaches

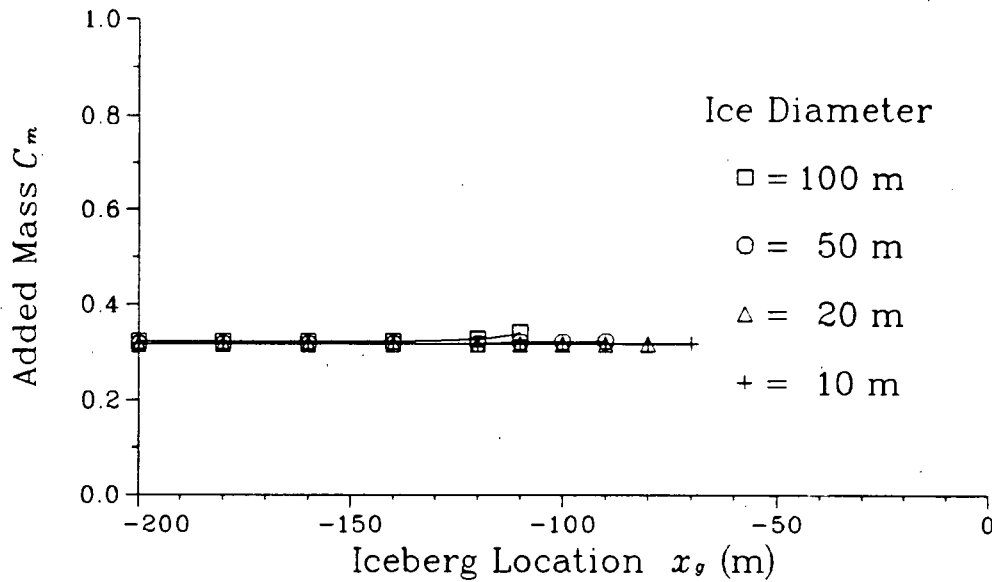


Figure 3.23: Variation of Infinite Frequency Added Mass with Proximity to Structure

were simulated using a time-stepping procedure commencing at a location where the modification of the flow field by the structure was negligible (i.e.  $5 D_s$  from the structure face).

Collision trajectories were simulated for icebergs having diameters  $D_i$  of 5 m, 10 m, 20 m, 50 m, and 100 m. Due to the minimal computational effort required for generating trajectories, four different aspect ratios were used for each iceberg diameter. It was assumed that each iceberg had a water drag coefficient  $C_d$  of 0.70. Zero frequency added masses were taken from Figure 3.19, and were assumed to be independent of iceberg proximity to the structure.

Figure 3.24 illustrates the ratio of impact velocity  $V_c$  to free-stream current velocity  $V_{wo}$  for the simulated trajectories. For a 10% or greater reduction in impact velocity, the relative iceberg size  $D_i/D_s$  must be less than 0.3. The influence of aspect ratio  $h/D_i$  appears to be very small and is due solely to the variation of added mass coefficients.

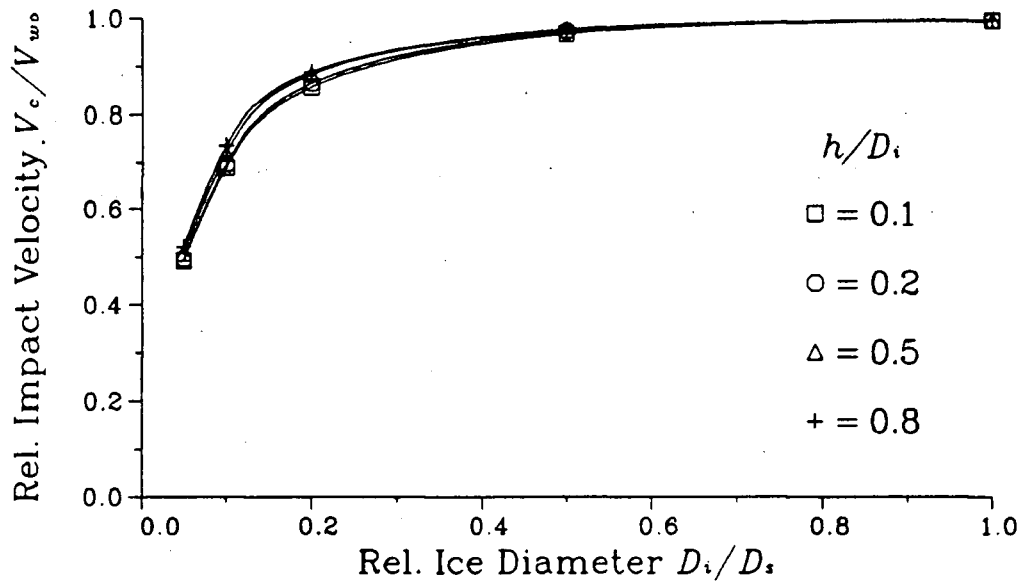


Figure 3.24: Relative Impact Velocities for Current Driven Head-on Collisions

### 3.4.5 Variation of Wave Drift Forces

Previous investigations (e.g. Kokkinowrachos et al. [53], Loken [65], Van Oortmerssen, [112]) have indicated that the wave drift forces acting on a body can be significantly modified by the presence of a second body. The significance of this phenomenon on iceberg drift motions has been illustrated by Isaacson [44].

Using the program ICEMOT, wave drift forces were computed for icebergs at various locations in front of the example structure. The iceberg dimensions and facet grids were identical to those used for studying the variation of added masses with proximity to the structure. Computed wave drift coefficients for a wave period  $T$  of 12 s are presented in Figure 3.25. It appears that wave drift forces for the larger icebergs are only moderately affected by the presence of the structure during a head-on impact. Wave drift coefficients for the 50 m and 100 m icebergs fluctuate near their open water values, while forces acting on the 10 m and 20 m icebergs exhibit a pronounced variation with location.

The development of negative drift forces suggests that the 10 m and 20 m icebergs will not impact the structure if no current is present. This result is in agreement with experiments by Salvalaggio and Rojansky [99], who observed that wave driven icebergs would not impact a structure when the relative iceberg size  $D_i/D_s$  was less than 0.5. Their experiments also indicated that the occurrence of iceberg impacts was independent of the incident wavelength.

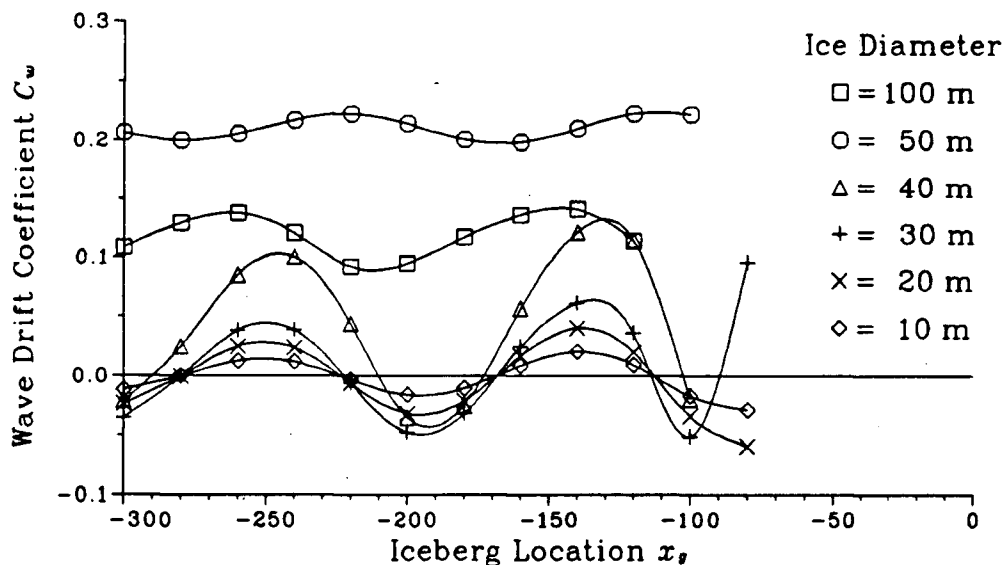


Figure 3.25: Variation of Wave Drift Coefficients with Proximity to Structure

To examine the influence of wave period, additional computations for the 20 m iceberg were made for wave periods of 10 s and 14 s, as shown in Figure 3.26. For each wave period the wave drift force exhibits a cyclic variation with distance from the structure, with a cycle length equal to half a wavelength. In addition to the cyclic variation, the wave drift forces acting on the 10 m and 20 m iceberg decay with distance from the structure. Diffraction computations far away from the structure confirmed this observation. The following equation is proposed for modelling wave drift forces acting

on an iceberg in front of a large structure:

$$C_w = C_{wo} + A_{C_w} \exp[B_{C_w} x_g] \cos[2k(x_g - C_{C_w})] \quad (3.52)$$

where:

$A_{C_w}$  = amplitude term

$B_{C_w}$  = decay term ( $\text{m}^{-1}$ )

$C_{C_w}$  = phase term (m)

$C_{wo}$  = open water wave drift coefficient

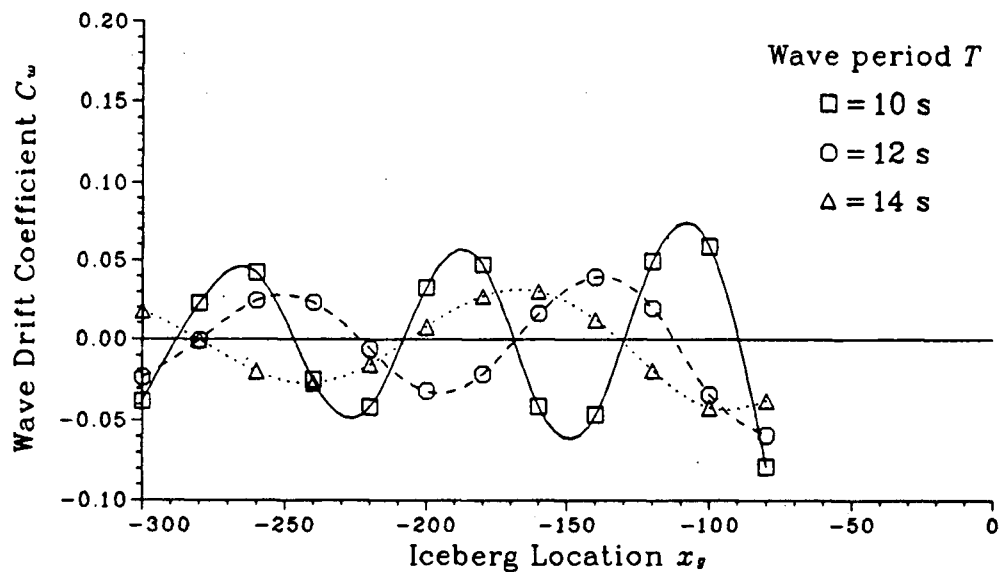


Figure 3.26: Influence of Wave Period on Wave Drift Forces near Structure

Coefficients of equation 3.52 have been evaluated for icebergs with aspect ratios of 0.5 approaching the example structure. Wave drift coefficients for icebergs approaching the structure were computed using the program ICEMOT. Coefficients of equation 3.52 were then determined using a least squares fit to the computed wave drift forces and are presented in Figures 3.27 - 3.30.

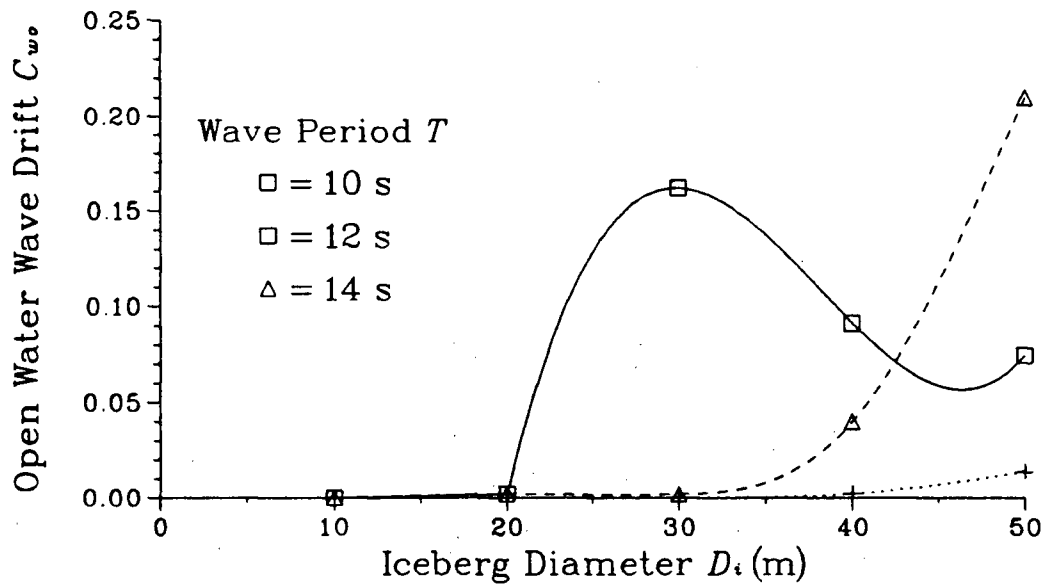


Figure 3.27: Open Water Wave Drift Force Coefficient  $C_{w0}$

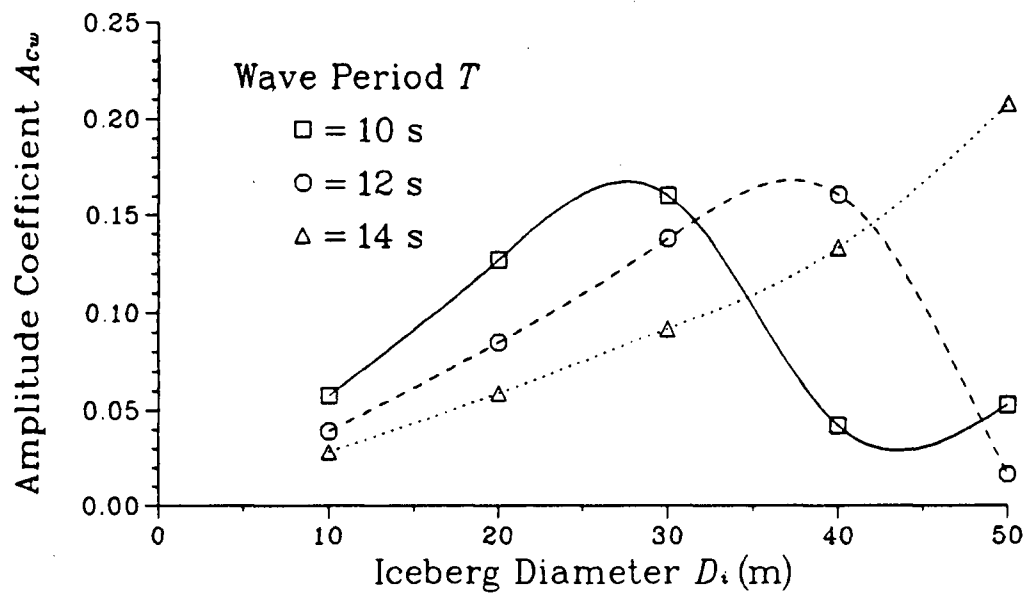


Figure 3.28: Wave Drift Force Variation Amplitude Coefficient  $A_{Cw}$

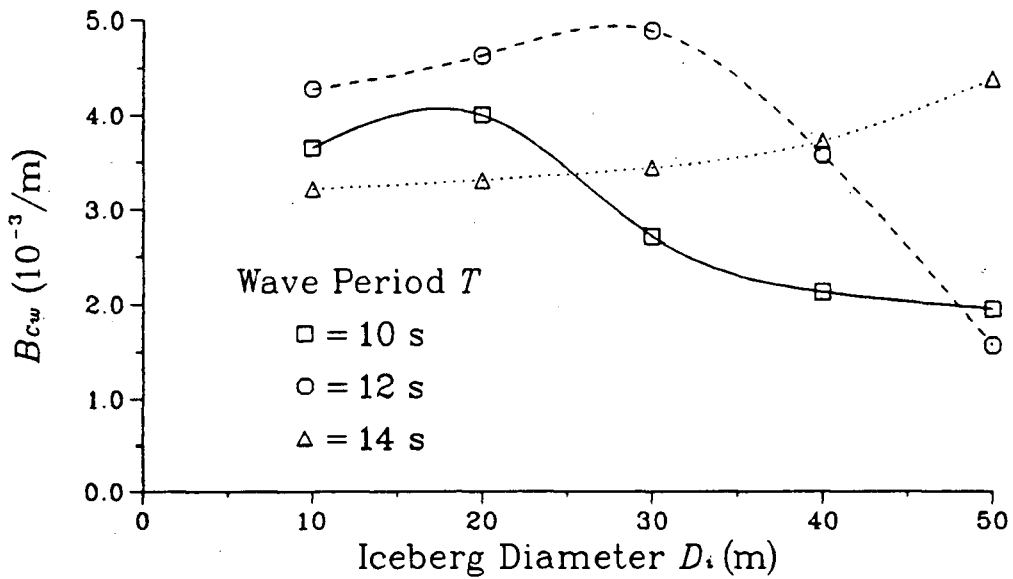


Figure 3.29: Wave Drift Force Variation Decay Coefficient  $B_{C_w}$

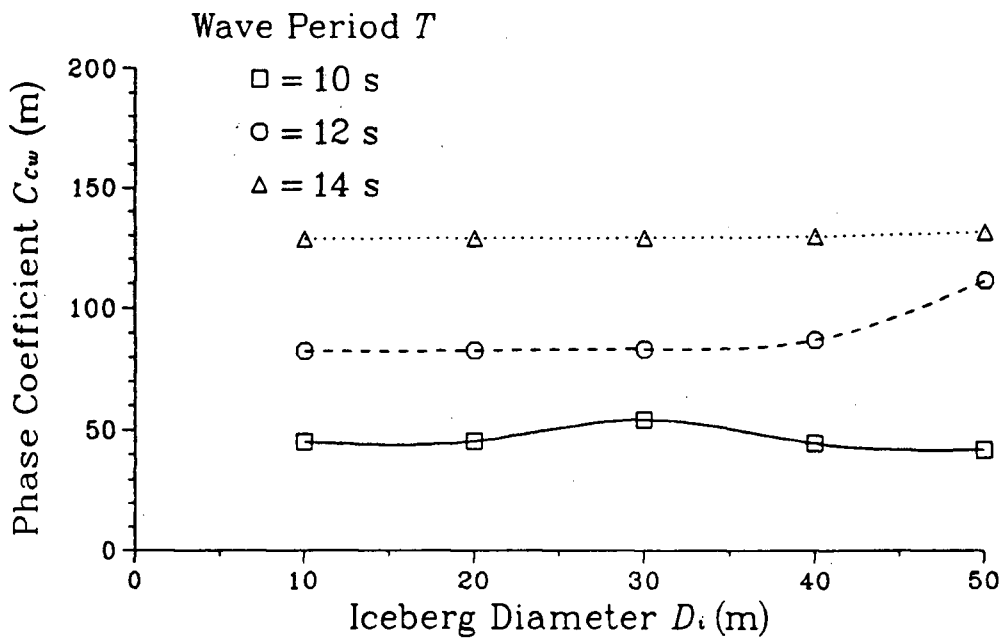


Figure 3.30: Wave Drift Force Variation Phase Coefficient  $C_{C_w}$

Wave drift coefficients presented thus far have been for icebergs having aspect ratios  $h/D_i$  of 0.5. Because wave drift forces are primarily due to effects near the waterline of an iceberg, it is suggested that the results presented above will not vary greatly with aspect ratio. Wave drift forces near a structure for 20 m diameter icebergs with aspect ratios of 0.2, 0.5, and 0.8 have been computed for a wave period of 12 s. The results presented in Figure 3.31 indicate that wave drift forces do not vary significantly with iceberg aspect ratio.

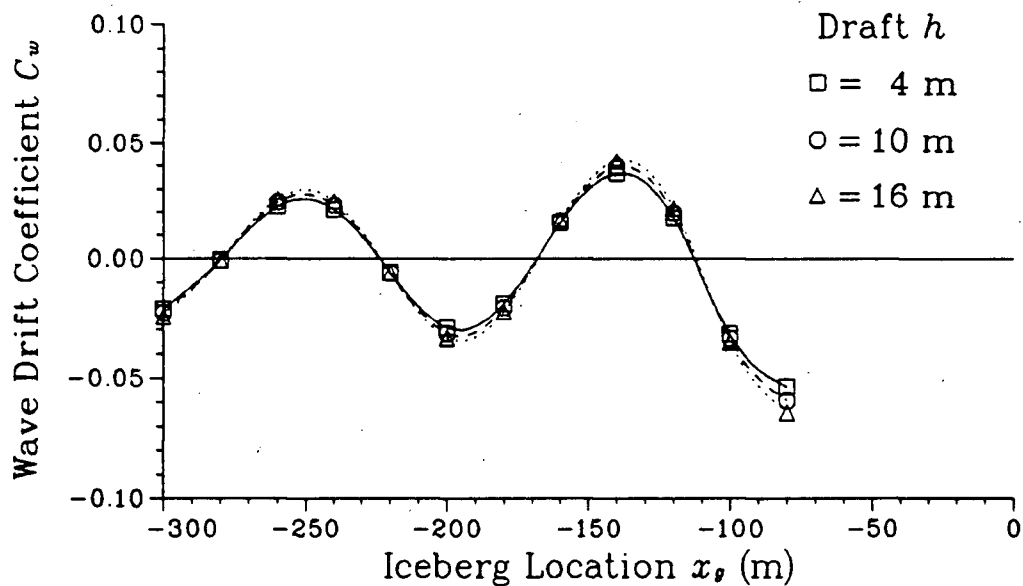


Figure 3.31: Influence of Aspect Ratio  $h/D_i$  on Wave Drift Forces near Structure

Wave drift forces near a structure will also vary with the iceberg lateral offset relative to the direction of propagation of incident waves. Drift forces for a 20 m diameter iceberg have been evaluated for offset distances of 25 m and 50 m. It is evident in Figure 3.32 that drift forces in the direction of wave propagation do not vary significantly with the lateral position of the iceberg. In addition to longitudinal wave drift forces, lateral drift forces were encountered for the offset distances of 25 m and 50 m; however, the lateral

drift forces were negligible in comparison to the longitudinal forces.

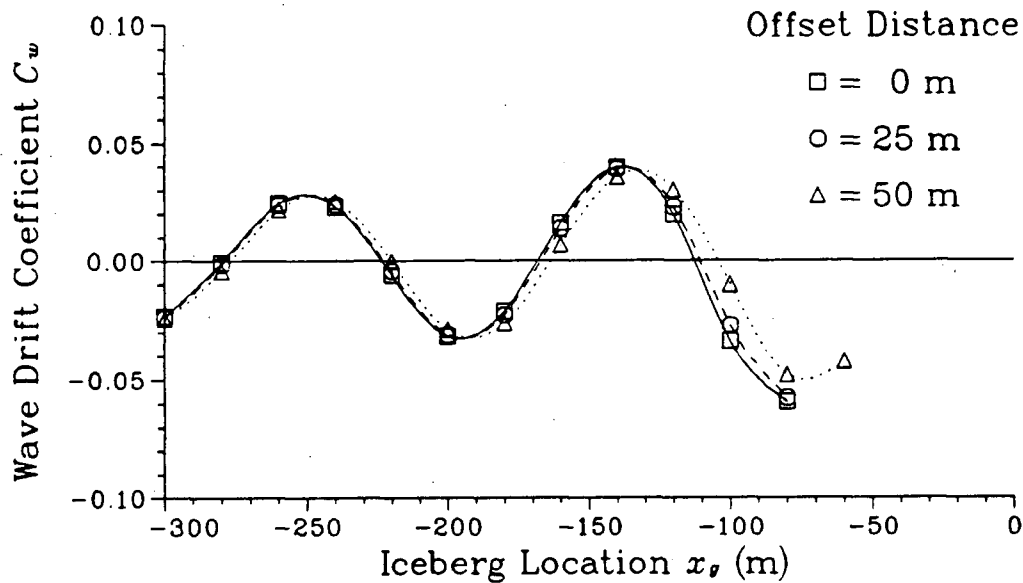


Figure 3.32: Influence of Lateral Offset on Wave Drift Forces near Structure

To examine the influence of wave drift forces on iceberg drift velocity, it is useful to consider the equilibrium velocity of an iceberg in collinear waves and currents. Taking the acceleration from wave drift and water drag forces to be zero (equation 2.62), the equilibrium velocity for a cylindrical iceberg in collinear currents and regular waves is as follows:

$$V = V_w + \frac{C_w}{|C_w|} H \sqrt{\frac{|C_w| g}{C_d h}} \quad (3.53)$$

Equation 3.53 can be used to assess whether negative wave drift forces will have a significant effect on the velocity of icebergs approaching a large structure.

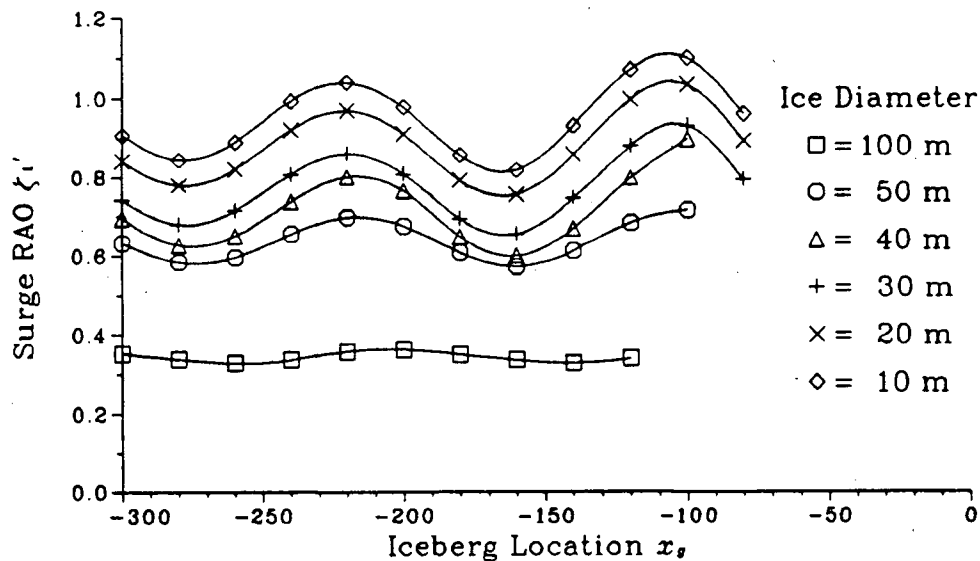


Figure 3.33: Variation of Oscillatory Surge Motions near Structure

### 3.4.6 Variation of Oscillatory Surge Motions

The diffraction computations used for obtaining wave drift forces also provide oscillatory motions near the structure. Figure 3.33 shows the variation of surge response near the structure for a wave period of 12 s. The degree of variation of surge RAO's with proximity to the structure decreases with increasing iceberg size.

Experimental results by NORDCO [90] were useful for confirming the numerical results for the large icebergs. Their investigation examined wave-induced motions of icebergs in the vicinity of a large cylindrical structure. The relative size of icebergs to the structure,  $D_i/D_s$ , was approximately 0.7 for all tests. It was concluded that the oscillatory motions were not significantly affected by the presence of the structure.

### 3.4.7 Implications of Hydrodynamic Interaction Effects for Modelling Iceberg Collisions

A comprehensive series of numerical tests has been conducted to investigate hydrodynamic interaction between icebergs and a large structure. The numerical results have been confirmed by available experimental data.

Zero and infinite frequency added masses exhibited little variation with proximity to the structure. It is suggested that open water added mass can be used for estimating added mass upon impact.

For current driven iceberg motions, the modification of the flow field by the structure will have a significant effect on impact velocities only if the relative iceberg diameter  $D_i/D_s$  is less than 0.3. The prediction of current driven iceberg trajectories near a cylindrical structure requires little computational effort and can prove to be very useful.

Wave drift forces showed significant variation near the structure when  $D_i/D_s$  was less than 0.5. The development of negative wave drift forces for  $D_i/D_s$  values of 0.1 and 0.2 indicates that impacts will not occur if drift motions are solely wave driven. The wave drift forces acting on smaller icebergs exhibit a cyclic variation with distance from the structure. An observed cycle length of a half wavelength should be considered when evaluating the number of drift force computations required for accurate modelling of drift trajectories. Due to the large degree of computational effort required for predicting wave drift forces, it is suggested that equation 3.52 be adopted for estimating wave drift forces on small icebergs approaching a large structure.

Oscillatory surge response for smaller icebergs showed fluctuations of approximately 10% as the icebergs approached the structure. For  $D_i/D_s > 0.5$ , the presence of the structure caused little variation in surge response and surge motions could be considered constant.

## Chapter 4

### Physical Modelling of Iceberg Drift

#### Near a Large Structure

The numerical model described previously can be used for predicting iceberg drift motions in waves and currents near a large structure. To validate the numerical iceberg drift model, suitable physical modelling data were required. NORDCO [90] conducted a series of experiments of wave driven iceberg motions near a large structure, with icebergs of comparable size to the structure. Salvalaggio and Rojansky [99] examined wave driven drift motions for icebergs of various sizes relative to a large structure. Neither of the above investigations considered the influence of currents on iceberg motions near the structure.

To supplement existing physical modelling data, a series of experiments was conducted to examine iceberg drift motions near a large structure. Iceberg motions driven by both waves and currents were examined. Iceberg size relative to the structure,  $D_i/D_s$ , ranged between 0.1 and 0.8. The influence of the structure on iceberg drift motions was of principal interest. Specifically, the variation of iceberg velocity and trajectory eccentricity approaching the structure were evaluated and compared to the predictions of the numerical model.

## 4.1 Similitude Requirements

Similitude requirements for physical modelling of offshore structures are well established, and have been discussed in various textbooks (Chakrabarti [16], Newman [89], Sarpkaya and Isaacson [103]). In addition to geometric similarity requirements, kinematic and dynamic similarity requirements must also be met or approximated.

The modelling of a cylindrical iceberg approaching a surface piercing cylindrical structure extending to the seabed is considered in greater detail here. For an iceberg approaching a structure in collinear waves and currents, the iceberg impact velocity is a function of the following variables:

$$V_c = f(D_i, D_s, h, d, e_o, \rho, \rho_i, V_{wo}, g, H, \omega_c, \nu) \quad (4.1)$$

where:

$e_o$  = initial approach eccentricity (m)

$\nu$  = kinematic water viscosity (m<sup>2</sup>/s)

$\omega_c$  = angular wave frequency in current (rad/s)

In terms of dimensionless variables, equation 4.1 can be re-written as:

$$\frac{V_c}{\sqrt{g D_i}} = f\left(\frac{D_i}{D_s}, \frac{h}{D_i}, \frac{h}{d}, \frac{e_o}{1/2(D_i + D_s)}, \frac{\rho_i}{\rho}, \frac{V_{wo}}{\sqrt{g D_i}}, \frac{\omega_c^2 d}{g}, \frac{\omega_c^2 H}{g}, \frac{V_{wo} D_i}{\nu}\right) \quad (4.2)$$

For practical reasons, water must be used in the model. With the exception of Reynolds number  $V_{wo} D_i / \nu$ , all of the above dimensionless variables can be modelled correctly if geometric similarity is maintained and the following relationship is obeyed:

$$\lambda_t = \lambda_L^{1/2} \quad (4.3)$$

where:

$\lambda_L$  = length scale

$\lambda_t$  = time scale

Reynolds numbers for small-scale models are typically much smaller than those for prototypes; thus, viscous effects are accentuated in physical models. Scaling problems associated with Reynolds number effects can be alleviated if sufficiently high  $Re$  values (e.g.  $Re > 10,000$ ) can be achieved during experiments. In practice, Reynolds number effects are minimized by using the largest possible model scale for a given situation.

## 4.2 Description of Experiments

The experimental investigation was conducted in the towing tank at the BC Research Ocean Engineering Centre. The drift motions of four model icebergs near a large offshore structure were examined. Both waves and currents were modelled in the physical investigation.

### 4.2.1 Towing Tank

Dimensions of the BC Research towing tank are given in Table 4.1, with an elevation view of the tank given in Figure 4.1. The towing tank is intended primarily for model testing of ships, and is equipped with an instrumented towing carriage for measuring drag forces on models. The velocity of the towing carriage is controlled manually from a station located at one end of the towing tank equipped with a manual control potentiometer and a digital read-out of the towing velocity. A Digital PDP 11/23 mini-computer system situated on the towing carriage is available for recording carriage velocity and forces acting on towed models. A series of horizontal planks located along the sides of the tank

at water level is used to reduce reflections of waves produced by towed models.

In addition to towing capabilities, the BC Research towing tank has a computer controlled wave generator which is capable of producing regular sinusoidal and random uni-directional waves. The wave generator is of the flapper type, and is thus most appropriate for generating deep water waves (i.e.  $\lambda/d < 0.5$ ). Water elevations in the tank can be measured using resistance-type wave probes which can be connected to a micro-computer and a chart recorder. An IBM Personal Computer situated on the side of the towing tank completes a closed-loop system between the wave generator and wave probes, enabling constant monitoring and re-adjustment of the sea state produced at a given test section. A sloped beach consisting of perforated sheet metal has been installed at the downstream end of the tank to minimize wave reflection. The beach design was taken from Miles and Murdey [78], who reported reflection coefficients of less than 5% for wave periods less than 2 s and wave heights under 100 mm.

Due to the possibility of undesirable phenomenon occurring when generating waves in the towing tank, care must be taken when preparing for an experiment. Sarpkaya and Isaacson [103] warn that cross-waves can develop when incident wavelengths are smaller than the tank width. During iceberg drift tests conducted by NORDCO [90] significant interference was observed between waves diffracted by a model structure and the side walls of the towing tank. This interference was largely due to the significant blockage (25%) of the towing tank width by a model structure. To allow for generated waves to reach a freely travelling form, the test section for an experiment should be located a sufficient distance away from the wave generator. The present set of iceberg drift experiments was conducted at the mid-length section of the towing tank.

### 4.2.2 Structure Model

The structure model was intended to be representative of that used in Chapter 3 for numerical modelling of iceberg motions near a large structure. Recall that the structure used for numerical modelling had a diameter  $D_s$  of 100 m and traversed the entire water depth of 100 m.

Due to the limited towing tank width, the model structure was given a diameter of 0.5 m, thus introducing a model length scale  $\lambda_L$  of 1/200 and a tank width blockage of 14%. The influence of the tank walls on currents and waves near the structure appeared to be negligible during experiments. The resulting structure was rolled out of 0.8 mm thick sheet aluminum. The draft of the model structure was 1.6 m, which was considered sufficient to produce the desired flow field in the upper 0.5 m of water. Elevation views of the structure and iceberg models are given in Figure 4.2.

Table 4.1: Specifications for BC Research Towing Tank

Length	67 m
Width	3.7 m
Depth	2.4 m
Maximum carriage speed	4.52 m/s
Maximum wave height	0.25 m

### 4.2.3 Iceberg Models

Four model icebergs were constructed, with dimensions as given in Table 4.2. Each model was constructed to have an aspect ratio  $h/D_i$  of approximately 0.5. The two smaller icebergs were made from aluminum disks, with the centres machined to obtained

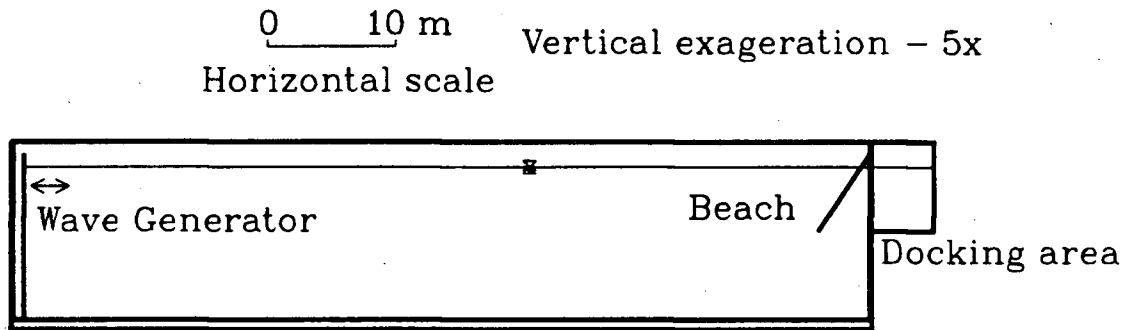


Figure 4.1: Elevation View of BC Research Towing Tank

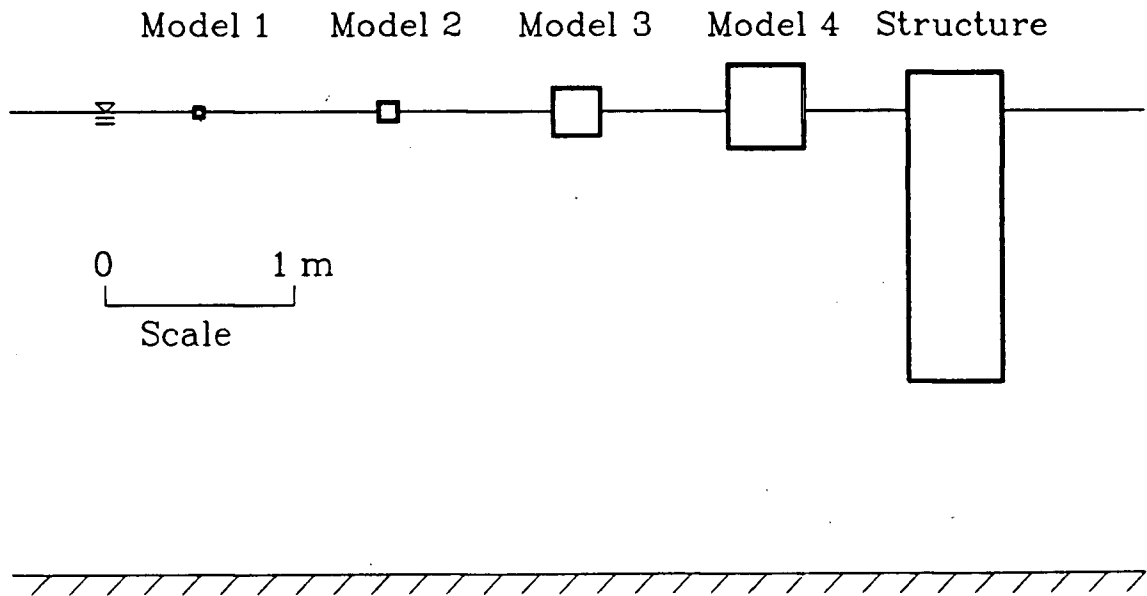


Figure 4.2: Elevation View of Structure and Iceberg Models

the desired model draft. The two larger models consisted of shells made of sheet aluminum. Ballast weights were added to both models to obtain the desired drafts.

Table 4.2: Dimensions of Model Icebergs

	Model 1	Model 2	Model 3	Model 4
Diameter, $D_i$ (mm)	51	100	253	400
Draft, $h$ (mm)	28	51	132	197
Total height, $h_t$ (mm)	50	100	253	445
Centre of gravity, $z_g$ (mm)	-10	-19	-81	-131
Mass, $M$ (kg)	.058	.423	6.65	24.8

The inertial properties of the model aluminum icebergs were somewhat different than those for prototype icebergs, which are of uniform density. The ballast for each model iceberg could have been adjusted to simulate the centre of gravity and radii of gyration for a prototype iceberg; however, this was not considered necessary because the objective of the experiments was simply to validate the numerical model. Measured model inertial properties were subsequently given as input to the numerical model.

#### 4.2.4 Model Iceberg Drag Coefficients

It was mentioned in Chapter 3 that a circular cylinder with an aspect ratio  $h/D_i < 2$  travelling through water at low Froude numbers ( $Fr < 0.15$ ) will have a drag coefficient value of approximately 0.70. Although it was postulated that this  $C_d$  value would be valid for the model icebergs, there was some concern regarding the influence of low Reynolds numbers and associated viscous drag forces on model iceberg drag coefficients. A series of towing tests conducted on the 400 mm diameter model indicated that a drag coefficient of 0.7 was valid for the model icebergs. Drag coefficients from the towing tests are shown in Figure 4.3. It should be noted that the iceberg model was allowed to rotate freely

in pitch during the towing tests. The increased drag with Froude number is likely due to greater pitch angles at higher towing velocities, with a maximum pitch angle of  $11^\circ$  experienced for the highest towing velocity.

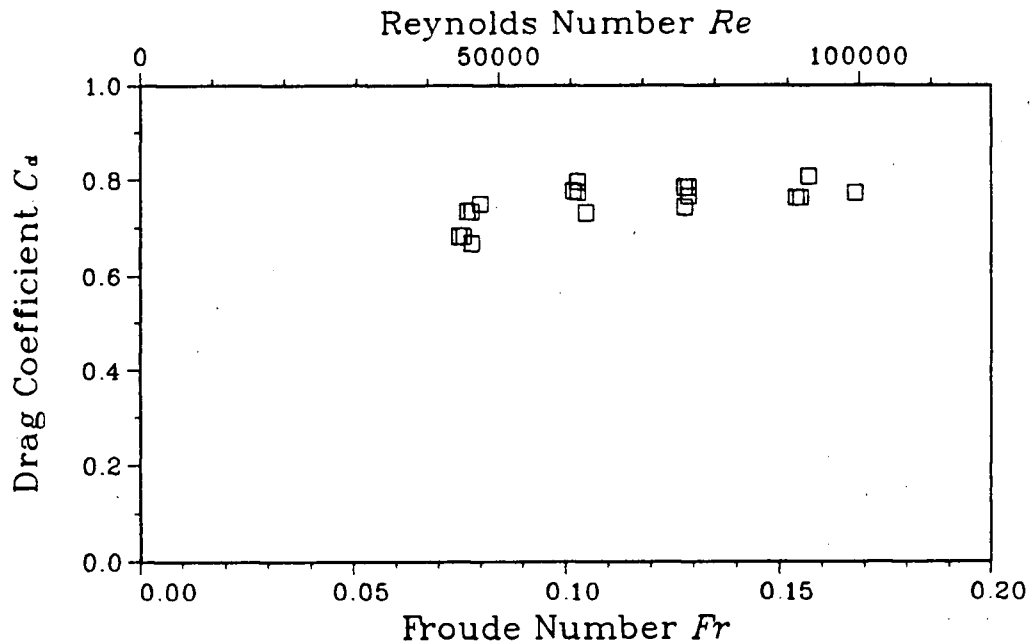


Figure 4.3: Drag Coefficients for 400 mm Diameter Iceberg Model

#### 4.2.5 Environmental Conditions for Drift Studies

The motions of icebergs were examined for conditions involving currents only, waves only, and combined waves and currents. The five different environmental conditions are given in Table 4.3. Tests with currents are denoted by C, and tests including waves are denoted by W.

To simulate currents around a fixed structure, the model structure was moved through the water using the towing carriage. Iceberg trajectory statistics reported by Pearson and Ro [93] indicated that a suitable prototype current velocity would be 0.5 m/s,

Table 4.3: Environmental Conditions for Model Tests

	C	W1	W2	WC1	WC2
Incident current, $V_{wo}$ (m/s)	0.1	0.0	0.0	0.1	0.1
Wave height, $H$ (mm)	0	21	61	19	59
Wave period, $T_c^*$ (s)	0.0	0.7	1.0	0.7	1.0

\*relative to structure

corresponding to a model velocity of 0.04 m/s through Froude number scaling. The towing carriage was capable of maintaining steady speed for a minimum velocity of 0.10 m/s. Consequently, a towing velocity of 0.1 m/s was used, corresponding to a relatively large prototype current of 1.4 m/s.

To examine the influence of Reynolds number effects on the experiments it is useful to consider the Reynolds number  $V_{wo}D_s/\nu$  for the structure in the current. For a prototype structure diameter of 100 m and a current velocity of 0.5 m/s, the Reynolds number is approximately  $50 \times 10^6$ . In comparison, the Reynolds number for the model structure is approximately 50,000. Corresponding Reynolds numbers for the model icebergs would be significantly smaller (e.g. 0.01-0.1 times smaller) due to the smaller iceberg sizes, and more importantly, due to the small relative velocities between the icebergs and the water. Detailed discussions on Reynolds number effects for circular cylinders have been given by Sarpkaya and Isaacson [103] and Simiu and Scanlan [105]. For the model structure and icebergs in the present study, Reynolds number effects cause the model drag coefficients to be somewhat larger than prototype drag coefficients. In addition, the wakes behind the models would be significantly different from the wakes behind the prototypes.

At the relatively low Reynolds numbers corresponding to the experiments, periodic shedding of vortices alternating from each side of the model may arise and induce significant periodic lift forces perpendicular to the direction of the relative velocity between

the water and iceberg. This vortex shedding typically occurs for  $Re$  values between 30 and 5000. In contrast, the turbulent wake behind the prototype icebergs and structure would induce relatively small lift forces.

For tests involving waves, regular waves with nominal heights of 20 mm and 60 mm (4m and 12 m prototype) were generated. Wave periods of 0.7 s and 1.0 s were based on the following equation obtained by LeBlond et al. [57] relating wave periods to wave heights for observed ocean wave records from several sites off the Canadian east coast:

$$T_p = 13.88 \sqrt{H_s / g} \quad (4.4)$$

For tests with simultaneous waves and currents, the wave periods of 0.7 s and 1.0 s were maintained relative to the moving structure. Corresponding wave periods of 0.74 s and 1.06 s were generated by the fixed generator, and were calculated using the following equation from Sarpkaya and Isaacson [103]:

$$\omega_c = \omega + V_{wo} k \quad (4.5)$$

where:

$\omega$  = angular wave frequency in reference frame moving with current (rad/s)

$\omega_c$  = angular wave frequency in fixed frame (rad/s)

For the present series of experiments in which the structure was towed to simulate a current,  $\omega$  is the frequency of the wave generator motion and  $\omega_c$  is the frequency of waves encountered by the structure.

#### 4.2.6 Experimental Procedure

Iceberg model drift motions were observed for trajectories commencing in front of the structure. For tests involving only wave driven motions, each model was launched from

a platform extended across the towing tank. The platform was located approximately 3 m in front of the structure.

For tests requiring movement of the towing carriage and structure to simulate currents, the icebergs were launched from a cantilever extending partially across the tank width. The cantilever was placed such that the structure and towing carriage could pass by freely. The starting point of the structure for each test was approximately 8 m from the launch point. The structure would then be accelerated to a steady velocity of 0.1 m/s, with the iceberg being launched when the structure was approximately 4 m away.

In the planning stages of the experimental program, it was considered desirable to observe icebergs with both head-on and eccentric approaches. During the initial series of tests it was found that head-on approaches were difficult to obtain. It was ultimately decided to launch each model from a position centred with the structure. Despite the initial centred iceberg position, significant lateral iceberg motions were observed for almost all tests. A summary of the number of tests conducted for each model and environmental condition is given in Table 4.4.

Table 4.4: Number of Tests Conducted for Each Model and Environmental Condition

	C	W1	W2	WC1	WC2
50 mm model	8	6	9	12	15
100 mm model	8	6	7	10	15
250 mm model	20	6	9	11	15
400 mm model	6	6	8	0	0

Iceberg motions were monitored using an overhead video camera, with details of the camera configuration given in the next section. Figure 4.4 shows the 400 mm iceberg approaching the structure as viewed from the camera position. An electronic timer attached to the video camera displayed the time on the video tape to a resolution of

0.01 s. The motions of each iceberg were recorded until the iceberg drifted outside the camera field of view or until the iceberg drifted behind the structure.

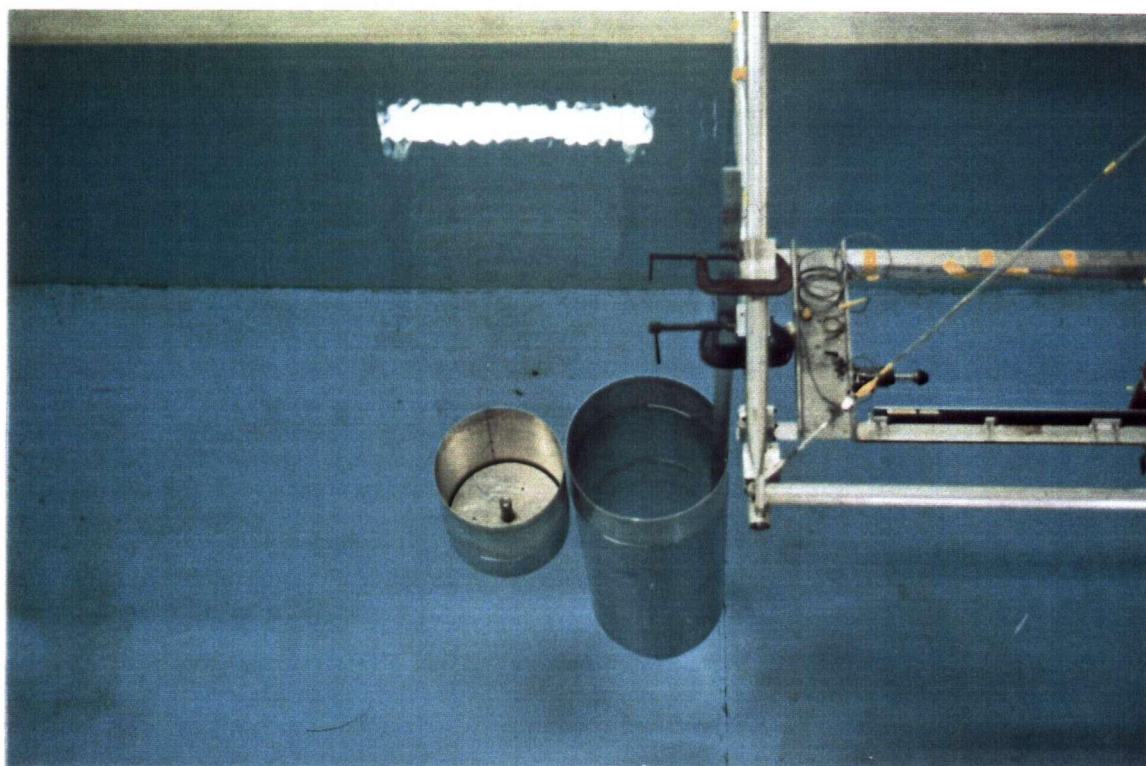


Figure 4.4: Overhead View of 400 mm Iceberg Approaching Structure

### 4.3 Digitizing of Iceberg Trajectories

The videotape recorded during the experiments provided a permanent record of observed drift trajectories. A micro-computer system was developed for digitizing the drift trajectories from the videotape. Although the model iceberg motions consisted of both drift and oscillatory components, only the drift motions were of interest. The restriction of drift motions to the horizontal plane allowed for trajectory co-ordinates to be obtained using observations from a single camera. A time interval between digitized co-ordinates of the order of one second was considered adequate for analysing drift trajectories.

### 4.3.1 Video Camera Configuration

The video camera was placed on a balcony above the towing tank at an elevation of 5.2 m above water level and at a horizontal distance of 2.7 m from the centreline of the towing tank. This location and the settings of the camera correspond to a field of view at the waterline plane which was approximately 4 m  $\times$  3 m. All relevant dimensions were measured such that co-ordinates in the waterline plane could be evaluated from the video images as indicated below.

### 4.3.2 Reduction of Video Co-ordinates

A suitable method was required for reducing observed co-ordinates from video images to co-ordinates in the waterline plane. The following three co-ordinate systems illustrated in Figures 4.5 and 4.6 were adopted:

$x$ - $y$ - $z$ :  $x$ - $y$  plane coinciding with waterline plane. Origin coinciding with video image centreline (i.e. camera is in  $y$ - $z$  plane),

$x'$ - $y'$ : Plane parallel to video image, passing through a given observation point. Origin aligned with  $x$ - $y$ - $z$  system origin,

$x''$ - $y''$ : Video image plane. Origin at the centre of the video image. Dimensions given in terms of image pixel units.

Note that both the  $x'$ - $y'$  and  $x''$ - $y''$  planes are normal to the centreline of the video camera field of view and that the location of the  $x'$ - $y'$  plane is dependent on the location of a given observation point. Scaling from the video image to the  $x'$ - $y'$  system for a point can be easily carried out as follows:

$$x' = k_s L x'' \quad (4.6)$$

$$y' = k_s L y'' \quad (4.7)$$

where:

$k_s$  = video image scale factor (/pixel)

$L$  = distance from camera to  $x' - y'$  plane (m)

$x', y'$  = co-ordinates in  $x' - y'$  plane (m)

$x'', y''$  = co-ordinates in  $x'' - y''$  plane (pixels)

The scale factor  $k_s$  is dependent on the video camera system and zoom lens setting. The distance  $L$  from the camera to the  $x'-y'$  plane can be expressed as:

$$L = L_t + y \sin \theta - z \cos \theta \quad (4.8)$$

where as indicated in Figure 4.6:

$L_t$  = distance from camera to  $x - y - z$  origin (m)

$\theta$  = angle of camera orientation from vertical ( $^\circ$ )

Equations 4.6 and 4.7 can then be re-written in terms of the  $x - y$  co-ordinate system:

$$x = k_s (L_t + y \sin \theta - z \cos \theta) x'' \quad (4.9)$$

$$y \cos \theta + z \sin \theta = k_s (L_t + y \sin \theta - z \cos \theta) y'' \quad (4.10)$$

Actual reduction of video image co-ordinates can be done by re-writing equation 4.10 in closed form as:

$$y = \frac{k_s (L_t - z \cos \theta) y'' - z \sin \theta}{\cos \theta - k_s y'' \sin \theta} \quad (4.11)$$

Thus, the iceberg drift co-ordinates  $x$  and  $y$  can be determined provided that the other terms of equations 4.9 and 4.11 are known, including the  $z$  co-ordinate of the reference point on the iceberg used for digitizing. The scaling factor  $k_s$  can be determined using two

observation points having known  $y$ ,  $y''$ , and  $z$  values. For the present set of experiments, a survey rod was laid across the top of the towing tank (0.3 m above water level) to provide reference points for determining the scale factor  $k_s$ .

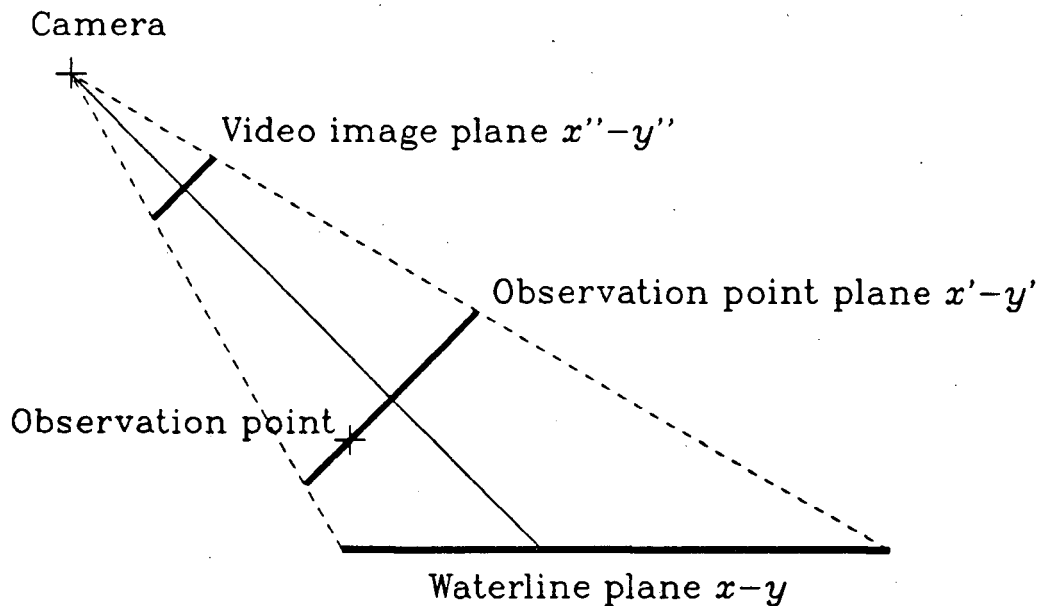
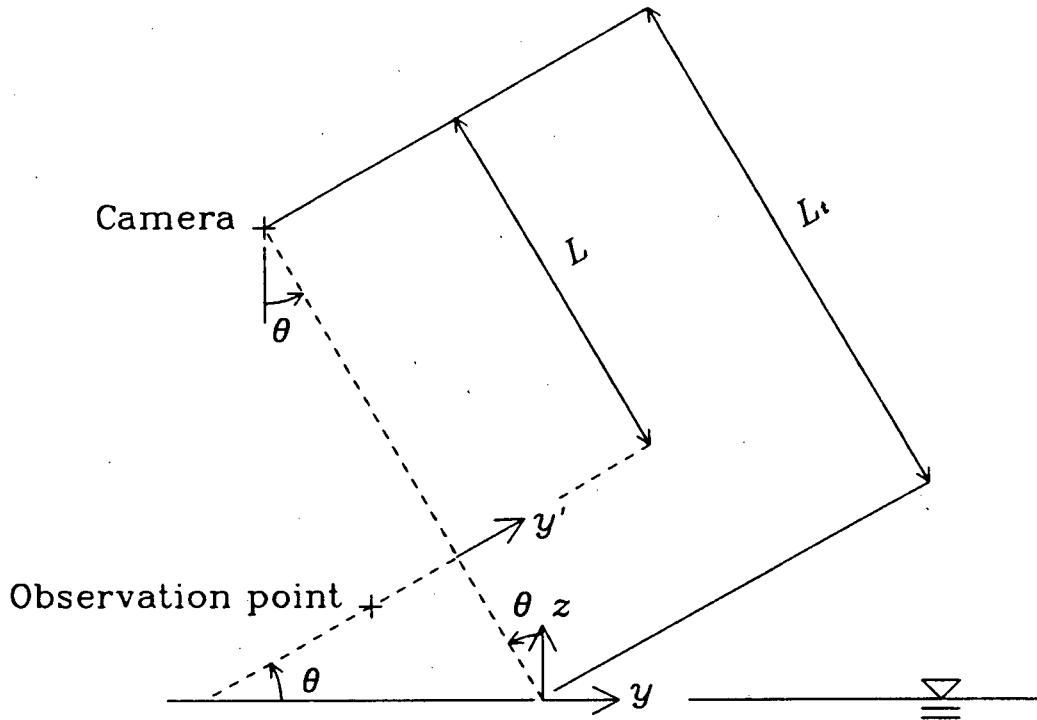


Figure 4.5: Elevation View of Video Image Planes

#### 4.4 Micro-Computer Digitizing System

The analysis of observed iceberg trajectories required that iceberg locations be digitized from the recorded videotape. A schematic of the system developed for digitizing iceberg locations is shown in Figure 4.7. Using the framegrabber, a single frame from the videotape can be displayed on the monitor of the micro-computer. A cursor is superimposed on the monitor image, and can be moved anywhere on the image using a mouse. An iceberg location can be recorded by moving the cursor to a reference point on the iceberg and clicking the mouse.

### Elevation View



### Plan View

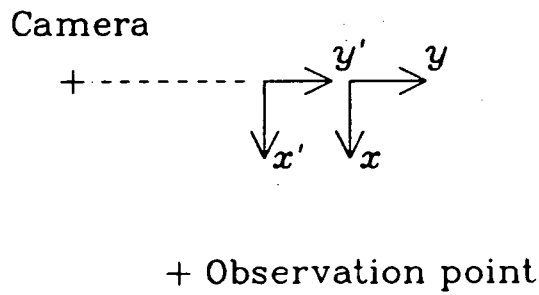


Figure 4.6:  $x-y$  and  $x'-y'$  Co-ordinate Systems and Relevant Dimensions

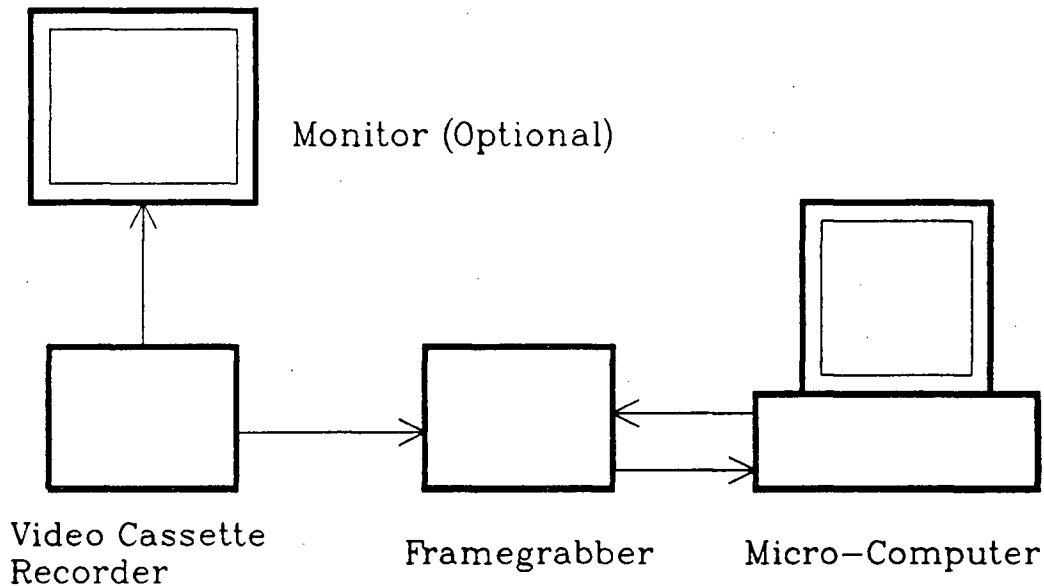


Figure 4.7: Schematic of Video Digitizing System

#### 4.4.1 Description of Hardware

The system hardware shown in Figure 4.7 consists of standard off-the-shelf components. The video cassette recorder (VCR) uses the VHS tape format. The micro-computer is an Apple Macintosh II, which has a Motorola 68020 processor, Motorola 68881 co-processor, and 5 megabytes of random access memory (RAM).

A Data Translation Limited QuickCapture framegrabber board was installed in an expansion slot of the Macintosh II. The framegrabber converts the analogue signal from the VCR to a digital pixel map of a single frame which is stored in RAM resident on the framegrabber board. The resolution of the QuickCapture pixel map is 640 pixels horizontally  $\times$  480 pixels vertically, corresponding to the resolution of the Macintosh monitor. The intensity of each pixel is stored as a grey level varying between 0 and 255. The on-board RAM of the QuickCapture hardware is 512 k, which is sufficient for storing a single video frame. A product review of QuickCapture has been given by West and

Newton [116].

#### 4.4.2 Description of Software

Included with QuickCapture is software for various tasks, including displaying video images on the Macintosh II screen and storing images on disk. The software is intended primarily for graphic arts applications. Complementary software products for graphics work is available from other vendors. A review of available commercial software indicated that no products were suitable for the present digitizing application. Consequently, it was decided to develop a program for digitizing iceberg motion co-ordinates.

The initial step in the development of the digitizing software was the selection of a suitable programming language. The acquisition and display of video images with QuickCapture is carried out using memory-mapped input and output (see Lawrence and Mauch [56]). Of the various common programming languages, C is among the most suitable for operation of memory-mapped systems. Graphical display of images on the Macintosh monitor was also a consideration when selecting a programming language. Graphics programming with the Macintosh II is most readily accomplished using the Macintosh Toolbox (see Apple [3]), a set of subroutines residing in read-only memory (ROM). Although documentation examples for the Toolbox are written in PASCAL, translation to C is very straightforward. Consequently, the C programming language was selected for writing the digitizing software.

The resulting digitizing program ICEDIGITIZE was written to obtain iceberg co-ordinates for a given series of tests. The program consists of two distinct phases. In the first part of the program, input regarding the camera configuration and environmental conditions of a test series is read. The program user is asked to click the mouse on two reference points on a captured frame so that the scale factor  $k_s$  for equations 4.9 and

4.11 can be determined. A lateral reference point on the structure is taken to determine the location of the structure relative to the centreline of the screen image.

The second part of the program obtains iceberg and structure co-ordinates during the drift experiments. Beginning with the first frame of a test, the user aligns the mouse with the centre point of the iceberg at the waterline plane. The iceberg location is stored in memory, and the framegrabber automatically displays the next frame. The VCR is run continuously during digitizing; thus, the time interval between frames can be determined using the internal clock of the computer. The time interval between captured frames is typically 3 s. Digitizing of an iceberg location is indicated by a single mouse click. For some frames the location of the structure is also required. A double mouse click will store the structure location, and will delay the frame advance until a single click indicating an iceberg location is detected.

Once all points for an iceberg trajectory have been entered, the program user can request that the digitized co-ordinates be written to an output file. The user is asked to input the time displayed on the last video frame, thus allowing the display time for each iceberg point to be stored.

One drawback of the digitizing system was the 3 s time interval between digitized points. A finer time interval was desired in many cases, particularly when the structure was being towed to simulate a current. More frequent observations for a given trajectory were obtained by rewinding the videotape and repeating the digitizing procedure several times.

## **4.5 Error Analysis of Digitized Co-ordinates**

Digitized iceberg co-ordinates were prone to various errors, of which the two primary sources were:

1. Variation of the mouse location from the actual point to be digitized,
2. Variation of the  $z$  co-ordinate of an observation point from its assumed constant value.

An analysis was conducted to determine the magnitudes of errors from both of the above sources.

#### 4.5.1 Mouse Operation Error

Co-ordinates digitized using a mouse are subject to errors by the human operator. The magnitude is dependent mainly on the resolution of the image from which points are digitized.

A trial of the digitizing program was conducted to examine the variability of digitized co-ordinates. The location of a stationary iceberg model was digitized 14 times. The digitized  $x''$  and  $y''$  co-ordinates had standard deviations  $\sigma_{x''}$  and  $\sigma_{y''}$  of 0.7 pixel units.

The magnitude of the mouse operation error for reduced co-ordinates can be determined through equations 4.9 and 4.11. It should be noted that mouse operation error is not only caused by the error in digitizing a single point, but is also caused by errors in digitizing two reference points used to determine the scaling factor  $k_s$ . The error analysis is simplified by approximating  $y''$  and  $z$  as zero in equation 4.11. The  $y$  co-ordinate for a digitized point can be estimated in terms of the distance between two reference points, denoted  $\Delta y_s$ , in the  $x$ - $y$  plane, and  $\Delta y_s''$  in the image plane, as shown in Figure 4.8. The  $y$  co-ordinate is then:

$$y = \frac{\Delta y_s}{\Delta y_s''} y'' \quad (4.12)$$

where:

$\Delta y_s$  = distance between reference points for evaluating  $k_s$  (m)

$\Delta y_s''$  = image distance between reference points (pixels)

If the reference image distance  $\Delta y_s''$  and the digitized image co-ordinate  $y''$  have errors of  $\epsilon_s''$  and  $\epsilon''$  respectively, the reduced  $y$  co-ordinate will have the following value:

$$(y + \epsilon_y) = \frac{\Delta y_s}{(\Delta y_s'' + \epsilon_s'')} (y'' + \epsilon'') \quad (4.13)$$

where:

$\epsilon_y$  = error in reduced  $y$  co-ordinate (m)

$\epsilon''$  = error in digitized  $y''$  co-ordinate (pixels)

$\epsilon_s''$  = image error for reference distance (pixels)

Applying a first-order binomial expansion for the denominator and discarding terms of order  $\epsilon^2$ , the error due to mouse operation is:

$$\epsilon_y = \epsilon'' \frac{\Delta y_s}{\Delta y_s''} - \epsilon_s'' \frac{y}{\Delta y_s''} \quad (4.14)$$

Note that each of the above error terms can have a positive or negative value. The magnitude of the mouse error term  $\epsilon''$  can be taken to be approximately 0.7 pixels, which corresponds to the standard deviation  $\sigma_{y''}$  obtained from digitizing a point several times. The magnitude of the error term  $\epsilon_s''$  for the image distance between two reference points can be estimated by assuming  $\epsilon''$  to have a normal distribution, thus giving  $\sigma_{\Delta y_s''}$  equal to  $\sqrt{2} \sigma_{y''}$ .

When digitizing reference points for evaluating the scale factor  $k_s$ , the reference distance  $\Delta y_s$  was 1.0 m, with a corresponding image distance  $\Delta y_s''$  of approximately 300 pixels. The standard error of reduced  $y$  co-ordinates due to mouse operation can thus be approximated from equation 4.14 as:

$$\sigma_y = 2.3 \text{ mm} + 0.003 |y| \quad (4.15)$$

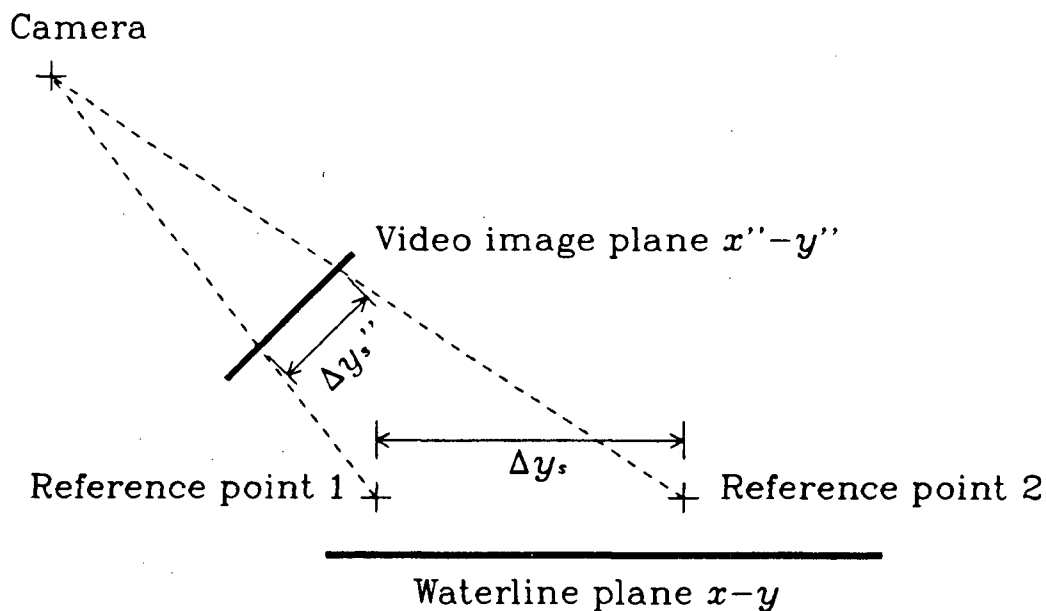


Figure 4.8: Elevation View of Reference Distance  $\Delta y_s$  and Image Distance  $\Delta y_s''$

Only points with  $|y| < 0.5$  m were of interest for the observed model trajectories; thus, the maximum standard error  $\sigma_y$  due to mouse operation is approximately 4 mm.

A similar analysis could be conducted to assess errors in reduced  $x$  co-ordinates. Due to the inclusion of  $y$  in the equation for reducing  $x$  co-ordinates (4.9), the error analysis would be significantly more complex. However, it is expected that the standard error of  $x$  reduced co-ordinates due to mouse operation error is approximately the same as for  $y$  co-ordinates.

#### 4.5.2 Error Due to Variation of $z$ Co-ordinate

When evaluating iceberg co-ordinates using equations 4.9 and 4.11, it was assumed that the observation point for each iceberg remained at the still waterline  $z = 0$ . Wave-induced motions caused the reference points on the icebergs to vary significantly from the assumed elevation of zero. Deviations for smaller icebergs likely approached the wave

amplitude, which was equal to 30 mm for the largest waves.

The influence of varying  $z$  values on the calculated values of the reduced co-ordinates can be estimated using equations 4.9 and 4.11. The sensitivity of  $y$  co-ordinates to  $z$  fluctuations is:

$$\epsilon_y = -\epsilon_z \frac{k_s y'' \cos \theta + \sin \theta}{\cos \theta - k_s \sin \theta y''} \quad (4.16)$$

where:

$$\epsilon_z = \text{variation in } z \text{ from assumed value (m)}$$

For the camera configuration used in the experiments, equation 4.16 exhibits little variation with  $y''$ . The error in  $y$  co-ordinates for the experimental configuration can thus be reduced to:

$$\epsilon_y = -0.5 \epsilon_z \quad (4.17)$$

The corresponding standard error due to elevation variations is  $0.5 \sigma_z$ , which will have a maximum value of approximately 15 mm for the smaller models in the 61 mm waves.

The reduced  $x$  co-ordinates obtained from equation 4.9 are much less sensitive to variations in  $z$  values:

$$\epsilon_x = k_s [\epsilon_y \sin \theta - \epsilon_z \cos \theta] x'' \quad (4.18)$$

Substituting known values into the above equation, the  $x$  error reduces to:

$$\epsilon_x = -0.00057/\text{pixel } x'' \epsilon_z \quad (4.19)$$

If  $x''$  and  $\epsilon_s$  have their maximum magnitudes of 320 pixels and 30 mm respectively, then the standard error of co-ordinates  $x$  due to variation of  $z$  can be estimated to be 5 mm.

### 4.5.3 Summary of Digitizing Errors

The above analysis indicates that the standard error for digitized co-ordinates is approximately 10 mm. The largest co-ordinate errors will occur for  $y$  values of smaller models in large waves, with the standard error  $\sigma_y$  approaching 20 mm. Additional errors are introduced by the recorded time values of digitized points, which have a resolution of 0.1 s. For an iceberg model travelling at 0.1 m/s, the displacement error due to an average time error of 0.025 s will be 2.5 mm; thus, the error due to time resolution will contribute slightly to the error of reduced co-ordinates.

## 4.6 Variability of Environmental Conditions

The variability of simulated currents and waves in the towing tank must also be considered when evaluating results from the physical modelling tests. Fluctuations in wave paddle motions and wave reflections from the ends and sides of tank were possible sources of irregularities for the generated wave conditions. Because the towing carriage was controlled manually using a potentiometer and digital readout of carriage velocity, deviations in simulated current velocities also existed.

Wave records for each set of wave conditions were obtained from a resistance-type wave probe located in the test section that was connected to an amplifier and chart recorder. Due to the regular, sinusoidal nature of the waves generated for the experiments, measurement of wave heights from the chart record was straightforward. Chart records obtained for each of the four wave conditions indicated that the standard deviation of wave height for each record was between 2 mm and 3 mm, and appeared to be independent of wave height.

The towing carriage velocity for each test was estimated by taking a least-squares

linear fit to observed structure co-ordinates. The estimated towing carriage velocities for all tests with a simulated current had a mean value of 0.110 m/s (compared with the target value of 0.1 m/s) and a standard deviation of 0.018 m/s. Although it was assumed that the towing velocity was constant for each test, the standard deviation of 0.018 m/s among tests can likely be considered as an upper bound to the variability of current velocity during a given test, with the actual variation of current velocity for a given test being closer to 0.01 m/s.

To estimate the influence of variable current velocity and wave height on iceberg drift velocity, it is useful to consider equation 3.53 which gives the equilibrium velocity of an iceberg drifting in collinear waves and currents. If it is assumed that the iceberg responds instantaneously to changes in wave height, then the wave-induced iceberg drift velocity will have the same coefficient of variation as the incident wave height (approximately 15% for the 20 mm waves, 5% for the 60 mm waves). In reality, the iceberg drift velocity does not respond instantaneously to changes in wave height but requires time to accelerate to a new equilibrium velocity; thus, the variability of iceberg drift velocity due to variation of incident wave height is likely to be no greater than 5%. Because currents were simulated by towing the structure, the variability of the effective current-induced iceberg drift velocity during a given test is equal to the variability of the towing carriage velocity (approximately 0.01 m/s for a mean towing velocity of 0.11 m/s). In summary, the variability of environmental conditions likely resulted in a drift velocity fluctuation of the order of 10% during each test.

## 4.7 Analysis of Observed Trajectories

Once digitizing of the iceberg co-ordinates from the videotape was completed, the observed trajectories were analysed to determine the influence of the structure on drift

motions of approaching icebergs.

### 4.7.1 Reduction of Iceberg Co-ordinates Relative to Structure

The iceberg co-ordinates obtained from the videotape were subsequently reduced to those relative to the structure. Reduction of iceberg co-ordinates was particularly important for tests involving movement of the structure to simulate a current. Due to the nature of the carriage control system, the structure velocity deviated from the desired value of 0.10 m/s. The observed structure trajectory for each test was approximated with a least squares linear fit; thus, it was assumed that the structure velocity was constant for a given test. Iceberg co-ordinates relative to the structure were then evaluated accordingly.

### 4.7.2 Plotting of Iceberg Trajectories

The iceberg trajectory and displacement versus time relative to the structure were plotted for each test, as shown in Figure 4.9. The iceberg models were drawn to scale on the trajectory plots at the initial observation point, final observation point, and observation point nearest the structure. A plot of the iceberg nearest the structure was very useful for indicating the occurrence of collisions and for indicating possible errors in reduced co-ordinates (e.g. overlap between the structure and iceberg).

Qualitative observations of the plotted iceberg trajectories were useful for indicating whether collisions occurred during a given series of tests. Results from qualitative observations are presented in Table 4.5 and indicate that the likelihood of impact appears small for  $D_i/D_s \leq 0.2$  when only waves are present. For the smaller wave condition, the two smaller models veered away from the structure long before impact could occur. A representative trajectory is shown in Figure 4.10. It appeared that the two smaller

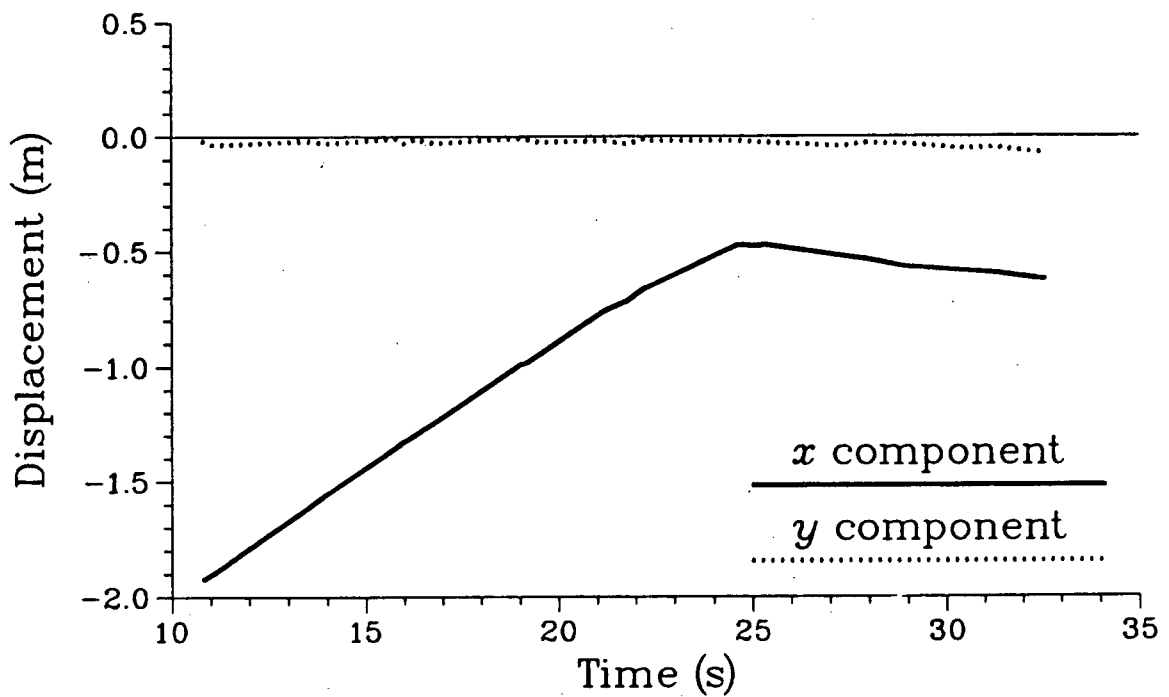
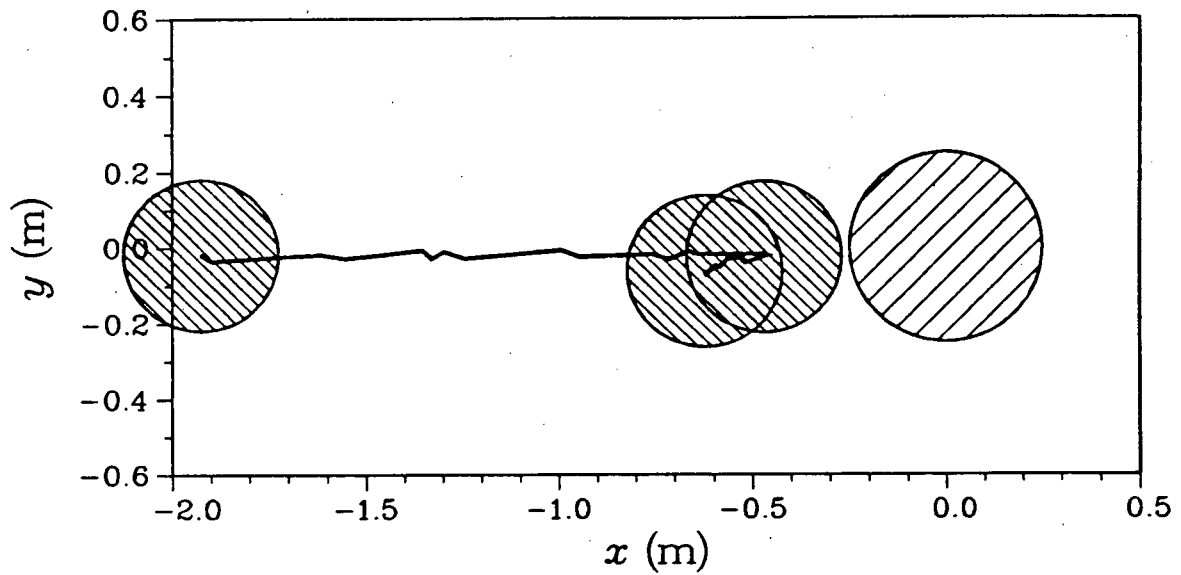


Figure 4.9: Observed Iceberg Trajectory and Displacement vs. Time Graphs

Table 4.5: Occurrence of Impacts for Experiments

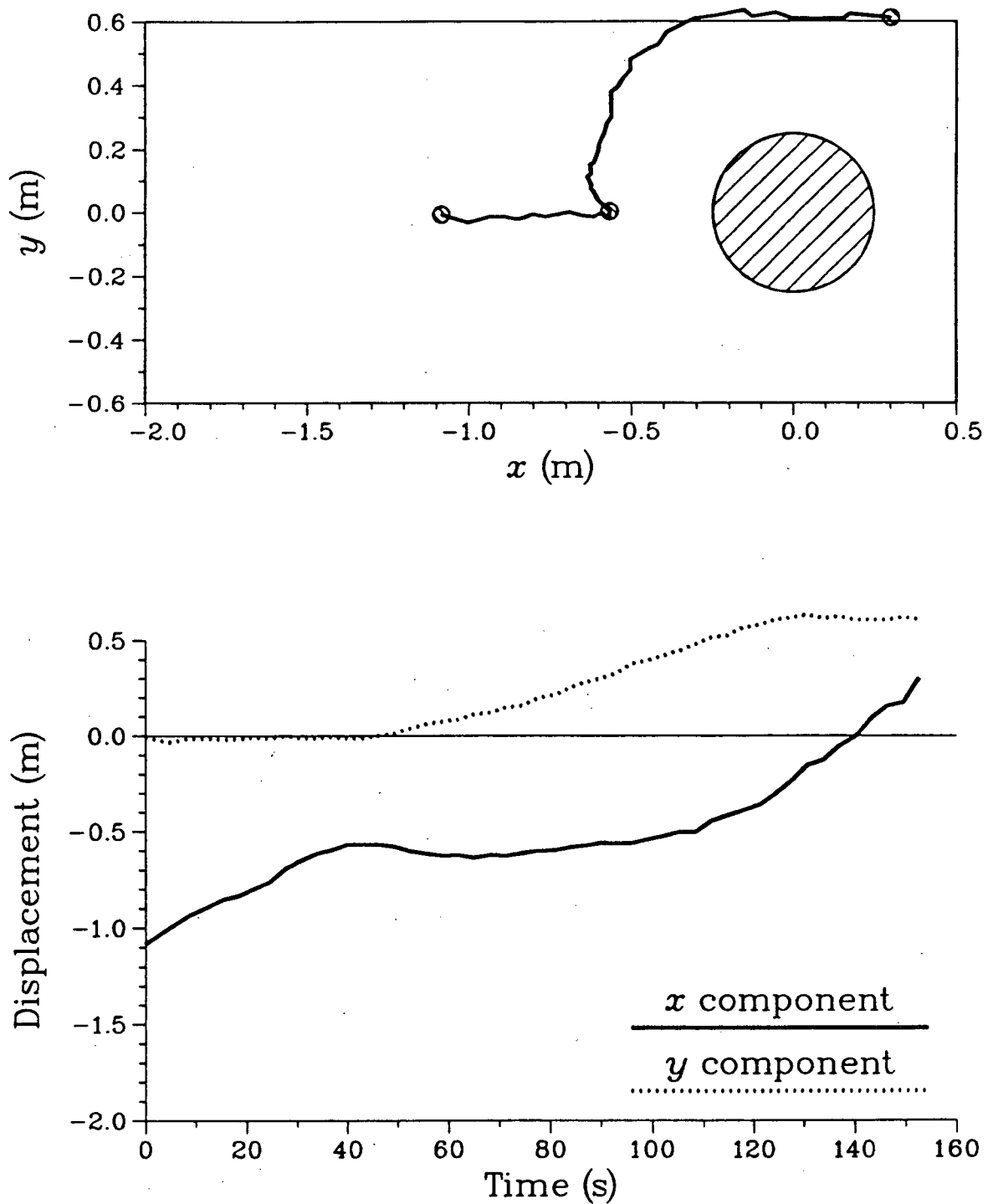
$D_i/D_s =$	0.1	0.2	0.5	0.8
Currents	Yes	Yes	Yes	Yes
Waves 1 ( $H = 21$ mm)	No	No	Yes	Yes
Waves 2 ( $H = 61$ mm)	Maybe	Maybe	Yes	Yes
Wave-currents 1 ( $H = 19$ mm)	Yes	Yes	Yes	Yes
Wave-currents 2 ( $H = 59$ mm)	Yes	Yes	Yes	Yes

models could make glancing impacts under the large wave condition.

The qualitative observations are in general agreement with the numerical iceberg drift model and with the experimental observations of Salvalaggio and Rojansky [99]. Salvalaggio and Rojansky observed that wave driven icebergs near a structure would not impact when  $D_i/D_s$  was less than 0.5. The numerical model results of Figure 3.25 indicate that negative wave drift forces can develop in front of a structure when  $D_i/D_s$  is less than 0.4; thus, the experimental results observed for wave driven iceberg drift are as expected. It was also shown in Chapter 3 that the influence of the structure on current driven motions is negligible for most icebergs. The experimental observations confirm this result. For experiments combining waves and currents, the currents appeared to have a dominant effect on iceberg motions.

### 4.7.3 Estimation of Impact Velocity and Eccentricity

The influence of the structure on observed model iceberg drift motions was of primary interest. Specifically, the variation of iceberg velocity and approach eccentricity (see Figure 4.11) with proximity to the structure were to be considered. The approach eccentricity of an iceberg at a given point is defined as the closest distance between the

Figure 4.10: Observed Trajectory for Wave Condition 1,  $D_i/D_s = 0.1$

iceberg and structure centres if the iceberg velocity (speed and direction) remains constant; thus, an approach eccentricity of zero is representative of a head-on approach. It should be noted that approach eccentricity varies with time as the iceberg location and velocity vary.

A method was required for estimating observed iceberg drift velocities in the far-field (i.e. far away from the structure) and near-field (i.e. near the structure). Various methods were considered for estimating observed drift velocities. Although finite difference methods could have been used for estimating observed drift velocities, it was felt that oscillatory motions in waves and errors in observed positions would lead to inaccurate estimates of drift velocities. It was decided that a least squares technique would provide the best estimate of model drift velocities. Far-field and near-field segments of observed trajectories were approximated as follows:

$$x_F(t) = A_{F_x} t^2 + B_{F_x} t + C_{F_x} \quad (4.20)$$

$$y_F(t) = A_{F_y} t^2 + B_{F_y} t + C_{F_y} \quad (4.21)$$

$$x_N(t) = A_{N_x} t^2 + B_{N_x} t + C_{N_x} \quad (4.22)$$

$$y_N(t) = A_{N_y} t^2 + B_{N_y} t + C_{N_y} \quad (4.23)$$

where:

$A_F, B_F, C_F$  = approximating coefficients for far-field motions

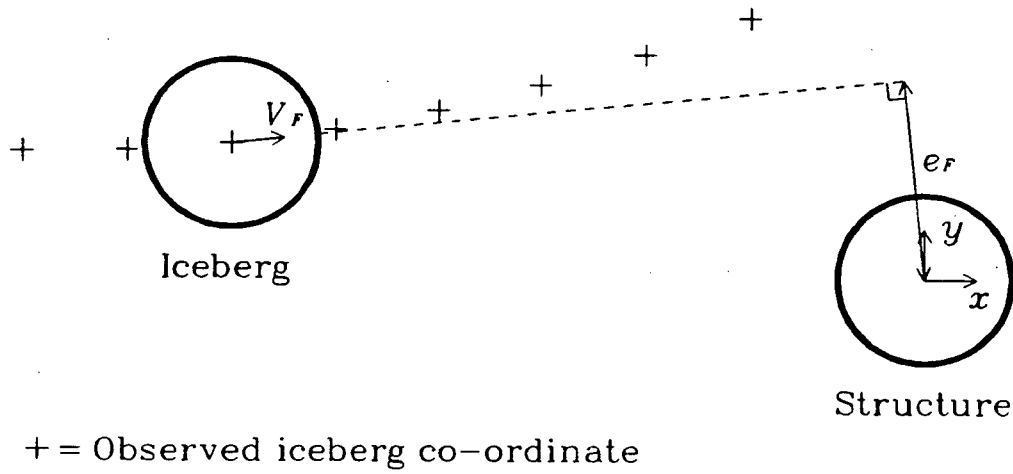
$A_N, B_N, C_N$  = approximating coefficients for near-field motions

$x_F, y_F$  = iceberg co-ordinates in far-field (m)

$x_N, y_N$  = iceberg co-ordinates in near-field (m)

Equation coefficients for the far-field were evaluated using a least squares fit to the first four points of an observed trajectory. To reduce the degree of numerical error, it was also stipulated that the observation points representing the far-field motions must traverse a

### Far-field Eccentricity



### Near-field Eccentricity

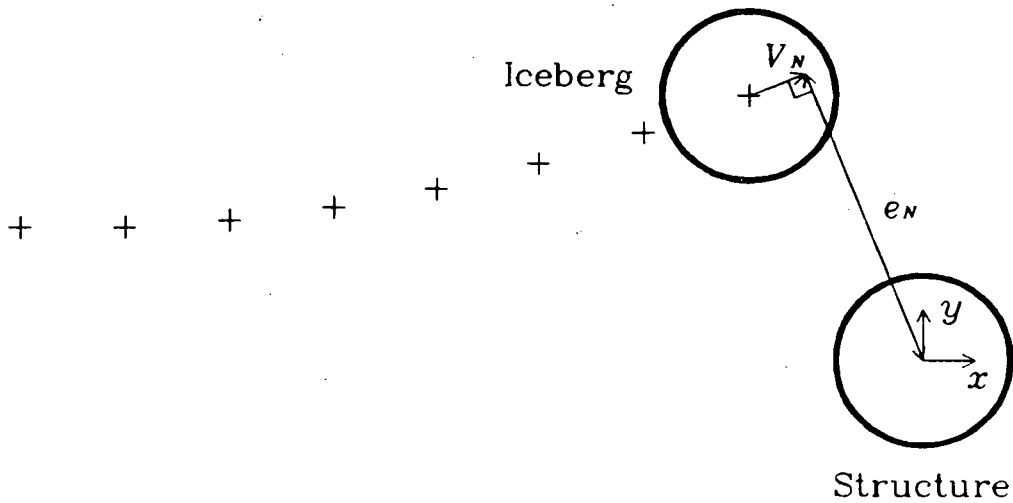


Figure 4.11: Far-field and Near-field Eccentricities of Approach for an Iceberg

distance of at least 0.5 m; thus, more than four observation points were used in some cases.

The quadratic approximation to the near-field trajectory was based on the iceberg observation point closest to the structure taken together with previous three observation points. A minimum traversing distance of 0.3 m was specified for the near-field observation points. In cases where contact with the structure appeared possible, steps were taken to ensure that all near-field observation points were taken prior to impact.

Iceberg velocity components in the far-field and near-field, corresponding to the time of the last observation point for each of the respective fields, were estimated by differentiating equations 4.20 - 4.23. The eccentricity of approach, illustrated in Figure 4.11, was calculated for each field as follows:

$$e_F = \frac{|y_F - x_F \frac{V_{Fy}}{V_{Fx}}|}{\sqrt{\left(\frac{V_{Fy}}{V_{Fx}}\right)^2 + 1}} \quad (4.24)$$

$$e_N = \frac{|y_N - x_N \frac{V_{Ny}}{V_{Nx}}|}{\sqrt{\left(\frac{V_{Ny}}{V_{Nx}}\right)^2 + 1}} \quad (4.25)$$

where:

$e_F$  = far-field eccentricity of approach (m)

$e_N$  = near-field eccentricity of approach (m)

$V_{Fx}, V_{Fy}$  = far-field velocity components (m/s)

$V_{Nx}, V_{Ny}$  = near-field velocity components (m/s)

The corresponding dimensionless eccentricity of approach was given as:

$$e' = \frac{e}{1/2 (D_i + D_s)} \quad (4.26)$$

A dimensionless eccentricity of 0 is representative of a head-on approach, while a value greater than 1 is indicative of no contact occurring between the iceberg and structure if the iceberg direction remains constant.

#### 4.7.4 Error Estimates for Velocities and Eccentricities

The estimated iceberg velocities and eccentricities were subjected to errors caused by the digitized iceberg co-ordinates and the variability of the environmental conditions. It was shown previously that each digitized co-ordinate had a standard error of approximately 10 mm, and that the variable environmental conditions led to  $x$  velocity fluctuations of approximately 10%.

Recalling that far-field and near-field velocity estimates were obtained from data points over distances of at least 0.5 m and 0.3 m respectively, a conservative estimate of the error in estimated velocities can be made by assuming that velocities were evaluated using a finite difference scheme as follows:

$$V = \frac{x_2 - x_1}{t_2 - t_1} \quad (4.27)$$

where:

$t_1$  = time of observation point at beginning of field (s)

$t_2$  = time of observation point at end of field (s)

$x_1$  = co-ordinate of observation point at beginning of field (s)

$x_2$  = co-ordinate of observation point at end of field (s)

The corresponding error in the estimated velocity due to the error of digitized co-ordinates is as follows:

$$\epsilon_V = \frac{\epsilon_{x_2} - \epsilon_{x_1}}{t_2 - t_1} \quad (4.28)$$

where:

$\epsilon_V$  = error in velocity estimate (m/s)

Dividing equation 4.28 by equation 4.27, the error in the estimated velocity can be

expressed as a fraction of the velocity:

$$\frac{\epsilon_V}{V} = \frac{\epsilon_{x_2} - \epsilon_{x_1}}{x_2 - x_1} \quad (4.29)$$

Taking the standard error for a digitized co-ordinate to be 10 mm, the numerator in the above equation has an expected magnitude of 14 mm, while the denominator is of the order of 0.3 m. Thus, the error in estimated velocities due to digitized co-ordinate errors is approximately 5%. The total error in estimated velocities caused by the variability of both digitized co-ordinates and environmental conditions is approximately 15%.

Estimates of errors in eccentricities obtained from equations 4.24 and 4.25 can be made most easily by considering the limiting cases where  $V_x/V_y$  approaches zero and infinity:

$$\epsilon_e = |\epsilon_y| \text{ for } V_x/V_y \rightarrow 0 \quad (4.30)$$

$$\epsilon_e = |\epsilon_x| \text{ for } V_x/V_y \rightarrow \infty \quad (4.31)$$

Thus, the estimated error in the approach eccentricity  $e$  due to the digitized co-ordinate error is approximately 10 mm. From equation 4.26, the corresponding error in the estimated dimensionless eccentricity  $e'$  is approximately 0.04.

#### 4.7.5 Presentation of Results

The far-field velocity and eccentricity were used to approximate open water values  $V_o$  and  $e_o$  respectively. Likewise, the near-field velocity and eccentricity were used to approximate "collision" values  $V_c$  and  $e_c$  corresponding to the instant of contact or minimum separation distance. Thus the experimental results for the far-field are expressed in terms of open water velocity  $V_o$  and corresponding dimensionless eccentricity  $e'_o$ , while near-field results are expressed in terms of collision velocity  $V_c$  and corresponding dimensionless eccentricity  $e'_c$ . Graphs showing the variation of approach eccentricities and

velocities are given in Figures 4.12 - 4.25. The graphs also show corresponding numerical predictions, which are described in detail in the following section.

Results are shown for trajectories having initial approaches which would lead to contact with the structure (i.e.  $e'_F \leq 1$ ). If the iceberg model remained stationary in front of the structure due to negative wave drift forces, the estimated near-field velocity  $V_N$  cannot be equated to the collision velocity  $V_c$ ; thus, results are not presented for tests with no currents and  $D_i \leq 0.2$ . Due to problems with the towing carriage, no wave-current tests were conducted with the 400 mm diameter iceberg model.

Results for the current driven motions (Figures 4.12 - 4.15) indicate that the influence of the structure on approach eccentricity is significant for the smaller models. The deflection of the 100 mm model away from the structure is particularly striking (Figure 4.13). Velocities of the current driven icebergs appear to decrease somewhat as they approach the structure. Figures 4.16 - 4.19 show significant scatter for the two larger icebergs when driven by waves only; however, it appears that the motions are relatively unaffected by the presence of the structure. The combined wave-current results are very similar to those shown for currents only. It appears that the iceberg motions for the wave-current tests were dominated by the currents.

## 4.8 Numerical Modelling of Wave Tank Experiments

A series of numerical simulations was conducted to compare observed experimental results with the numerical iceberg drift model. Drift trajectories for icebergs approaching the structure were computed for the five different conditions and six initial dimensionless eccentricities varying between 0 and 1. Results for the numerical drift model are plotted with the experimental results in Figures 4.12 - 4.25.

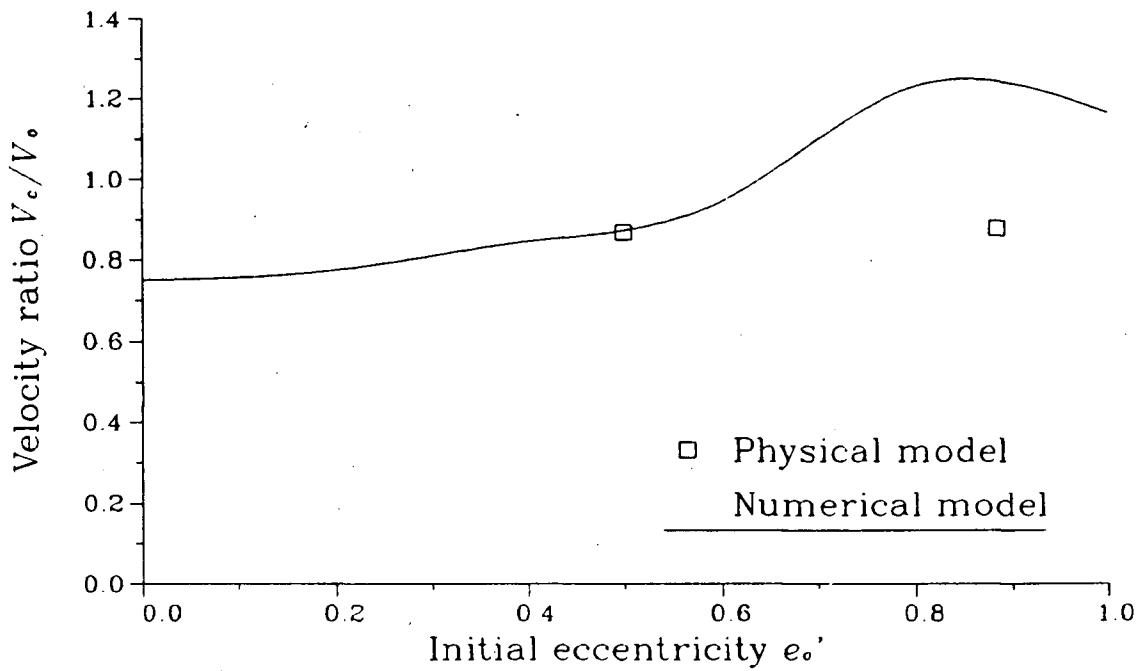
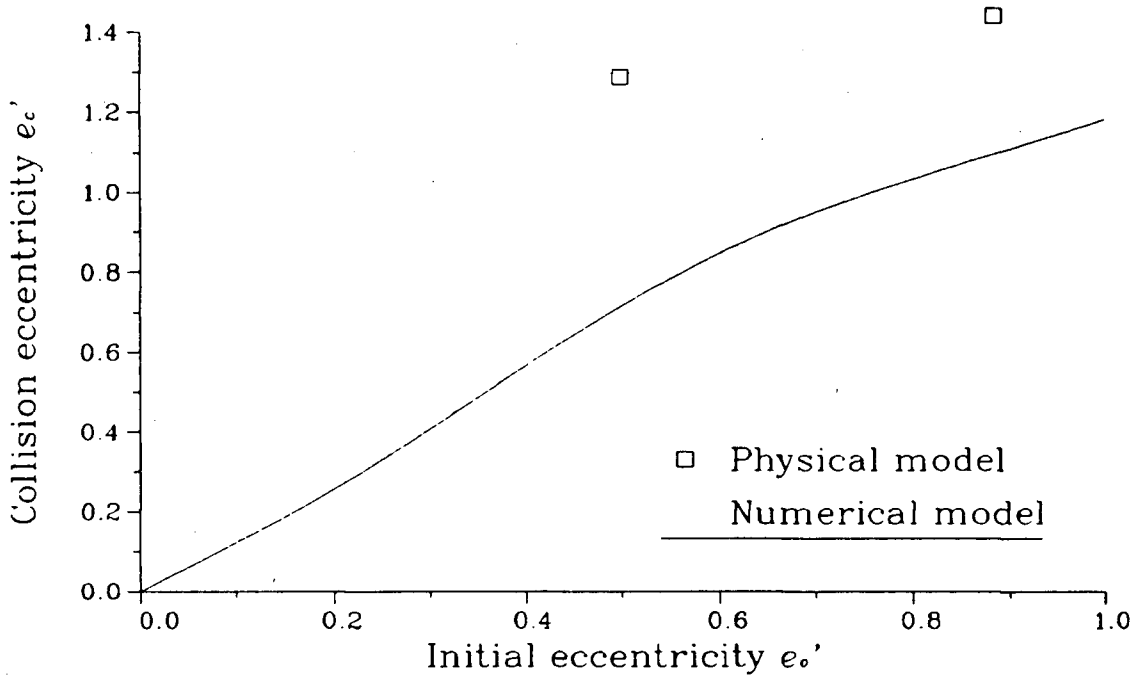


Figure 4.12: Variation of Iceberg Eccentricity and Velocity, Currents,  $D_i/D_s = 0.1$

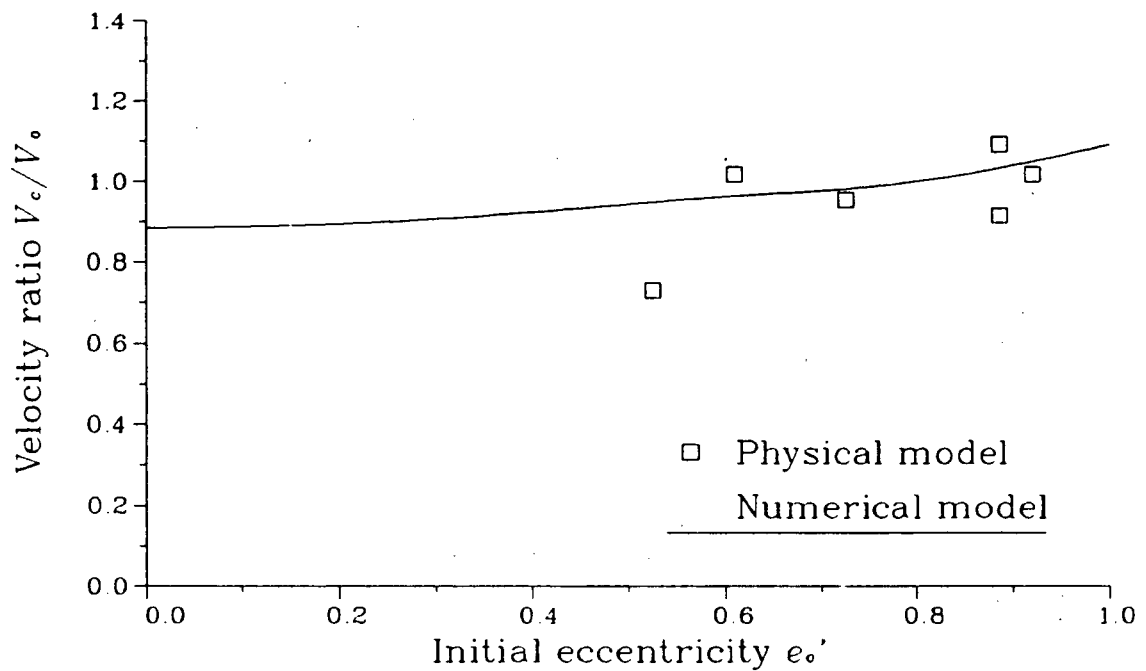
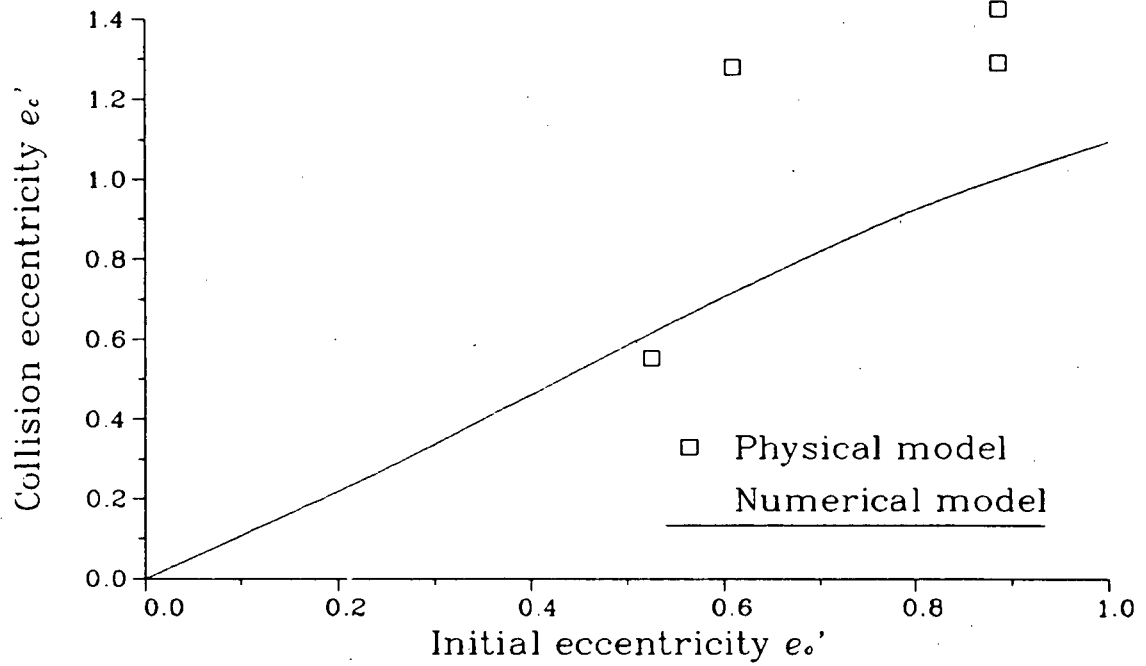
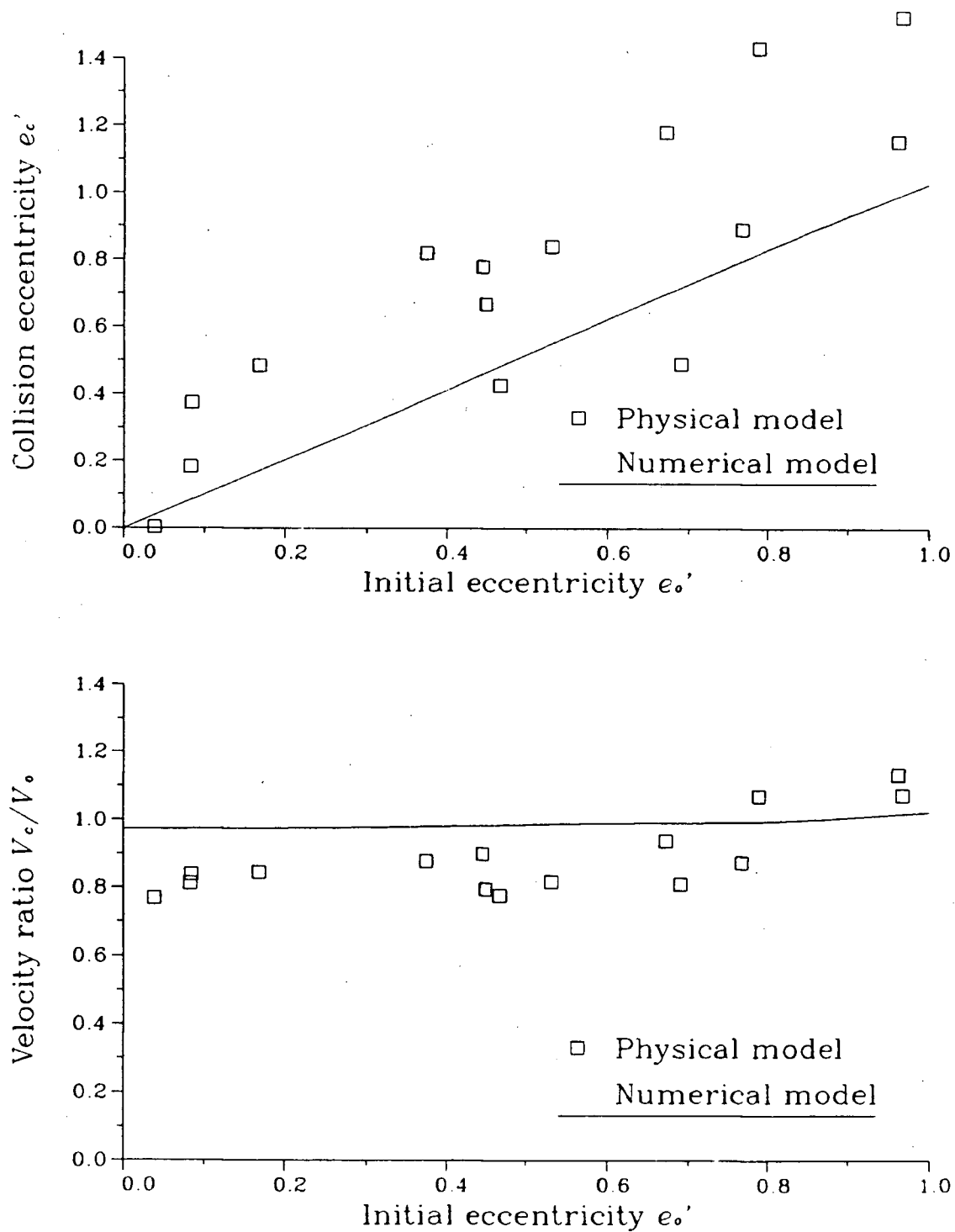
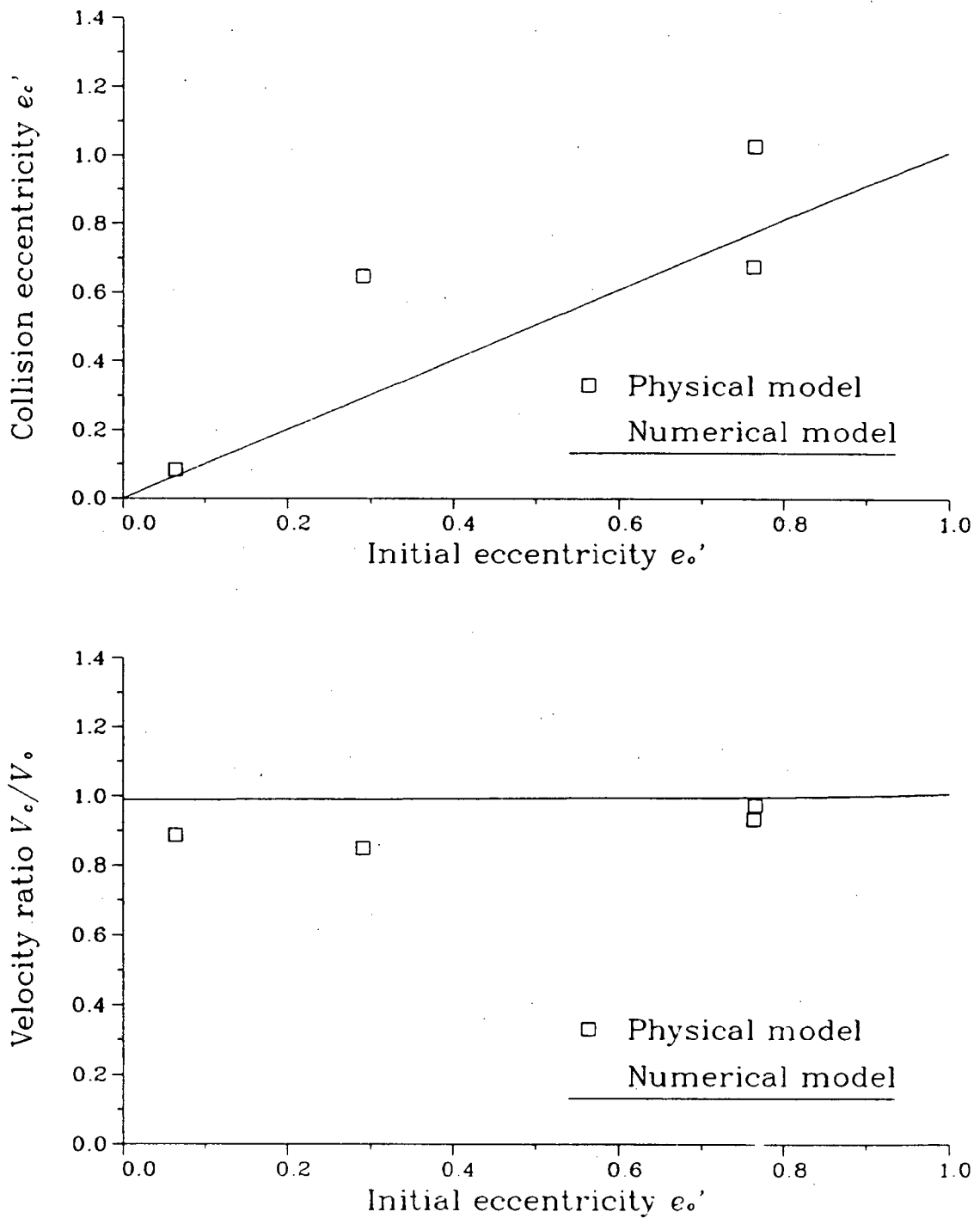


Figure 4.13: Variation of Iceberg Eccentricity and Velocity, Currents,  $D_i/D_s = 0.2$

Figure 4.14: Variation of Iceberg Eccentricity and Velocity, Currents,  $D_i/D_s = 0.5$

Figure 4.15: Variation of Iceberg Eccentricity and Velocity, Currents,  $D_i/D_s = 0.8$

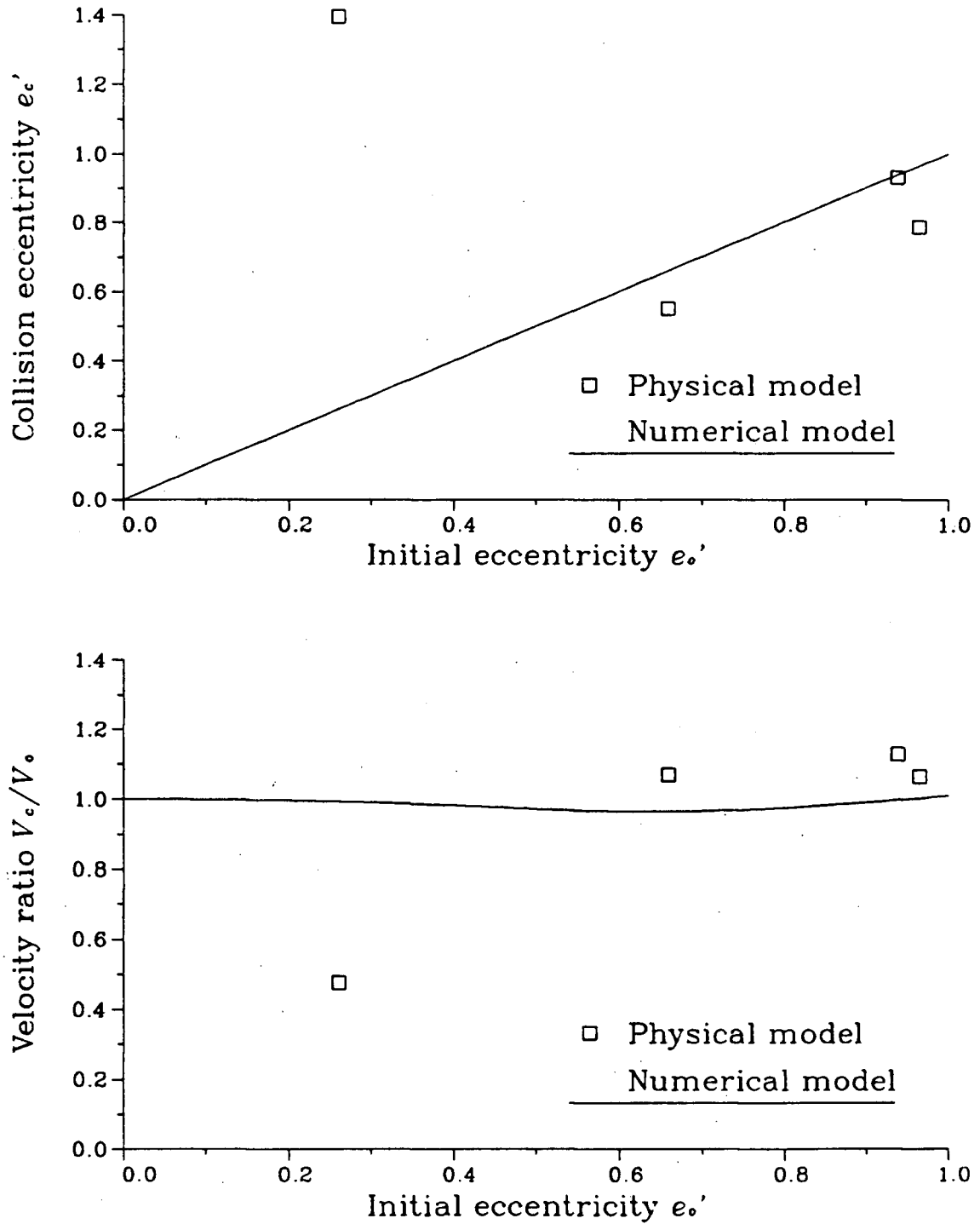


Figure 4.16: Variation of Iceberg Eccentricity and Velocity, Wave Condition 1,  $D_i/D_s = 0.5$

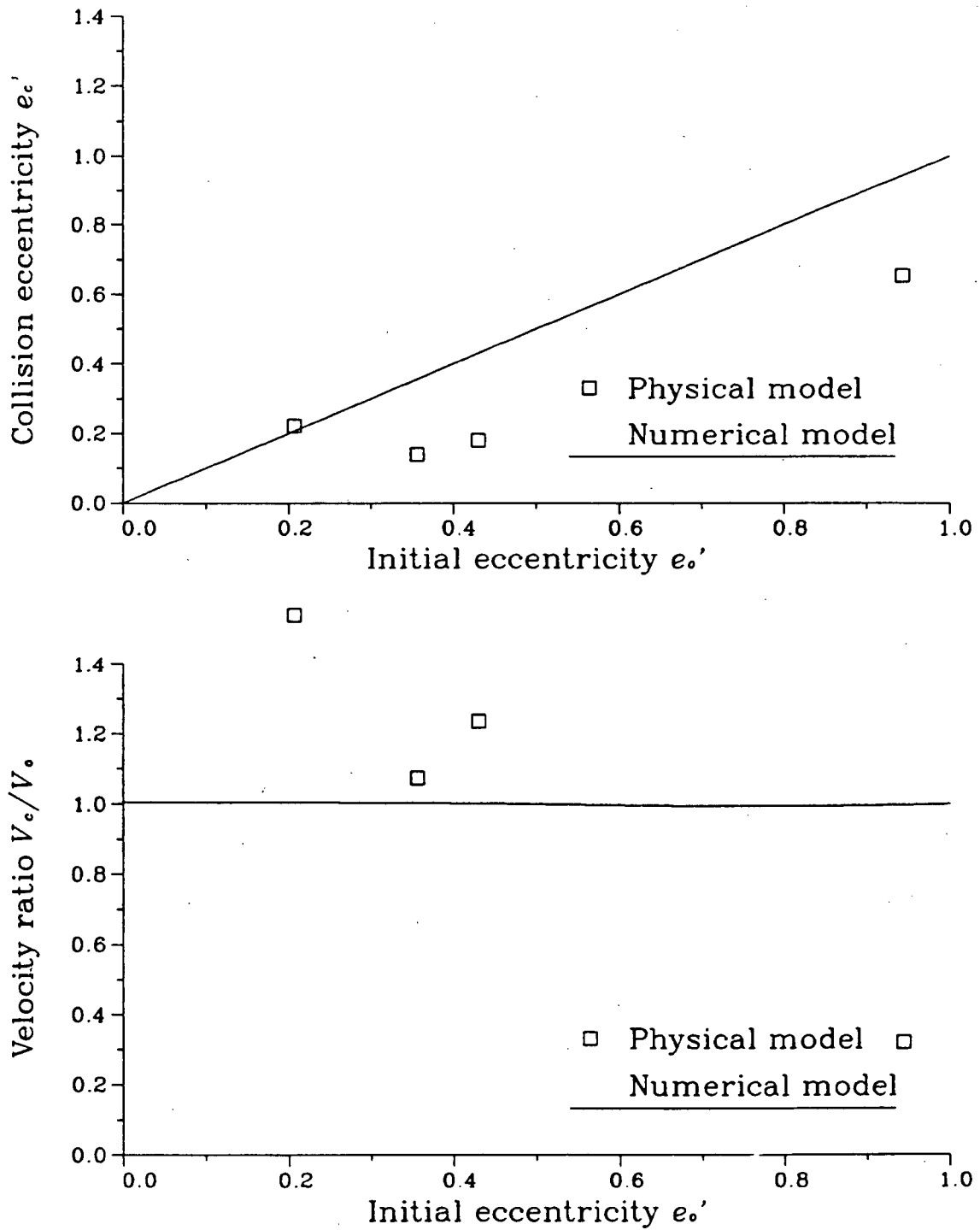


Figure 4.17: Variation of Iceberg Eccentricity and Velocity, Wave Condition 1,  $D_i/D_s = 0.8$

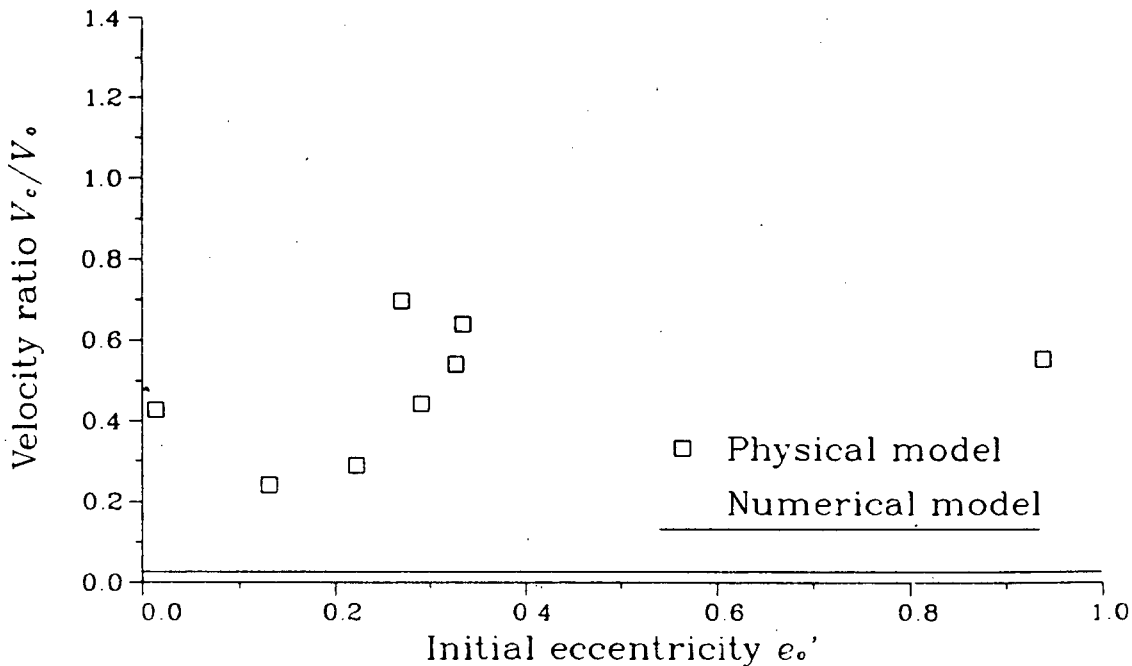
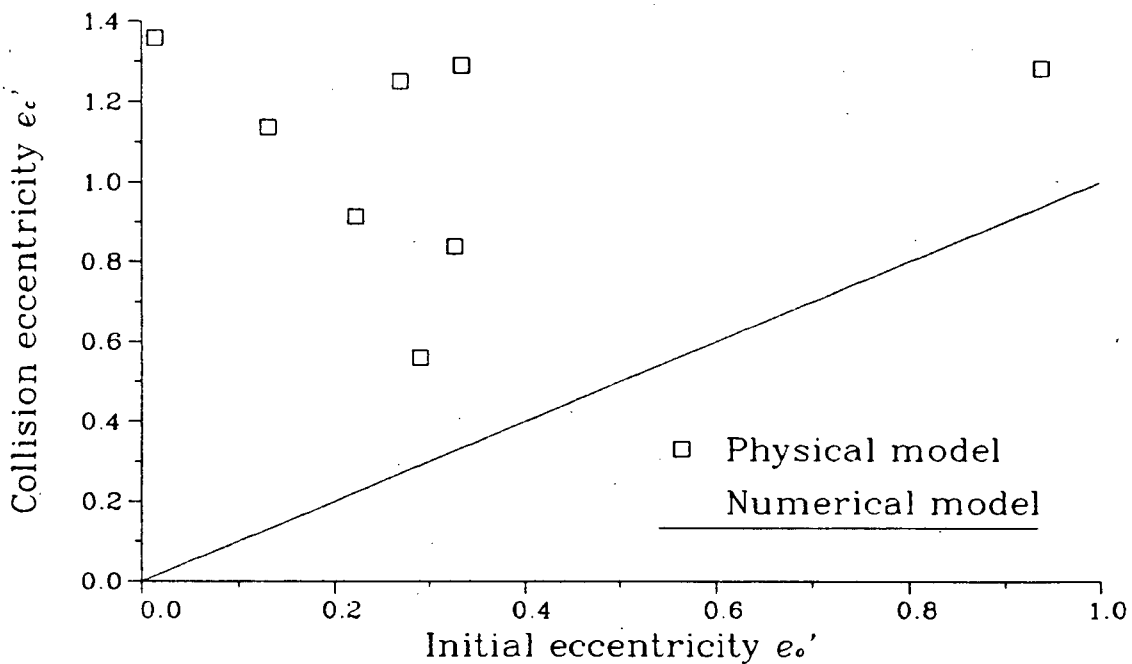


Figure 4.18: Variation of Iceberg Eccentricity and Velocity, Wave Condition 2,  $D_i/D_s = 0.5$

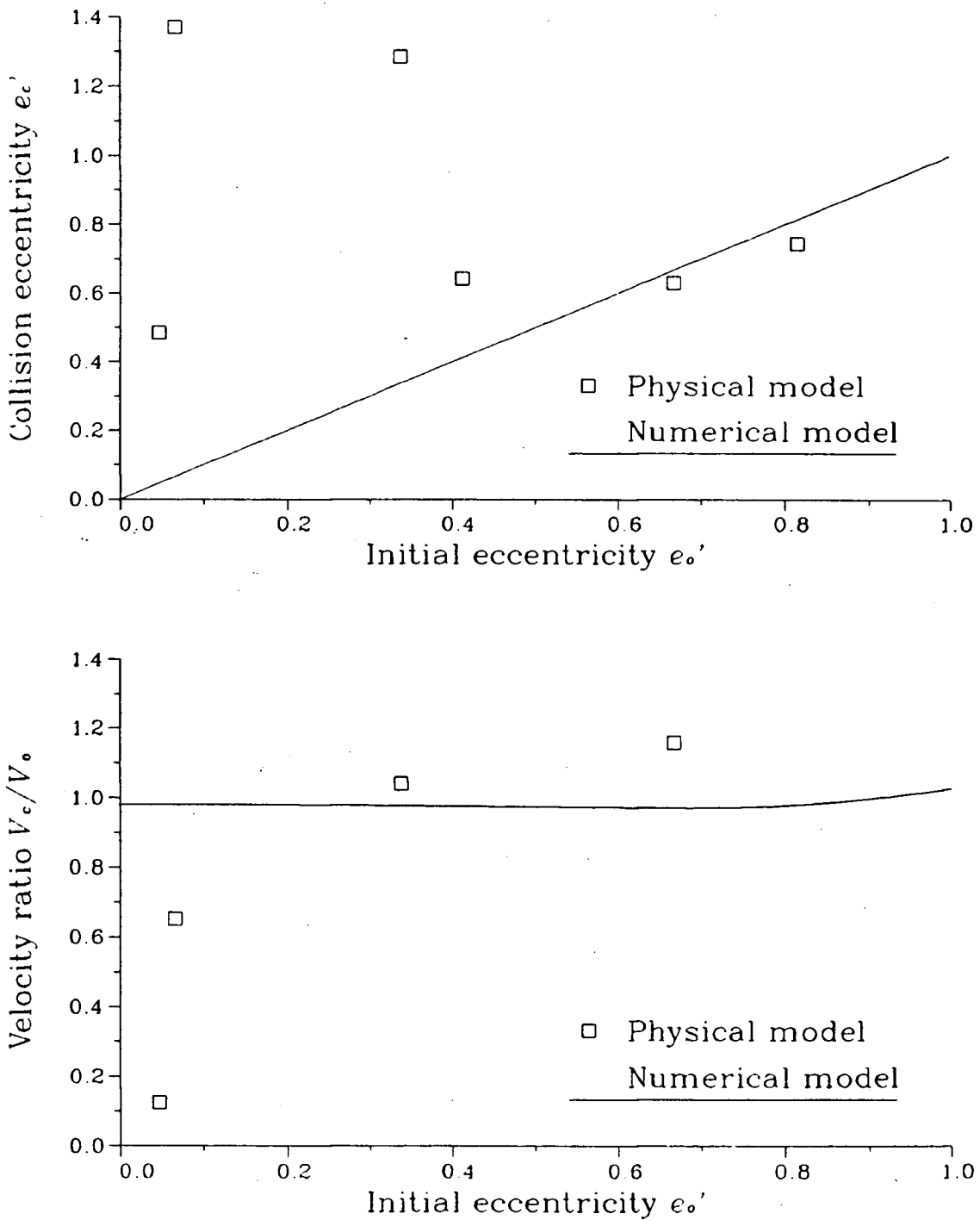


Figure 4.19: Variation of Iceberg Eccentricity and Velocity, Wave Condition 2,  $D_i/D_s = 0.8$

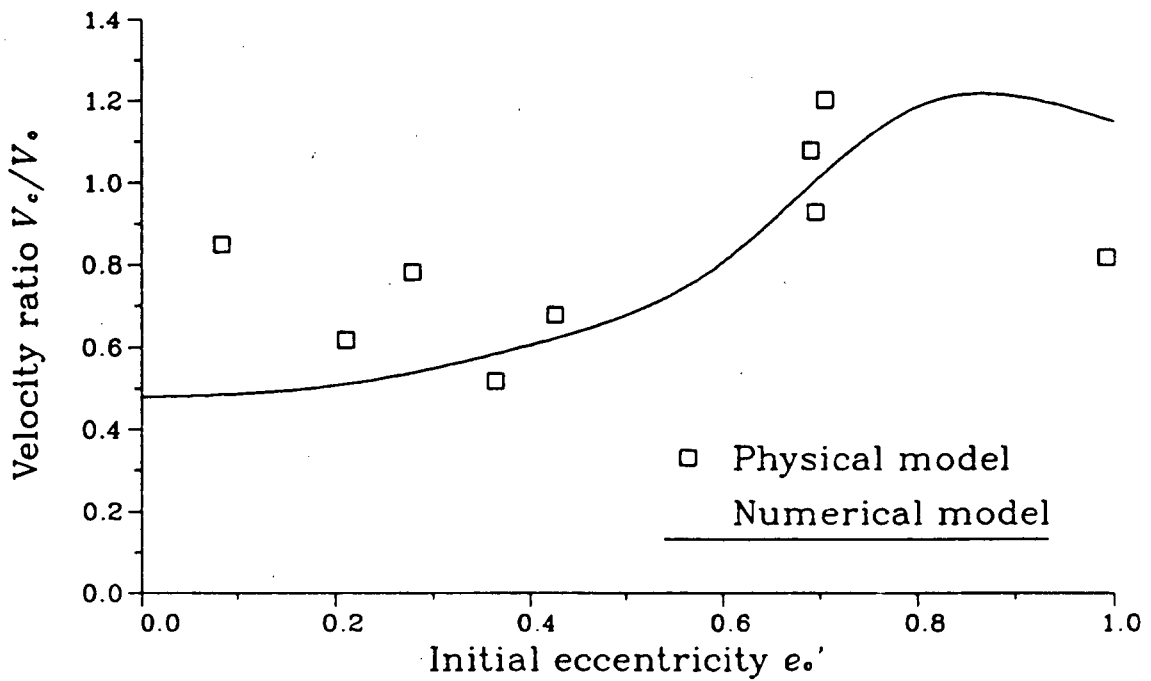
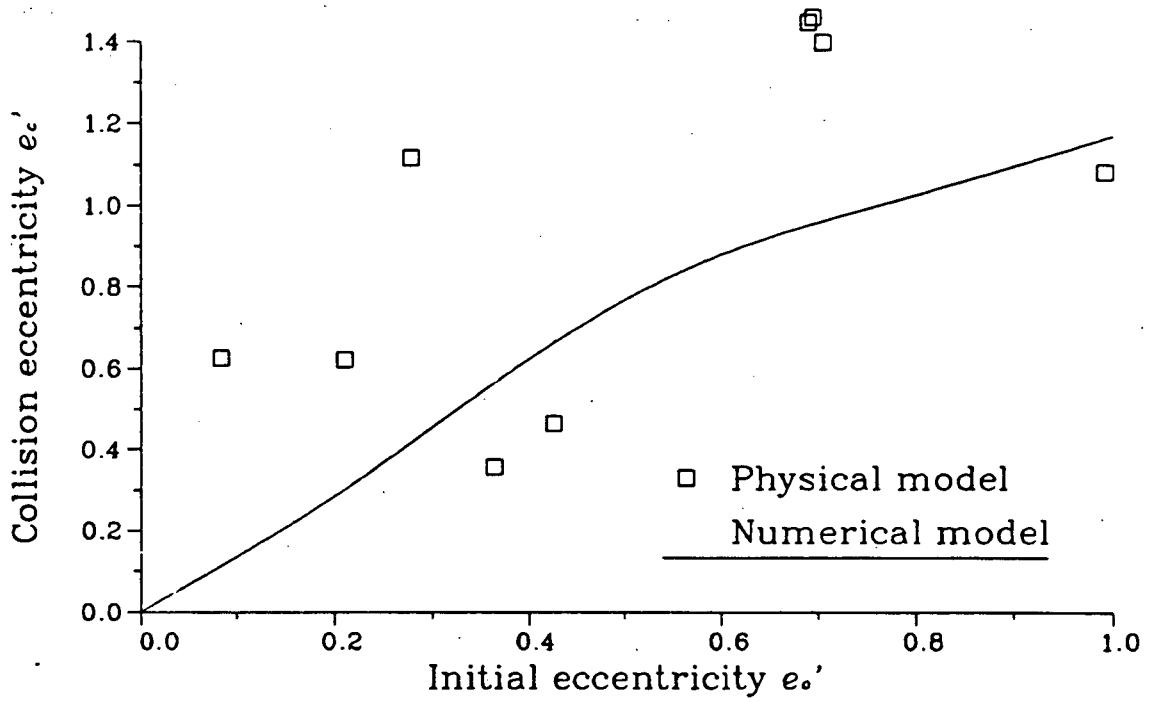


Figure 4.20: Variation of Iceberg Eccentricity and Velocity, Wave-Current Condition 1,  $D_i/D_s = 0.1$

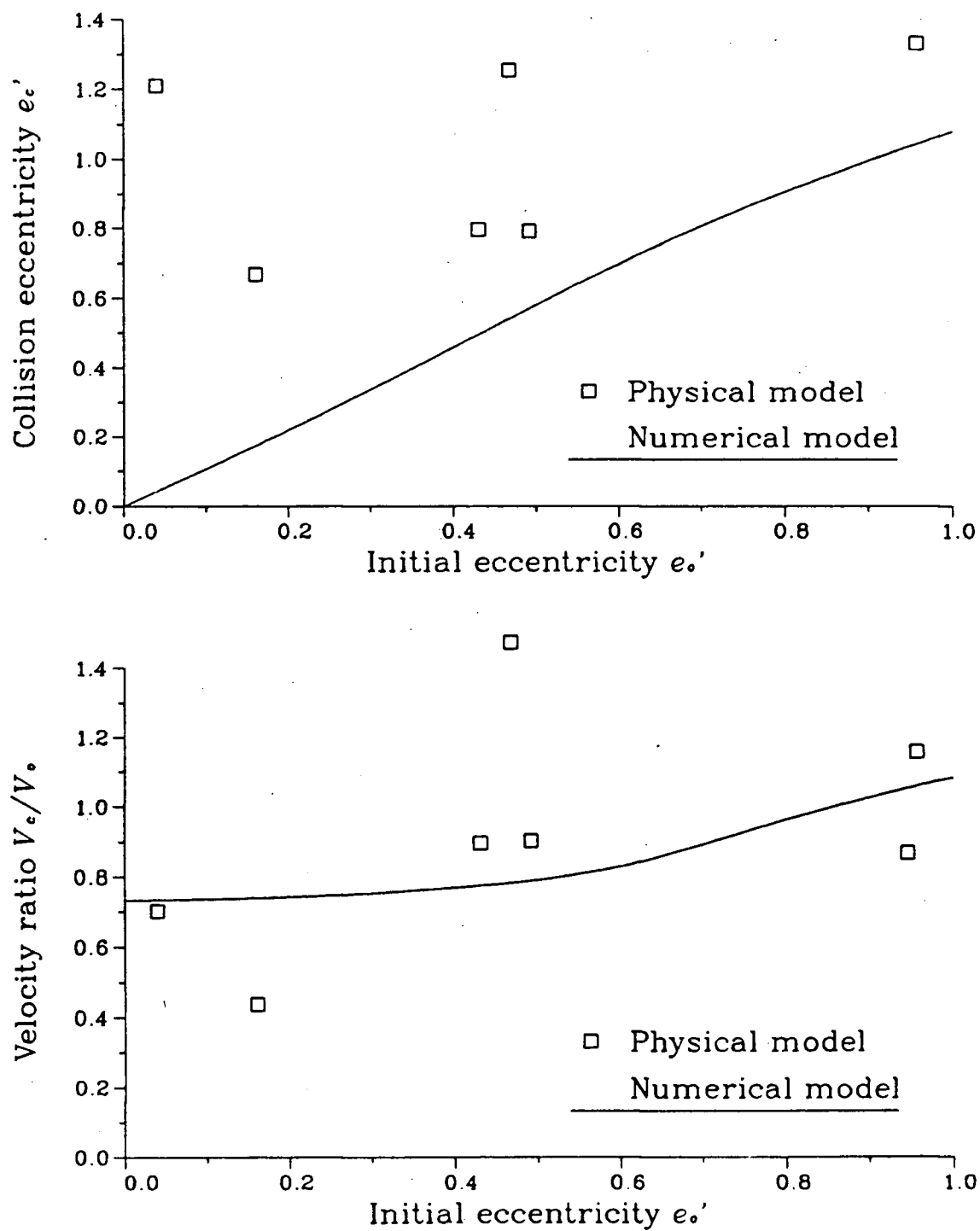


Figure 4.21: Variation of Iceberg Eccentricity and Velocity, Wave-Current Condition 1,  $D_i/D_s = 0.2$

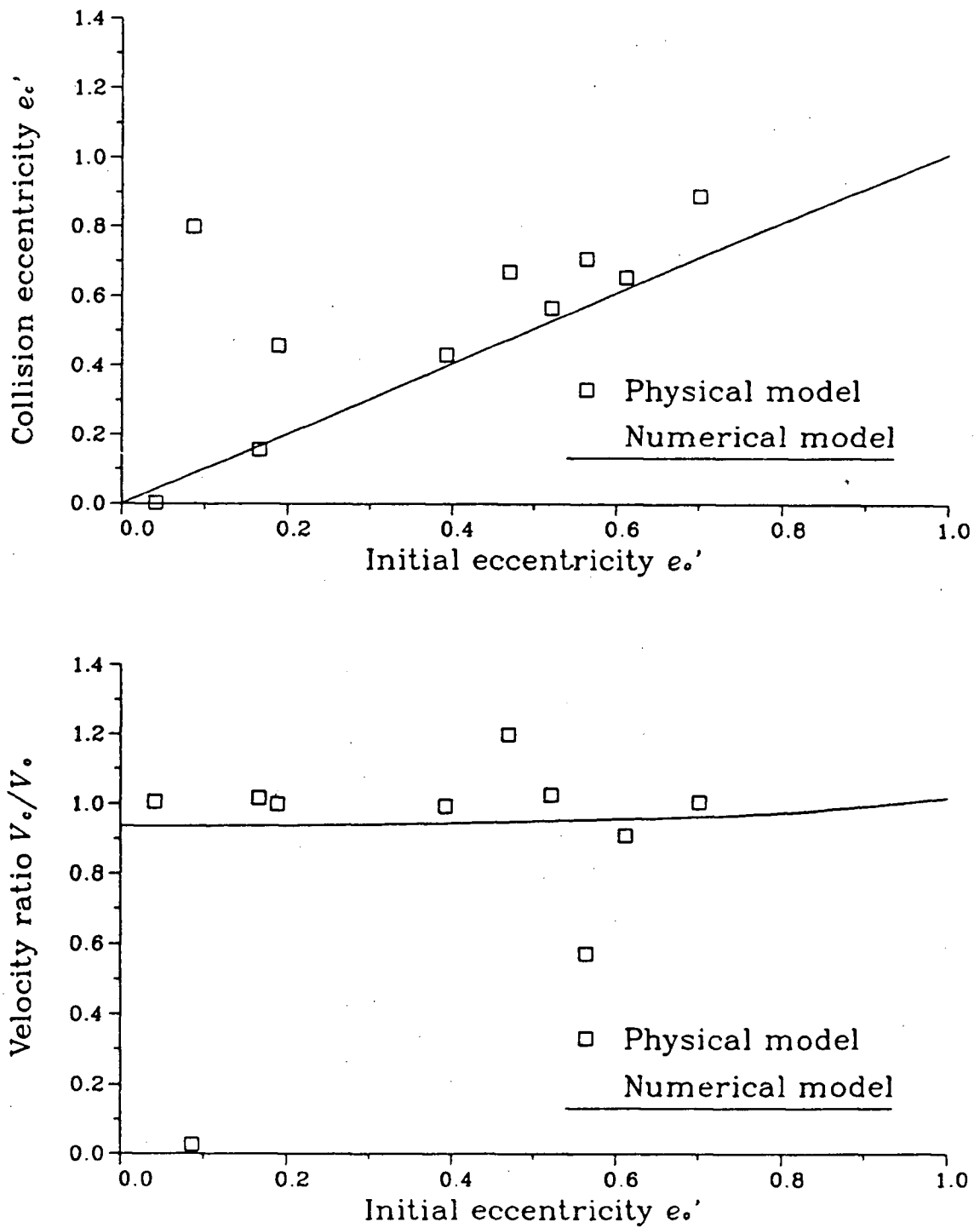


Figure 4.22: Variation of Iceberg Eccentricity and Velocity, Wave-Current Condition 1,  $D_i/D_s = 0.5$

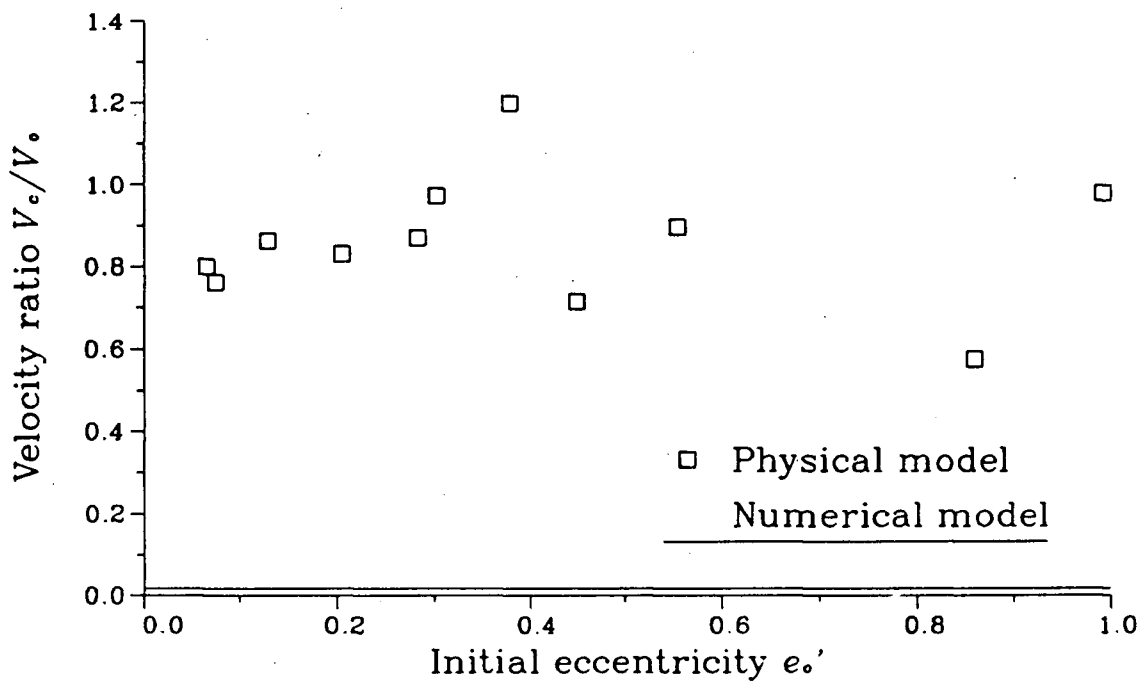
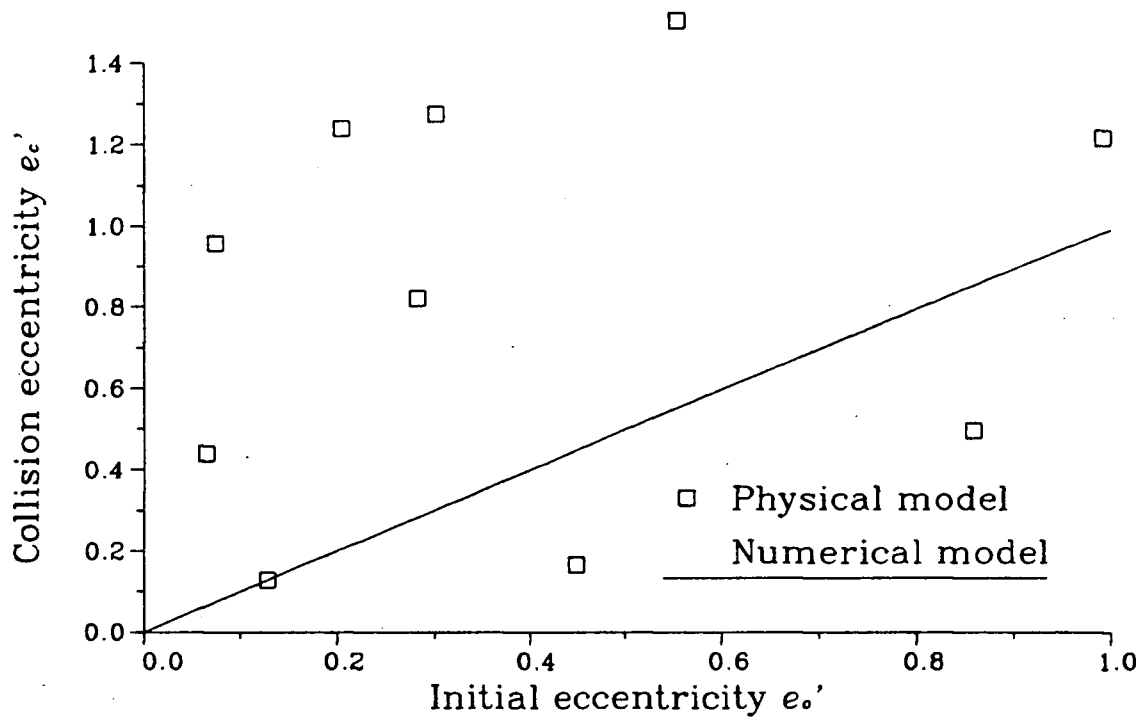


Figure 4.23: Variation of Iceberg Eccentricity and Velocity, Wave-Current Condition 2,  $D_i/D_s = 0.1$

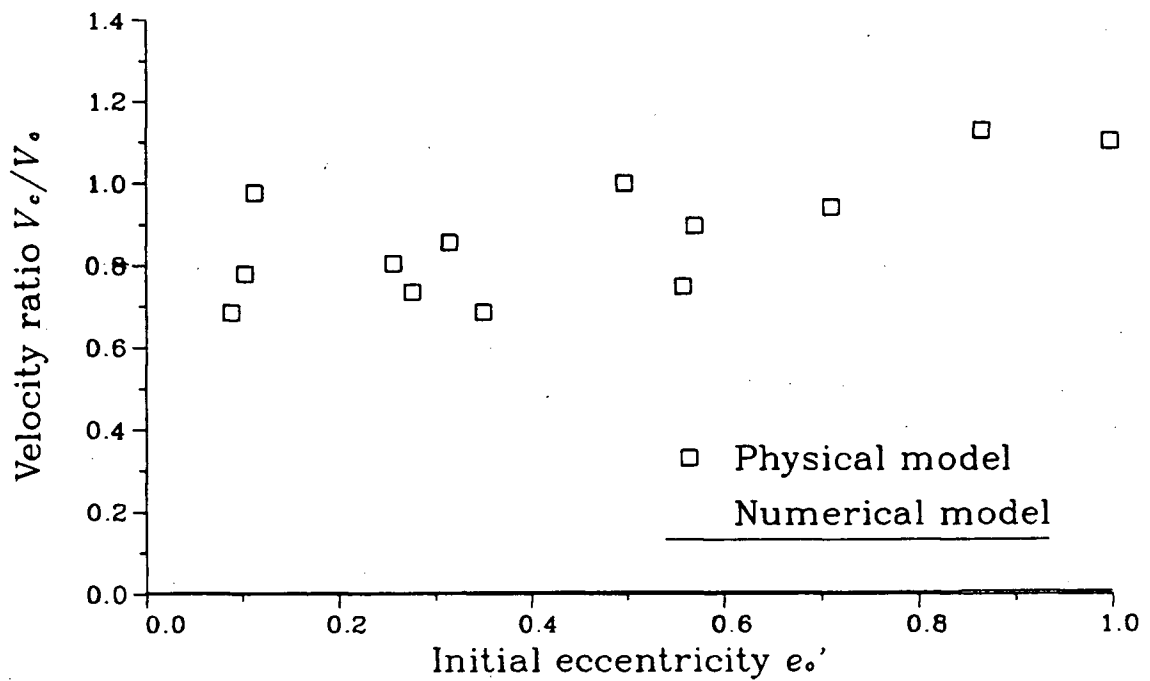
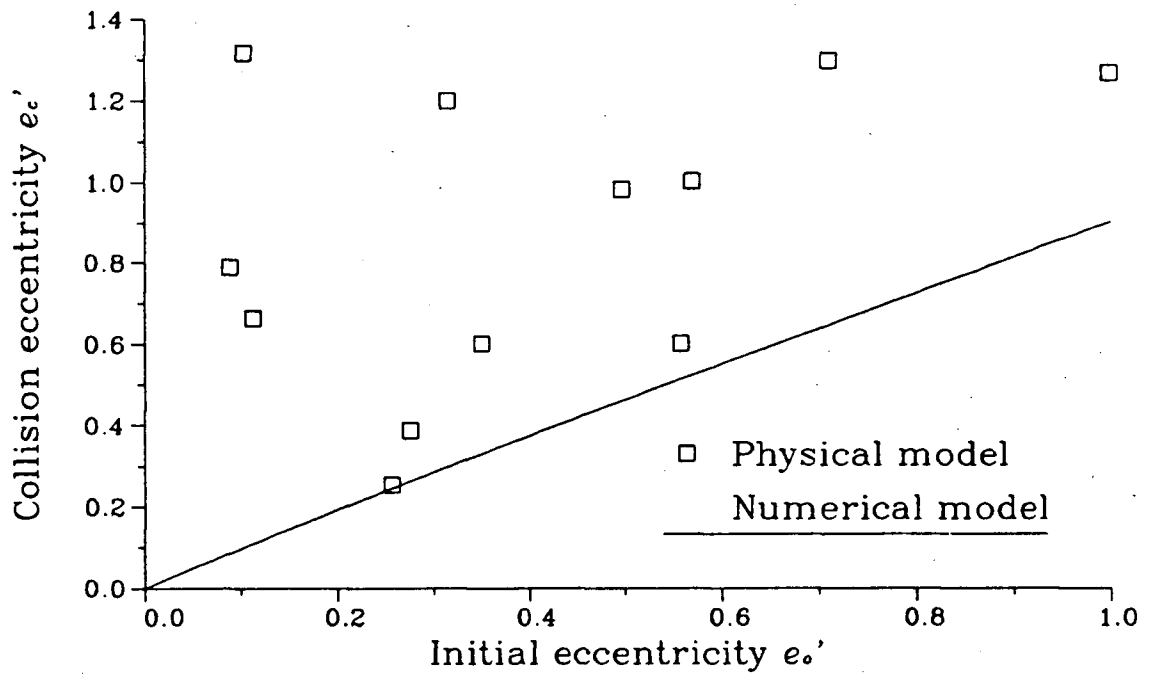


Figure 4.24: Variation of Iceberg Eccentricity and Velocity, Wave-Current Condition 2,  $D_i/D_s = 0.2$

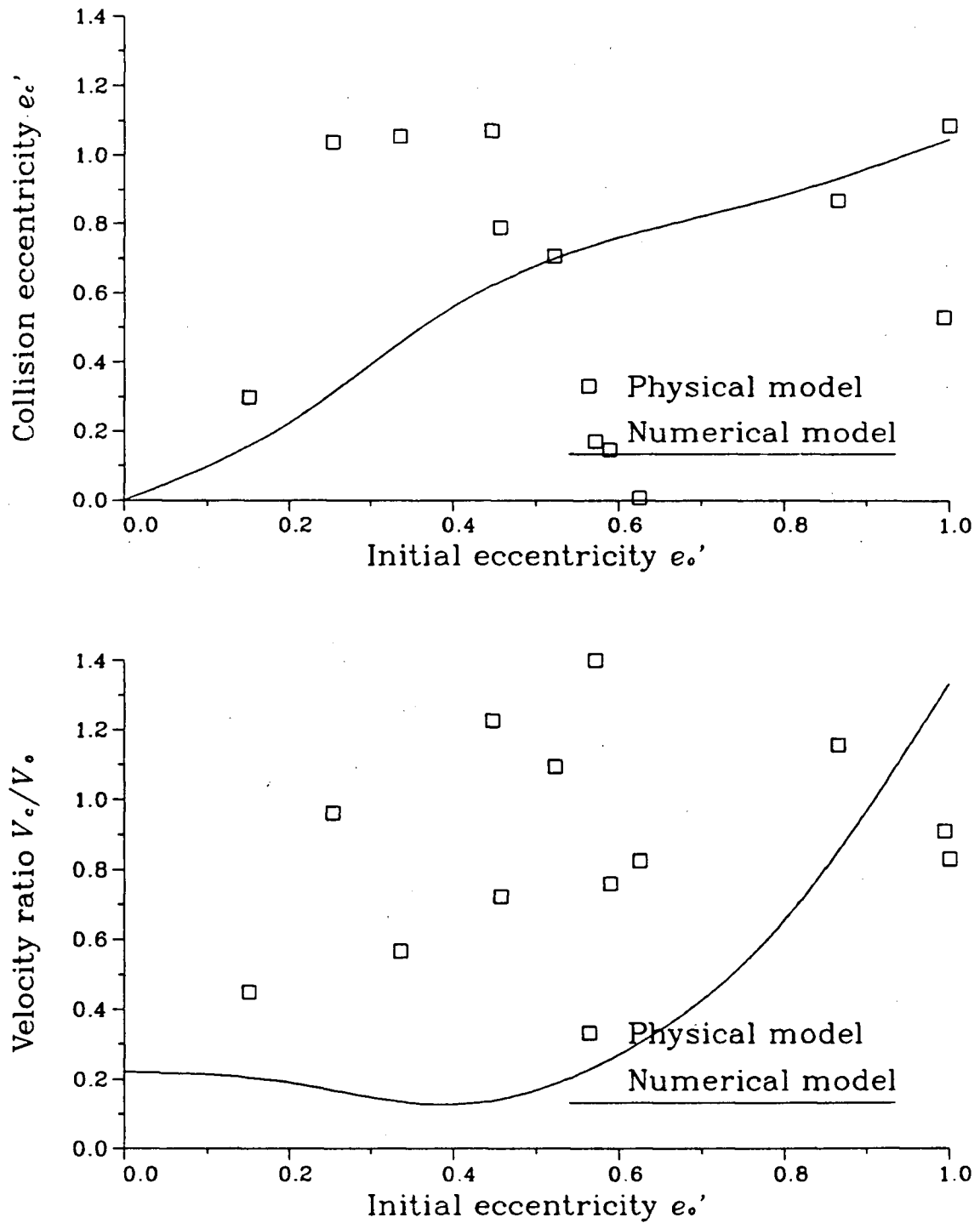


Figure 4.25: Variation of Iceberg Eccentricity and Velocity, Wave-Current Condition 2,  $D_i/D_s = 0.5$

### 4.8.1 Simplified Numerical Drift Model

The simulation of iceberg drift trajectories near the structure could have been most readily accomplished using the program ICEMOT described in Chapter 2. Unfortunately, the number of diffraction computations required to determine wave drift forces near the structure would have made running the model prohibitively expensive. A simplified drift model was developed for simulating the observed experiments.

The main purpose for developing the simplified numerical drift model was to reduce the computational effort required for estimating wave drift forces. Based on the results of Chapter 3, it was assumed that lateral wave drift forces (i.e. perpendicular to the incident wave direction) could be considered negligible. The equations of drift motion could then be written as:

$$(1 + C_m) M a_x = \frac{1}{2} \rho C_d A_w |\vec{V}_w - \vec{V}| (u_w - u) + \frac{1}{2} \rho g C_w D_i H^2 \quad (4.32)$$

$$(1 + C_m) M a_y = \frac{1}{2} \rho C_d A_w |\vec{V}_w - \vec{V}| (v_w - v) \quad (4.33)$$

Wave drift forces for equation 4.32 were determined using the simplified wave drift force equation 3.52. Diffraction computations for each iceberg model and wave condition were made to determine wave drift forces at various locations in front of the structure. Computed wave drift forces are presented in Figures 4.26 - 4.29. Coefficients for the approximate wave drift force equation 3.52 were determined using a least squares fit to values from the diffraction computations, and are shown in Figures 4.30 - 4.33.

Zero frequency added mass coefficients for equations 4.32 and 4.33 were taken from Figure 3.19. It was assumed that added mass was independent of proximity to the structure. Water velocities in the vicinity of the structure were evaluated using the analytical solution for flow around a two dimensional circular cylinder (equation 2.92).

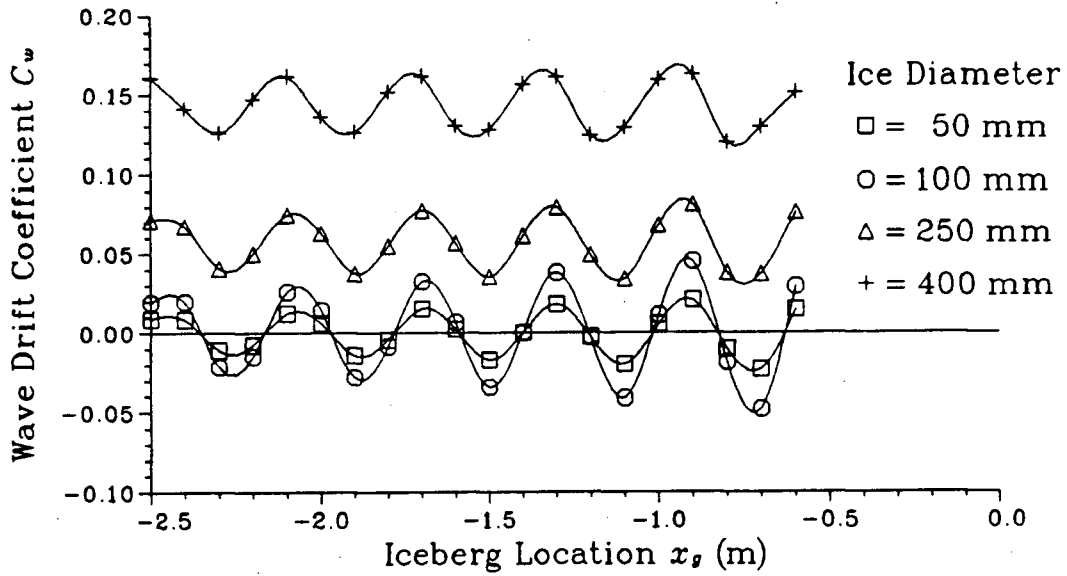


Figure 4.26: Wave Drift Forces in Front of Structure, No Current,  $T = 0.7$  s

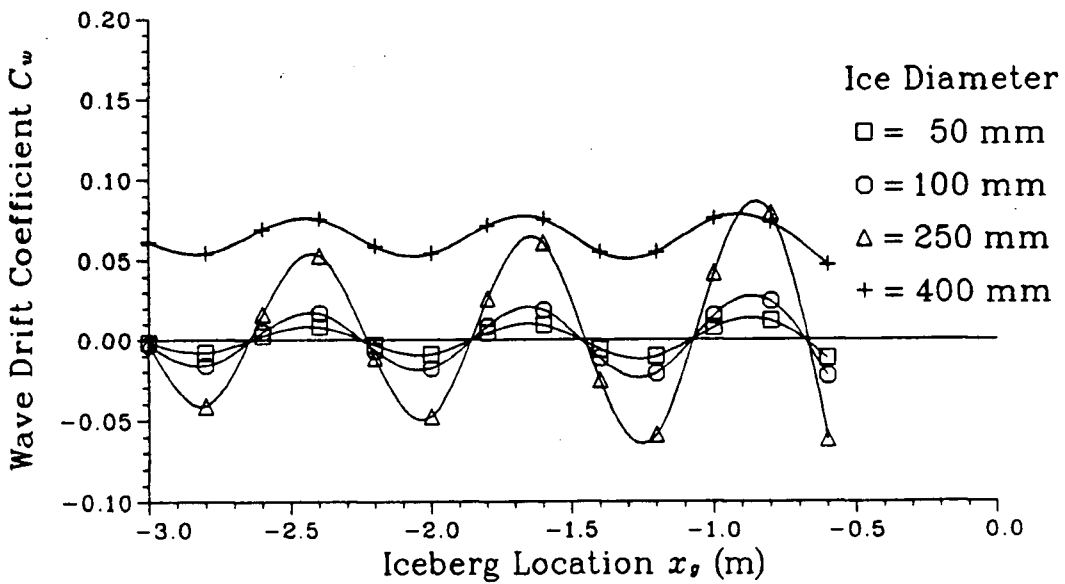


Figure 4.27: Wave Drift Forces in Front of Structure, No Current,  $T = 1.0$  s

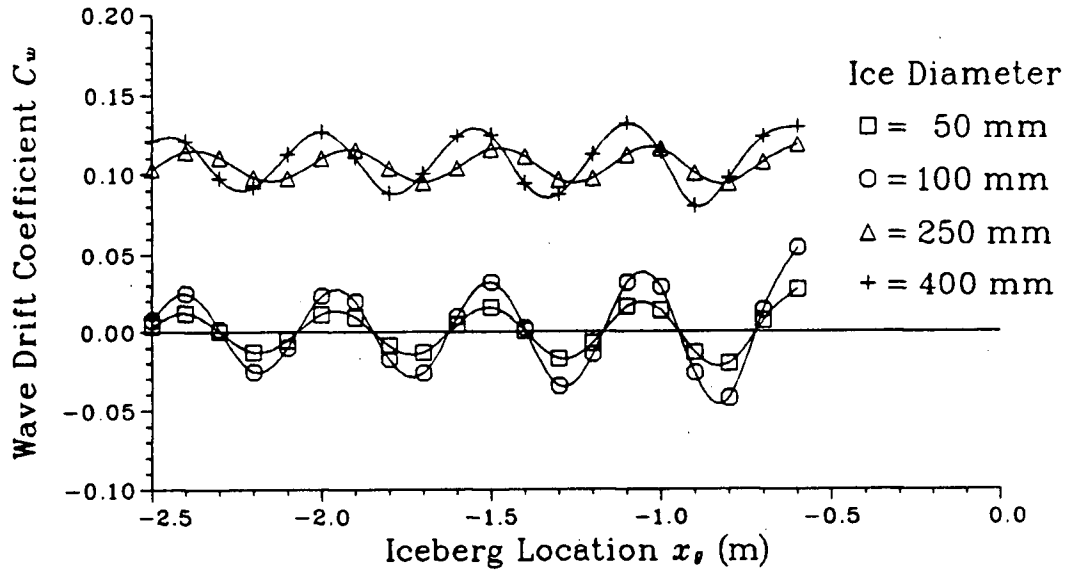


Figure 4.28: Wave Drift Forces in Front of Structure, Current,  $T_c = 0.7$  s

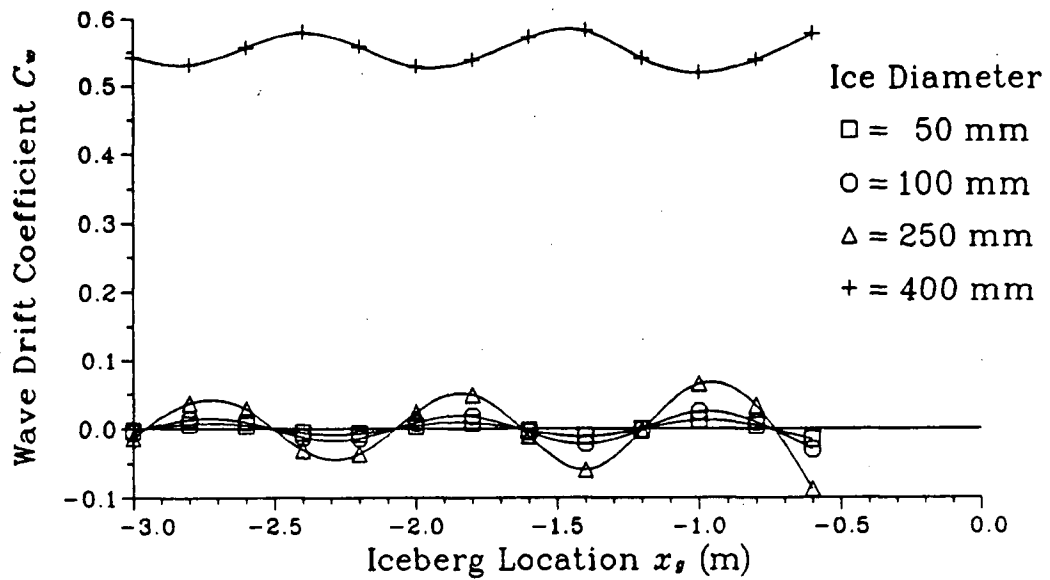


Figure 4.29: Wave Drift Forces in Front of Structure, Current,  $T_c = 1.0$  s

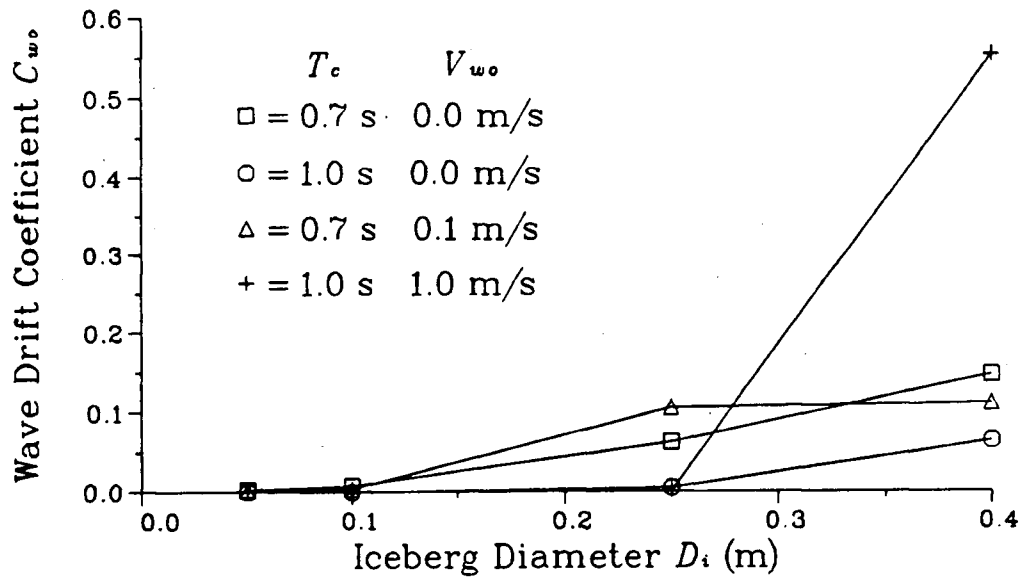


Figure 4.30: Open Water Wave Drift Force Coefficients

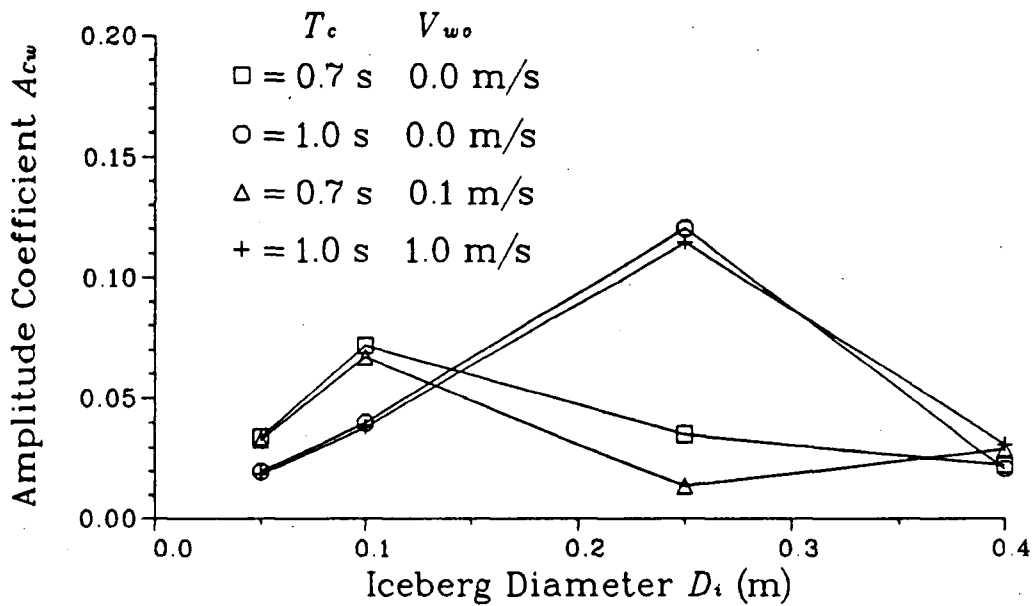


Figure 4.31: Amplitude Coefficient  $A_{C_w}$  for Variation of Wave Drift Forces

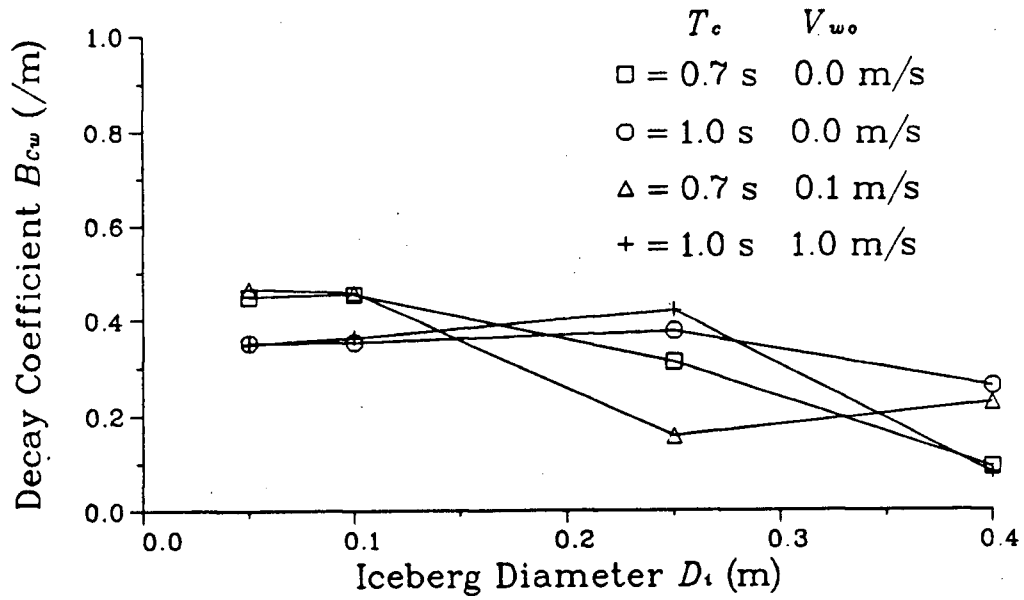


Figure 4.32: Decay Coefficient  $B_{C_w}$  for Variation of Wave Drift Forces

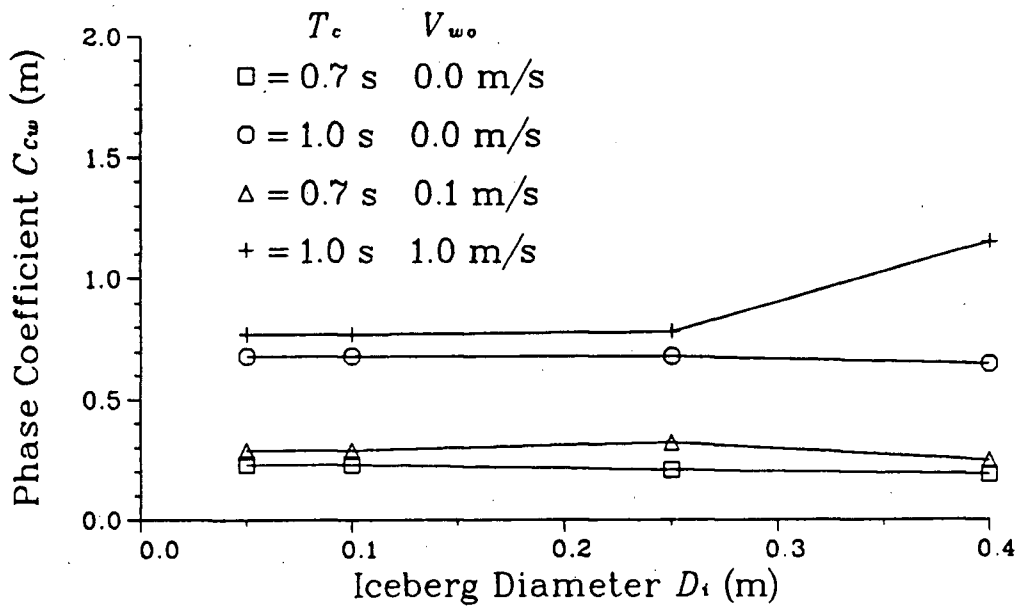


Figure 4.33: Phase Coefficient  $C_{C_w}$  for Variation of Wave Drift Forces

A water drag coefficient value of 0.7 determined by towing tests described earlier was used for all models.

Each iceberg trajectory was evaluated commencing at an  $x_g$  value of  $-3D_s$ , and an initial  $y_g$  value corresponding to the initial dimensionless eccentricity  $e'_o$ . The initial velocity for each iceberg was taken as its open water equilibrium velocity  $V_o$ , taken from equation 3.53 to be as follows:

$$V_o = V_{wo} + \frac{C_{wo}}{|C_{wo}|} H \sqrt{\frac{|C_{wo}| g}{C_d h}} \quad (4.34)$$

A time step interval  $\Delta t$  of 0.1 s was used to evaluate each trajectory until one of the following occurred:

1. The iceberg impacted the structure,
2. The  $x$  velocity component became negative,
3. The iceberg drifted freely past the structure.

The collision velocity  $V_c$  and impact eccentricity  $e_c$  were then evaluated at the final time step.

### 4.8.2 Comparison of Numerical and Physical Models

Output from the numerical model is plotted with the experimental data in Figures 4.12 - 4.25. The experimental data show significant scatter, with experimental trends generally following the predictions of the numerical model. In many cases the numerical model appears to be conservative, under-estimating the collision eccentricity  $e'_c$  and over-estimating the velocity ratio  $V_c/V_o$ .

To provide a quantitative basis for comparing agreement between numerical and physical models, the standard error between values of collision eccentricity and velocity

ratio can be evaluated as follows:

$$\sigma_{e'_c} = \sqrt{\frac{1}{N_{obs}} \sum_{i=1}^{N_{obs}} (e'_N - e'_c)^2} \quad (4.35)$$

$$\sigma_{V_c/V_o} = \sqrt{\frac{1}{N_{obs}} \sum_{i=1}^{N_{obs}} (V_N/V_F - V_c/V_o)^2} \quad (4.36)$$

where:

$N_{obs}$  = number of observation for physical model with  $e'_F \leq 1$

$\sigma_{e'_c}$  = standard error for predicted collision eccentricity

$\sigma_{V_c/V_o}$  = standard error for predicted velocity ratio

Standard errors for collision eccentricities and velocity ratios are presented in Tables 4.6 and 4.7.

Observed trajectories for current driven motions (Figures 4.12 - 4.15) indicate significant increases of approach eccentricities as the icebergs approach the structure. Collision eccentricity predictions by the numerical model tend to be conservative when compared with the experimental results. Observed and numerically modelled iceberg velocities appear to be relatively unaffected by the structure. The 50 mm model exhibits high velocity ratios for  $e'_c > 1$  because of the high water velocities around the sides of the structure.

Agreement between the physical and numerical models is reasonably good for the first wave condition with  $T = 0.7$  s and  $H = 21$  mm (Figures 4.16 and 4.17); however, the numerical model severely under-estimates impact velocities of the 250 mm iceberg for the second wave condition with  $T = 1.0$  s and  $H = 61$  mm (Figure 4.22). Examination of Figure 4.29 indicates that the numerical model predicts that a negative drift force will act on the 250 mm iceberg when it is immediately in front of the structure for a wave period of 1.0 s. The physical model indicates that the velocity of the 250 mm iceberg will be reduced in front of the structure, but not to the same degree as predicted by the numerical model.

Table 4.6: Standard Errors between Numerical and Physical Models for Collision Eccentricity  $e'_c$ 

$D_i/D_s =$	0.1	0.2	0.5	0.8
Currents	0.48	0.46	0.32	0.22
Waves 1 ( $H = 21$ mm)	-	-	0.58	0.22
Waves 2 ( $H = 61$ mm)	-	-	0.84	0.69
Wave-currents 1 ( $H = 19$ mm)	0.43	0.65	0.26	-
Wave-currents 2 ( $H = 59$ mm)	0.79	0.64	0.47	-

Table 4.7: Standard Errors between Numerical and Physical Models for Velocity Ratio  $V_c/V_o$ 

$D_i/D_s =$	0.1	0.2	0.5	0.8
Currents	0.23	0.11	0.14	0.09
Waves 1 ( $H = 21$ mm)	-	-	0.27	0.45
Waves 2 ( $H = 61$ mm)	-	-	0.48	0.60
Wave-currents 1 ( $H = 19$ mm)	0.20	0.30	0.33	-
Wave-currents 2 ( $H = 59$ mm)	0.86	0.88	0.67	-

Figures 4.20 - 4.22 indicate that the physical and numerical models are in relatively good agreement for the first wave-current condition ( $T_c = 0.7$  s,  $H = 19$  mm). For the second wave-current condition ( $T_c = 1.0$  s,  $H = 59$  mm), the large waves have a more dominant influence on iceberg motions (Figures 4.23 - 4.25). Collision velocities predicted by the numerical model are reduced to nearly zero because of negative wave drift forces in front of the structure, as shown in the diffraction computations of Figure 4.29.

### 4.8.3 Comparison of Open Water Velocities for Wave Driven Motions

The results presented above indicate that significant discrepancies exist between the physical and numerical models when predicting velocities for wave driven drift motions. To examine the agreement between the numerical and physical models for the case of no structure, open water drift velocities for wave driven motions have been evaluated using equation 4.34 and compared with observed far-field velocities from the experiments. Although the observed far-field velocities were somewhat affected by the presence of the structure, they provide a useful source for comparison with predicted open water velocities.

The open water drift velocities presented in Tables 4.8 and 4.9 show a high degree of variation of observed drift velocities among tests. The coefficient of variation for the drift velocity of a given model and wave condition is typically greater than 30%, and cannot be explained by digitizing or other errors. Consistent drift velocities were observed only for the iceberg with  $D_i/D_s = 0.5$ . This was also the only iceberg for which good agreement was obtained between the numerical and physical models.

Table 4.8: Comparison of Open Water Drift Velocities for First Wave Condition,  $T = 0.7$  s,  $H = 21$  mm

$D_i/D_s =$	0.1	0.2	0.5	0.8
Number of Tests	6	2	5	5
Mean Observed $V_f$ (m/s)	.008	.012	.049	.027
Standard Deviation of $V_f$ (m/s)	.004	.010	.009	.012
Wave Drift Coefficient $C_{wo}$	.00295	.00736	.06242	.14682
Predicted $V_o$ (m/s)	.026	.030	.054	.068

Table 4.9: Comparison of Open Water Drift Velocities for First Wave Condition,  $T = 1.0$  s,  $H = 61$  mm

$D_i/D_s =$	0.1	0.2	0.5	0.8
Number of Tests	9	8	9	8
Mean Observed $V_f$ (m/s)	.012	.024	.055	.044
Standard Deviation of $V_f$ (m/s)	.004	.005	.005	.017
Wave Drift Coefficient $C_{wo}$	-0.00015	-0.00026	.00514	.06447
Predicted $V_o$ (m/s)	-0.017	-0.016	.045	.131

#### 4.8.4 Sources of Discrepancies between Physical and Numerical Models

For iceberg motions driven by currents, it is likely that convective forces had a significant influence on the eccentricity of the icebergs as they approached the structure. As indicated in Chapter 2, convective forces will cause smaller icebergs to travel as water particles, thus causing the icebergs to drift around the side of the structure rather than to impact the structure. Neglecting convective forces in the numerical model was the most probable cause of the under-estimates of impact eccentricities for current driven motions.

Discrepancies between the physical and numerical models are greatest when wave drift forces acting on an iceberg vary significantly with proximity to the structure. One possible explanation can be developed by examining the computed wave drift forces in Figures 4.26 - 4.29. The wave drift force acting on an iceberg at a given location is highly dependent on the wave frequency  $\omega_c$  and the incident current velocity  $V_{wo}$ . The frequency of waves relative to the iceberg will vary with the drift velocity of the iceberg; thus, wave drift forces are likely to be significantly influenced by iceberg drift motions. The influence of drift motions on wave drift forces is not included in the numerical diffraction model.

The evaluation of wave drift forces using the far-field method by the program ICE-MOT could also be a source of significant errors. A major assumption of the far-field method is that the rotational orientation of a floating body about the  $x'$  and  $y'$  axes (i.e. pitch and roll) will vary negligibly during a given wave cycle; however, Pinkster [96] has noted that the oscillatory pitch and roll motions of a body in low frequency waves can be sufficiently large to affect wave drift force significantly. This effect would be most pronounced for the smaller icebergs of the present investigation whose wave-induced oscillatory motions are relatively large, thus resulting in significant variation of the iceberg

rotational orientation and corresponding geometry during a given wave cycle.

## Chapter 5

# Selection of a Design Collision Event Based on Iceberg Kinetic Energy

The development of environmental loading criteria is a key aspect in the design of offshore structures, with the selection of design loads most commonly done using probabilistic methods (see Vanmarke and Angelides [113]). Design load levels are associated with long return periods (e.g. 100 years) and/or acceptably low exceedence probabilities during the operating life of a structure (e.g. 10%). Probabilistic methods for evaluation of design iceberg collisions have been developed by Maes et al. [69] and Salvalaggio and Rojansky [99]. Collision velocities for both of these models are based primarily on iceberg drift velocities. To account for wave-induced motions of smaller icebergs, Salvalaggio and Rojansky applied a correlation coefficient of -0.4 between iceberg diameter and velocity.

The incorporation of wave-induced motions into iceberg velocity statistics has been examined by Lever and Sen [60]. Using wave climate data and the surge response transfer function for a given iceberg, the oscillatory velocity probability density function (PDF) for the iceberg can be evaluated. Although this technique can be used to obtain the velocity PDF for a given iceberg, it appears to have limited application for the evaluation of design loads.

A new approach for the selection of a design iceberg collision event is discussed in the present chapter. The load level associated with the design event is based on an

acceptably low exceedence probability. A key aspect of the proposed model is its inclusion of wave-induced iceberg motions, which are computed using linear wave diffraction theory. Results from the model can be used to examine the importance of wave-induced motions for a design collision event.

## 5.1 Design Criteria for Iceberg Collisions

The nature of a design collision will depend on the following two factors:

1. Exceedence probability associated with the design event,
2. Criterion used for ranking collision severity.

The specified exceedence probability can be based on various factors, such as the consequences of structural failure. The magnitude of the design load will increase as the specified acceptable exceedence probability decreases. Guidelines for acceptable exceedence probabilities are given in various design codes such as the Canadian Standards Association (CSA) *Code for the Design, Construction, and Installation of Fixed Offshore Structures* [15]. For design against iceberg collisions, the CSA code recommends that the design iceberg load should have an annual exceedence probability between  $10^{-4}$  and  $10^{-2}$ , depending on the structure safety class and location.

The design event will also depend on the method used for ranking collision severity. Iceberg kinetic energy and impact force are two alternative criteria which can be used for ranking collision severity. Evaluation of impact force requires that structure properties be known; thus, determination of a design event based on impact force is most suited to the final stages of design. Iceberg kinetic energy is a useful ranking criterion for preliminary design, and can be expressed as follows:

$$KE = \frac{1}{2} (1 + C_m) M V_c^2 \quad (5.1)$$

where:

$C_m$  = added mass coefficient

$KE$  = iceberg kinetic energy (Joules)

$M$  = iceberg mass (kg)

$V_c$  = iceberg impact velocity (m/s)

Hydrodynamic interactions between a structure and approaching icebergs are neglected when evaluating equation 5.1 in the present design model. Studies by Isaacson and Dello Stritto [48] and Salvalaggio and Rojansky [99] indicate that the presence of a large structure will reduce impact velocities of smaller icebergs; thus, neglecting hydrodynamic interactions will likely yield conservative results.

## 5.2 Description of Second-Order Reliability Method

The second-order reliability method (SORM) was selected for evaluating kinetic energy exceedence probabilities because of its high degree of efficiency for analysis of complex systems. A general description of the method is given by Madsen et al. [67]. Application of the second-order reliability method was carried out using the computer program RELAN developed by Foschi [30]. In addition to being very efficient, the second-order reliability method gives output parameters which are very useful in engineering design. In the present context, the SORM model gives the most probable values of input random variables (e.g. iceberg mass and drift velocity) for a given kinetic energy level. Sensitivity coefficients for input random variables are useful indicators of the relative importance of each variable in determining iceberg kinetic energy.

### 5.2.1 Introduction of Failure Function

The second-order reliability method is most commonly used to estimate the probability of structural failure, which is expressed in terms of a failure function  $G(\vec{X})$ . The relationship between the probability of structural failure and the failure function is as follows:

$$P(\text{failure}) = P(G(\vec{X}) < 0) \quad (5.2)$$

$$= \int_{G(\vec{X} < 0)} f_{\vec{X}}(\vec{X}) d\vec{X} \quad (5.3)$$

where:

$f_{\vec{X}}(\vec{X})$  = joint probability density function of  $\vec{X}$

$G(\vec{X})$  = failure function

$\vec{X}$  = vector of input random variables

The probability of failure is estimated using an approximate solution to the integral of equation 5.3. The following guidelines should be followed when formulating the failure function  $G(\vec{X})$ :

1. Statistical distributions for each of the input random variables should be known or easily obtainable,
2. Input random variables should ideally be independent, or have low correlation coefficients,
3. Combinations of input random variable values which defy prescribed physical constraints should not be possible.

With regard to condition 2 above, it should be noted that correlation coefficients between input random variables can be given as input to the reliability model. However,

correlation coefficients are only representative of the degree of linear dependence between variables and cannot adequately describe non-linear relationships between random variables.

### 5.2.2 Solution in Standard Normal Space

Due to computational limitations, the integral of equation 5.3 is not suited to direct evaluation but must instead be solved approximately. The following transformation is used so that the failure function can be expressed in terms of a vector of independent, standard normal variables:

$$\{Y\} = [T] \{X\} \quad (5.4)$$

where:

$[T]$  = transformation matrix

$\{Y\}$  = transformed vector of independent, standard normal variables

An example of the resulting standard space for two input variables is shown in Figure 5.1. The failure probability of equation 5.3 can be expressed in terms of the new standard space:

$$P(\text{failure}) = \int_{G(\vec{Y}) < 0} \phi(Y_1) \phi(Y_2) \phi(Y_3) \dots \phi(Y_{N_{rv}}) d\vec{Y} \quad (5.5)$$

where:

$N_{rv}$  = number of input random variables

$\phi(Y_i)$  = probability density function for standard normal distribution

### 5.2.3 Failure Probability for Linearized Failure Surface

Evaluation of the integral of equation 5.5 is greatly simplified if the failure surface  $G(\vec{Y}) = 0$  is approximated by a first-order Taylor series expansion about a design point

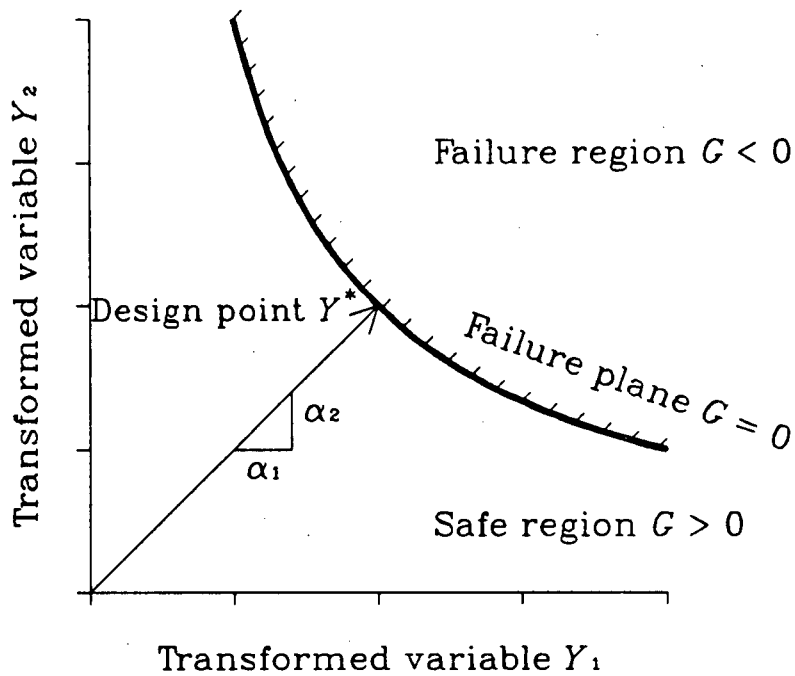


Figure 5.1: Standard Space for 2 Random Variables

$\{Y^*\}$  located on the failure plane. The selected linearization point  $\{Y^*\}$  is the most probable occurrence of  $\{Y\}$  given  $G(\vec{Y}) = 0$ . In terms of the standard space of Figure 5.1, the design point  $\{Y^*\}$  is the point on the failure plane which is closest to the origin of the standard space.

Solution of the design point is solved using an iterative procedure given by Madsen et al. [67]:

$$\{Y^*\}_{j+1} = (\{Y^*\}_j^T \{G(\vec{Y}^*)_j\} - G(\vec{Y}^*)_j) \frac{1}{|\{G'(\vec{Y}^*)_j\}|^2} \{G'(\vec{Y}^*)_j\} \quad (5.6)$$

where:

$\{G'(\vec{Y}^*)\}$  = vector of first-order partial derivatives of  $G$

The origin of the standard space is commonly taken as a starting point for the above equation, with convergence to the design point  $\{Y^*\}$  typically obtained within a few iterations.

Once the design point  $\{Y^*\}$  has been found, the reliability index  $\beta$  and associated failure probability can be determined. The reliability index can be expressed in terms of the effective mean and standard deviation of the failure function at the design point:

$$\beta = \frac{\mu_G}{\sigma_G} \Big|_{\{Y^*\}} \quad (5.7)$$

where:

$\beta$  = reliability index

$\mu_G$  = effective mean value of failure function

$\sigma_G$  = effective standard deviation of failure function

Since the variables  $Y_i$  are independent and standard normal,  $\beta$  is easily found from  $\{Y^*\}$ :

$$\beta^2 = \sum_{i=1}^{N_{rv}} Y_i^{*2} \quad (5.8)$$

The design point values also yield sensitivity coefficients which indicate the relative importance of the random variables. The sensitivity coefficients are evaluated by:

$$\{\alpha^*\} = \frac{1}{\beta} \{Y^*\} \quad (5.9)$$

The sensitivity coefficients are useful indicators of which variables are dominant in causing structural failure.

## 5.2.4 Failure Probability for Curved Failure Surface

The linearization of the failure surface  $G(\vec{Y}) = 0$  can introduce significant error in the evaluation of the failure integral of equation 5.5. Figure 5.2 illustrates two cases where failure probabilities are over-estimated and under-estimated respectively.

An improved estimate of failure probability can be obtained based on the following second-order expansion about the design point  $\{Y^*\}$ :

$$G(\vec{Y}) = G(\vec{Y}^*) + \{G'(\vec{Y}^*)\}^T \{Y - Y^*\}$$

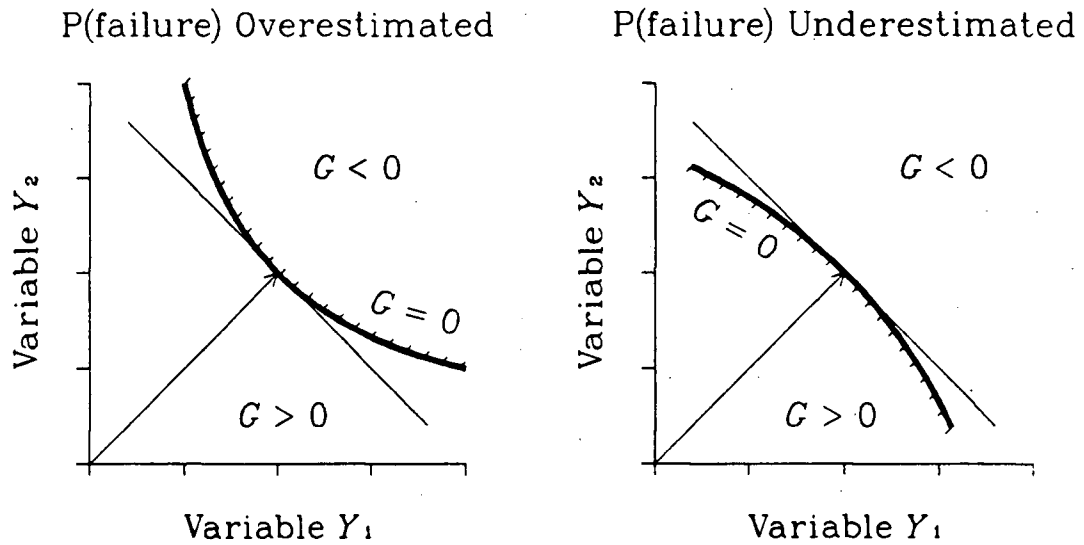


Figure 5.2: Influence of Curved Failure Surface

$$+ \frac{1}{2} \{Y - Y^*\}^T [G''(\vec{Y}^*)] \{Y - Y^*\} \quad (5.10)$$

where:

$[G''(\vec{Y}^*)]$  = matrix of second-order partial derivatives of  $G$

Utilization of the curved failure surface is simplified by making an orthogonal transformation from  $\vec{Y}$  to a new vector space  $\vec{Z}$  containing  $\vec{\alpha}^*$  as a unit normal vector. The orthogonal transformation is made using matrix  $[H]$ , which contains  $\vec{\alpha}^*$  as its  $n$ 'th row:

$$\{Z\} = [H]^{-1} \{Y\} \quad (5.11)$$

where:

$[H]$  = transformation matrix

$\{Z\}$  = vector in transformed space

The failure surface in the transformed co-ordinate system is approximated to second-order

by:

$$Z_n = \beta + \{Z'\}^T [C] \{Z'\} \quad (5.12)$$

Terms in the above equation are:

$$\{Z'\} = (Z_1, Z_2, \dots, Z_{N_{rv}-1}) \quad (5.13)$$

$$C_{ij} = \frac{-1}{2 \left| \{G'(\vec{Y})\} \right|} \left( [H][G''(\vec{Y})][H] \right)_{ij} \quad i, j = 1, 2, \dots, N_{rv} - 1 \quad (5.14)$$

Various methods are available for solving the failure probability associated with the second-order failure surface of equation 5.12. The following solution by Tvedt [111] is used by the computer program RELAN:

$$P(G < 0) = A_1 + A_2 + A_3 \quad (5.15)$$

$$A_1 = \Phi(-\beta) \det([I] + 2\beta [C])^{-1/2} \quad (5.16)$$

$$A_2 = (\beta \Phi(-\beta) - \phi(\beta)) \times \\ \left( \det([I] + 2\beta [C])^{-1/2} \right. \\ \left. - \det([I] + 2(\beta + 1)[C])^{-1/2} \right) \quad (5.17)$$

$$A_3 = (\beta + 1) (\beta \Phi(-\beta) - \phi(\beta)) \times \\ \left( \det([I] + 2\beta [C])^{-1/2} \right. \\ \left. - \operatorname{Re} \left\{ \det([I] + 2(\beta + i)[C])^{-1/2} \right\} \right) \quad (5.18)$$

where:

$[I]$  = identity matrix

$\phi(\beta)$  = PDF of standard normal distribution

$\Phi(\beta)$  = CDF of standard normal distribution

Results from equation 5.15 are typically very close to those obtained assuming a flat failure surface.

### 5.2.5 SORM Solution for Dependent, Non-Normal Variables

The SORM solution presented thus far is limited to the case of independent, standard normal variables. For practical applications, a method is required for dealing with input random variables that are dependent and have various distribution types. A solution can be obtained by transforming the input random variables  $\{X\}$  to the standard space set  $\{Y\}$  as given by Der Kiureghian and Liu [21]:

$$\{Y\} = [\Gamma_0] [D']^{-1} \{X - M'\} \quad (5.19)$$

where:

$[D']$  = diagonal matrix of effective standard deviations for  $\{X\}$

$\{M'\}$  = vector of effective means for  $\{X\}$

$[\Gamma_0]$  = transformation matrix accounting for correlation of  $\{X\}$  variables

Evaluation of the above terms is now described in greater detail.

#### Solution of Correlation Transformation Matrix

Input to the reliability program includes a correlation matrix  $[R]$  for the random variables  $\{X\}$ . Solution of the transformation matrix  $[\Gamma_0]$  is based on the input correlation matrix. The input matrix  $[R]$  is modified to account for input variables having non-normal distributions to obtain a modified correlation matrix  $[R_0]$  as follows:

$$R_{0ij} = R_{ij} \delta_{ij} \quad i, j = 1, n \quad (5.20)$$

where:

$R_{ij}$  = element of original correlation matrix

$R_{0ij}$  = element of modified correlation matrix

$\delta_{ij}$  = correlation correction factor

The correction factors  $\delta_{ij}$  are dependent on the input distributions for variables  $i$  and  $j$ . Semi-empirical  $\delta_{ij}$  values have been obtained by Der Kiureghian and Liu [21] for commonly used input distributions, and in most cases results in corrections of less than 5%.

Once the modified correlation matrix  $[R_0]$  is obtained, a Cholesky decomposition is performed to obtain a lower triangular matrix  $[L_0]$  defined by:

$$[R_0] = [L_0] [L_0]^T \quad (5.21)$$

The transformation matrix  $[\Gamma_0]$  is then taken as the inverse of  $[L_0]$ :

$$[\Gamma_0] = [L_0]^{-1} \quad (5.22)$$

### Evaluation of Effective Means and Standard Deviations

The transformation to standard normal space requires that the effective means and standard deviations of the input variables be evaluated. Elements of  $[D']$  and  $\{M'\}$  can be expressed as:

$$D'_{ii} = \frac{\phi(\Phi^{-1}[F_{X_i}(x_i)])}{f_{X_i}(x_i)} \quad i = 1, N_{rv} \quad (5.23)$$

$$M'_i = x_i - D'_{ii} \Phi^{-1}[F_{X_i}(x_i)] \quad i = 1, N_{rv} \quad (5.24)$$

where:

$f_{X_i}(x_i)$  = PDF for variable  $X_i$

$F_{X_i}(x_i)$  = CDF for variable  $X_i$

Values for  $D'_i$  and  $M'_i$  are dependent on the the point  $\{X\}$  used for the transformation. Equations 5.23 and 5.24 are evaluated for each iteration of the Rackwitz-Fiessler algorithm (equation 5.6) until convergence to the design point  $\{X^*\}$  is reached.

### Flow Chart for SORM Algorithm

A flow chart of the SORM algorithm is given in Figure 5.3. As stated previously, the correlation transformation matrix  $[\Gamma_0]$  is only evaluated once. Successive iterations are made to converge on the design point  $\{X^*\}$ , with the transformation from  $\{X^*\}$  to  $\{Y^*\}$  being re-evaluated during each iteration. Once convergence is obtained, the final probability of  $G < 0$  is estimated using a second-order expansion of the failure surface about the design point.

## 5.3 Formulation of Failure Function for Iceberg Kinetic Energy

Application of the second-order reliability method requires the formulation of an appropriate failure function  $G(\vec{X})$ . The failure function for predicting kinetic energy exceedence probabilities has the following form:

$$G(\vec{X}) = R_{KE} - KE(\vec{X}) \quad (5.25)$$

where:

$KE$  = iceberg kinetic energy

$R_{KE}$  = input kinetic energy level

The SORM algorithm can be run for various  $R_{KE}$  values to obtain the portion of the cumulative distribution function (CDF) relevant to structural design.

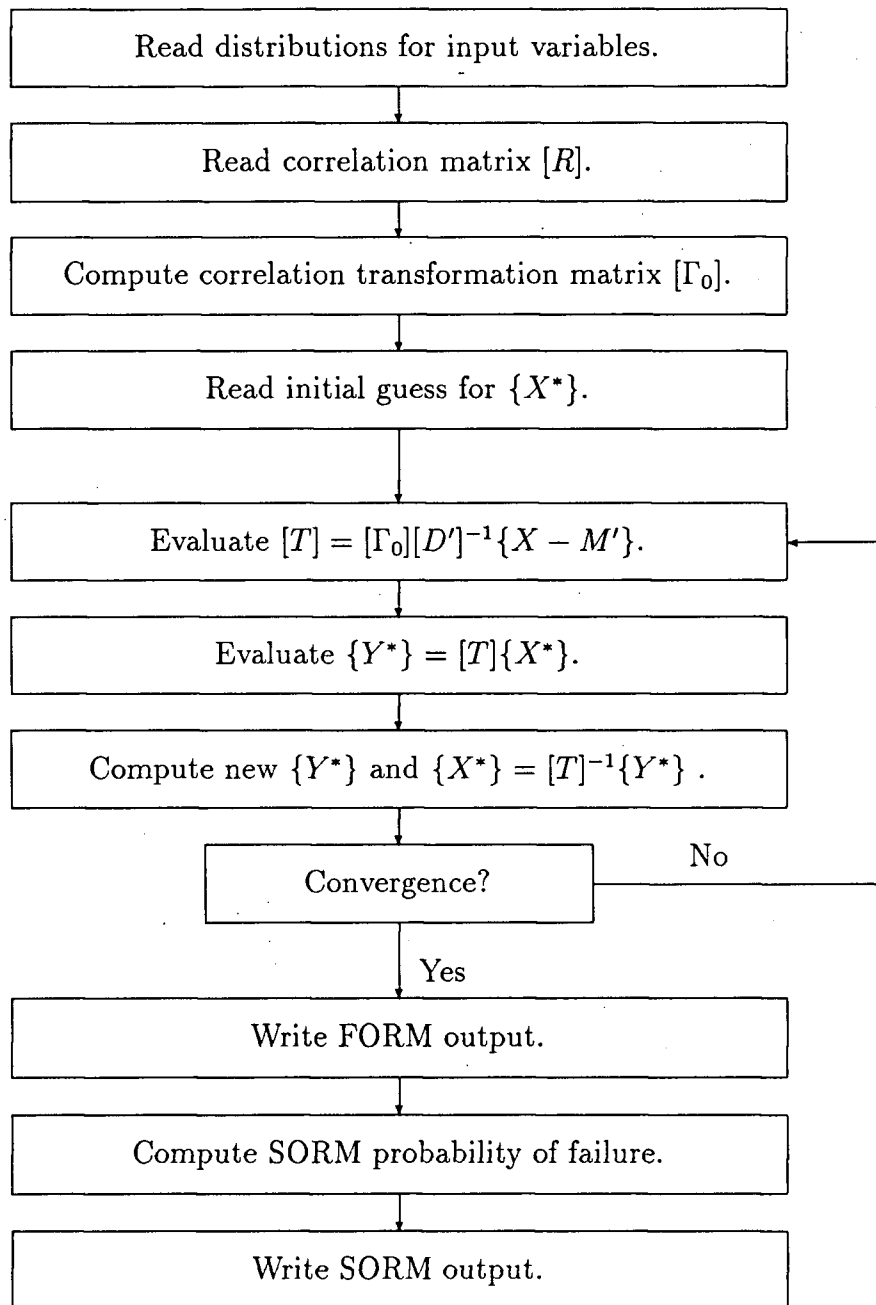


Figure 5.3: Flow Chart for Second-Order Reliability Method

The selection of input random variables for the failure function is of critical importance. For the present reliability model, the kinetic energy of an iceberg at a given site is expressed as a function of the following four variables:

1. Iceberg mass,  $M$ ,
2. Iceberg aspect ratio,  $h/D_i$ ,
3. Iceberg drift velocity,  $V_d$ ,
4. Significant wave height,  $H_s$ .

The above random variables have been selected primarily because of the ease with which statistical data can be obtained for each variable. Iceberg dimensions and drift velocities are recorded by petroleum operators working in iceberg-prone regions, while wave climate data is available for most offshore areas. The four variables selected for iceberg kinetic energy are likely to have low correlation coefficients, and are thus well suited to application of the second-order reliability method.

### 5.3.1 Idealization of Iceberg Geometry

Due to the infinite number of possible iceberg shapes, it is necessary to select an idealized iceberg geometry. A vertical circular cylinder having 1/7'th of its mass above water is used in the present model. The geometrical properties of a cylindrical iceberg can be described by its mass  $M$  and aspect ratio  $h/D_i$  (draft/diameter). The aspect ratio of a cylindrical iceberg will have an upper limit of 0.86 imposed by hydrostatic stability requirements.

### 5.3.2 Iceberg Added Mass

Evaluation of iceberg kinetic energy requires that iceberg added mass be known. The added mass at the zero-frequency limit is used for the present application, and is considered to provide a conservative estimate of the iceberg kinetic energy that could be dissipated during an impact (see Chapter 3). The zero-frequency added mass coefficient for a cylinder can be expressed as a function of two dimensionless parameters:

$$C_m = f(h/d, h/D_i) \quad (5.26)$$

Since water depth  $d$  is constant for a given site,  $C_m$  can be expressed as a function of the iceberg geometry variables:

$$C_m = f(M, h/D_i) \quad (5.27)$$

When evaluating the kinetic energy failure function, equation 5.27 is treated as a deterministic relationship. Added mass coefficients are obtained by interpolation of tabulated values for equation 5.26 presented in Figure 3.19.

### 5.3.3 Iceberg Velocity

The accurate evaluation of iceberg kinetic energy requires that both drift and oscillatory velocity components be considered. If drift and oscillatory motions are assumed to be collinear, then the following expression from Lever and Sen [60] can be adopted:

$$V_c = V_d + V_s \quad (5.28)$$

where:

$V_c$  = total collision velocity (m/s)

$V_d$  = drift velocity (m/s)

$V_s$  = significant surge velocity (m/s)

Due to the influence of wave drift forces on iceberg drift motions [40,44], the assumption of collinear drift and oscillatory components is quite reasonable. Statistical data for iceberg drift velocity can be obtained from observed iceberg trajectories; thus, drift velocity is a suitable input variable for the probabilistic model.

When evaluating the influence of oscillatory motions on impact velocity, consideration must be given to the variation of iceberg velocity during a wave cycle and to the variability of wave heights in a random wave field. When accounting for this, the significant wave height provides a reasonable nominal value of the height to be used in calculating oscillatory velocity amplitude since this represents the 86-th percentile of wave height. In summary, the significant oscillatory velocity amplitude  $V_s$  based on the significant wave height is used for predicting the oscillatory velocity on impact.

Oscillatory surge velocity  $V_s$  cannot be used as a model input parameter because of problems associated with obtaining oscillatory velocity measurements. An alternative method must be used for evaluating wave-induced motions. The following expression is adopted for evaluating the significant surge velocity:

$$V_s = \frac{1}{2} H_s \omega_p \zeta'_1 \quad (5.29)$$

where:

$H_s$  = significant wave height (m)

$\zeta'_1$  = surge response amplitude operator

$\omega_p$  = peak angular frequency (rad/s)

The availability of wave climate data makes significant wave height a suitable input random variable for the probabilistic model. The oscillatory velocity can be subsequently evaluated using deterministic relationships.

The peak wave period  $T_p$  is strongly dependent on the incident wave height. Lever and Sen [60] have adopted the following expression obtained by LeBlond et al. [57] using

a least squares fit to a variety of ocean wave records from the Canadian East Coast:

$$T_p = 13.88 \sqrt{H_s / g} \quad (5.30)$$

Similar expressions can be developed for other sites (e.g. see Thoft-Christensen and Baker [110]). Equation 5.30 indicates that the effect of increasing wave height on  $V_s$  will be offset by decreasing  $\omega_p$ .

The surge RAO  $\zeta'_1$  in equation 5.29 is evaluated using linear wave theory, which can be considered valid when wave height is small relative to incident wavelength and water depth. Using the idealized cylindrical iceberg geometry, the surge RAO can be expressed as a function of 3 dimensionless parameters:

$$\zeta'_1 = f(\omega^2 D_i / 2g, h/D_i, h/d) \quad (5.31)$$

If water depth  $d$  is constant for a given site and  $\omega$  is considered to be a function of  $H_s$ , equation 5.31 can be re-written in terms of the model input random variables:

$$\zeta'_1 = f(M, h/D_i, H_s) \quad (5.32)$$

Deterministic evaluation of surge RAO's is done using tabulated values from Figures 3.8 - 3.12 which were obtained from diffraction computations for  $0.5 < \omega^2 D_i / 2g < 3.14$ . If an RAO is required for  $\omega^2 D_i / 2g < 0.5$ , it is conservatively assumed that the iceberg moves as a water particle at the water surface (equation 3.39). In the high frequency range  $\omega^2 D_i / 2g > 3$ , the surge RAO is determined using the high frequency approximation of equation 3.46.

When calculating iceberg impact velocity using the kinetic energy model, the influence of the structure on iceberg motions is not considered. It was shown in Chapter 3 that the influence of a structure on iceberg drift velocity can be significant for wave driven drift motions when the iceberg diameter is less than half the structure diameter.

This phenomenon suggests that the significant wave height  $H_s$  could have a negative influence on the drift velocity  $V_d$  upon impact. It is suggested that the influence of the structure on impact velocity be neglected when performing the initial evaluation of a design event. If the design iceberg diameter is then determined to be less than half the structure diameter and the drift velocity is driven primarily by waves, detailed numerical and physical studies of the hydrodynamic interactions between the iceberg and structure would be warranted.

### 5.3.4 Summary of Failure Function

The failure function for iceberg kinetic energy has been formulated in terms of four random variables as follows:

$$G(M, h/D_i, V_d, H_s) = R_{KE} - KE(M, h/D_i, V_d, H_s) \quad (5.33)$$

The failure function is used to estimate the exceedence probability of the kinetic energy level  $R_{KE}$  for an iceberg. Iceberg added mass and oscillatory velocity are evaluated deterministically using the four random variables as input parameters for computation.

## 5.4 Application to Selection of a Design Iceberg Collision

The above method can be used to determine an iceberg collision event for structural design. The kinetic energy of the design collision is based on an acceptably low exceedence probability during the life of the structure. Because the failure function is formulated to compute exceedence probabilities for a single iceberg, results must be modified to account for the variable number of collisions which can occur during the structure lifetime. The general design process will now be described in detail.

### 5.4.1 Exceedence Probabilities for a Single Collision

The failure function outlined in the previous section is well suited to estimating the kinetic energy CDF for a single collision, denoted  $F_{KE}(KE | n_c = 1)$ . For design purposes, the upper portion of this CDF is of primary interest (e.g.  $F_{KE}(KE) > 0.99$ ).

Input distributions for ice mass and velocity must be modified to account for the greater likelihood of larger and faster icebergs impacting the structure, as proposed by Dunwoody [22]. Through application of Bayes' theorem [101], diameter and velocity PDF's for icebergs impacting a finite size structure are obtained by:

$$f_{D_i}(D_i | n_c = 1) = \frac{D_i + D_s}{\mu_{D_i} + D_s} f_{D_i}(D_i) \quad (5.34)$$

$$f_{V_d}(V_d | n_c = 1) = \frac{V_d}{\mu_{V_d}} f_{V_d}(V_d) \quad (5.35)$$

where:

$$f_{D_i}(D_i) = \text{diameter PDF for all icebergs (m}^{-1}\text{)}$$

$$f_{D_i}(D_i | n_c = 1) = \text{diameter PDF for impacting icebergs (m}^{-1}\text{)}$$

$$f_{V_d}(V_d) = \text{drift velocity PDF for all icebergs (s/m)}$$

$$f_{V_d}(V_d | n_c = 1) = \text{drift velocity PDF for impacting icebergs (s/m)}$$

$$n_c = \text{number of collisions}$$

The mass PDF for impacting icebergs can be evaluated using equation 5.34. If a characteristic aspect ratio  $\mu_{h/D_i}$  is assumed, then the modified mass PDF is:

$$f_M(M | n_c = 1) = \frac{\gamma M^{1/3} + D_s}{\gamma E(M^{1/3}) + D_s} f_M(M) \quad (5.36)$$

$$\gamma = \left( \frac{4}{\pi \mu_{h/D_i} \rho} \right)^{1/3} \quad (5.37)$$

where:

$$E(x^r) = \text{mean value of } x^r$$

$$f_M(M) = \text{mass PDF for all icebergs (kg}^{-1}\text{)}$$

$$f_M(M | n_c = 1) = \text{mass PDF for impacting icebergs (kg}^{-1}\text{)}$$

$$\rho = \text{water density (kg/m}^3\text{)}$$

Application of equation 5.36 requires that the mean value of  $M^{1/3}$  for all icebergs be evaluated.

Various methods such as numerical integration are available for utilizing equations 5.35 and 5.36. Perhaps the most convenient method is to select parent mass and velocity distributions which have analytical solutions for the  $r$ 'th moments:

$$E(x^r) = \int_{-\infty}^{\infty} f_x(x) x^r dx \quad (5.38)$$

Distributions which have analytical solutions for moments include the lognormal and gamma distributions (see Bury [12]). Solutions to equation 5.38 can be combined with equations 5.35 and 5.36 to obtain moments (e.g. mean, standard deviation, skewness coefficient) of the distributions for impacting icebergs.

Once distributions have been selected for input variables, the SORM program can be run for various  $R_{KE}$  values to obtain the upper portion of the kinetic energy CDF for a single iceberg collision.

## 5.4.2 Extension to Multiple Collisions

Due to the possibility of multiple iceberg collisions during the life of a structure, the kinetic energy CDF obtained for a single collision must be modified accordingly (see Maes and Jordaan [70]). If the number of iceberg collisions occurring during the life of the structure is a fixed quantity  $N_L$ , then the CDF of the extreme load can be determined

as:

$$F_{KE}(KE | n_c = N_L) = [F_{KE}(KE | n_c = 1)]^{N_L} \quad (5.39)$$

where:

$F_{KE}(KE | n_c = 1)$  = kinetic energy CDF for single collision

$F_{KE}(KE | n_c = N_L)$  = extreme value kinetic energy CDF for  $N_L$  collisions

$N_L$  = fixed number of collisions during lifetime

In reality, the number of collisions to occur during the life of the structure is a random quantity and the following expression must be used to account for a variable number of collisions:

$$F_{KE}(KE) = \sum_{n_L=0}^{\infty} p_{n_L}(n_L) [F_{KE}(KE | n_c = 1)]^{n_L} \quad (5.40)$$

where:

$n_L$  = variable number of collisions during lifetime of structure

$p_{n_L}(n_L)$  = probability mass function for number of collisions

Evaluation of equation 5.40 is greatly simplified if the occurrence of iceberg collisions is modelled as a Poisson process. The probability mass function for  $n_L$  appears as follows:

$$p_{n_L}(n_L) = \exp(-\mu_{n_L}) \frac{\mu_{n_L}^{n_L}}{n_L!} \quad (5.41)$$

Substitution of equation 5.41 into equation 5.40 yields:

$$F_{KE}(KE) = \sum_{n_L=0}^{\infty} \exp(-\mu_{n_L}) \frac{\mu_{n_L}^{n_L}}{n_L!} [F_{KE}(KE | n_c = 1)]^{n_L} \quad (5.42)$$

$$= \exp \{ -\mu_{n_L} [1 - F_{KE}(KE | n_c = 1)] \} \quad (5.43)$$

The simple form of this equation lends itself to easy application. If an acceptable exceedence probability for the structure life is specified, then an associated exceedence probability for a single collision can be evaluated. The kinetic energy failure function for a single collision can then be used to determine the lifetime design load.

## 5.5 Example Design Problem for Large Iceberg Population

The method described above has been used to determine a design event for a hypothetical structure. The operating environment for the example structure is similar to that for the Hibernia area off the coast of Newfoundland, with icebergs in the area being relatively large in size. A structure diameter of 100 m was chosen to operate in a water depth of 100 m.

### 5.5.1 Design Criterion

The kinetic energy of the design event was specified to have a 10% exceedence probability during the life of the structure. For application of the kinetic energy failure function it was necessary to compute an associated exceedence probability for a single collision.

The mean number of collisions expected during the structure lifetime can be expressed as follows:

$$\mu_{n_L} = \lambda_c T_L \quad (5.44)$$

where:

$T_L$  = operating life for structure (years)

$\lambda_c$  = mean rate of iceberg collisions (/year)

A mean value of 20 collisions during the structure lifetime was used for the present problem. The associated exceedence probability of 0.0052 for a single collision was subsequently evaluated using equation 5.43.

### 5.5.2 Statistical Distributions for Input Variables

Statistical distributions for input variables were estimated from available data for the Hibernia oilfield and surrounding areas. A summary of input distributions is given in Table 5.1. Lognormal distributions have been used in the present example for modelling iceberg mass and drift velocity largely for the sake of computational convenience. In an actual design situation, care must be taken to select the statistical distribution model (e.g. lognormal or gamma) which best represents the variable under consideration. For each variable, particular care must be given to modelling the distribution tail (e.g. the upper or lower decile) that will have the greatest influence on the design load.

Table 5.1: Input Distributions for Example Design Problem

Variable	Distribution	Parameters
$M$ ( $10^6$ tonnes)	Lognormal	$\mu = 0.50, \sigma = 1.74$
$h/D_i$	Uniform	0.1 - 0.8
$V_d$ (m/s)	Lognormal	$\mu = 0.34, \sigma = 0.29$
$H_s$ (m)	Lognormal	$\mu = 2.44, \sigma = 1.22$

Statistical moments for iceberg masses at Hibernia were estimated from a graph presented by NORDCO [91]; thus, they can only be considered as rough estimates of actual values. Due to the greater likelihood of larger icebergs impacting the structure, the iceberg mass distribution had to be modified according to equation 5.36. Evaluation of statistical moments for impacting icebergs was done using the moment equation for a lognormally distributed variable (from Bury [12]):

$$E(x^r) = \exp\left(r \mu_{\ln x} + \frac{1}{2} r^2 \sigma_{\ln x}^2\right) \quad (5.45)$$

where:

Table 5.2: Distribution Moments for All Icebergs and Impacting Icebergs

Variable	All Icebergs	Impacting Icebergs
$M$ ( $10^6$ tonnes)	$\mu = 0.33, \sigma = 1.05$	$\mu = 0.50, \sigma = 1.74$
$V_d$ (m/s)	$\mu = 0.20, \sigma = 0.17$	$\mu = 0.34, \sigma = 0.29$

$E(x^r)$  = expected value of  $x^r$

Combining equation 5.45 with equation 5.36, the mean and standard deviation for impacting icebergs were evaluated as follows:

$$\begin{aligned} \mu_{M|n_c=1} &= \frac{\gamma}{\gamma E(M^{1/3}) + D_s} E(M^{4/3}) \\ &+ \frac{D_s}{\gamma E(M^{1/3}) + D_s} \mu_M \end{aligned} \quad (5.46)$$

$$\begin{aligned} E(M^2 | n_c = 1) &= \frac{\gamma}{\gamma E(M^{1/3}) + D_s} E(M^{7/3}) \\ &+ \frac{D_s}{\gamma E(M^{1/3}) + D_s} E(M^2) \end{aligned} \quad (5.47)$$

$$\sigma_{M|n_c=1} = \left( E(M^2 | n_c = 1) - \mu_{M|n_c=1}^2 \right)^{1/2} \quad (5.48)$$

A characteristic aspect ratio of 0.45 was used for evaluating  $\gamma$ . Statistical moments for the general iceberg population and impacting icebergs are given in Table 5.2. Note that the mean and standard deviation of mass for impacting icebergs are much greater than values for the parent population. It was assumed that the mass of impacting icebergs was lognormally distributed; however, use of alternative statistical models could be examined if higher quality input data were available.

Moments for iceberg drift velocity were taken from Pearson and Ro [93], who analysed 9920 hourly drift trajectories for the Labrador Sea. It was assumed that drift

velocity was lognormally distributed. Statistical moments for impacting icebergs were evaluated using equations 5.35 and 5.45 and are given in Table 5.2.

Iceberg aspect ratio  $h/D_i$  was assumed to be uniformly distributed between 0.1 and 0.8. The upper limit on  $h/D_i$  was chosen to insure hydrostatic stability. The significant wave height parameters for Hibernia were taken from Neu [86]. Results from Neu's analysis indicate that a lognormal distribution provides an excellent fit to observed wave data.

### 5.5.3 Correlated Input Variables

Input to the SORM program can include correlation coefficients for random variables. Studies of observed iceberg dimensions by Brooks [11] and El-Tahan and Davis [26] indicate that iceberg aspect ratio decreases with increasing waterline length. This trend was modelled using a correlation coefficient of -0.1 between mass  $M$  and aspect ratio  $h/D_i$ . Utilization of a negative correlation coefficient was necessary from a computational viewpoint to avoid iceberg drafts larger than the input water depth. The influence of wave drift forces on iceberg drift motions will likely cause a positive correlation to exist between drift velocity  $V_d$  and significant wave height  $H_s$ . This possible correlation was neglected for the present problem due to the lack of supporting field data.

### 5.5.4 Computation of Exceedence Probabilities

The SORM program was used to estimate exceedence probabilities for various kinetic energy levels. Energy levels with exceedence probabilities near the design value of 0.0052 for a single collision were of primary interest. Results for the SORM computations presented in Figure 5.4 indicate that the design event for the specified design criterion has a kinetic energy of  $2.1 \times 10^9$  Joules.

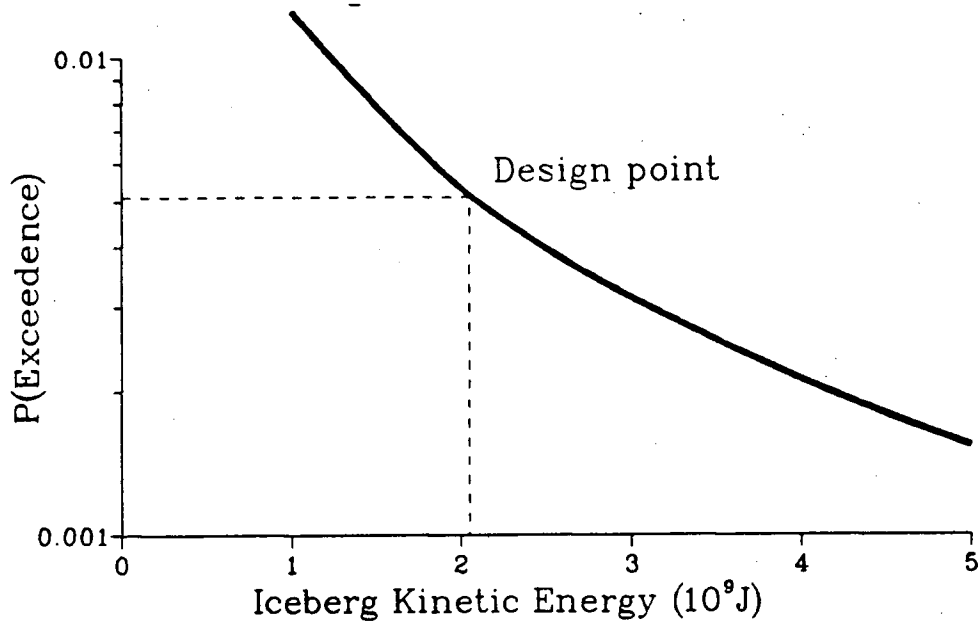


Figure 5.4: Kinetic Energy Exceedence Probabilities for a Single Collision

### 5.5.5 Parameters for Design Collision Event

Output parameters for the design collision event are given in Table 5.3. The design values for the random variables represent the most likely values for the given kinetic energy level while the magnitudes of the sensitivity coefficients indicate the relative importance of the variables. Other collision parameters based on the values of the input random variables for the design event are listed at the bottom of Table 5.3.

The high sensitivity coefficients for  $M$  and  $V_d$  indicate that these variables are dominant for the design event. Particular emphasis should be given to the quality of the input data for these two variables. The low  $H_s$  sensitivity coefficient suggests that wave-induced motions have a minor influence on kinetic energy, with the significant oscillatory velocity being less than 1% of the drift velocity.

Table 5.3: Results for Large Iceberg Design Collision

Variable	Design Value	Sensitivity
$M$ ( $10^6$ tonnes)	3.08	0.75
$h/D_i$	0.30	0.09
$V_d$ (m/s)	0.90	0.65
$H_s$ (m)	2.20	0.01

Other parameters associated with above design values:

$$D_i = 235 \text{ m}, h = 69 \text{ m}, C_m = 0.67, T_p = 6.6 \text{ s}, \\ \omega_p^2 D_i / 2g = 10.9, \zeta'_1 = 0.006, V_s = 0.006 \text{ m/s}$$

### 5.5.6 Exceedence Probabilities without Wave-Induced Motions

Due to the small influence of  $H_s$  on the design event, it is suggested that wave-induced motions can be neglected when evaluating the upper portion of the kinetic energy CDF for the present example. Iceberg kinetic energy can be modelled using a lognormal distribution if the following assumptions are made:

1. Added mass is independent of iceberg geometry,
2. Wave-induced motions are negligible,
3. Iceberg mass and drift velocity are lognormally distributed.

The resulting lognormal model for iceberg kinetic energy can provide a useful comparison with SORM results.

If the design event added mass of 0.67 is treated as a constant, iceberg kinetic energy will have a mean value of  $1.49 \times 10^9$  Joules and a standard deviation of  $16.0 \times 10^9$  Joules. Figure 5.5 shows excellent agreement of exceedence probabilities evaluated using the

SORM and analytical models. It appears that wave-induced motions have a negligible influence on iceberg kinetic energy at the upper tail of the CDF.

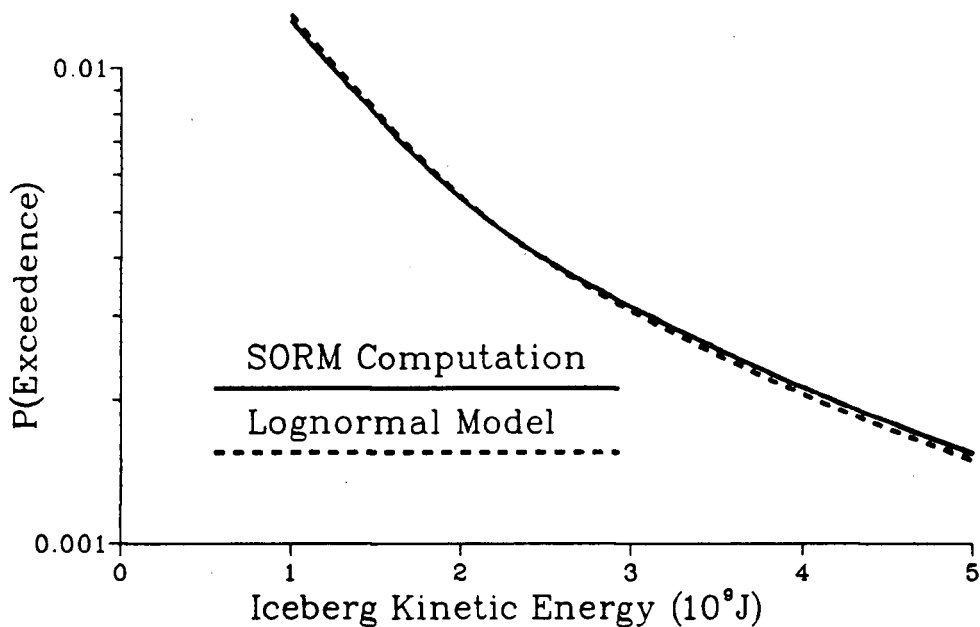


Figure 5.5: Comparison of SORM and Analytical Model Results

## 5.6 Example Design Problem for Small Iceberg Population

The relative importance of wave-induced iceberg motions will increase as the size of impacting icebergs becomes smaller. This trend can be examined by varying the size of impacting icebergs for the example problem given in the previous section. If the parent iceberg population has masses which are 1/1000'th of those for the first example, then the mass distribution for impacting icebergs will have a mean value of  $0.36 \times 10^6$  kg and a standard deviation of  $1.19 \times 10^6$  kg. Note that the smaller iceberg population could be encountered at a structure site farther away from the original source of icebergs, or

could be caused by iceberg management methods such as towing of larger icebergs or site evacuation by a mobile drilling unit when large icebergs come within a prescribed distance.

If the remaining input parameters remain the same as for the previous example, then the kinetic energy exceedence probabilities are as given in Figure 5.6. Using the acceptable exceedence probability of 0.0052 for a single collision, the kinetic energy of the design event is  $5.5 \times 10^6$  J. Reliability model parameters for the small iceberg example given in Table 5.4 indicate that wave-induced motions dominate the impact velocity for the design collision. Due to the small size of the design iceberg relative to the structure ( $D_i/D_s = 0.2$ ), it is suggested that the influence of negative wave drift forces acting on the iceberg could significantly reduce the impact velocity predicted by the kinetic energy reliability model, and that a refined model accounting for this influence should be developed.

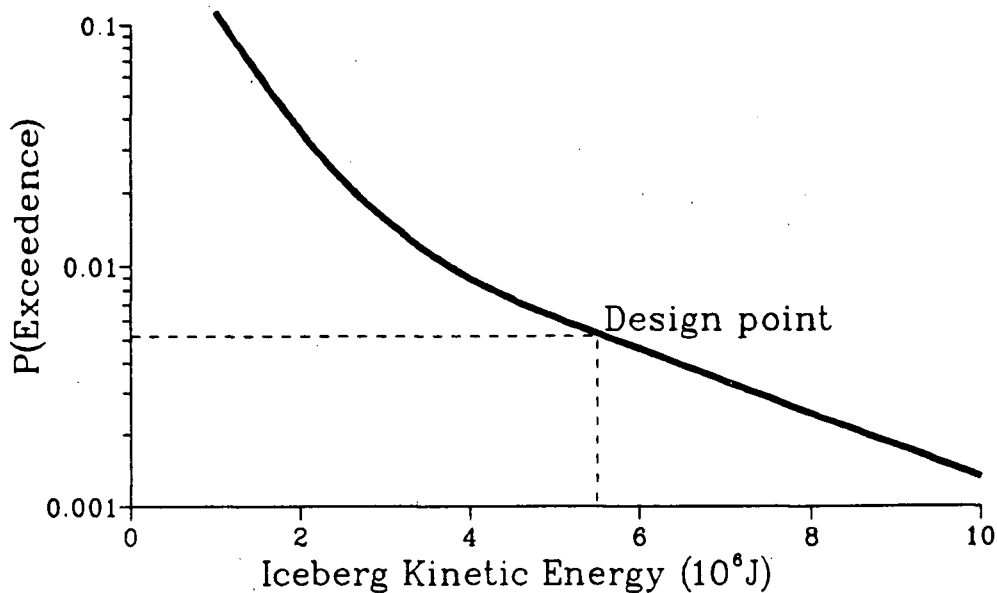


Figure 5.6: Kinetic Energy Exceedence Probabilities for Small Iceberg Example

Table 5.4: Results for Small Iceberg Design Collision

Variable	Design Value	Sensitivity
$M$ ( $10^3$ tonnes)	3.03	0.85
$h/D_i$	0.45	-0.02
$V_d$ (m/s)	0.47	0.31
$H_s$ (m)	3.76	0.43

Other parameters associated with above design values:

$$D_i = 20 \text{ m}, h = 9 \text{ m}, C_m = 0.55, T_p = 8.6 \text{ s},$$

$$\omega_p^2 D_i / 2g = 0.55, \zeta'_1 = 0.77, V_s = 1.06 \text{ m/s}$$

## Chapter 6

# Selection of a Design Event Based on Global Impact Sliding Force

In the previous chapter a probabilistic method was described for selection of a design collision event based on iceberg kinetic energy. Although kinetic energy is a useful ranking criterion for preliminary design, the ultimate design criterion should be based on the expected mode of structural failure. The present chapter discusses the selection of an iceberg collision design event based on global impact sliding force, which is likely to determine whether structural failure will occur. Required input parameters include structure dimensions; thus, the model is most suited to the latter stages of design.

A time-stepping procedure which considers hydrodynamic interaction is used to model the trajectory of an iceberg approaching a structure. Impact forces are subsequently evaluated once a collision commences. The maximum horizontal force developed during the impact phase is used as the collision severity ranking criterion.

The primary objective of the impact force reliability model is to illustrate the importance of hydrodynamic effects in collision risk analysis. Structural dynamic effects are neglected, and relatively simple methods are used for evaluating ice forces. Despite these shortcomings, the model is a useful starting point for more sophisticated examination of ice-structure interactions.

## 6.1 Iceberg Loading of Offshore Structures

The evaluation of ice loads on offshore structures has been the subject of extensive research in recent years, as described in reviews by presented by Cammaert and Mugeridge [13], Nessim et al. [85], and Sanderson [100]. The prediction of ice forces on offshore structures requires an understanding of the possible failure modes for ice. In general, the following three failure modes are dominant:

1. Bending,
2. Buckling,
3. Crushing.

The bending mode is likely to occur when a thin sheet of ice is forced upon the face of a sloping structure, while buckling can occur if a thin ice sheet encounters a vertical sided structure. If neither bending or buckling occurs, then the impact energy will be dissipated by crushing. Due to the relatively high aspect ratio of icebergs, failure will almost always be in the form of crushing.

### 6.1.1 Ice Forces for Head-on Impact

Head-on impact is often used as a worst case scenario for predicting forces from iceberg collisions (e.g. Cammaert and Tsinker [14], Cox [18] Johnson and Nevel [50]). A head-on impact of an iceberg with an offshore structure is shown in Figure 1.2. The force acting on the structure during head-on impact can be expressed as follows:

$$F_{cr} = p_{cr} A_n(\Delta) \quad (6.1)$$

where:

$A_n$  = normal contact area between ice and structure ( $m^2$ )

$F_{cr}$  = ice crushing force (N)

$p_{cr}$  = effective ice crushing pressure ( $N/m^2$ )

$\Delta$  = penetration distance of structure into ice (m)

The normal contact area  $A_n$  is merely a function of the collision geometry. The effective crushing pressure  $p_{cr}$  will depend on several factors which are discussed later in this chapter.

Further insight can be gained by examining the relationship between iceberg kinetic energy and impact force. If environmental forces other than those influencing iceberg added mass are considered negligible relative to impact force, then the following relationship can be used:

$$\frac{1}{2} (1 + C_m) M V_c^2 = \int_0^{\Delta_c} F_{cr}(\Delta) d\Delta \quad (6.2)$$

where:

$V_c$  = initial iceberg velocity (m/s)

$\Delta_c$  = maximum penetration distance (m)

Thus, impact will progress until the entire kinetic energy of the iceberg is dissipated. The added mass in equation 6.2 is an effective added mass based on a kinetic energy balance. It should be noted that the following momentum relationship is also valid for head-on impact:

$$(1 + C_m) M V_c = \int_0^{t_c} F_{cr}(t) dt \quad (6.3)$$

where:

$t_c$  = duration of impact (s)

Unlike the effective added mass of equation 6.2, the effective added mass of 6.3 is based on momentum and will be slightly different than the effective added mass based on kinetic energy.

### 6.1.2 Ice Forces for Eccentric Impact

Evaluation of collision forces is significantly complicated if eccentric impacts are considered. Time-stepping procedures for computing eccentric impact forces have been developed by Bass et al. [7], Duthinh and Marsden [25], and Salvalaggio and Rojansky [99]. Frictional forces which act tangentially on a structure will arise during eccentric impacts. The tangential force will apply torque to the structure and will also contribute to the sliding force. The kinetic energy balance equation for eccentric impacts must include energy dissipated through friction. In addition, the iceberg will possess some remaining kinetic energy after impact. The revised kinetic energy equation is as follows:

$$\begin{aligned} \frac{1}{2} (1 + C_m) M V_c^2 &= \int_0^{s_{nc}} F_{cr}(s_n) ds_n + \int_0^{s_{tc}} F_t(s_t) ds_t \\ &+ \frac{1}{2} (1 + C_m) M V_f^2 + \frac{1}{2} (1 + C_I) I \omega_f^2 \end{aligned} \quad (6.4)$$

where:

$C_I$  = coefficient of added inertia

$F_t$  = tangential force acting on iceberg (N)

$I_\omega$  = iceberg rotational inertia (N·m<sup>2</sup>)

$s_n$  = normal displacement of iceberg relative to structure (m)

$s_{nc}$  = total normal displacement (m)

$s_t$  = tangential displacement of iceberg relative to structure (m)

$s_{tc}$  = total tangential displacement (m)

$V_f$  = final translational velocity after collision (m/s)

$\omega_f$  = final rotational velocity after collision (rad/s)

The last term of the above equation is due to the rotational motion of the iceberg induced by the tangential force  $F_t$ . The tangential force component  $F_t$  is typically expressed in terms of a friction coefficient  $\mu_f$ :

$$F_t = \mu_f F_n \quad (6.5)$$

It should be noted that the existence of normal and tangential forces are conditional upon the iceberg motions. For the normal force to exist, the iceberg must be moving with a normal velocity into the structure. The existence of a tangential force component is dependent upon a corresponding normal force (equation 6.5). The tangential force acting on the structure will act in the direction of the tangential velocity of the iceberg relative to the structure.

### 6.1.3 Selection of Effective Ice Pressure

The evaluation of ice loads requires that the effective ice pressure  $p_{cr}$  be estimated during impact. Extensive reviews of methods for predicting ice pressures have been compiled by Nessim et al. [85] and Sanderson [100]. The most commonly used methods for estimating effective ice pressure are:

1. Constant pressure,
2. Korzhavin's equation,
3. Pressure vs. area.

These three methods will be discussed in greater detail.

## Constant Ice Pressure

The simplest method for computing ice loads is to assume a constant ice pressure. The assumption of constant ice pressure lends itself to the development of analytical solutions for ice forces, such as those developed by Cammaert and Tsinker [14] and Johnson and Nevel [50]. Selection of a suitable effective ice pressure is difficult due to the wide range of published results. Bass et al. [7] cited laboratory tests giving iceberg crushing strengths ranging from 10 MPa to 30 MPa. Laboratory test results surveyed by Nevel [87] indicated crushing strengths in the range 6-10 MPa. Field measurements of the strength of iceberg ice conducted by Johnson and Benoit [49] indicated highly varying ice pressures. It should be emphasized that the assumption of a constant ice pressure does not account for dependence of ice strength on factors such as strain rate, impact geometry, confinement effects, and size of contact area.

## Korzhaven's Equation

An empirical equation accounting for geometric effects on ice pressure has been developed by Korzhavin [54]. The prediction of ice impact loads using Korzhavin's equation has been adopted by several investigators, including Cox [18] and Croteau [20]. Korzhavin's results are based on laboratory measurements of forces acting on a long narrow indenter impacting a sheet of ice, as shown in Figure 6.1.

Korzhaven's equation for effective ice pressure appears as follows:

$$p_{cr} = I m k \sigma_c \quad (6.6)$$

where:

$I$  = indentation factor

$k$  = contact factor

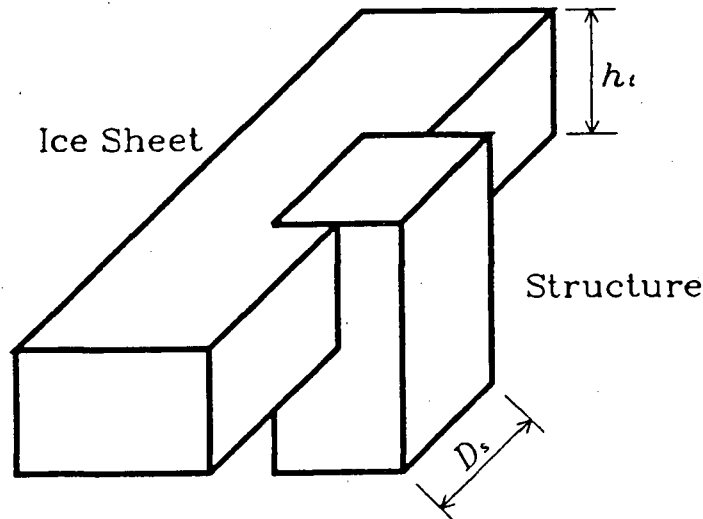


Figure 6.1: Ice Indentation for Korzhavin's Experiments

$m$  = indenter shape factor

$\sigma_c$  = uni-axial compressive strength of ice ( $\text{N}/\text{m}^2$ )

The indentation factor  $I$  arises from confinement effects, which increase the effective ice pressure. Croasdale [19] reports  $I$  values ranging from 1.0 to 4.0, and generally increasing with the ratio of ice height to structure diameter ( $h_t/D_s$  using the notation of the present thesis). The indenter shape factor  $m$  exhibits little variation, ranging from 0.92 for a circular indenter to 1.0 for a flat indenter. Non-simultaneous failure of ice is modelled using the contact factor  $k$ , which generally varies between 0.4 and 0.7 (Nessim et al. [85]). The uni-axial compressive strength of ice  $\sigma_c$  is dependent upon several factors, including ice composition, temperature, and strain rate. Croasdale [19] has presented  $\sigma_c$  values ranging from 0.5 MPa to 5.5 MPa for strain rates of  $10^{-6} \text{ s}^{-1}$  -  $10^{-2} \text{ s}^{-1}$ .

When selecting a method for predicting iceberg impact loads, it should be remembered that Korzhavin's equation has two major limitations. Its experimental basis is limited to the case of a narrow vertical structure impacted by a wide, thin ice sheet (see Figure 6.1). The second limitation is imposed by the small scale of the laboratory tests which are the basis of the equation. Recent full-scale measurements [102] indicate that ice pressures can exhibit significant scale effects.

### Pressure-Area Methods

Ideally, design ice pressures should be based on full-scale field measurements. Although several full-scale ice force measurement programs have been conducted, results have only recently been released to the public domain. A summary of full-scale and laboratory pressure measurements has been compiled by Sanderson [102] (see Figure 6.2). It is evident that effective pressure decreases significantly with increasing cross-sectional area. Sanderson has proposed the following relationship for large areas (i.e.  $A \geq 0.1\text{m}^2$ ):

$$p_{cr} \propto A^{-1/2} \quad (6.7)$$

Various explanations have been proposed for the dependence of ice pressure on scale. One possibility is the larger size of flaws which lead to lower ice strength at larger scales. The occurrence of non-simultaneous failure at larger scales is another hypothesis. While the above two explanations appear quite plausible, a comprehensive understanding of ice pressure scale effects is still lacking.

The pressure-area curve of Figure 6.2 offers a useful empirical method for selecting design pressures; however, one should be aware of the limitations of the compiled results. The majority of large-scale ice force measurements to date have been for thin ice sheets with low aspect ratios ( $h_i/D_i$ ). For icebergs impacting a large structures, aspect ratios are likely to be significantly greater, thus leading to three-dimensional confinement effects. It

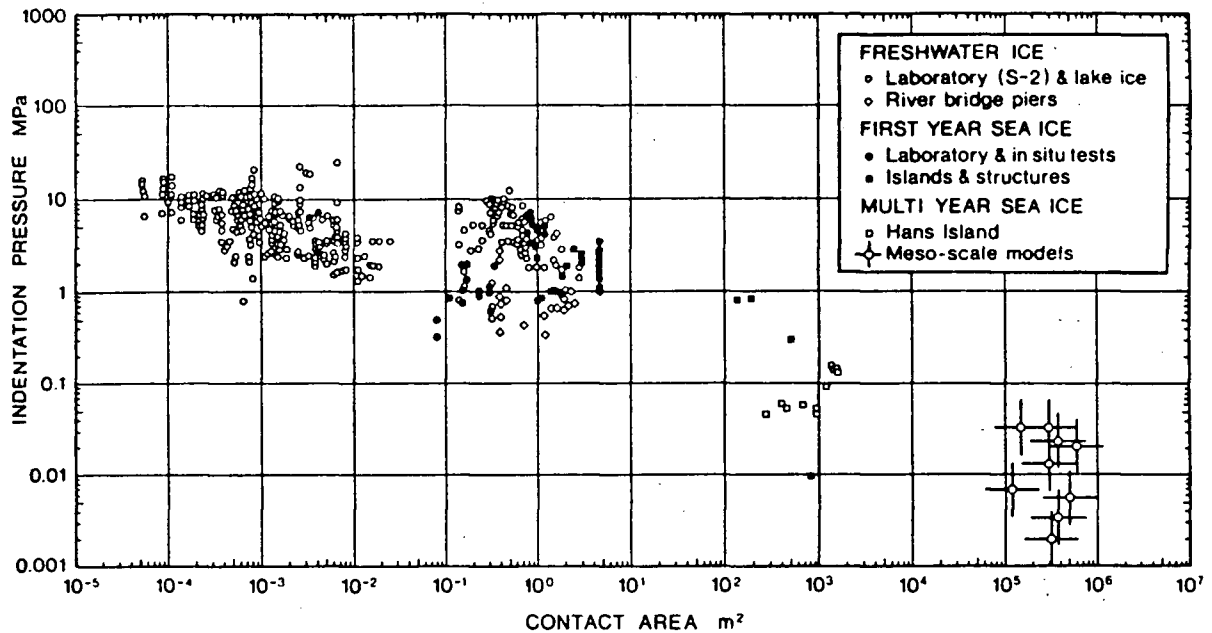


Figure 6.2: Pressure vs. Area Measurements for Ice Strength (from Sanderson [102])

is postulated that large-scale iceberg collision pressures could be somewhat greater than those shown in Figure 6.2; however, supporting field data is lacking.

## 6.2 Failure Function for Iceberg Impact Force Reliability Model

A reliability model has been developed for determining a design iceberg collision based on global impact force. The model utilizes the second-order reliability method (SORM) to evaluate exceedence probabilities for iceberg impact forces. A description of the SORM has been given in the previous chapter.

The failure function for the impact force model is:

$$G(\vec{X}) = F_R - F_L(\vec{X}) \quad (6.8)$$

where:

$F_L$  = impact force load (N)

$F_R$  = structure impact force resistance (N)

$G$  = failure function (N)

$\vec{X}$  = vector of input random variables (N)

The SORM program can be run for various  $F_R$  values to obtain the desired portion of the impact force cumulative distribution function (CDF).

The random variables used as input for the impact force failure function are as follows:

1. Iceberg mass,  $M$  (kg),
2. Iceberg aspect ratio,  $h/D_i$ ,
3. Iceberg drift velocity in open water,  $V_{do}$  (m/s),
4. Significant wave height,  $H_s$  (m),
5. Initial dimensionless eccentricity of iceberg approach,  $e'_o$ ,
6. Reference ice crushing pressure,  $p_r$  (N/m<sup>2</sup>),
7. Ice friction coefficient,  $\mu_f$ .

Deterministic parameters given as input to the model are:

1. Water depth,  $d$  (m),
2. Structure diameter,  $D_s$  (m).

Evaluation of the failure function proceeds in two distinct phases. In the first phase, the trajectory of the iceberg is modelled beginning at a point far away from the structure. The trajectory evaluation phase is used to obtain the iceberg velocity and location upon impact. During the second phase, the maximum global impact force is evaluated to determine the value of the failure function.

Output from the model is given as a force exceedence probability given a potential impact. A potential impact occurs when an iceberg has an initial velocity and approach eccentricity which would cause an impact if the iceberg velocity (speed and direction) remained constant. Due to the influence of the structure on wave and current fields, a potential impact will not always lead to an actual impact; thus, there is a finite probability of the failure function  $G(\vec{X})$  being equal to zero.

### 6.3 Impact Velocity Phase of Reliability Model

The evaluation of impact velocity required the development of an iceberg trajectory model. Although a general model for icebergs approaching a structure has been developed by Isaacson [43], this model requires significant computational effort due to repeated diffraction calculations. A simplified trajectory model was developed for use in the reliability program. An important aspect of the trajectory model is the assumption of collinear waves and currents which is likely to be quite reasonable if one considers the influence of wind on both waves and currents. Input drift velocities for the model are based on observed iceberg velocities; thus, the assumption of collinear waves and currents will not influence estimates of open water drift velocities.

### 6.3.1 Equations of Drift Motion

The motions of an iceberg approaching a structure are modelled using a numerical time-stepping procedure. The direction of propagation for incident waves and the incident current direction are both along the  $x$  axis. The following equations are used to evaluate the  $x$  and  $y$  iceberg acceleration components:

$$M(1 + C_m) a_x = \frac{1}{2} \rho C_d A_w |\vec{V}_w - \vec{V}| (u_w - u) + \frac{1}{2} \rho g C_w D_i H_{rms}^2 \quad (6.9)$$

$$M(1 + C_m) a_y = \frac{1}{2} \rho C_d A_w |\vec{V}_w - \vec{V}| (v_w - v) \quad (6.10)$$

Variations in water velocities can be modelled as an iceberg approaches a structure.

Iceberg velocities are evaluated using an Adams-Bashford method:

$$u(t + \Delta t) = u(t) + \frac{\Delta t}{2} [3 a_x(t) - a_x(t - \Delta t)] \quad (6.11)$$

$$v(t + \Delta t) = v(t) + \frac{\Delta t}{2} [3 a_y(t) - a_y(t - \Delta t)] \quad (6.12)$$

Iceberg displacements are computed using the following second-order Taylor series expansion:

$$x_g(t + \Delta t) = x_g(t) + \Delta t u(t) + \frac{1}{2} \Delta t^2 a_x(t) \quad (6.13)$$

$$y_g(t + \Delta t) = y_g(t) + \Delta t v(t) + \frac{1}{2} \Delta t^2 a_y(t) \quad (6.14)$$

### 6.3.2 Initial Conditions for Simulated Drift Trajectories

The drift trajectory for a potential impact is modelled beginning at a point far away from the structure, as shown in Figure 6.3. The dimensionless initial eccentricity  $e'_o$  will vary between 0 and 1, with the corresponding dimensional eccentricity  $e_o$  being evaluated

as follows:

$$e_o = e'_o \frac{1}{2} (D_i + D_s) \quad (6.15)$$

The initial  $x_g$  value for trajectory simulations is  $-5 D_s$ . The flow field is relatively unaffected by the structure at this location, with the  $x$  component of water velocity being equal to 99% of the incident velocity.

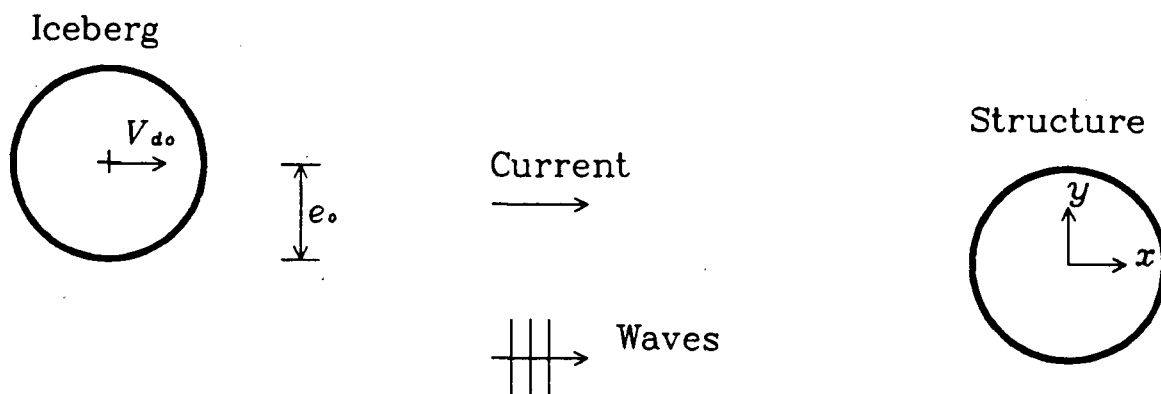


Figure 6.3: Initial Conditions for Iceberg Drift Trajectory toward Structure

Due to the limited availability of ocean current data, input water velocities are based on iceberg drift velocity  $V_d$  and significant wave height  $H_s$ . The assumption of collinear waves and currents allows one to estimate the incident current velocity. Using a force balance between wave drift and water drag forces, the incident current velocity is:

$$V_{wo} = V_{do} - H_{rms} \frac{C_w}{|C_w|} \sqrt{\frac{g |C_w|}{h C_d}} \quad (6.16)$$

### 6.3.3 Hydrodynamic Coefficients for Drift Motions

The evaluation of iceberg drift motions using equations 6.9 and 6.10 requires the following hydrodynamic coefficients:

1. Zero frequency added mass coefficient  $C_m$ ,
2. Water drag coefficient  $C_d$ ,
3. Wave drift force coefficient  $C_w$ .

Zero frequency added mass and water drag coefficients are assumed to be independent of iceberg proximity to the structure. Zero frequency added masses are obtained from tabulated values, as discussed in Chapter 5. A water drag coefficient of 0.7 is used for the cylindrical icebergs in the present model.

It was shown in Chapter 3 that wave drift forces on smaller icebergs ( $D_i/D_s < 0.5$ ) can vary significantly near a structure. The numerical ice motion model suggests that negative wave drift forces can prevent smaller icebergs from impacting a structure; however, the experimental results of Chapter 4 suggest that the numerical model underestimates impact velocities for small icebergs. For the impact reliability model it is conservatively assumed that wave drift coefficients do not vary with proximity to the structure. It is suggested that the influence of negative wave drift forces be investigated once a design event has been selected using the reliability model.

### 6.3.4 Variation of Water Velocity

The current field near the structure is modelled using the analytical solution for flow around a circular cylinder (equation 2.92). Figure 3.24 illustrates that the modification of the flow field by the structure will have a negligible effect on impact velocities for large icebergs; thus, the modification of the flow field is neglected for  $D_i \geq D_s$ .

### 6.3.5 Iceberg Impact Velocity

The drift trajectory time-stepping procedure begins at an initial location, as shown in Figure 6.3, and continues until one of the following occurs:

1.  $x_g$  becomes greater than 0 (the iceberg drifts freely past structure),
2. The iceberg collides with the structure.

The impact force for a potential collision is zero if the iceberg drifts freely past the structure. If an impact occurs, the significant oscillatory velocity is added to the drift velocity to obtain the total impact velocity components:

$$V_{c_x} = V_{d_x} + V_s \quad (6.17)$$

$$V_{c_y} = V_{d_y} \quad (6.18)$$

It is assumed that oscillatory motions are unaffected by the presence of the structure; thus, the method described in Chapter 5 for estimating oscillatory motions in open water is also used in the interaction model. Diffraction computations results presented in Chapter 3 confirmed that the presence of the structure had a relatively minor effect on oscillatory motions.

## 6.4 Impact Force Model

The second phase of the impact force reliability model involves the computation of iceberg forces acting on the structure. Impact forces are evaluated using a numerical time-stepping procedure similar to models developed by Bass et al. [7], Duthinh and Marsden [25], and Salvalaggio and Rojansky [99]. Due to the possibility of eccentric impacts, both radial and tangential forces can develop on the structure. Environmental forces from

waves and currents are assumed to be negligible during impact. Due to the modelling of iceberg geometry as a vertical circular cylinder, the contact area  $A_n$  and associated forces for a given penetration distance  $\Delta$  will likely be greater than contact areas and forces for actual iceberg geometries. Thus, the idealized iceberg geometry will lead to conservative predictions of design impact forces. The inclusion of non-cylindrical iceberg geometries would be a justified improvement to the model if sufficient observations of iceberg geometries were available for a given site. Bass et al. [7] and Salvalaggio and Rojansky [99] have shown that impact forces can be significantly reduced if the contact face of an iceberg has a non-vertical profile.

### 6.4.1 Development of Impact Forces

The present model considers impact forces due to ice crushing and friction. Iceberg geometry and velocity components associated with collision forces are shown in Figure 6.4.

The magnitude of the crushing force is given by equation 6.1. For a cylindrical iceberg impacting a cylindrical structure, the crushing force  $F_{cr}$  is directed toward the centre of the structure. The existence of crushing forces requires that the iceberg have a positive normal velocity  $V_n$  toward the centre of the structure, as shown in Figure 6.4. The frictional force  $F_f$  is evaluated using equation 6.5. For the existence of a frictional force, it is necessary for the iceberg face to have a tangential velocity component  $V_t$  relative to the structure. The resulting frictional force  $F_f$  will act in a direction opposite to that of  $V_t$ .

### 6.4.2 Collision Geometry

The evaluation of ice force requires that the normal contact area  $A_n$  be known. For the present case of an axisymmetric iceberg impacting an axisymmetric structure,

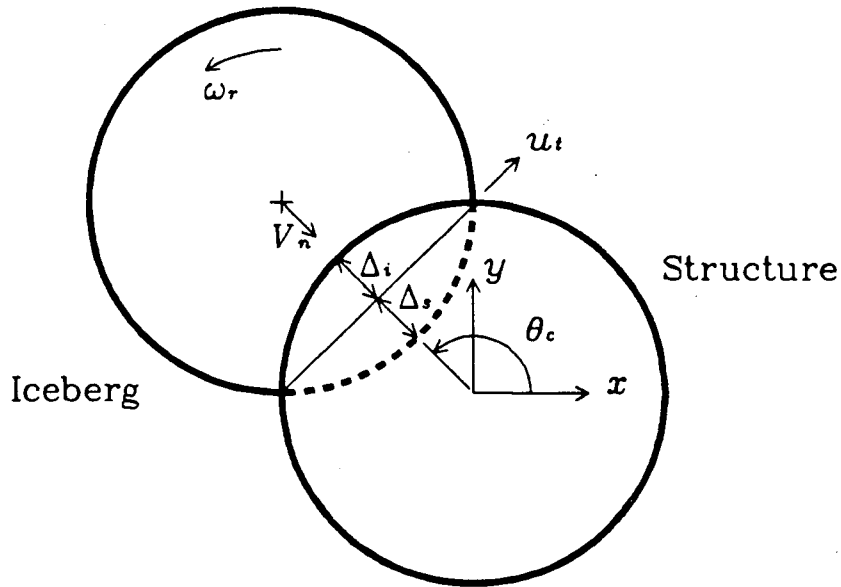


Figure 6.4: Eccentric Iceberg Collision Schematic, Plan View

the impact geometry is dependent merely on the iceberg location in the  $x - y$  plane. Figure 6.4 illustrates the geometry of an iceberg collision, with the origin of the  $x - y$  plane located at the structure centre. The penetration distance of the structure into the iceberg is as follows:

$$\Delta = r_i + r_s - \sqrt{x_g^2 + y_g^2} \quad (6.19)$$

Solving for the normal contact area  $A_n$  is easily accomplished if the penetration distance  $\Delta$  is broken into components  $\Delta_i$  and  $\Delta_s$ , as shown in Figure 6.4. The contact area can then be evaluated using either  $\Delta_i$  or  $\Delta_s$ :

$$A_n = 2 h_t \sqrt{2 r_s \Delta_i - \Delta_i^2} \quad (6.20)$$

$$= 2 h_t \sqrt{2 r_i \Delta_s - \Delta_s^2} \quad (6.21)$$

Given that the areas given by equations 6.20 and 6.21 must be equal and that  $\Delta = \Delta_i + \Delta_s$ , it is possible to solve for  $\Delta_s$  given  $\Delta$ :

$$\Delta_s = \frac{r_s \Delta - \frac{1}{2} \Delta^2}{r_i + r_s - \Delta} \quad (6.22)$$

Thus, the contact area  $A_n$  can be determined by successive evaluation of equations 6.19, 6.22, and 6.21.

Once  $A_n$  is known, the crushing and frictional forces are evaluated using equations 6.1 and 6.5 respectively. The frictional force  $F_f$  will cause a rotational torque between the structure and iceberg. The effective moment arm for the torque acting on the iceberg is approximated as:

$$r_{ti} = r_i - \frac{1}{2} \Delta_i - \Delta_s \quad (6.23)$$

where:

$r_{ti}$  = moment arm for frictional torque acting on iceberg (m)

### 6.4.3 Pressure Calculation Method

The impact force reliability model allows the user to select one of the following two methods for evaluating effective ice pressure:

1. Constant pressure method,
2.  $P$ -Area method.

Both methods are based on a reference ice pressure  $p_r$ , which is an input random variable to the reliability model. For the constant pressure method, the effective crushing pressure  $p_{cr}$  is equal to  $p_r$  for the duration of a collision.

Effective ice pressure computed using the  $P$ -Area method is evaluated as follows:

$$p_{cr} = \begin{cases} p_r & \text{for } A_n \leq 0.1\text{m}^2 \\ p_r (A_n / 0.1\text{m}^2)^{-0.4} & \text{for } A_n > 0.1 \text{ m}^2 \end{cases} \quad (6.24)$$

The above equation is an approximation of the  $P$ -Area curve developed by Sanderson [102]. Equation 6.24 is evaluated at each time step of a collision.

#### 6.4.4 Iceberg Equations of Motion

Evaluation of iceberg motions during a collision is based on the normal and tangential forces acting on the iceberg during impact. It is useful to introduce the contact point angle  $\theta_c$  between the iceberg and the structure (see Figure 6.4). The tangential velocity of the iceberg relative to the structure can then be expressed as:

$$u_t = \omega_r r_{ti} + u_g \sin \theta_c - v_g \cos \theta_c \quad (6.25)$$

where:

$\theta_c$  = contact point angle between iceberg and structure (rad)

$\omega_r$  = rotational velocity of iceberg (rad/s)

The sign convention for  $u_t$  is such that a positive value will represent counter-clockwise rotation relative to the structure. The friction force  $F_f$  acting on the iceberg will act in a direction opposite to  $u_t$ . Considering  $F_f$  to be positive if it induces counter-clockwise rotation of the iceberg, the friction force can be written as:

$$F_f = \frac{-u_t}{|u_t|} p_{cr} A_n \mu_f \quad (6.26)$$

Once the crushing force  $F_{cr}$  and frictional force  $F_f$  are determined, the associated translational force components and torsion acting on the iceberg can be evaluated:

$$F_x = F_{cr} \cos \theta_c + F_f \sin \theta_c \quad (6.27)$$

$$F_y = F_{cr} \sin \theta_c - F_f \cos \theta_c \quad (6.28)$$

$$T_r = F_f r_{ti} \quad (6.29)$$

where:

$F_x, F_y = x - y$  force components acting on iceberg (N)

$T_r =$  rotational torsion acting on iceberg (N·m)

The corresponding equations of motion for the iceberg are:

$$\frac{\partial u_g}{\partial t} = \frac{F_x}{(1 + C_m) M} \quad (6.30)$$

$$\frac{\partial v_g}{\partial t} = \frac{F_y}{(1 + C_m) M} \quad (6.31)$$

$$\frac{\partial \omega_r}{\partial t} = \frac{T_r}{I_{zz}} \quad (6.32)$$

where:

$I_{zz} =$  iceberg rotational inertia about  $z$  axis (N·m<sup>2</sup>)

It should be noted that the added rotational inertia of a cylindrical iceberg is zero.

As stated previously, the iceberg must have a positive normal velocity relative to the structure for crushing forces to develop. The normal velocity can be expressed as:

$$V_n = -u_g \cos \theta_c - v_g \sin \theta_c \quad (6.33)$$

The development of frictional forces requires the existence of corresponding normal forces. In addition, the relative tangential velocity  $u_t$  must be non-zero for frictional forces to exist.

#### 6.4.5 Time-Stepping Procedure

Iceberg motions during the impact phase are determined using a numerical time-stepping procedure. The impact phase commences when the iceberg first comes into

contact with the structure, and continues until the normal velocity  $V_n$  becomes negative. Translational and rotational accelerations are determined using equations 6.30 - 6.32, with associated velocities and displacements computed as follows:

$$u_{g\ i+1} = u_{g_i} + \frac{\Delta t}{2} \left[ 3 \left( \frac{\partial u_g}{\partial t} \right)_i - \left( \frac{\partial u_g}{\partial t} \right)_{i-1} \right] \quad (6.34)$$

$$v_{g\ i+1} = v_{g_i} + \frac{\Delta t}{2} \left[ 3 \left( \frac{\partial v_g}{\partial t} \right)_i - \left( \frac{\partial v_g}{\partial t} \right)_{i-1} \right] \quad (6.35)$$

$$\omega_{r\ i+1} = \omega_{r_i} + \frac{\Delta t}{2} \left[ 3 \left( \frac{\partial \omega_r}{\partial t} \right)_i - \left( \frac{\partial \omega_r}{\partial t} \right)_{i-1} \right] \quad (6.36)$$

$$x_{g\ i+1} = x_{g_i} + \Delta t u_{g_i} + \frac{1}{2} \Delta t^2 \left( \frac{\partial u_g}{\partial t} \right)_i \quad (6.37)$$

$$y_{g\ i+1} = y_{g_i} + \Delta t v_{g_i} + \frac{1}{2} \Delta t^2 \left( \frac{\partial v_g}{\partial t} \right)_i \quad (6.38)$$

$$\theta_{r\ i+1} = \theta_{r_i} + \Delta t \omega_{r_i} + \frac{1}{2} \Delta t^2 \left( \frac{\partial \omega_r}{\partial t} \right)_i \quad (6.39)$$

where:

$\theta_r$  = iceberg rotational displacement (rad)

Of critical importance in the impact phase model is the selection of an appropriate time step size. Trial simulations indicated that 40 time steps were sufficient for obtaining accurate force predictions and energy balances. An initial estimate for the collision duration  $t_c$  is made using the estimated collision duration for a head-on collision (equation 3.23). The impact phase model is then run using a time interval  $\Delta t$  of  $t_c/100$ . If the numerical model requires less than 40 time steps, the model is re-run using a finer time interval. Conversely, a larger time interval is selected if the initial simulation is not finished after 500 time steps.

Special attention must be given to the evaluation of frictional forces in the time-stepping model. The friction force  $F_f$  will typically induce rotation of the iceberg, causing

its tangential velocity relative to the structure to be reduced to zero. Disregard for this phenomenon when running the time-stepping model can cause the tangential velocity  $u_t$  to fluctuate about zero (Duthinh and Marsden, [25]). This problem was alleviated by restricting the maximum possible frictional force during any given time step:

$$|F_f| \leq \frac{|u_t| I_{zz}}{\Delta t r_{ii}^2} \quad (6.40)$$

The impact force reliability model is based on the maximum sliding force experienced during a collision. The magnitude of the sliding force is giving by:

$$F_s = \sqrt{F_{cr}^2 + F_f^2} \quad (6.41)$$

The sliding force is evaluated at each time step and compared to the previous maximum value that has occurred during a collision.

## 6.5 Example Problem for Large Iceberg Population

The impact force reliability model has been used to determine design iceberg collisions for an offshore structure with a diameter of 100 m located in water of 100 m depth. Design events have been evaluated for the case of constant ice pressure, and for varying ice pressure with contact area as given by equation 6.24.

### 6.5.1 Design Criterion and Input Distributions

The design criterion for the impact force examples is the same as for the kinetic energy examples. The design load level will have an exceedence probability of 0.1 during the life of the structure. Given that 20 collisions are expected during the structure life, the acceptable exceedence probability for a single collision is 0.0052, as given by equation 5.43.

Input distributions for the large iceberg example are given in Table 6.1 and are considered to be representative of conditions at the Hibernia oilfield off the coast of Newfoundland. Distributions for iceberg mass, aspect ratio, drift velocity, and significant wave height are the same as those for the large iceberg example of Chapter 5. The correlation coefficient for iceberg mass and aspect ratio is again assigned a value of -0.1.

Table 6.1: Input Distributions for Large Iceberg Example Design Problem

Variable	Distribution	Parameters
$M$ ( $10^6$ tonnes)	Lognormal	$\mu = 0.50, \sigma = 1.74$
$h/D_i$	Uniform	Range 0.1 - 0.8
$V_{do}$ (m/s)	Lognormal	$\mu = 0.34, \sigma = 0.29$
$H_s$ (m)	Lognormal	$\mu = 2.44, \sigma = 1.22$
$e'_o$	Uniform	Range 0.0 - 1.0
$p_r$ (MPa)	Lognormal	$\mu = 5.0, \sigma = 5.0$
$\mu_f$	Lognormal	$\mu = 0.08, \sigma = 0.04$

Initial approach eccentricity  $e'_o$  is uniformly distributed between 0 and 1 for potential impacts. A compilation of measured ice pressures by Sanderson [102] suggests that the reference ice pressure  $p_r$  should have a mean value of 5 MPa. Significant scatter of measured ice pressures indicates that the coefficient of variation for  $p_r$  is of the order of unity. Laboratory studies by Forland and Tatinclaux [29] indicate that the ice friction coefficient  $\mu_f$  should have a mean value of approximately 0.08 and a standard deviation of approximately 0.04. Because ice pressure and friction coefficient must both be positive, they are both modelled with lognormal distributions.

### 6.5.2 Design Event for Constant Ice Pressure

The reliability model has been run for various impact force levels to determine the sliding force exceedence probabilities for constant ice pressure presented in Figure 6.5. For the acceptable exceedence probability of 0.0052 for a single collision, the corresponding impact force is  $6.2 \times 10^9$  N with design values and sensitivity coefficients as given in Table 6.2.

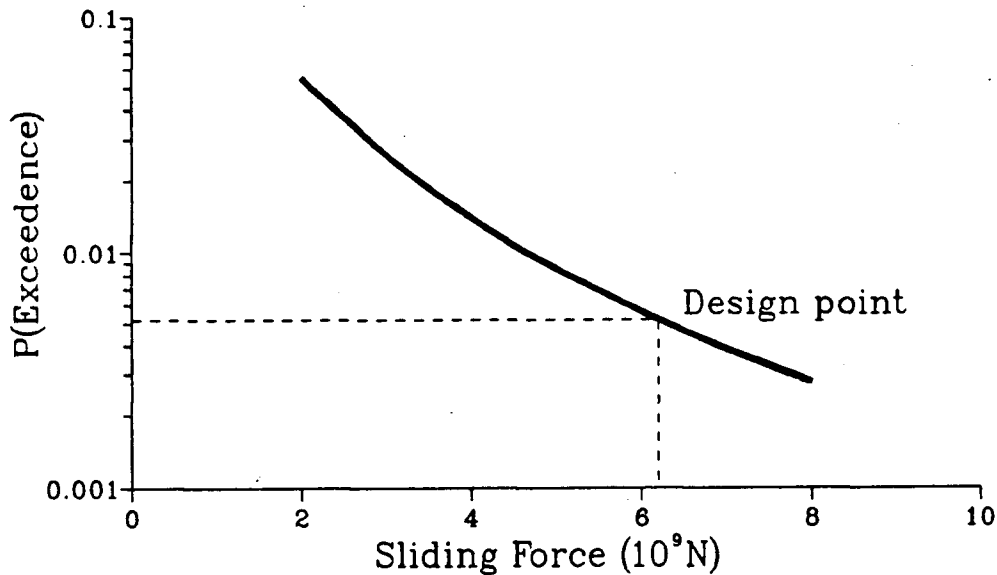


Figure 6.5: Sliding Force Exceedence Probabilities for Large Iceberg Example, Constant Ice Pressure

Due to the large size of the design iceberg, its oscillatory velocity and the influence of the structure on the iceberg drift velocity are both negligible. The sensitivity coefficient for approach eccentricity  $e'_0$  has a value of -0.10, suggesting that the influence of eccentricity is relatively small. To examine the influence of eccentricity on impact force, the design collision was re-evaluated for a head-on impact keeping all other parameters the same. It was found that the impact eccentricity for the design event resulted in a 5%

Table 6.2: Results for Large Iceberg Design Collision, Constant Ice Pressure

Variable	Design Value	Sensitivity
$M$ ( $10^6$ tonnes)	2.86	0.74
$h/D_i$	0.41	0.27
$V_{do}$ (m/s)	0.56	0.40
$H_s$ (m)	2.20	0.008
$e'_o$	0.40	-0.10
$p_r$ (MPa)	9.41	0.46
$\mu_f$	0.072	0.002

Other parameters associated with above design values:

$$D_i = 205 \text{ m}, h = 84 \text{ m}, C_m = 0.81, T_p = 6.6 \text{ s},$$

$$\omega_p^2 D_i / 2g = 9.54, \zeta'_1 = 0.005, V_s = 0.006 \text{ m/s}, t_c = 0.57 \text{ s}$$

force reduction.

The very small sensitivity coefficient for the friction factor  $\mu_f$  suggests that the friction factor has a negligible influence on the design event, and that  $\mu_f$  could be treated as a constant. Note that  $\mu_f$  would likely become very important if the design event were based on the torsion acting on the structure.

The small collision duration indicates that the infinite frequency added mass should be used for the effective iceberg added mass during impact. The infinite frequency added mass coefficient for the design iceberg is 0.31, compared with 0.81 for the zero frequency value. Despite the great difference in the added mass values, the impact force computed using the infinite frequency added mass is only 10% less than the force obtained using the zero frequency added mass.

The sensitivity coefficient for aspect ratio  $h/D_i$  is much greater for the impact force reliability model than for the kinetic energy model. Although aspect ratio does not

significantly affect iceberg kinetic energy, it has a major influence on impact force.

### 6.5.3 Design Event for Varying Ice Pressure with Area

When the variation of ice pressure with area (equation 6.24) is incorporated into the reliability model, impact sliding forces become significantly lower as shown in Figure 6.6. The impact force of the design event is reduced to  $0.43 \times 10^9$  N, only 7% of the design load for constant ice pressure. Design values and sensitivity coefficients are given in Table 6.3.

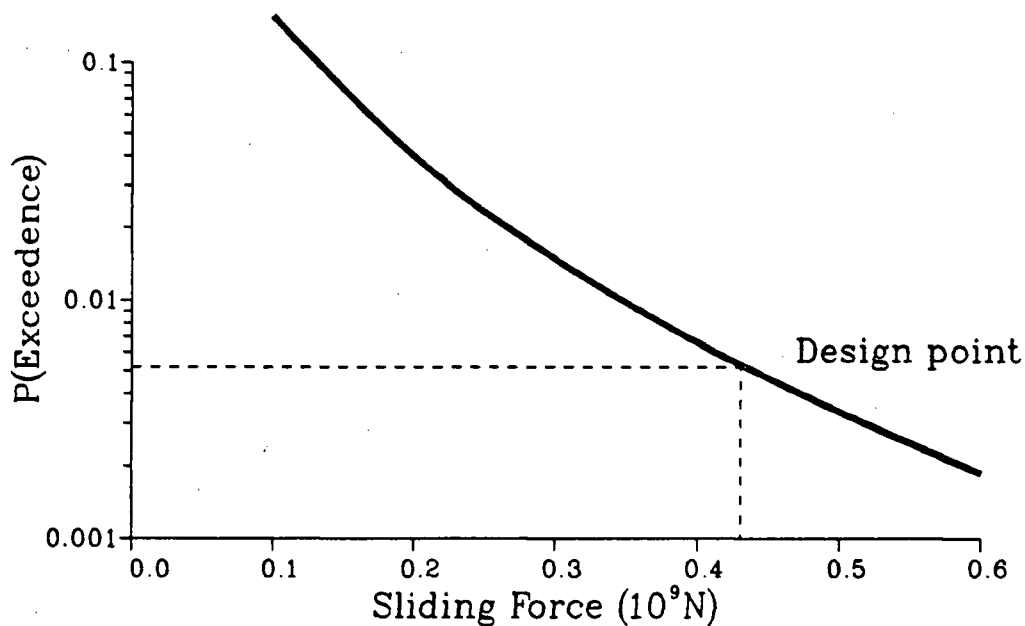


Figure 6.6: Force Exceedence Probabilities for Large Iceberg Example,  $P$ -Area Variation

The sensitivity coefficient for reference pressure  $p_r$  is significantly greater when the  $P$ -Area force method is used. Accordingly, sensitivity coefficients for other variables such as iceberg mass and drift velocity are somewhat smaller. The collision duration of 3.8 s for the design collision is approximately 7 times greater than the corresponding duration for constant ice pressure. Due to the relatively long duration, effective added mass during impact is approximated reasonably well by the zero frequency added mass.

Table 6.3: Results for Large Iceberg Design Collision,  $P$ -Area Variation

Variable	Design Value	Sensitivity
$M$ ( $10^6$ tonnes)	1.73	0.62
$h/D_i$	0.41	0.21
$V_{do}$ (m/s)	0.50	0.35
$H_s$ (m)	2.21	0.012
$e'_o$	0.41	-0.09
$p_r$ (MPa)	14.6	0.67
$\mu_f$	0.072	0.003

Other parameters associated with above design values:

$D_i = 174$  m,  $h = 71$  m,  $C_m = 0.70$ ,  $T_p = 6.6$  s,

$\omega_p^2 D_i / 2g = 8.03$ ,  $\zeta'_1 = 0.008$ ,  $V_s = 0.009$  m/s,  $t_c = 3.8$  s

## 6.6 Example Problem for Small Iceberg Population

To investigate the influence of iceberg size on collision properties, the impact force reliability model has been re-run for an iceberg population with masses that are 1/1000'th of those in the large iceberg example. A similar example problem was investigated using the kinetic energy reliability model. Input distributions are the same as those given in Table 6.1, with the exception of the mass distribution for impacting icebergs. The mass distribution for the smaller iceberg problem has a mean value of 360 tonnes and a standard deviation of 1190 tonnes. The specified exceedence probability for a single collision is 0.0052, as was used for the large iceberg example.

### 6.6.1 Design Collision for Constant Ice Pressure

Sliding force exceedence probabilities for constant ice pressure are shown in Figure 6.7. Parameters for the design load of  $135 \times 10^6$  N are given in Table 6.4.

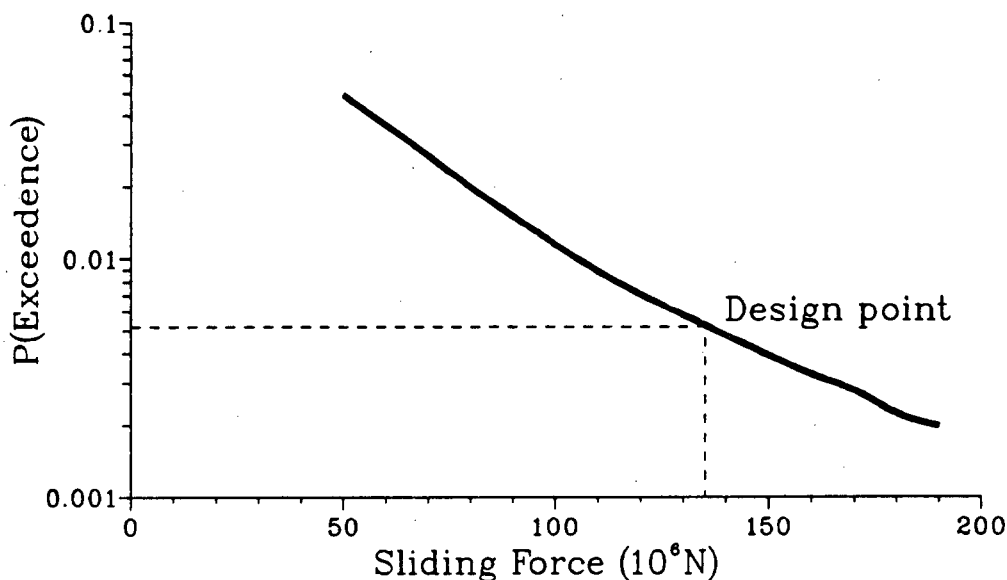


Figure 6.7: Force Exceedence Probabilities for Small Iceberg Example, Constant Ice Pressure

Due to the small size of the design iceberg relative to incident wavelength, oscillatory motions are significant. The oscillatory velocity of the iceberg is 2.6 times its drift velocity. The small size of the iceberg relative to the structure suggests that negative wave drift forces could prevent the design iceberg from impacting the structure; however, the variation of wave drift forces with proximity to the structure has been neglected in the reliability model, and thus a detailed investigation into the influence of variable wave drift forces would be worthwhile for the design event.

As was observed for the large iceberg examples, the influence of collision eccentricity and frictional forces appears to be very small. The short collision duration again suggests

Table 6.4: Results for Small Iceberg Design Collision, Constant Ice Pressure

Variable	Design Value	Sensitivity
$M$ (tonnes)	2500	0.74
$h/D_i$	0.36	0.28
$V_{do}$ (m/s)	0.31	0.10
$H_s$ (m)	2.80	0.22
$e'_o$	0.38	-0.07
$p_r$ (MPa)	10.9	0.56
$\mu_f$	0.072	0.002

Other parameters associated with above design values:

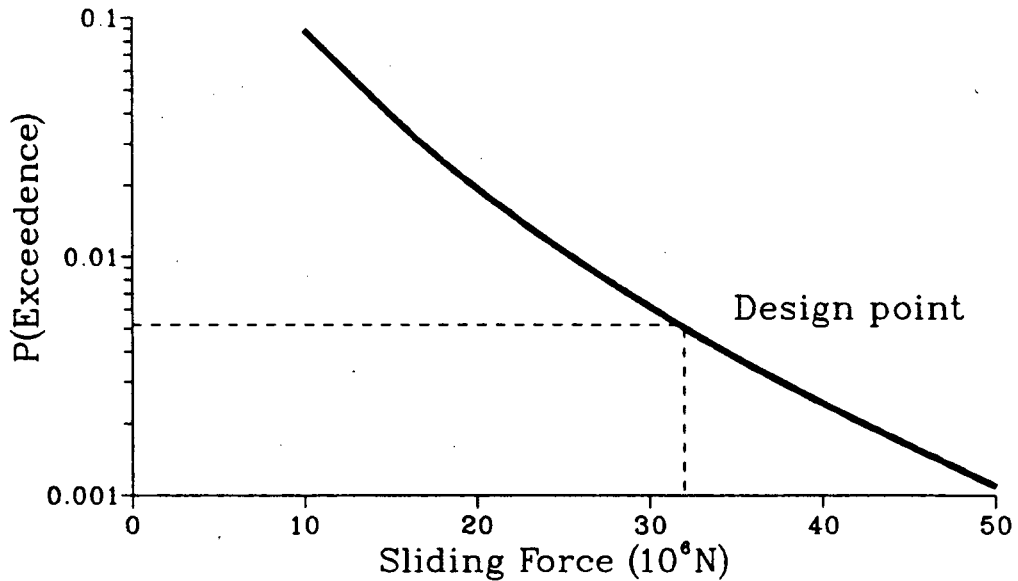
$D_i = 20.6$  m,  $h = 7.3$  m,  $C_m = 0.49$ ,  $T_p = 7.4$  s,

$\omega_p^2 D_i / 2g = 0.75$ ,  $\zeta'_1 = 0.68$ ,  $V_s = 0.81$  m/s,  $t_c = 0.044$  s

that infinite frequency added mass should be used for evaluating impact forces. If the infinite frequency added mass of 0.24 is used, the resulting impact force for the design collision is reduced by 8%.

### 6.6.2 Design Collision for Varying Ice Pressure

If the  $P$ -Area method is used for predicting ice pressure, impact forces are significantly reduced as shown in Figure 6.8. The design load level is  $32 \times 10^6$  N, approximately 1/4 of the load for constant ice pressure, with design collision parameters as given in Table 6.5. The sensitivity coefficients indicate that reference ice pressure becomes more important when the  $P$ -Area method is used, as was observed for the large iceberg example. As expected, the reduction of design load due to  $P$ -Area variation is not as great for the small iceberg example.

Figure 6.8: Force Exceedence Probabilities for Small Iceberg Example,  $P$ -Area VariationTable 6.5: Results for Small Iceberg Design Collision,  $P$ -Area Variation

Variable	Design Value	Sensitivity
$M$ (tonnes)	1350	0.69
$h/D_i$	0.42	0.12
$V_{do}$ (m/s)	0.29	0.04
$H_s$ (m)	2.56	0.12
$e'_o$	0.39	-0.10
$p_r$ (MPa)	16.6	0.69
$\mu_f$	0.072	0.003

Other parameters associated with above design values:

$$D_i = 15.8 \text{ m}, h = 6.7 \text{ m}, C_m = 0.53, T_p = 7.1 \text{ s}, \\ \omega_p^2 D_i / 2g = 0.63, \zeta'_1 = 0.73, V_s = 0.82 \text{ m/s}, t_c = 0.088 \text{ s}$$

## Chapter 7

### Conclusions

Various factors influencing the risk of iceberg collisions with a fixed offshore structure have been examined. Special emphasis has been given to the evaluation of iceberg added mass and impact velocity, which are determined by hydrodynamic effects. Findings from hydrodynamic studies have been incorporated into probabilistic models for evaluating design events based on iceberg kinetic energy and impact force. The probabilistic models can be used to examine the importance of hydrodynamic effects in the design of a particular structure.

#### 7.1 Effective Added Mass

Due to the transient nature of iceberg motions during drifting and collisions with structures, iceberg motions are dependent on hydrodynamic memory effects. It is useful to adopt an effective added mass for evaluating iceberg drift motions or iceberg kinetic energy.

For a drifting iceberg subjected to forces which vary slowly with time, zero frequency added mass can be adopted for evaluating accelerations. Effective added mass is also useful for estimating the kinetic energy or momentum that can be dissipated during an iceberg collision with an offshore structure. For collisions of short duration (i.e.  $t_c\sqrt{g/D_i} < 0.5$ ), the infinite frequency added mass can be used to approximate effective

added mass. The effective added mass for long duration collisions (i.e.  $t_c \sqrt{g/D_i} > 3$ ) will approach the zero frequency value.

If a vertical circular cylinder is selected to model iceberg geometry, the aspect ratio  $h/D_i$  is restricted to a maximum value of 0.86 due to hydrostatic stability requirements. The zero frequency added mass for a circular cylinder increases with relative draft  $h/d$ , and approaches a limiting value of 1.0. Alternatively, the infinite frequency added mass for a circular cylinder increases with aspect ratio  $h/D_i$ , and approaches a limiting value of approximately 0.45 when  $h/D_i$  approaches 0.86. Thus, the effective added mass for an impacting iceberg can vary considerably depending on collision duration. Despite the large difference between zero and infinite frequency added mass values, computations presented in Chapter 6 indicate that the maximum impact force will vary by only 5-10% depending on whether the zero frequency or infinite frequency added is used for force computations. It is recommended that zero frequency added mass can be used in iceberg collision design for all impact scenarios, with the resulting impact force levels having a reasonable degree of conservatism.

## 7.2 Oscillatory Surge Motions

When evaluating iceberg impact velocities, both oscillatory and mean drift velocity components should be considered. Oscillatory motions can be particularly important for smaller icebergs.

Due to the general availability of wave climate data, it is recommended that oscillatory velocities be estimated using response amplitude operators (RAO's). For the low frequency range  $\omega^2 D_i/2g < 0.5$ , it is reasonable to assume that an iceberg will oscillate like a water particle, with its corresponding surge RAO given by equation 3.39. The MacCamy-Fuchs solution for the exciting force on a circular cylinder provides a useful

closed-form solution (equation 3.46) for high frequency surge motions ( $\omega^2 D_i/2g > 3$ ). For the intermediate frequency range, computed RAO's from a numerical diffraction model such as those presented in Chapter 3 should be used for determining oscillatory motions. Results from the kinetic energy and sliding force reliability models indicated that oscillatory motions had a negligible influence on design impact velocities when the frequency parameter  $\omega^2 D_i/2g$  was greater than three for the design event; however, it should be remembered that the relative importance of oscillatory motions is dependent on the magnitude of drift velocities.

### 7.3 Influence of Structure on Iceberg Hydrodynamics

The velocity and added mass of an iceberg can be significantly modified as it approaches a large structure. Hydrodynamic interactions appear to be important when the iceberg diameter is less than half the structure diameter.

The analytical solution for potential flow around a circular cylinder can be used for computing current driven iceberg motions near a large structure. Reasonably good agreement was observed between physical and numerical models for current driven motions near a large structure. It is suggested that the inclusion of convective forces in the numerical drift model could lead to improved estimates of impact eccentricities for current driven motions. The modification of the flow field by the structure can reduce iceberg impact velocities by 10% or more when the relative iceberg size  $D_i/D_s$  is less than 0.3. Experimental observations indicated that approach eccentricities can be significantly increased as icebergs come toward a structure when  $D_i/D_s$  is less than 0.3.

Surge response amplitude operators have been computed for icebergs in the vicinity

of a large structure. The variation in surge response with proximity to the structure appears to be relatively small.

The greatest influence that a structure will have on motions of approaching icebergs is through the modification of wave drift forces. The numerical diffraction model indicates that wave drift forces vary significantly when the iceberg diameter is less than half the structure diameter. Wave drift forces vary cyclically with distance in front of the structure, with a cycle length equal to half the incident wavelength. Due to the large degree of computational effort required for determining wave drift force coefficients, it is suggested that equation 3.52 be used for estimating wave drift forces while evaluating drift trajectories in front of a structure.

A comparison of physical and numerical model results revealed large discrepancies in iceberg impact velocities when wave drift forces varied significantly with proximity to a structure. Impact velocities predicted by the numerical model were significantly lower than velocities for the physical model. When calculating wave drift forces using the far-field method, various second-order effects such as the variation of iceberg rotational orientation due to oscillatory motions were ignored, thus leading to possible errors. Note that the wave drift force coefficient of a small iceberg in front of a structure is highly dependent on wave frequency; thus, the variation of effective wave frequency due to iceberg drift motions will likely have a significant influence on wave drift forces near a structure.

In consideration of the above findings, it is suggested that hydrodynamic interactions between a structure and approaching icebergs can be neglected when designing for iceberg collisions in most cases. Although hydrodynamic interactions can significantly reduce drift velocities of smaller icebergs ( $D_i/D_s < 0.5$ ) in waves near a large structure, additional numerical and experimental studies need to be conducted before conclusive recommendations can be made regarding the degree of velocity reductions that will occur.

## 7.4 Kinetic Energy Reliability Model

A probabilistic model has been presented for evaluating a design collision event based on iceberg kinetic energy. The model has been formulated such that input statistical distributions can be obtained from commonly available environmental data. Iceberg added mass and oscillatory motions are evaluated through deterministic relationships.

The two example problems indicate that iceberg kinetic energy is relatively insensitive to aspect ratio  $h/D_i$ ; thus, it would seem reasonable to infer that iceberg kinetic energy will exhibit little variation with iceberg geometry for a given mass. The example problem for a population of large icebergs indicated that wave-induced oscillatory motions had a negligible influence on iceberg kinetic energy for a design collision event; however, the wave-induced oscillatory component dominated the design impact velocity for a population of smaller icebergs.

## 7.5 Impact Force Reliability Model

If failure of an offshore structure is most likely to be caused by the global load experienced during an iceberg collision, then the design collision should be evaluated using an impact force reliability model such as the one described in Chapter 6. The variation of current velocities near the structure is considered in the model; however, the variation of wave drift forces is neglected.

Sensitivity coefficients for example problems indicated that iceberg approach eccentricity has a relatively small effect on design loads; thus, the assumption of head-on collisions would not be overly conservative. The extremely low sensitivity of the ice friction coefficient suggests that  $\mu_f$  can be treated as a constant.

It was previously shown that iceberg aspect ratio  $h/D_i$  has a minor influence on

iceberg kinetic energy; however, sensitivity coefficients for the impact force examples show a strong dependence on aspect ratio. This result is due to the influence of contact geometry on impact forces. For the vertical sided cylindrical icebergs used in the impact force model, contact areas and associated forces are likely to be greater than values for actual iceberg geometries; thus, the present model can be considered to be conservative. The inclusion of random iceberg geometries would be a significant improvement to the model if sufficient field data concerning actual iceberg shapes were available.

The inclusion of varying wave drift forces with iceberg proximity to a structure is an additional improvement to the impact force model that should be considered more closely. For a structure located in an area of relatively small icebergs ( $D_i/D_s < 0.5$ ), the influence of the structure on iceberg wave drift forces could significantly reduce the impact velocity for a design iceberg collision event.

As shown in the example problems, the variation of ice pressure with contact area can have drastic effect on design forces. For a structure situated in a population of large icebergs, the design impact force for  $P - Area$  variation was shown to be less than one-tenth the corresponding design force based on constant ice pressure. As expected, the importance of  $P - Area$  effects increases with the size of impacting icebergs. There remains great uncertainty regarding ice pressures for large contact areas. Sources of this uncertainty include limited force measurements for large contact areas, and the lack of a comprehensive theory explaining the variation of ice pressure with contact area.

## 7.6 Recommendations for Future Research

There remain many areas of theoretical and practical interest where further research is warranted. The evaluation of iceberg added mass near a structure using the boundary element method is limited by the number of facets that can be modelled. Reliable

values can only be obtained when the separation distance between the iceberg and structure is greater than half a facet length. Isaacson and Cheung [46] have developed a two-dimensional model for predicting zero frequency added mass of an iceberg near a structure. Since the effective added mass of an impacting iceberg is likely to be closer to the infinite frequency added mass, it is suggested that a solution be found for infinite frequency added mass near a structure.

Multi-directional wave effects have been neglected in the present study, resulting in over-predictions of wave drift forces and oscillatory motions. Multi-directional wave effects could significantly reduce impact velocities, particularly for smaller icebergs.

For current driven iceberg motions near a large structure, further work should be done to examine the influence of convective forces on iceberg motions. Further experimental and numerical work should particularly address the influence of convective forces on iceberg approach eccentricities.

Of the various hydrodynamic effects influencing iceberg collisions, the greatest uncertainty lies with the variation of wave drift forces on small icebergs near a large structure. A greater understanding of second-order effects influencing wave driven drift motions is required. Due to the sensitivity of wave drift forces to wave frequency, the influence of random waves on wave drift forces also needs to be addressed.

At this point in time the greatest uncertainty in the analysis of iceberg impact forces is the prediction of ice pressures for large contact areas. Ongoing experimental and theoretical research will lead to a better understanding of the variation of ice pressure with contact area.

## Bibliography

- [1] Allyn, N.F.B., Bein, P., and Tseng, J., "Probabilistic Approaches to Arctic Offshore Engineering", *Proceedings of Arctic '85, Civil Engineering in the Arctic Offshore*, ASCE, San Francisco, 1985, pp. 412-420.
- [2] Ang, A. H.-S., and Tang, W.H., *Probability Concepts in Engineering Planning and Design, Volume II - Decision, Risk, and Reliability*, John Wiley and Sons, New York, 1984, 562 pp.
- [3] Apple Computer Inc., *Inside Macintosh*, Addison-Wesley, Reading, Mass. 1985, 5 Volumes.
- [4] Arunachalam, V.M., Bobby, W., Muggeridge, D.B., and Stacey, R.A., "A Review of Interaction of Icebergs with Offshore Structures", *Proceedings of the Fourth International Conference on Behaviour of Offshore Structures*, Delft, 1985, pp. 693-704.
- [5] Arunachalam, V.M., Murray, J.J., and Muggeridge, D.B., "Short Term Motion Analysis of Icebergs in Linear Waves", *Cold Regions Science and Technology*, Vol. 13, 1987, pp. 247-258.
- [6] Banke, E.G., and Smith, S.D., *A Hindcast Study of Iceberg Drift on the Labrador Coast*, Canadian Technical Report of Hydrography and Ocean Sciences, No. 49, 1984, 161 pp.
- [7] Bass, D., Gaskill, H., and Riggs, N., "Analysis of Iceberg Impacts with Gravity Base Structures at Hibernia", *Proceedings of the Fourth International Symposium*

- on Offshore Mechanics and Arctic Engineering*, Dallas, 1985, Vol. 2, pp. 255-259.
- [8] Bass, D.W. and Sen, D., "Added Mass and Damping Coefficient for Certain 'Realistic' Iceberg Models", *Cold Regions Science and Technology*, Vol. 12, 1986, pp. 163-174.
- [9] Blevins, R.D., *Applied Fluid Dynamics Handbook*, Van Nostrand Reinhold, New York, 1984, 558 pp.
- [10] Borthwick, I., Hadley, R.D., "Ice and Iceberg Contingency Planning and Management for Offshore Oil and Gas Operations", *Proceedings of POLARTECH '86*, Helsinki, 1986, Vol. 1, pp. 323-339.
- [11] Brooks, L.D., "Iceberg Dimensions", *Workshop on Ice Scouring*, Associated Committee on Geotechnical Research, National Research Council of Canada, Technical Memorandum No. 136, 1985, pp. 148-154.
- [12] Bury, K.V., *Statistical Models in Applied Science*, John Wiley & Sons, 1975, 625 pp.
- [13] Cammaert, A.B., and Muggeridge, D.B., *Ice Interaction with Offshore Structures*, Van Nostrand Reinhold, New York, 1988, 432 pp.
- [14] Cammaert, A.B., and Tsinker, G.P., "Impact of Large Ice Floes and Icebergs on Marine Structures", *Proceedings of the Sixth International Conference on Port and Ocean Engineering Under Arctic Conditions*, Quebec, 1981, pp. 653-662.
- [15] Canadian Standards Association, *General Requirements, Design Criteria, the Environment, and Loads*, Preliminary Standard S471-M1989, Part I of the Code for the Design, Construction, and Installation of Fixed Offshore Structures, Canadian Standards Association, Rexdale, Canada, 1989, 63 pp.

- [16] Chakrabarti, S.K., *Hydrodynamics of Offshore Structures*, Springer-Verlag, Berlin, 1987, 440 pp.
- [17] Cheung, K.F., *Hydrodynamic Interactions Between Ice Masses and Large Offshore Structures*, M.A.Sc. Thesis, Department of Civil Engineering, University of British Columbia, 1987, 85 pp.
- [18] Cox, J.R., "Ice Floe Impact Force on Vertical Sided Structures", *Proceedings of Arctic 85, Civil Engineering in the Arctic Offshore*, ASCE, San Francisco, 1985, pp. 211-219.
- [19] Croasdale, K.R., and Person, A., "A Logical Approach to Ice Loads", *The Second Arctic Offshore Symposium*, Houston, 1984, Paper 8, 36 pp.
- [20] Croteau, P., *Dynamic Interactions Between Floating Ice and Offshore Structures*, Earthquake Engineering Research Center, University of California, Berkeley, Report No. UCB/EERC-83/06, 1983, 335 pp.
- [21] Der Kiureghian, A., and Liu, P.-L., "Structural Reliability under Incomplete Probability Information", *Journal of Engineering Mechanics*, ASCE, Vol. 112, No. 1, January, 1986, pp. 85-104.
- [22] Dunwoody, A.B., "The Design Ice Island for Impact Against an Offshore Structure", Paper No. OTC 4550, *Proceedings of the Fifteenth Annual Offshore Technology Conference*, Houston, 1983, Vol. 2, pp. 325-330.
- [23] Dunwoody, A.B., "Ice Alert Levels for Arctic Operations", *Proceedings of the Sixth International Symposium on Offshore Mechanics and Arctic Engineering*, Houston, 1987, Vol. 4, pp. 41-46.

- [24] Dunwoody, A.B., "Utilizing Design Events within Risk-Based Design", *Proceedings of Arctic '85, Civil Engineering in the Arctic Offshore*, ASCE, San Francisco, 1985, pp. 395-402.
- [25] Duthinh, D., and Marsden, S., "Iceberg Impact Load on a Gravity Based Structure", *Cold Regions Engineering, Proceedings of the Fourth International Conference*, ASCE, Anchorage, 1986, pp. 82-92.
- [26] El-Tahan, M., and Davis, H.L., "Correlation Between Iceberg Draft and Above Water Dimensions", *Workshop on Ice Scouring*, Associated Committee on Geotechnical Research, National Research Council of Canada, Technical Memorandum No. 136, 1985, pp. 130-147.
- [27] El-Tahan, M., Venkatesh, S., and El-Tahan, H., "Validation and Quantitative Assessment of the Deterioration Mechanisms of Arctic Icebergs", *Transactions of the ASME, Journal of Offshore Mechanics and Arctic Engineering*, Vol. 109, February, 1987, pp. 102-108.
- [28] Faltinsen, O.M., and Michelsen, F.C., "Motions of Large Structures in Waves at Zero Froude Number", *Proceedings of the International Symposium on the Dynamics of Marine Vehicles and Structures in Waves*, London, 1974, pp. 91-106.
- [29] Forland, K.A., and Tatinclaux, J.-C., "Laboratory Investigation of the Kinetic Friction Coefficient of Ice", *Proceedings of the 1984 IAHR Ice Symposium*, Hamburg, 1984, pp. 19-28.
- [30] Foschi, R.O., *RELAN User's Manual*, Department of Civil Engineering, University of British Columbia, Vancouver, B.C., 1988.

- [31] Garrison, C.J., "Hydrodynamic Loading of Large Offshore Structures: Three-Dimensional Source Distribution Methods", *Numerical Methods in Offshore Engineering*, ed. Zienkiewicz, O.C., Lewis, R.W., and Stagg, K.G., John Wiley & Sons, Chichester, England, 1978, pp. 87-139.
- [32] Garrison, C.J., and Berklite, R.B., "Impulsive Hydrodynamics of Submerged Rigid Bodies", *Journal of the Engineering Mechanics Division*, ASCE, Vol. 99, No. EM1, February, 1973, pp. 99-120.
- [33] Harms, V.W., "Ice-Floe Wave Drift Experiments", Paper No. 5084, *Proceedings of the Eighteenth Annual Offshore Technology Conference*, Houston, 1986, Vol. 1 pp. 9-20.
- [34] Hasofer, A.M., and Lind, N.C., "Exact and Invariant Second-Moment Code Format", *Journal of the Engineering Mechanics Division*, ASCE, Vol. 100, No. EM1, February, 1974, pp. 111-121.
- [35] Hay and Company Consultants Inc. , *Motion and Impact of Icebergs*, Environmental Studies Revolving Funds of Canada, Report No. 044, Vancouver, 1986, 135 pp.
- [36] Hogben, N., and Standing, R.G., "Wave Loads on Large Bodies", *Proceedings of the International Symposium on the Dynamics of Marine Vehicles and Structures in Waves*, London, 1974, pp. 258-277.
- [37] Hohenbichler, M., and Rackwitz, R., "Non-Normal Dependent Vectors in Structural Safety", *Journal of the Engineering Mechanics Division*, ASCE, Vol. 107, No. EM6, December, 1981, pp. 1227-1238.
- [38] Hotzel, I.S., and Miller, J.D., "Icebergs: Their Physical Dimensions and the Presentation and Application of Measured Data", *Annals of Glaciology* 4, 1983, pp.

- 116-123.
- [39] Hotzel, I.S., Miller, J.D., Johansson, W.B., and Inkster, J., "Simulated Oil Exploration Operations in Baffin Bay", *Proceedings of the Third International Symposium on Offshore Mechanics and Arctic Engineering*, New Orleans, 1984, Vol. 3, pp. 316-323.
- [40] Hsiung, C.C., and Aboul-Azm, A.F., "Iceberg Drift Affected by Wave Action", *Ocean Engineering*, Vol. 9, No. 5, 1982, pp. 433-439.
- [41] Imai, K., Riho, Y., Matsumoto, T., Takahashi, T., and Bando, K., "Wave Force Analysis by the Finite Element Method", *Transactions of the ASME, Journal of Offshore Mechanics and Arctic Engineering*, Vol. 109, November, 1987, pp. 320-326.
- [42] Isaacson, M., "Iceberg Interactions with Offshore Structures", *Proceedings of Arctic '85, Civil Engineering in the Arctic Offshore*, San Francisco, 1985, pp. 276-284.
- [43] Isaacson, M., "Ice Mass Motions Near an Offshore Structure", *Transactions of the ASME, Journal of Offshore Mechanics and Arctic Engineering*, Vol. 109, May, 1987, pp. 206-210.
- [44] Isaacson, M., "Influence of Wave Drift Force on Ice Mass Motions", *Proceedings of the Third International Symposium on Offshore Mechanics and Arctic Engineering*, Houston, 1988, Vol. 2, pp. 125-130.
- [45] Isaacson, M., "Nonlinear Inertia Forces on Bodies", *Journal of Waterway, Port, Coastal, and Ocean Engineering*, ASCE, Vol. 105, No. WW3, August, 1979, pp. 213-227.
- [46] Isaacson, M., and Cheung, K.F., "Hydrodynamics of Ice Mass Near Large Offshore

- Structure", *Journal of Waterway, Port, Coastal, and Ocean Engineering*, ASCE, Vol. 114, No. 4, July, 1988, pp. 487-502.
- [47] Isaacson, M., and Cheung, K.F., "Influence of Added Mass on Ice Impacts", *Canadian Journal of Civil Engineering*, Vol. 15, No. 4, August, 1988, pp. 698-708.
- [48] Isaacson, M., and Dello Stritto, F., "Motion of an Ice Mass Near a Large Offshore Structure", Paper No. OTC 5085, *Proceedings of the Eighteenth Annual Offshore Technology Conference*, Houston, 1986, Vol. 1, pp. 21-27.
- [49] Johnson, R.C., and Benoit, J.R., "Iceberg Impact Strength", Paper No. OTC 5599, *Proceedings of the Nineteenth Annual Offshore Technology Conference*, Houston, 1987, Vol. 4, pp. 417-423.
- [50] Johnson, R.C., and Nevel, D.E., "Ice Impact Structural Design Loads", *Proceedings of the Eighth International Conference on Port and Ocean Engineering Under Arctic Conditions*, Greenland, 1985, pp. 569-578.
- [51] Jordaan, I.J., Appleby, J., and Fidjestoel, P., "Ice-structure Interaction - Some Recent Veritas Approaches", *The Journal of Canadian Petroleum Technology*, November-December 1983, pp. 55-57.
- [52] Kobayashi, N., and Frankenstein, S., "Wave Drift Force on Ice Floe", *Journal of Waterway, Port, Coastal, and Ocean Engineering*, ASCE, Vol. 113, No. 5, September, 1987, pp. 476-492.
- [53] Kokkinowrachos, K., Bardis, L., and Mavrakos, S., "Drift Forces on One and Two-Body Structures in Regular Waves", *Proceedings of the 3rd International Conference on Behaviour of Off-Shore Structures*, Cambridge, Mass., 1983, Vol. 1, pp. 467-489.

- [54] Korzhavin, K.N., *Action of Ice on Engineering Structures*, CRREL Translation TL260, U.S. Army Cold Regions Research and Engineering Laboratory, Hanover, N.H., 1971.
- [55] Kristensen, M., and Squire, V.A., "Modelling of Antarctic Tabular Icebergs in Ocean Waves", *Annals of Glaciology* 4, 1983, pp. 152-157.
- [56] Lawrence, P.D., and Mauch, K., *Real-time Microcomputer System Design: An Introduction*, McGraw-Hill, New York, 1987, 568 pp.
- [57] LeBlond, P.H., Calisal, S.M., and Isaacson, M. de St. Q., *Wave Spectra in Canadian Waters*, Canadian Contractor Report of Hydrography and Ocean Sciences, No. 6, 1982, 193 pp.
- [58] Lever, J.H., Attwood, D., and Sen, D., "Factors Affecting the Prediction of Wave-Induced Iceberg Motion", *Cold Regions Science and Technology*, Vol. 15, 1988, pp. 177-190.
- [59] Lever, J.H., Reimer, E., and Diemand, D., "A Model Study of the Wave-Induced Motion of Small Icebergs and Bergy Bits", *Transactions of the ASME, Journal of Offshore Mechanics and Arctic Engineering*, Vol. 110, February, 1988, pp. 101-107.
- [60] Lever, J.H., and Sen, D., "A Method to Upgrade Iceberg Velocity Statistics to Include Wave-Induced Motion", *Transactions of the ASME, Journal of Offshore Mechanics and Arctic Engineering*, Vol. 109, August, 1987, pp. 278-286.
- [61] Lever, J.H., Sen, D., and Attwood, D., "The Influence of Shape on Iceberg Wave-Induced Velocity Statistics", *Proceedings of the Seventh International Symposium on Offshore Mechanics and Arctic Engineering*, Houston, 1988, Vol. 4, pp. 125-132.

- [62] Lewis, J.K.C., and Benedict, C.P., "Burial Parameters: An Integrated Approach to Limit Overdesign", *Proceedings of the Symposium Production and Transportation Systems for the Hibernia Discovery*, St. John's, Canada, 1981, pp. 189-206.
- [63] Lighthill, J., "Waves and Hydrodynamic Loading", *Proceedings of the Second International Conference on the Behaviour of Off-Shore Structures*, London, 1979, Vol. 1, pp. 1-40.
- [64] Lindberg, K., and Andersson, L., "Ice Impacts on Semisubmersibles", *Proceedings of the Sixth International Symposium on Offshore Mechanics and Arctic Engineering*, Houston, 1987, Vol. 4, pp. 313-320.
- [65] Loken, A.E., "Hydrodynamic Interaction between Several Floating Bodies of Arbitrary Form in Waves", *Proceedings of the International Symposium on Hydrodynamics in Ocean Engineering*, Norway, 1981, Vol. 2, pp. 745-779.
- [66] Luk, C.-H., "Added Mass and Damping for Ice Floes by Long Water Wave Theory", *Journal of Waterway, Port, Coastal, and Ocean Engineering*, ASCE, Vol. 113, No. 5, September, 1987, pp. 523-539.
- [67] Madsen, H.O., Krenk, S., and Lind, N.C., *Methods of Structural Safety*, Prentice-Hall, Englewood Cliffs, N.J., 1986, 403 pp.
- [68] Madsen, M.N., Nielsen, J.B., Klinting, P., and Knudsen, J., "A Design Load Method for Offshore Structures Based Upon the Joint Probability of Environmental Parameters", *Proceedings of the Seventh International Symposium on Offshore Mechanics and Arctic Engineering*, Houston, 1988, Vol. 2, pp. 75-80.
- [69] Maes, M.A., Jordaan, I.J., Appleby, J.R., and Fidjestol, P., "Risk Assessment of Ice Loading for Fixed Structures", *Proceedings of the Third International Symposium*

- on *Offshore Mechanics and Arctic Engineering*, New Orleans, 1984, Vol. 3, pp. 220-227.
- [70] Maes, M.A. and Jordaan, I.J., "Arctic Environmental Design Using Short Data Extremal Techniques", *Proceedings of the Fifth International Symposium on Offshore Mechanics and Arctic Engineering*, Tokyo, 1986, Vol. 4, pp. 13-19.
- [71] Mansour, A.E., and Sinha, R.N., "Comparison of Reliability of Ocean Vehicles Using Asymptotic Wave Load Distribution", *Transactions of the ASME, Journal of Offshore Mechanics and Arctic Engineering*, Vol. 110, February, 1988, pp. 9-16.
- [72] Marko, J.R., Fissel, D.B., and Birch, J.R., *Physical Approaches to Iceberg Severity Prediction*, Environmental Studies Revolving Funds of Canada, Report No. 038, Sidney, B.C., 1986, 104 pp.
- [73] Martec Limited, *Iceberg Statistics*, Final report submitted to Ice Climatology Division of Environment Canada, Halifax, Canada, 1982, 134 pp.
- [74] Maruo, H., "The Drift of a Body Floating on Waves", *Journal of Ship Research*, December, 1960, pp. 1-10.
- [75] Masuda, K. Kato, W., and Ishizuka, H., "Second-Order Diffraction Loads on Plural Vertical Cylinder with Arbitrary Cross Sections", *Transactions of the ASME, Journal of Offshore Mechanics and Arctic Engineering*, Vol. 109, November, 1987, pp. 314-319.
- [76] McTaggart, K.A., and Davenport, A.G., "Wind/Wave Tank Tests of Drifting Iceberg Models", *Proceedings of POLARTECH '86*, Helsinki, 1986, Volume 1, pp. 364-379.

- [77] Mei, C.C., *The Applied Dynamics of Ocean Surface Waves*, John Wiley and Sons, New York, 1983, 740 pp.
- [78] Miles, M., and Murdey, D.C., *Results of Measurements of Beach Reflection for Two Beaches Fitted in the NRC Ship Tank*, Internal Report No. LTR-SH-192, Marine Dynamics and Ship Laboratory, Division of Mechanical Engineering, Division of Mechanical Engineering, National Research Council of Canada, Ottawa, 1976, 21 pp.
- [79] Miller, J.D., and Hotzel, J.D., "Iceberg Flux Estimation in the Labrador Sea", *Proceedings of the Third International Symposium on Offshore Mechanics and Arctic Engineering*, New Orleans, 1984, Vol. 3, pp. 298-304.
- [80] Mobil Oil Canada Limited, *Hibernia Development Project Environmental Impact Statement - Volume II, Project Description*, 1985, 150 pp.
- [81] Mobil Oil Canada Limited, *Hibernia Development Project Environmental Impact Statement - Volumes IIIa and IIIb, Biophysical Assessment*, 1985, 260 pp. and 238 pp.
- [82] Motora, S., Masataka, F., Sugiura, M., and Sugita, M., "Equivalent Added Mass of Ships in Collisions", *Selected Papers from the Journal of the Society of Naval Architects of Japan*, Vol. 7, 1971, pp. 138-148.
- [83] Murotsu, Y., Kishi, M., Okada, H., Ikeda, Y., and Matsuzaki, S., "Probabilistic Collapse Analysis of Offshore Structure", *Transactions of the ASME, Journal of Offshore Mechanics and Arctic Engineering*, Vol. 109, August, 1987, pp. 270-277.
- [84] Naylor, T.H., Balintfy, J.L., Burdick, D.S., and Chu, K., *Computer Simulation Techniques*, John Wiley and Sons, New York, 1966, 352 pp.

- [85] Nessim, M.A., Cheung, M.S., and Jordaan, I.J., "Ice Action on Fixed Offshore Structures: A State-of-the-Art Review", *Canadian Journal of Civil Engineering*, Vol. 14, No. 3, June, 1987, pp. 381-407.
- [86] Neu, H.J.A., *11-Year Deep Water Wave Climate of Canadian Atlantic Waters*, Canadian Technical Report of Hydrography and Ocean Sciences, No. 13, 1982, 48 pp.
- [87] Nevel, D.E., "Iceberg Impact Forces", *IAHR Working Group on Ice Forces, 3rd State-of-the-Art Report*, ed. Sanderson, T.J.O., U.S. Army Cold Regions Research and Engineering Laboratory, Hanover, N.H., 1987, pp. 197-221.
- [88] Newman, J.N., "The Drift Force and Moment on Ships in Waves", *Journal of Ship Research*, March, 1967, pp. 51-60.
- [89] Newman, J.N., *Marine Hydrodynamics*, MIT Press, Cambridge, Mass., 1977, 402 pp.
- [90] NORDCO Limited, *An Investigation of the Hydrodynamic Interaction of an Iceberg with a Gravity Based Offshore Structure - Final Report*, Report submitted to the National Research Council of Canada, St. John's, Canada, 1985, 130 pp.
- [91] NORDCO Limited, *A Review of Ice Information for Eastern Canada*, Report submitted to the Royal Commission on the Ocean Ranger Marine Disaster, St. John's, Canada, 1985, 161 pp.
- [92] Ostergaard, C., and Schelin, T.E., "Comparison of Experimental and Theoretical Wave Action", *Applied Ocean Research*, Vol. 9, No. 4, 1987, pp. 192-213.
- [93] Pearson, D.E., and Ro, C.-U., "Iceberg Trajectory Speed Evaluation for the

- Labrador Sea”, *Proceedings of the Ninth Canadian Symposium on Remote Sensing*, St. John’s, Canada, 1984, pp. 85-90.
- [94] Petersen, M.J., and Pedersen, P.T., “Collisions between Ships and Offshore Platforms”, Paper No. OTC 4134, *Proceedings of the Thirteenth Annual Offshore Technology Conference*, Houston, 1981, Vol. 4, pp. 163-171.
- [95] Pinkster, J.A., *Low Frequency Second Order Wave Exciting Forces on Floating Structures*, Netherlands Ship Model Basin Publication No. 650, Wageningen, Netherlands, 1980, 201 pp.
- [96] Pinkster, J.A., “Mean and Low Frequency Wave Drifting Forces on Floating Structures”, *Ocean Engineering*, Vol. 6., 1979, pp. 593-615.
- [97] Rackwitz, R., and Fiessler, B., “Structural Reliability under Combined Random Load Sequences”, *Computers & Structures*, Vol. 9, 1977, pp. 489-494.
- [98] Robe, R.Q., “Iceberg Climatology”, *Iceberg Management in Offshore Exploration, Production, and Transportation*, Memorial University of Newfoundland, St. John’s, Canada, 1982, pp. 1-25.
- [99] Salvalaggio, M.A., and Rojansky, M., “The Importance of Wave-Driven Icebergs Impacting an Offshore Structure”, Paper No. OTC 5086, *Proceedings of the Eighteenth Annual Offshore Technology Conference*, Houston, 1986, Vol. 1, pp. 29-38.
- [100] Sanderson, T.J.O. (ed.), *IAHR Working Group on Ice Forces, 3rd State-of-the-Art Report*, U.S. Army Cold Regions Research and Engineering Laboratory, Hanover, N.H., 1987, 232 pp.
- [101] Sanderson, T.J.O., *Ice Mechanics - Risks to Offshore Structures*, Graham & Trotman, London, 1988, 253 pp.

- [102] Sanderson, T.J.O., "A Pressure-Area Curve for Ice", *IAHR Working Group on Ice Forces, 3rd State-of-the-Art Report*, ed. Sanderson, T.J.O., U.S. Army Cold Regions Research and Engineering Laboratory, Hanover, N.H., 1987, pp. 75-98.
- [103] Sarpkaya, T., and Isaacson, M., *Mechanics of Wave Forces on Offshore Structures*, Van Nostrand Reinhold, New York, 1981, 651 pp.
- [104] Shirasawa, K., Riggs, N.P., and Muggeridge, D.B., "The Drift of a Number of Idealized Model Icebergs", *Cold Regions Science and Technology*, Vol. 10, 1984, pp. 19-30.
- [105] Simiu, E., and Scanlan, R.H., *Wind Effects on Structures*, John Wiley & Sons, New York, 1978, 458 pp.
- [106] Squire, V.A., "Numerical Modelling of Realistic Ice Floes in Ocean Waves", *Annals of Glaciology* 4, 1983, pp. 277-282.
- [107] Standing, R.G., Brendling, W., *Collisions of Attendant Vessels with Offshore Installations - Part 2, Detailed Calculations*, Report No. OTH 84 209, National Maritime Institute, England, 1985, 18 pp.
- [108] Standing, R.G., Dacunha, N.M.C., and Matten, R.B., *Mean Wave Drift Forces: Theory and Experiment*, Report No. OT-R-8175, National Maritime Institute, England, 1981, 68 pp.
- [109] Streeter, V.L., and Wylie, E.B., *Fluid Mechanics*, McGraw-Hill, New York, 1979, 562 pp.
- [110] Thoft-Christensen, P., and Baker, M.J., *Structural Reliability Theory and Its Applications*, Springer-Verlag, Berlin, 1982, 267 pp.

- [111] Tvedt, L., *Two Second-Order Approximations to the Failure Probability*, Veritas Report RDIV/20-004-83, Det norske Veritas, Oslo, Norway, 1983.
- [112] Van Oortmerssen, G., "Hydrodynamic Interaction Between Two Structures, Floating in Waves", *Proceedings of the Second International Conference on Behaviour of Off-Shore Structures*, London, 1979, Vol. 1, pp. 339-353.
- [113] Vanmarcke, E., and Angelides, D., "Risk Assessment for Offshore Structures: A Review", *Journal of Structural Engineering*, ASCE, Vol. 109, No. 2, February, 1983, pp. 555-571.
- [114] Vinogradov, O.G., and Croasdale, K.R., "Flow of Ice Floe Against a Cylindrical Structure", *Proceedings of the Sixth International Symposium on Offshore Mechanics and Arctic Engineering*, Houston, 1987, Vol. 4, pp. 365-370.
- [115] Wehausen, J.V., "The Motion of Floating Bodies", *Annual Review of Fluid Mechanics*, Vol. 3, 1971, pp. 237-268.
- [116] West, J., and Newton, D., "A Quick Look at QuickCapture", *Byte*, December, 1988, pp. 199-204.
- [117] White, F.M., Spaulding, M.L., and Gominho, L., *Theoretical Estimates of the Various Mechanisms Involved in Iceberg Deterioration in the Open Ocean Environment*, United States Coast Guard Report No. CG-D-62-80, 1980, 126 pp.
- [118] Yamamoto, T., "Hydrodynamic Forces on Multiple Circular Cylinders", *Journal of the Hydraulics Division*, ASCE, Vol. 102, No. HY9, September, 1976, pp. 1193-1210.
- [119] Yeung, R.W., "Added Mass and Damping of a Vertical Cylinder in Finite-Depth Water", *Applied Ocean Research*, Vol. 3, No. 3, 1981, pp. 119-133.

- [120] Zaleski-Zamenhof, L.C., and Rojansky, M., "Towards an Actual Probabilistic Approach in Predicting Offshore Structures Behaviour in Arctic Regions", *Proceedings of the Fourth International Conference on Behaviour of Offshore Structures*, Delft, 1985, pp. 705-716.